Neutral Strangeness Production with the ZEUS Detector at HERA

Chuanlei Liu
Department of Physics
McGill University, Montreal, QC Canada
January 2007

A thesis submitted to McGill University in partial fulfillment of the requirements of the degree of Doctor of Philosophy

Your file Votre référence
ISBN: 978-0-494-32307-6
Our file Notre référence
ISBN: 978-0-494-32307-6

Abstract

The inclusive production of the neutral strange particles, Λ, $\bar{\Lambda}$ and K^0_S, has been studied with the ZEUS detector at HERA. The measurement provides a way to understand the fragmentation process in *ep* collisions and to check the universality of this process. The strangeness cross sections have been measured and compared with Monte Carlo (MC) predictions. Over the kinematic regions of interest, no Λ to $\bar{\Lambda}$ asymmetry was observed. The relative yield of Λ and K^0_S was determined and the result was compared with MC calculations and results from other experiments. A good agreement was found except for the enhancement in the photoproduction process. Clear rapidity correlation was observed for particle pairs where either quark flavor or baryon number compensation occurs. The $K^0_S K^0_S$ Bose-Einstein correlation measurement gives a result consistent with those from LEP measurements. The Λ polarizations were measured to be consistent with zero for HERA I data.

Abstract in French

La mesure de production inclusive des particules étranges neutres Λ, $\bar{\Lambda}$ et K^0_S avec le détecteur ZEUS à HERA permet de comprendre le processus de fragmentation dans les collisions *ep* et de vérifier son universalité. Les sections efficaces de production d'étrangeté ont été mesurées et comparées avec les prédictions de simulations Monte-Carlo (MC). Dans les régions cinématiques d'intérêt, aucune asymétrie de production entre baryons et anti-baryons n'a été observée. Les taux relatifs de production entre les Λ et les K^0_S ont aussi été mesurés et comparés avec les calculs MC et les résultats d'autres expériences. L'accord est en général bon sauf pour un surplus observé dans le processus de photoproduction. De plus, des effects prononcés de corrélation en rapidité ont été mis en évidence pour des paires de particules pour lesquelles la compensation de saveur ou de nombre baryonique est possible. Les études de corrélation Bose-Einstein du système $K^0_S K^0_S$ donnent un résultat consistant avec celui des expériences du LEP. Enfin, les polarisations des Λ se sont avérées compatibles avec zéro pour les données de HERA I.

Contents

List of Figures

List of Tables

Acknowledgments

The four-year Ph.D. life indeed brought me much invaluable and memorable experience. Many thanks should be given to those people who made this period of time possible and enjoyable.

The first person to whom I would like to express my deep and sincere thanks is my supervisor, Prof. François Corriveau. It is him who made this thesis and my stay in ZEUS possible. He has been giving many supports on and much sound advice to the thesis work. Thanks also should go to him for many friendly helps and discussions on non-academic issues.

Working in the CAL group at the beginning of my stay in ZEUS is the time that I really got to know people here. Many thanks are to the CAL experts, Isabell Melzer, Alessandro Polini, Wladmir Hain and Cathy Farrow who got me started with the CAL work, helped me out in case of problems and showed me their selfless and invaluable dedication to the ZEUS experiment. I would like to thank the coordinators of the QCD/Hadronic-Final-States physics group. Special thanks should be given to Sergei Chekanov. His enthusiasm for physics, patient explanations and generous helps are greatly appreciated. I also would like to thank Andrew Cottrell for the innumerable and helpful discussions about the analyses. Although he has left physics, he has really done an excellent job in ZEUS and nice to know him. Furthermore, I am very grateful to Prof. Roman Walczak for his efforts to proceed the final publication. Thanks to ZEUS spokesperson, Rik Yoshida, Elisabetta Gallo and Yuji Yamazaki and physics chairmen, Matthew Wing and Massimo Corradi for their significant contributions to the ZEUS experiment and inviting me to present H1 and ZEUS results in international conferences.

Prof. Tommy Mark, the former director of physics department at McGill, means too much to me. It is him to make my stay at McGill feel like home. He took

care of me generously and thoroughly both on study and living. He has a very strong enthusiasm in Chinese traditional culture. He surprised me when he spoke a fluent Chinese and made a beautiful poem. A lot of thanks should go to Ms. Paula Domingues and Mrs. Elizabeth Shearon of physics department. They gave me many helps to make me settle down when I was just at McGill. After I moved to Hamburg, all of the communications, letter deliveries and other important things related to McGill even much more relied on their helps. Thanks for their important supports and helps. I also feel grateful to Dr. Roberval Walsh and Prof. Mauricio Barbi of physics department when I just got in ZEUS. They both showed me around DESY and got me started the work in ZEUS. Discussions and helps in the following years from they both are really grateful.

To live in Hamburg, a lot of fun was created and shared by many friends, who changed my life style from black-white to colorful. Thanks to all of you - Yujin Ning, Zhenhai Ren, Liang Li and Changyi Zhou etc. I remember many times we gathered together, taking parties, playing cards, ping-pang, basketball and ..., with laughs, fun and good foods.

Great thanks and top honors should be given to my parents. Wherever I am, your encouragements and words are always with me, and these are the endless source of my struggle for life. No matter how much you are able to understand what I am working on, this thesis is full of love and thanks to you both! Also many thanks to my sisters, nephews and nieces. I did enjoy each time being and talking with you. Another person whom I feel really owe much is my wife, Chengling Zhu. Her countless supports and taking care indeed bring me a life of ease and pleasant in Germany.

Chapter 1

Introduction

The Standard Model (SM) of particle physics is a very successful theory to describe the fundamental constituents of matter and the interactions between them. According to the present understanding, the basic constituents of matter are spin-1/2 fermions along with their anti-particles. The fermionic family is composed of three pairs of leptons (electron, muon, tau and their associated neutrinos) and three pairs of quarks (up, down, strange, charm, beauty and top). The interactions among these fermions are mediated and described by spin-1 bosons (the spin of the graviton is 2). The current known four basic forces are strong, electromagnetic, weak and gravitational forces. The gravitational force is not included in the SM. Different forces, characterizing the type of interactions, are carried by different groups of bosons. The neutral photon, γ, mediates the electromagnetic interaction. Three vector bosons, $W^{\pm}$ and Z^0, carry the weak forces and eight species of gluons, g, mediate the strong force. The SM has successfully predicted the existence of bosons like $W^{\pm}$, Z^0 and gluon, and of charm and top quarks, all of which make us have more confidence in the model. However, the model also faces a few challenges like the inability to describe the gravitational force. Therefore the SM is still an incomplete theory in particle physics, though successful in many aspects, and awaits further developments.

From an experimental point of view, there are two revolutionary developments which have been made in unraveling the structure of matter during the last century. The first one is the famous α-particle scattering experiment on a metal foil, carried out by Ernest Rutherford in 1911. This experiment relied on the very basic concept that the angular and energy distributions of the scattered point-like test particle are

related to and can reflect the inner structure of the target. The significance of this experiment is that it clearly showed that the atom has a hard compact component, the atomic nucleus. Many years later, nuclei were found to be composed of protons and neutrons. This brings our knowledge of the elementary block of matter from atom to proton and neutron. The original idea of the Rutherford scattering was proved to be marvelously successful and consequently led to the second breakthrough in the later sixties at the Stanford Linear Accelerator Center (SLAC). The electron-proton (ep) scattering at SLAC is essentially a repetition of the Rutherford scattering experiment but at a smaller scale and with higher collision energy. The experiment carried out at SLAC showed that the proton itself has inner constituents, later identified as quarks. The quark structure hence draws our understanding further from the proton to about a 1000 times smaller scale, thus mapping the quark content.

The Heisenberg uncertainty relationship tells us that higher energy is required in order to probe smaller size of matter. The storage rings and synchrotron accelerators were developed like HERA at DESY (Deutsches Elektronen Synchrotron) in the 1990s. The center-of-mass energy of the electron-proton collisions at HERA reaches up to 300 GeV compared to 30 GeV in the fixed target experiments. However, several new phenomenological issues like the existence of the Higgs bosons and the supersymmetric particles challenge the current colliders and wait to be confirmed by much higher energy colliders. Given these missions, the LHC (Large Hadron Collider) was proposed and constructed at CERN in the past several years. The LHC will provide proton-proton head-on collisions at a level of 14 TeV center-of-mass and is going to start operation for physics in 2007. The next proposed collider is ILC (International Linear Collider), which is designed for electron-positron collisions at a center-of-mass energy of up to 1 TeV. But over one decade is expected to be taken from the design to the construction and then to the physics data taking at the ILC.

The HERA project has been in operation since 1992 with two general purpose detectors, H1 and ZEUS, and two dedicated purpose detectors, HERMES and HERA-B. The latter two experiments are the fixed target experiments started in 1995 and 2002, respectively. HERMES was designed for nucleon spin structure studies while HERA-B concentrated on CP violation and Beauty physics.

This thesis is based on the data collected by the ZEUS detector at HERA with a total integrated luminosity of 121 pb^{-1}, during the running period from 1996 to

2000. The main purpose of thesis is to investigate the inclusive neutral strange particle production in *ep* collisions. With such a wealth of data, many aspects of the strangeness production have been measured and compared to the leading order (LO) Monte Carlo simulations or the results from other experiments. The related issues of the measurement cover the understanding of the strange hadron production in *ep* collisions and the test of the fragmentation models.

The thesis is arranged as follows. An introduction is given in this chapter. In chapter 2, HERA physics, strangeness physics and the motivations of the thesis are presented. The ZEUS experimental setup is described in chapter 3. The detailed information about event selection and particle reconstruction is presented in chapters 4 and 5, respectively. The following chapter 6 explains the Monte Carlo simulations used in this work. The experimental results of the measurement and the corresponding discussions are given in chapters 7 and 8. Chapter 9 concludes the thesis.

Chapter 2

Physics Overview

The first step towards the theory of the quark components of hadron was proposed by Gell-Mann [1] and Zweig [2] in 1964. They assumed that the fundamental constituents of the proton are spin-1/2 particles called quarks. Later observations at SLAC in 1968 showed evidence for the existence of quarks in deep inelastic lepton-proton scattering. In the framework of Quantum ChromoDynamics (QCD), each quark possesses one of three possible 'colors' and the interactions between quarks are mediated via eight colored gluons. Different from the photon mediator in Quantum ElectroDynamics (QED), the colored gluons in QCD may couple to each other. The self-coupling of gluons causes the strong coupling constant α_s to become large at a small energy scale and to decrease with increasing energy scale. These are respectively known as the 'confinement' and 'asymptotic freedom' properties of the observed behavior of the strong interaction.

2.1 Kinematics of ep Scattering

HERA (Hadron-Electron Ring Accelerator) provides collisions between 27.5 GeV electrons (or positrons) and 920 GeV (820 GeV until 1998) protons with a center-of-mass energy of $\sqrt{s} \simeq 318$ (300) GeV. Here s is equal to $4\mathrm{E}_e\mathrm{E}_p$ and the variables E_e and E_p represent the electron and proton beam energies, respectively. The ep scattering in the standard model is described by the electroweak interaction in terms of exchange of two types of intermediate bosons. One is that the electron emits an electrically neutral exchange-boson, such as γ or Z^0 particle, to collide with a

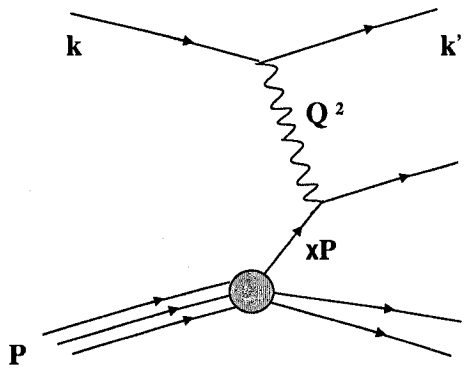

Figure 2.1: An illustration of the HERA kinematics for a lowest order NC process. The variables p, k and k' denote the four-momenta of the incident proton, electron and the scattered electron, respectively.

quark (or gluon) within the proton. This case is labeled as a Neutral Current (NC) process. The other case occurs when the exchanged boson emitted from the electron is a charged $W^{\pm}$ particle which collides with the proton, consequently leaving a neutrino in the final state. This type of interaction is called the Charged Current (CC) process.

An illustration of the HERA kinematics is given in Figure 2.1 in the case of a lowest order (Born diagram) NC process, $e(k) + p(p) \rightarrow e'(k') + X$. Here X could be any final hadronic state. The relevant variables to characterize this process are the virtuality Q^2, the Bjorken scaling variable x and the inelasticity y. Here the virtuality Q^2 is the negative square of the four-momentum-transfer of the exchanged boson, $-q^2$. The variable x represents the fraction of the proton momentum carried by the struck parton in the quark parton model and the inelasticity y is the fraction of the electron energy transferred in the proton rest frame. Any two of them are enough to describe the process since they are related to each other via $Q^2 = sxy$. The definitions of these variables are given below in the absence of QED radiation.

$$Q^2 = -q^2 = -(k - k')^2 \tag{2.1}$$

$$x = \frac{Q^2}{2p \cdot q} \tag{2.2}$$

$$y = \frac{q \cdot p}{k \cdot p} \tag{2.3}$$

Here k (k') denotes the four-momentum of the initial (final) electron. At HERA, the Q^2 extends from ~ 0 GeV^2 to values as high as 40000 GeV^2.

Two kinematic regimes are distinguished according to the magnitude of Q^2: the Deep Inelastic Scattering (DIS[1]) process with Q^2 values greater than 1 GeV^2 and the photoproduction process in which Q^2 is negligibly small. Here 'Deep' means that the photon penetrates the proton deeply and 'inelastic' indicates that the proton is broken up. A DIS event is characterized by the proton being probed deeply by the point-like virtual photon.

The photoproduction process is another major area of interest at HERA where the time-like exchanged boson carries a very small four-momentum transfer, $Q^2 < 1$ GeV^2. In most cases, the exchanged boson is a quasi-real photon rather than the heavier mediators like Z^0 and $W^{\pm}$. This is because of the much smaller four-momentum transfer in photoproduction compared to the mass of Z^0 and $W^{\pm}$ mediators. So contributions from weak interactions are significantly suppressed and negligible. Since the inclusive ep cross section is inversely proportional to Q^4 (see Equation 2.6), the photoproduction events, characterized by the small Q^2, are produced with a significantly higher rate than DIS events. Based on the early H1 and ZEUS measurements, the typical total cross section of γp events is at an order of 150 μb [3]. The cross section for DIS events, however, depends heavily on the selected kinematic regions and in general no overall cross section is given.

HERA offers the possibility of doing measurements in phase spaces similar to those appearing in both e^+e^- annihilation and hadron-hadron collision experiments. The longitudinal phase space of DIS events at HERA can be divided into three regions, each of which is expected to be dominated by different processes, as shown in Figure 2.2(a). The region labeled by 'A' is dominated by the struck quark fragmentation and it corresponds to one half of the e^+e^- phase space [5, 6] in Figure 2.2(b). The second region, denoted as 'B' in Figure 2.2(a), is the proton remnant fragmentation region which also appears in γp and pp collisions as shown in Figures 2.2(c) and (d). The third region is the rapidity region between the struck parton and the proton remnant where the color flow evolves, marked as 'C' in Figure 2.2(a). This region also exists in both e^+e^- and hadron-hadron collisions. Because of these

[1]Hereafter, DIS means the NC DIS process unless comparisons between NC and CC DIS processes are made.

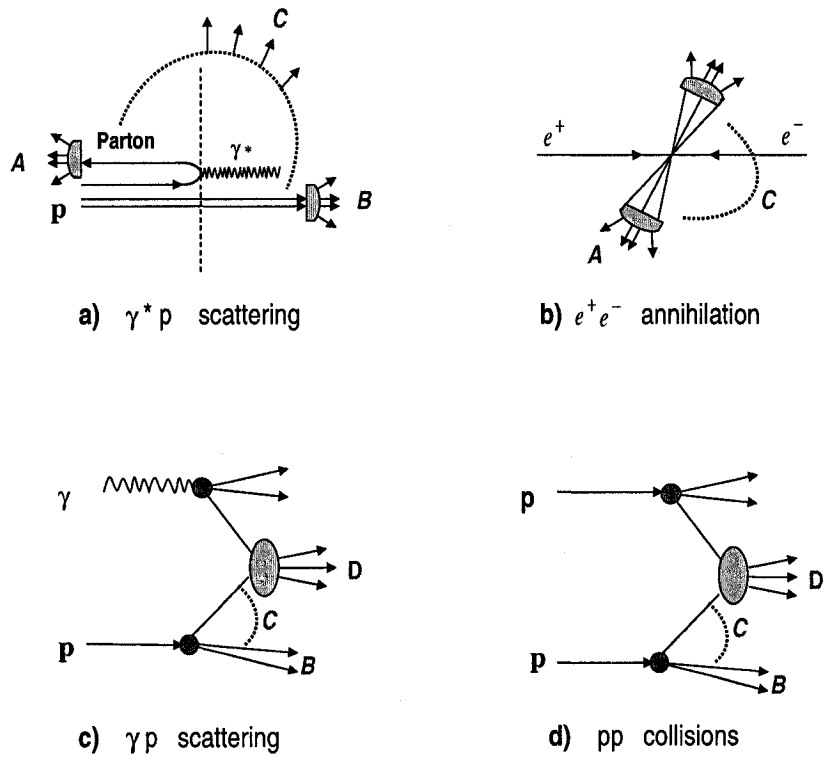

Figure 2.2: An illustration of the corresponding phase spaces in e^+e^-, ep and hadron-hadron collisions. (a) is the γ^*p scattering in the Breit frame, (b) is the e^+e^- annihilation, (c) is the resolved photoproduction and (d) represents the hadron-hadron collisions.

similarities, the measurements from different experiments in the likely phase spaces might hence be reasonably compared to each other. It is noted that studies at HERA revealed about 10% of DIS events are diffractive in nature [15, 16] whereby the third fragmentation region (C) between proton remnant and the struck quark mentioned above does not exist.

The dominant photoproduction process available at HERA is hadron-hadron like, see Figure 2.2(c): the photon can be resolved into partons and γp interactions are consequently considered as partons from the photon interacting with partons in the proton. This is quite similar to the pp collisions in which partons from different protons interact with each other, shown in Figure 2.2(d). Based on this argument, comparisons of the features between γp and hadron-hadron collisions are to some extent reasonable.

2.2 Inclusive NC DIS Cross Section

A general expression used to describe the NC deep inelastic scattering cross section will be discussed in the following. Before doing that, it is convenient to introduce one more variable which is proved to be useful later. This variable ν is defined by

$$\nu \equiv \frac{p \cdot q}{M} , \tag{2.4}$$

whereby again p is the proton momentum and q is the four-momentum-transfer. The variable M is the proton mass. In the rest frame of the proton, ν reduces to

$$\nu = E_e - E'_e , \tag{2.5}$$

where E_e and E'_e are the initial and final electron energies in the laboratory frame, respectively. So ν can be regarded as the energy transferred from the initial electron to the interaction in the proton rest frame. For an inelastic scattering process in which the energy and the scattering angle of the scattered electron are E'_e and θ, its inclusive differential cross section can be expressed in terms of two structure functions $W_1(\nu, \mathrm{Q}^2)$ and $W_2(\nu, \mathrm{Q}^2)$ in the laboratory frame [7],

$$\frac{d\sigma}{d\mathrm{Q}^2 d\nu} = \frac{4\pi\alpha^2}{\mathrm{Q}^4}\frac{E'_e}{E_e}[W_2(\nu, \mathrm{Q}^2)\cos^2(\theta/2) + 2W_1(\nu, \mathrm{Q}^2)\sin^2(\theta/2)] . \tag{2.6}$$

Here the α is the electromagnetic fine structure constant. The left hand side of this equation is from the experimental measurement. The two functions $W_1(\nu, \mathrm{Q}^2)$ and $W_2(\nu, \mathrm{Q}^2)$ describe the parton distribution in the proton and control the magnitude of the cross section.

Concerning the CC DIS process, the differential cross section was found to be similar to the one for NC DIS events in expression but suppressed in lower Q^2 regions due to the relative larger mass of the exchanged bosons in CC DIS. The ratio of inclusive NC to CC cross sections can be expressed as a function of Q^2 [8] by

$$\frac{\sigma(Z^0, W^{\pm})}{\sigma(\gamma^*)} \approx (\frac{\mathrm{Q}^2}{\mathrm{Q}^2 + M^2_{Z^0,W^{\pm}}})^2 . \tag{2.7}$$

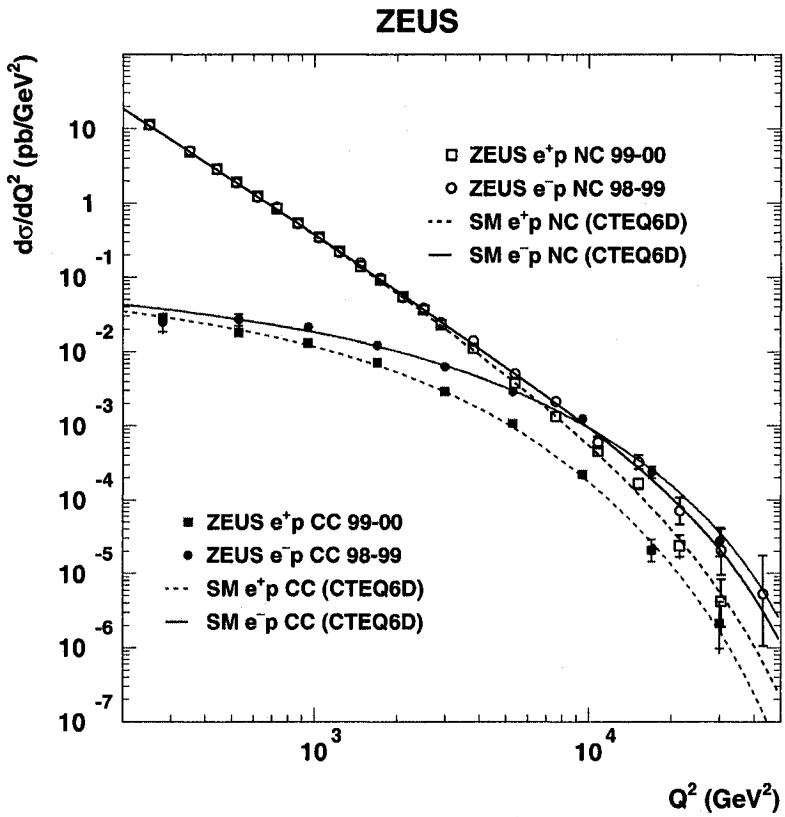

Figure 2.3: The NC and CC DIS cross section measurements at HERA as a function of Q^2 [8]. The predictions from the Standard Model are shown in lines.

The mass effect can be clearly seen from the inclusive NC and CC DIS cross section measurements in H1 and ZEUS experiments, shown in Figure 2.3. As anticipated from the theoretical predictions, the NC and CC DIS cross sections fall down with increasing Q^2 and converge at an approximate value of the squared of the mass of the exchanged Z^0 and $W^{\pm}$ bosons, $Q^2 \sim 10^4$ GeV^2.

2.3 Quark Parton Model (QPM)

The quark parton model is based on the essential assumption that the constituents of the proton or neutron are quasi-free point-like objects, partons, and that the interaction between the virtual photon and partons is regarded incoherently in *ep* scattering. The DIS cross section is therefore considered to be a sum of the individual contributions from each parton [7],

$$\frac{d\sigma}{dQ^2 d\nu} = \sum_i f_i(x) \frac{2Mx^2}{Q^2} (\frac{d\sigma}{dQ^2})_i \, . \tag{2.8}$$

Here $f_i(x)$ represents the probability of probing a parton i which carries a fraction x of the proton momentum. In 1969, Bjorken predicted that for an elastic scattering with a large Q^2 and ν, a simple scaled relationship between Q^2 and ν held, $\nu \equiv Q^2/2Mx$. Here x is called the Bjorken scaling variable indicating the structure function itself is independent of Q^2 (see Equations 2.9 and 2.10).

After rearranging Equation 2.6 in terms of y and comparing it with the parton model prediction on the cross section, Equation 2.8, we get [7]

$$\nu W_2(\nu, Q^2) \rightarrow F_2(x) = \sum_i e_i^2 x f_i(x) \, , \tag{2.9}$$

$$M W_1(\nu, Q^2) \rightarrow F_1(x) = F_2(x)/2x \, . \tag{2.10}$$

Here e_i denotes the electric charge of the parton. Equation 2.9 represents the structure function in terms of the parton density function $f_i(x)$ while Equation 2.10 is the so-called Callan-Gross relation for spin-1/2 partons. Replacing W_1 and W_2 functions with $F_{1,2}(x)$ and expressing the differential cross section in terms of Q^2 and x leads to

$$\frac{d\sigma}{dQ^2 dx} = \frac{4\pi\alpha^2}{xQ^4} [(1-y)F_2(x) + \frac{1}{2} y^2 2x F_1(x)] \, . \tag{2.11}$$

Here the weak structure of the proton is ignored. The above expression can also be rewritten in terms of the longitudinal structure function $F_L(x)$ and $F_2(x)$, giving

$$\frac{d\sigma}{dQ^2 dx} = \frac{2\pi\alpha^2}{xQ^4} \{[1 + (1-y)^2] F_2(x) - y^2 F_L(x)\} \tag{2.12}$$

So the statement of the Callan-Gross relation implies $F_L = F_2 - 2xF_1 = 0$ in the parton model.

2.4 Improved QPM

Further indications from experiments showed that the three valence quarks in the proton only account for half of the proton's momentum and the remaining half is

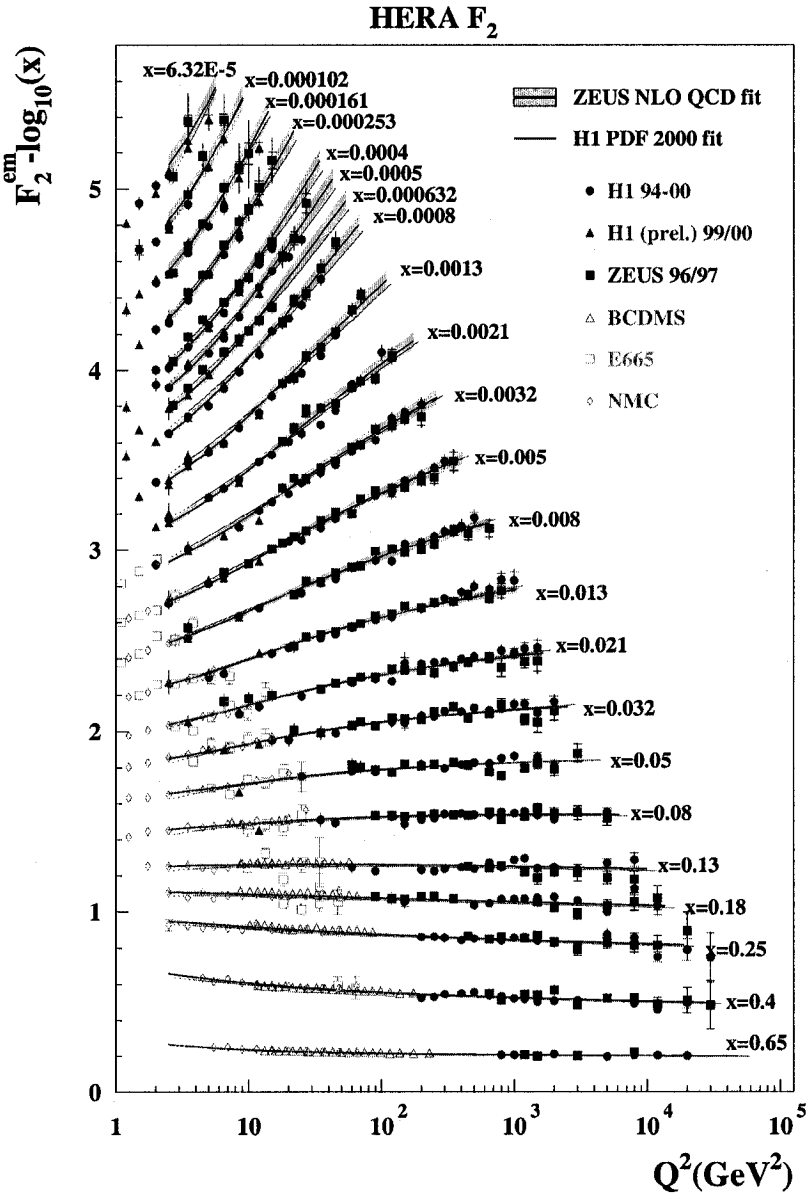

Figure 2.4: Summary of the F_2 measurements from HERA and fixed target experiments. F_2^{em} contains only the contribution from virtual γ exchange. A Next to Leading Order QCD fit is presented as well.

implied to be related to the electrically neutral partons inside the proton [7]. These neutral partons were later identified as gluons at DESY in 1979 [4]. Furthermore, Bjorken scaling turned out to be only approximately valid since it breaks down when Q^2 and x go to the extreme values. This better understanding of the structure of the proton made people realize that the dynamics in the QPM is just a reasonable rough description of the true one but not exactly. Therefore, improvements to the quark parton model are needed.

The inclusion of QCD effects into the QPM allows for the radiation of gluons from quarks and the splitting of gluons into $q\bar{q}$ pairs and consequently it must account for higher orders in α_s. The corrections, associated with an order of α_s^2 to the LO diagram (Figure 2.1), are conventionally called the Next to Leading Order (NLO) calculations. The NLO calculations are necessary because as Q^2 increases, the photon resolves not only into quarks but also into gluons. So interactions between quarks and gluons become important at larger Q^2 or lower x.

Figure 2.4 shows the proton structure function as a function of Q^2 and x measured at HERA and fixed target experiments. The F_2^{em} measured here contains only the contribution from the virtual photon exchange process. For x values larger than 0.1, the F_2^{em} is nearly independent of Q^2. However, as x decreases, contributions from the gluon radiation and quark pair creation from gluons can be resolved and become larger. Under such circumstances, Bjorken scaling is violated, leading to an increase of F_2^{em} at small x as Q^2 rises. NLO QCD correctly predicts the structure functions at all x values.

In addition, gluon radiation from a quark results in a transverse momentum of the quark with respect to the original quark momentum direction, which was assumed to be collinear with the initial proton beam direction. Changing the direction of quarks makes their coupling to the longitudinal polarized photons possible in an improved QPM. F_L hence may acquire a possibly large value, different from zero, and consequently the structure of the proton in the improved QPM involves the F_L term.

2.5 Strangeness Physics

Perturbative QCD (pQCD) stands for QCD theory in an energy regime where α_s is small and the perturbation theory can be applied. It is very successful in describing the hard scattering and hard QCD radiation processes in which a large momentum transfer is involved, but it breaks down in processes where a lower momentum transfer occurs, for instance in the hadronization process where the final hadrons are formed from quarks.

Heavy quark (charm, beauty or top) production is dominated by direct production from the hard interaction of gluon and photon at HERA, and therefore it can be described by pQCD. On the other hand, the production of the next relatively light quark, the strange quark, can be either from the hard interactions or from pure fragmentation processes. Therefore the fragmentation process becomes important for strangeness production. In the next section, different strange production mechanisms accessible at HERA are described.

2.5.1 Strangeness Production Mechanism

Figure 2.5 shows the strangeness production mechanisms in $\gamma^* p$ collisions. Since the photon in γp collisions can fluctuate into a $q\bar{q}$ pair, an s quark might be resolved inside the photon in the photoproduction process as well.

Figure 2.5(a) shows the hard scattering of a s sea quark inside the proton. Even though there is no s valence quark among proton constituents, as Q^2 increases, the $s(\bar{s})$ sea quarks can be resolved by the virtual photon and can be knocked out to form a final strange hadron. This production mechanism is expected to become important at higher Q^2 and lower x.

The second strange production mechanism is given in Figure 2.5(b), describing a coupling of the exchanged boson and a gluon from the proton. This is the dominant process for the heavy flavor production, and here it is also a major channel to produce strangeness.

The previous H1 [11] and ZEUS [12] publications showed that strangeness production occurs dominantly through the hadronization process where the universal parton pure fragmentation is considered to take place. The understanding of this type of mechanism heavily relies on the phenomenological models. An illustration

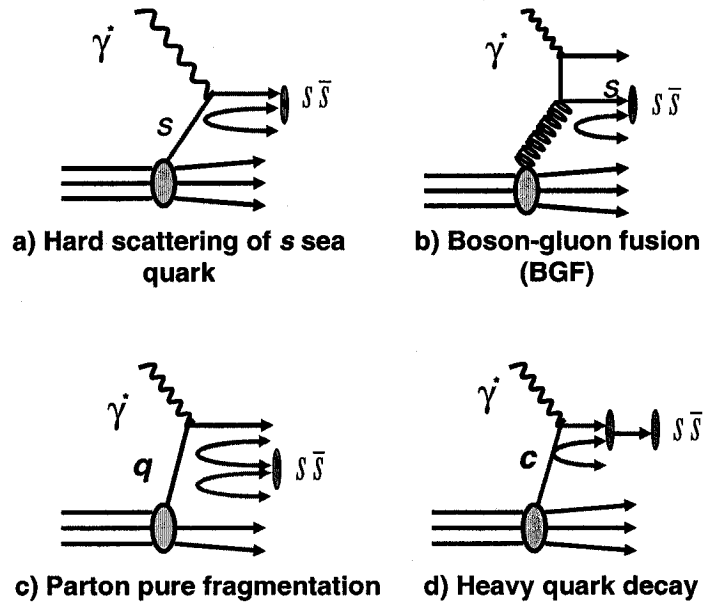

Figure 2.5: Strange production mechanisms in *ep* collisions

of this process is given in Figure 2.5(c): a parton from the hard scattering process is followed by a fragmentation shower in which a $s\bar{s}$ pair can be created from a gluon splitting. Details about hadronization models can be found in Chapter 6.

The fourth strangeness production channel is the heavy flavor decay, shown in Figure 2.5(d). However, due to the larger mass of the heavy flavor of charm and beauty quarks and limitation of the production phase space, the strange production from this mechanism is already constrained by the low rates of the heavy flavor production.

2.5.2 The Strangeness Suppression Factor

Since strangeness is dominantly produced during the pure fragmentation process, the phenomenological models which are used to describe the non-perturbative nature of this process are essential to describe the strange hadron production.

One successful fragmentation model is the LUND string model [60, 61, 62]. In the scheme of this model, strangeness production is controlled by one key parameter, the strange suppression factor $\lambda_s = \mathcal{P}_s/\mathcal{P}_u$, which describes the relative ratio of s quark to u(or d) quark production during the fragmentation process. The λ_s value 0.3 was found to be appropriate in e^+e^- annihilation [14, 85, 86] and this value was also set to be the default value in JETSET [61, 62]. However, some indications [10, 13]

show that different values may be needed for different experiments, or a single λ_s value cannot accommodate the data in all kinematic regions in one experiment [14]. Due to this unclear situation, the string model was tuned with two λ_s values in this thesis, 0.3 and 0.22, in order to get a basic idea of how the alternative value works in case the other λ_s fails to reproduce the data. The value of 0.22 is suggested by the previous ZEUS publication [80]. One may extrapolate, in comparing to data, from the two predictions with different λ_s values. So in this sense, an extra λ_s check is necessary and meaningful.

However, one may argue that it would be simplistic to try to fit the data by adjusting the parameter λ_s only in Monte Carlo (MC), provided several other parameters, for instance the diquark suppression factor and the extra spin-1 diquark suppression, etc. in the string model, exist to control strange hadron production. This is a good argument, but the original motivation is that a simple check on λ_s is necessary and helpful to understand the strange production during the fragmentation process. However, it is NOT the purpose of this thesis to tune all the available parameters to find out their best fitting values for HERA measurements, which will be left for the dedicated MC studies by someone else. Therefore no attempt was made to find out the best parameter set to fit the data in this thesis.

2.6 Physics Motivations of the Thesis

The H1 and ZEUS collaborations have published a few results on strange hadron production, based on the data collected in the first few years of running at HERA [9, 10, 11, 12]. These measurements were limited by the low data statistics, from an integrated luminosity of 0.6 to 3.0 pb^{-1}, and the restricted scope of the measurements, mostly with emphasis on the multiplicity study. As an example, the total integrated luminosity was only about 0.6 pb^{-1} in the previous strangeness measurements in ZEUS and the main results given were the average and differential multiplicities of $\Lambda + \bar{\Lambda}$ and K^0_S production [10]. The reconstructed $\Lambda + \bar{\Lambda}$ and K^0_S signals in that publication are given in Figure 2.6.

With the wealth of data accumulated at HERA, more precise, more comprehensive and new measurements on strange hadron production have been done in this thesis. The total integrated luminosity used in this work is 121 pb^{-1}, tens to hun-

dreds times as many as what the early measurements used, which definitely led to much more precise results. The kinematic regions covered by the thesis are photoproduction, low Q^2 DIS and high Q^2 DIS regions. These regions were divided into subsamples for specific studies. In this thesis, measurements have been done

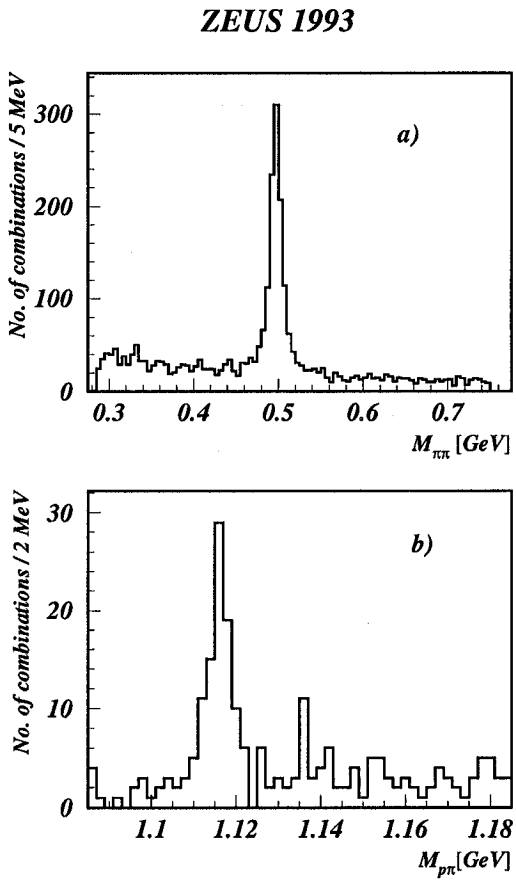

Figure 2.6: Early ZEUS measurements on K^0_S and Λ production in DIS [10]. a) shows the reconstructed K^0_S mass distribution in which the total number of K^0_S signal and background were estimated to be 971 and 150 respectively. The fitted mass is 497.4 ± 0.3 MeV. b) shows the reconstructed $\Lambda + \bar{\Lambda}$ mass distribution in which the total number of signal and background were estimated to be 80 and 18 respectively. The fitted mass is 1116.2 ± 0.4 MeV.

extensively on cross section, baryon to antibaryon production asymmetries, baryon to meson ratios, rapidity correlations, Bose-Einstein correlations and strange hadron polarizations. Many of those measurements were investigated for the first time at HERA such as the fireball events, baryon to meson ratios, rapidity correlations and

polarizations.

Since similar phase spaces to the one in e^+e^- or hadron-hadron collisions can be obtained at HERA, it is of interest to examine whether the similarity persists between the results in the likely regions.

According to the results obtained in this thesis, a few of the physics issues listed below are expected to be better understood in *ep* scattering experiments.

2.6.1 Test of the MC Models

As discussed in the previous sections, the understanding of the strange hadron production relies on the phenomenological models which we currently use to describe the hadronization process. On the other hand, experimental data provide a reference to test the universality of these models, i.e. whether the values of the parameters found in one type of experiments are appropriate for the others. After all, comparisons between different experiments will consequently lead to a better understanding of strangeness production in the universe. Therefore strangeness measurements in different types of experiments are definitely needed, with no exception from *ep* collisions. With our data, different hadronization models and MC predictions are checked and, as a result, constraints on these models are obtained for *ep* experiment.

2.6.2 Baryon Number Flow

The overall formation of baryons in the final states at HERA must leave the net baryon number of +1 appearing in the initial *ep* state in order to conserve the baryon number in the whole process. It is of interest to study how the baryon number flow transfers from the initial state to the final hadronic states.

According to QPM, the baryon number of the initial proton is carried by the *ud* diquark. The Monte Carlo study shows that the baryon number flow from the initial proton is expected to transport to a very far forward region at HERA, $6 \sim 8$ units of rapidity, because of the asymmetric beam energies. Since this forward region is not covered by the ZEUS main detectors, the measurement on the baryon number flow will thus not be reachable in the framework of QPM.

However, a new so-called gluon junction mechanism [92] predicts that a non-vanishing baryon number flow can be found even in the central region of the detector.

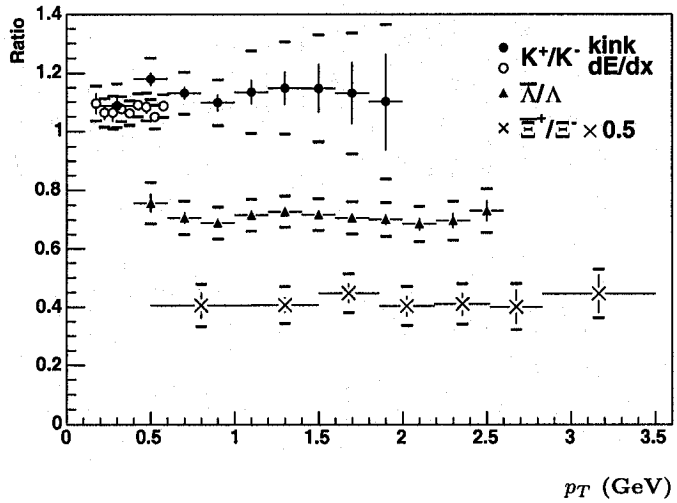

Figure 2.7: Anti-baryon to baryon asymmetries measured at RHIC [17] as a function of p_{T}.

This mechanism can give an $\bar{\Lambda}$ to Λ production asymmetry which is in an approximate agreement [18] with the observation in Au-Au collisions at RHIC [17], as shown in Figure 2.7.

Therefore the baryon number investigations made in this thesis, by studying baryon to antibaryon production asymmetry, will serve as a test to these different predictions.

2.6.3 Baryon Production Enhancement

The relative yield of baryon and meson production tells by which factor baryons rather than mesons are produced in a reaction. It is of interest to check this ratio in different types of experiments and different collision energies to understand the hadron formation. A significant enhancement of the baryon production with respect to meson was observed in Au-Au collisions at RHIC [19], shown in Figure 2.8. It was found that the $\bar{\Lambda}/K^0_S$ ratio in a intermediate p_{T} region was quite large and could be greater than 1. This enhancement however cannot be predicted and explained by the traditional mechanism of fragmentation process. Therefore alternative models exist to attempt to describe the large ratio. Furthermore, a similar study from BRAHMS collaboration shows that this ratio is enhanced in nucleus-nucleus collisions compared to pp collisions [110].

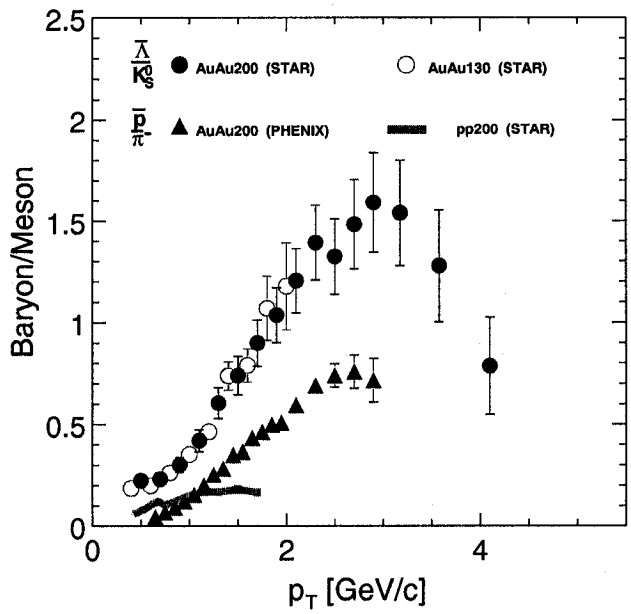

Figure 2.8: Relative baryon to meson production ratios measured at RHIC experiments [19].

As discussed in Section 2.1, HERA covers some phase space common to hadron-hadron collisions. Therefore the baryon to meson relative production measurement at HERA facilitates the possibilities to check the dependence of this ratio on the type of phase space, and furthermore to see if the similar enhancement to that at RHIC happens in elementary particle collisions.

2.6.4 Dynamics of Hadron Formation

How hadrons are created, especially how baryons are created, is not well understood yet, and therefore we rely on phenomenological models to describe the process of hadron formation. Based on many assumptions made for the hadronization process such as the local conservation of quantum numbers, we can check with our data to see if the predictions are reasonable or not.

By studying Bose-Einstein correlations (BEC) between bosons, dynamic information about the particle production source like its size can be extracted. A lot of work on BEC measurements has been done by different experiments. In this thesis, two interesting issues about BEC will be stressed. The first one is the BEC independence on Q^2 which was proposed by the ZEUS experiment [98]. A picture to show

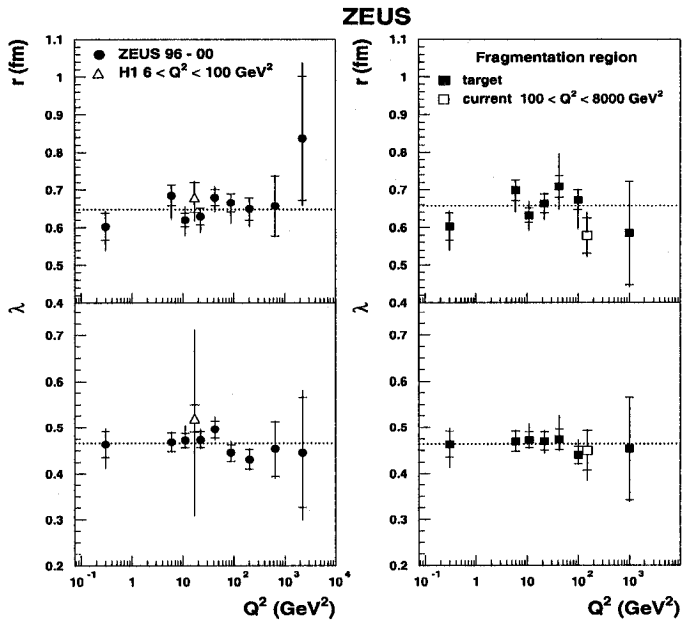

Figure 2.9: The previous BEC measurement results from ZEUS [98]. The measurements were based on the charged pion BEC studies in a wide Q^2 region from 0.1 to 8000 GeV^2 at HERA. The definitions of the radius r and correlation strength λ are given in Formula 8.2.

the insensitivity of BEC to Q^2 is given in Figure 2.9. This independence supports the LUND string fragmentation model in which the BEC is determined only by the soft fragmentation process.

Preliminary BEC measurements on $K^0_S K^0_S$ have been obtained in ZEUS at Q^2 values larger than 2 GeV^2 [97]. For completeness and a check of the Q^2 dependence, the $K^0_S K^0_S$ BEC study at a Q^2 value extending down to $\sim$0 GeV^2 has been performed in this thesis.

The second physics issue addressed from BEC studies in this thesis is the dependence of the radius on the hadron mass. Such trend can be illustrated by the BEC results from e^+e^- data [99], shown in Figure 2.10. In order to obtain a better understanding of the dependence, more BEC checks are needed for each of these hadron pairs. The thesis provides results from $K^0_S K^0_S$ BEC studies in ep collisions.

A further dynamic picture of the hadronization stage can be obtained by studying rapidity correlations (RC) of two particles. The early LEP experiments [108] showed results to support the local quantum number conservation during the hadronization

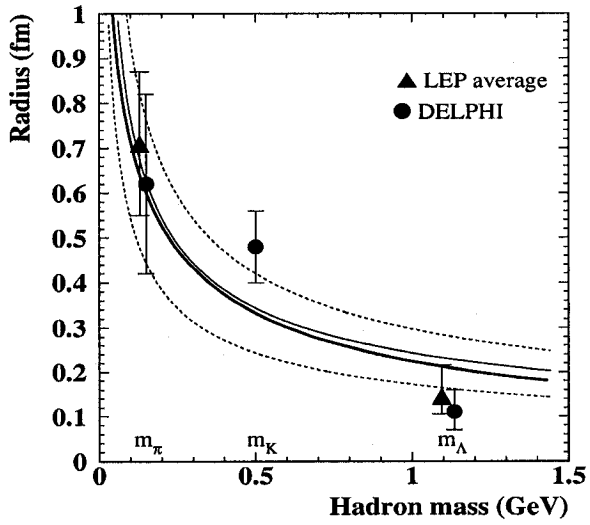

Figure 2.10: The dependence of radius on the hadron mass based on the LEP results [99].

process which are adopted in the current LUND string model and the cluster model. The effect resulting from the local compensation of quantum numbers will signify an enhancement of the close production in rapidity between particles which have such compensation. Therefore the particle rapidity correlations can be used to study the local quantum number conservation during the hadronization process. For example, in Figure 2.11, the previous DELPHI RC study showed that clear enhancement of baryon-antibaryon pair production in the small rapidity difference region was observed compared to non-zero baryon number pairs.

The first check of RC in *ep* collisions was made in this thesis. Instead of simple repetition of measurements as what DELPHI did, the features of the RC were parameterized here for the first time. These quantitative values characterizing the RC were offered to allow comparisons between results from different particle pairs and different experiments.

2.6.5 Strange Hadron Polarizations

The hadron polarization measurement is used to study spin physics and to understand the formation of hadrons by studying the spin transfer from the beam to the final hadrons. The present focus of the polarization studies is mainly on the measurement of the strange particle polarizations. There could be two reasons to explain

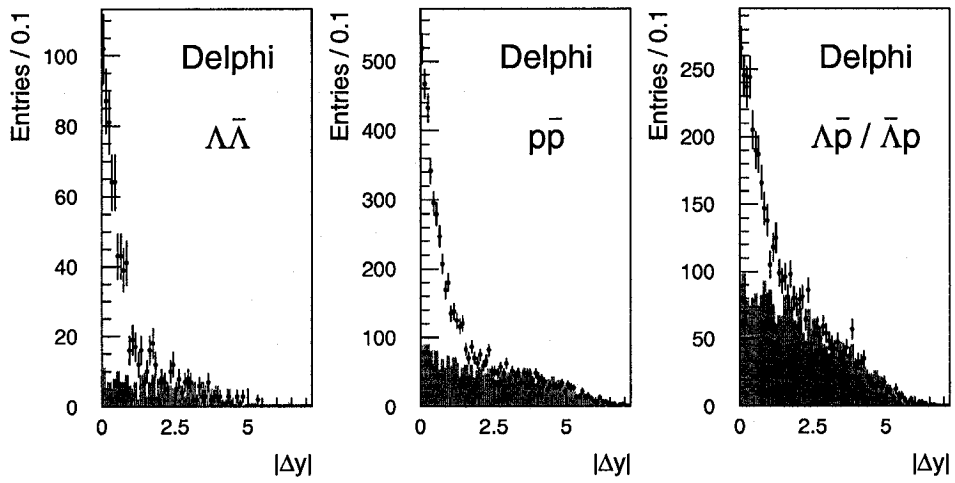

Figure 2.11: Rapidity correlations on different baryon pairs measured in DELPHI [109].

why people are so interested in the strange hadron polarizations. These are that strange hadrons have relatively light masses and that some of them are polarization self-analyzing. The light mass makes larger statistics possible and the self-analyzing means that the polarization can be measured by studying the distribution of their decay products. With the help of a large data sample and easier means of analyzing, the spin features of the s quark in the strange hadron can be investigated.

In this thesis, the Λ and $\bar{\Lambda}$ polarizations have been investigated with HERA I data. Since the HERA I data were produced with unpolarized electron and proton beams, the possible contributions of the spin transfer from the electron to the final hadrons should not exist. However, one can argue that, even without the spin contribution from the beam, the changing of the s quark kinematic dynamics during the process from the s quark creation to the strange hadron formation may also result in polarization of the final strange hadrons. Under the current circumstances where the underlying physics of the hadron polarization is still in debate, the results from ep collisions presented in this thesis may indeed provide a better understanding of the polarization.

Chapter 3

Experimental Setup

HERA, the natural extension of the electron-nucleon fixed target experiments, is the first and unique high energy electron-proton collider so far in the world. It started to deliver luminosity in 1992 and is expected to remain in operation until mid-2007. The physics data used in this thesis were collected with the ZEUS detector, one of the two colliding experiments at HERA.

In this chapter, a general description of the HERA collider and the ZEUS detector is presented. Some components of the ZEUS detector which are essential for this thesis will be addressed in more detail.

3.1 The HERA *ep* Collider

HERA is a unique high energy *ep* collider which provides collisions at a center-of-mass energy above 300 GeV. It was built at a depth of 15-30 m underground in a tunnel of 6.3 km circumference at the research center DESY in Hamburg, Germany. The construction of HERA began in 1984 and ended in 1991. An aerial view of DESY site is given in Figure 3.1.

After the pre-acceleration with PETRA (Positron-Electron Tandem Ring Accelerator), electrons/positrons[1] and protons are injected into and stored in two independent storage rings on top of each other inside the HERA tunnel. Electrons and protons are then accelerated separately one after the other until the desired energies

[1]Hereafter, electron and positron are referred to as electron in a circumstance of an expression of *ep* collision is given.

are reached. The *ep* collisions take place and are detected at two intersecting points of the electron and proton beam lines where two general purpose detectors, the H1 and ZEUS detectors, are located, in the north and south halls of DESY, respectively.

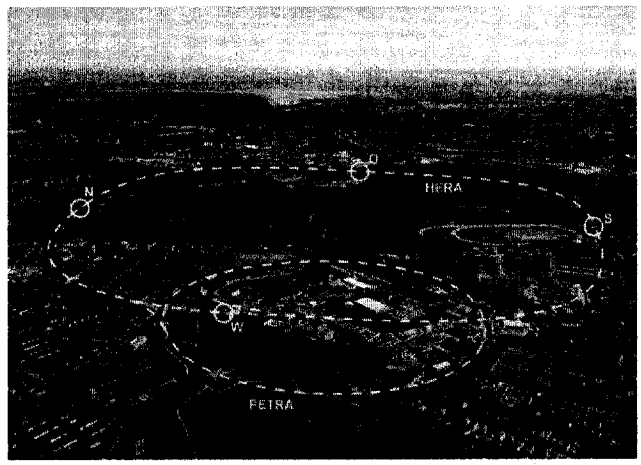

Figure 3.1: A bird-eye view of the DESY site. The positions of HERA tunnel and PETRA pre-accelerator are outlined as two contours.

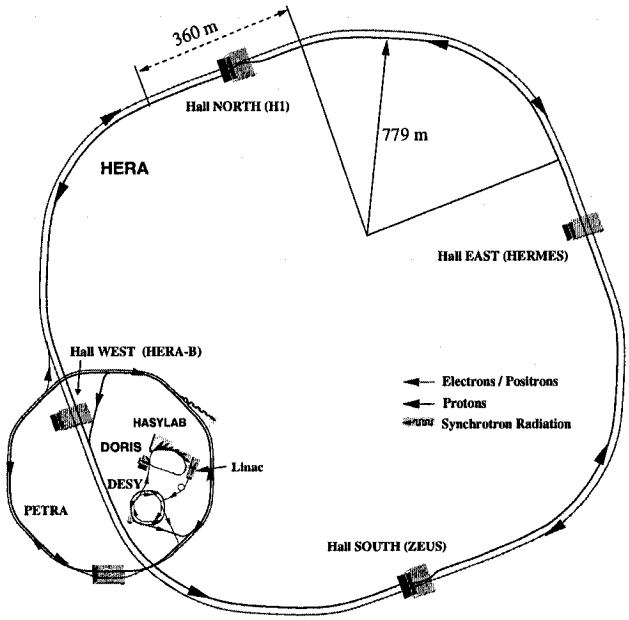

Figure 3.2: The HERA accelerator, PETRA pre-accelerator and the experiments.

In addition to the H1 and ZEUS, two more fixed target experiments were built for dedicated purposes. The HERMES experiment in the east hall was designed

Data taking period	HERA I	ZEUS gated luminosity
1996-1997	27.5 GeV(e^+)+820 GeV(p)	38.62 pb^{-1}
1998-1999	27.5 GeV(e^-)+920 GeV(p)	16.68 pb^{-1}
1998-2000	27.5 GeV(e^+)+920 GeV(p)	65.87 pb^{-1}
	HERA II	
2003-2004	27.5 GeV(e^+)+920 GeV(p)	40.59 pb^{-1}
2004-2006	27.5 GeV(e^-)+920 GeV(p)	196.83 pb^{-1}
2006-2007	27.5 GeV(e^+)+920 GeV(p)	128.88 pb^{-1}

Table 3.1: HERA beam conditions and the ZEUS gated luminosities in different data taking periods. Note that luminosity for 2007 is available only for the first two months as the thesis is finished (as in Figure 3.3).

to study the spin structure of the nucleon by using the polarized electron beam to collide on the polarized gas target. The other fixed target experiment in the west hall was the HERA-B pN experiment, whose goal was to measure CP violation and B physics. The HERA-B experiment was decommissioned in 2002. The layout of HERA and its experiments is shown in Figure 3.2.

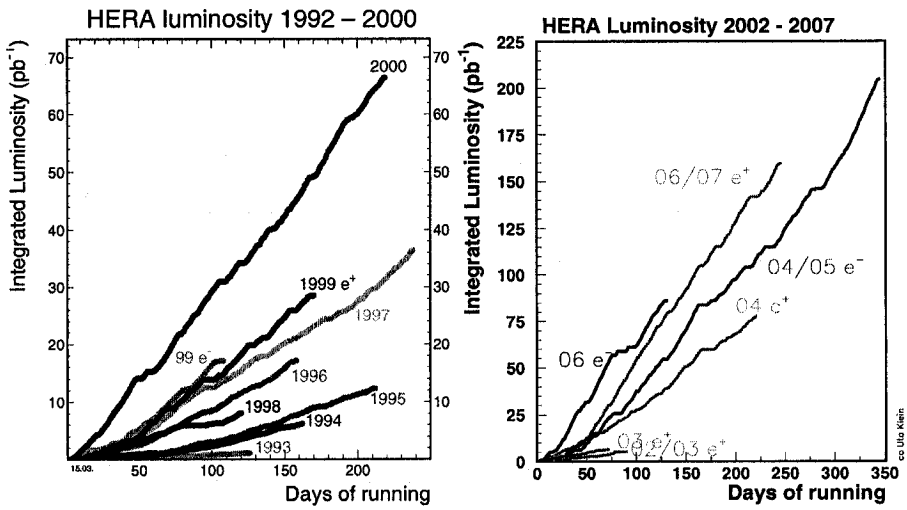

Figure 3.3: The luminosity delivered by HERA for the 1992-2000 running period (HERA I, left) and the 2002-2006 running period (HERA II, right).

The data sets produced at HERA vary with different running periods due to different beam conditions. HERA was initially designed to provide collisions between

27.5 GeV electrons and 820 GeV protons. However a more energetic proton beam has been used later after a few years of running. Since 1998, the proton energy was increased to 920 GeV while the electron energy was kept unchanged. Furthermore, electron and positron beams have been used alternatively for collisions during the running period from 1996 to 2006. The information about HERA beam conditions and the luminosities gathered for different data-taking periods is given in Table 3.1 and Figure 3.3.

A significant upgrade of HERA was done during the long 2000/2001 shutdown, aiming to achieve a higher integrated luminosity in the following years. In addition, the electron beam was also tuned to be longitudinally polarized with sets of spin rotators installed before and after the ZEUS detector. By convention, the physics data taking period before the 2001 upgrade is referred to as HERA I while the postupgrade running period is called HERA II.

3.2 The ZEUS Detector

The ZEUS detector is a general purpose detector designed and built to study a wide range of physics in ep collisions [21]. The ZEUS coordinate system is a Cartesian right-handed system with the origin at the nominal interaction point (IP). The direction of incident proton beam is defined as the positive z direction and y direction goes up-wards while x direction points to the center of the HERA ring. The forward and backward parts of the detector refer to the regions in positive and negative z directions, respectively. Due to the highly asymmetric energy of the incident electron and proton beams, the ZEUS detector exhibits a large forward-backward asymmetry, with more elements and absorber materials in the forward region than in the rear region. Cross sections of the ZEUS detector are presented in Figures 3.4 and 3.5.

The main parts of the ZEUS detector will be briefly described in sequence from the inner components to the out-wards ones in the following. It is clearly seen from Figures 3.4 and 3.5 that the innermost part[2] of the detector is the Micro Vertex Detector (MVD) [20]. The MVD is a silicon-strip vertex detector, installed during the 2000/2001 shutdown in order to improve the resolution of the tracking system.

[2]The MVD is placed at the position where the former vertex detector (VXD) was located but with much closer to IP than the VXD. The damaged VXD was taken out in 1995.

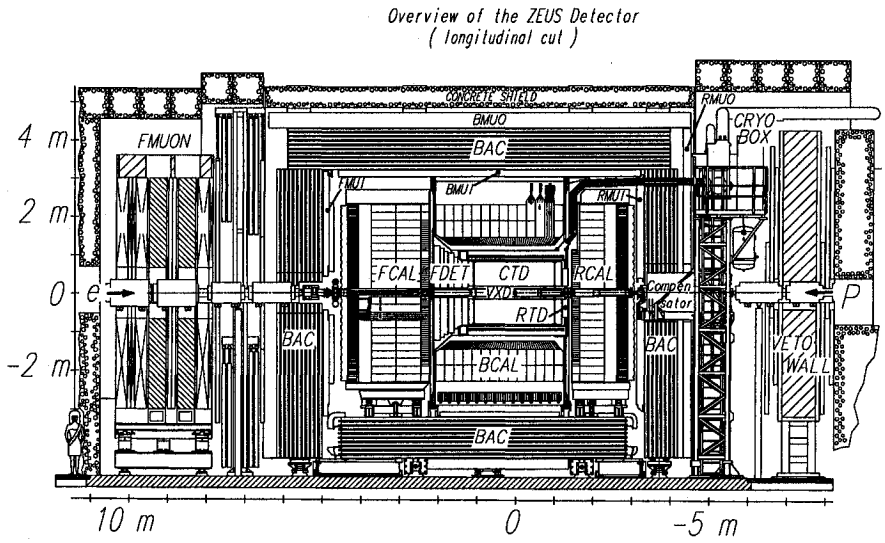

Figure 3.4: Cross section of the ZEUS detector parallel to beam pipe.

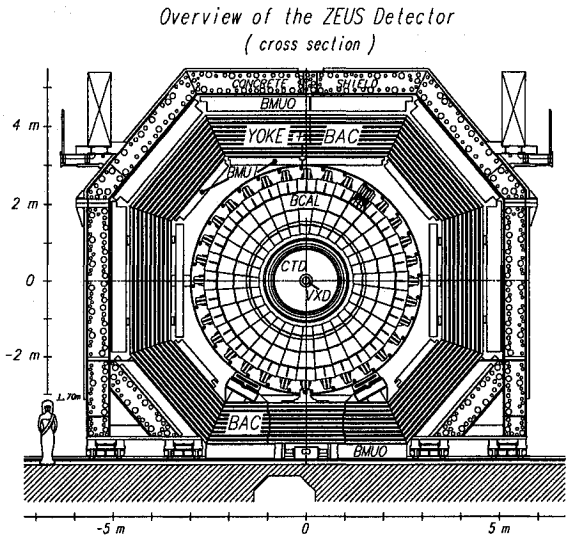

Figure 3.5: Cross section of the ZEUS detector perpendicular to beam pipe.

With it, the measurement of the impact parameters with respect to the primary and the secondary vertices is more accurate than before. Note that the MVD information is only available for HERA II data.

The next outer component is the Central Tracking Detector (CTD) with which the momenta of the charged particles were measured. An extensive description of the CTD will be given in Section 3.2.1.

Another major constituent of the ZEUS detector is the uranium CALorimeter (CAL) which surrounds the CTD. The CAL plays a critical role in the energy measurement of particles and jets. Three sections compose of the CAL: the Forward Calorimeter (FCAL), the Barrel Calorimeter (BCAL) and the Rear Calorimeter (RCAL). More detailed information about CAL will be revealed in Section 3.2.2.

The CAL is enclosed by an iron yoke which is also referred to as BAcking Calorimeter (BAC). In addition to be acting as the return path of the magnetic field flux of the solenoid, the yoke is also functioning as a tracking calorimeter and muon detector. The dedicated muon detectors are placed both inside (inner muon chambers, FMUI, BMUI and RMUI) and outside (FMUO, BMUO and RMUO) of the BAC.

Three other components of the ZEUS detector are also relevant to this analysis. One is the vetowall in the rear region of the detector as shown in Figure 3.4. It is composed of iron plates and scintillators and is used to reject proton-related background. Another one is the Small angle Rear Tracking Detector (SRTD) which is critical for measurement of the scattered electron in deep inelastic scattering events, see Section 3.2.3 for details. The last one is the luminosity monitoring detector (LUMI) which is placed in $z = -107$ m upstream of the IP. It is a small calorimeter made of lead and scintillators and used to determine the luminosity by measuring photons from bremsstrahlung events. More details about LUMI are available in Section 3.2.4.

3.2.1 The Central Tracking Detector (CTD)

The tracking detectors play a very important role in measuring the direction and momentum of charged tracks in experimental particle physics. The ZEUS CTD [21, 22, 23, 24] was conceived to detect and identify the charged particles with a high precision over a wide range of Q^2.

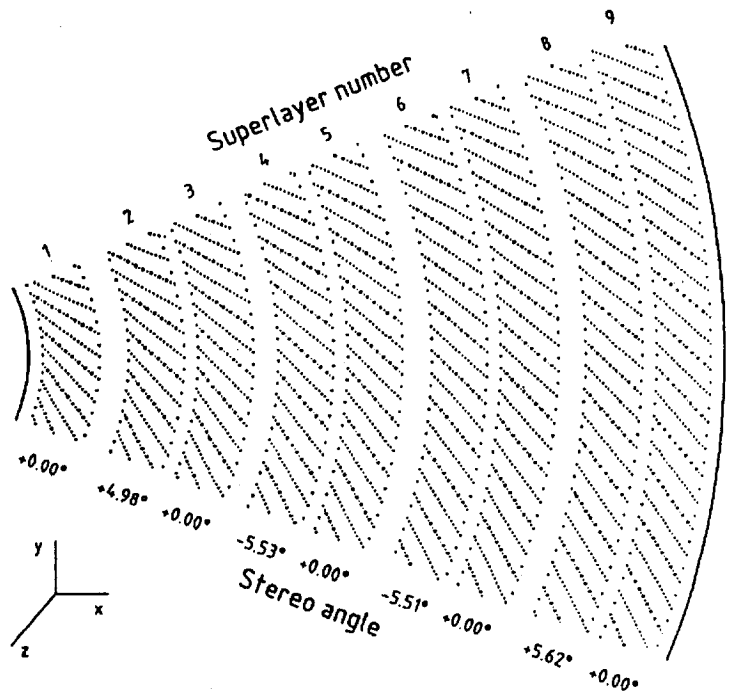

Figure 3.6: Cross section of one ZEUS CTD octant. 9 Superlayers are shown with their angles w.r.t. z direction.

The ZEUS CTD covers the polar angle from 15° to 164° and has a full azimuthal angular coverage. Its total active length is 205 cm and its inner(outer) radius is 18.2 (79.4) cm. It is a cylindrical wire chamber with 9 superlayers (SL), as seen in Figure 3.6. The sense wires in the five odd numbered layers are set along the beam direction while the other 4 even numbered layers have a small stereo angle (±5%). This small angle is chosen so that a roughly equal angular resolution in polar and azimuthal angles can be obtained. The spatial resolution of the charged tracks is 180 - 190 μm in the r - ϕ plane and 2 mm in the z direction.

The CTD is filled with a gas mixture of 82% Argon (Ar), 13% Carbon-dioxide (CO_2) and 5% Ethane (C_2H_6). The gas is ionized, by the passage of a charged particle, into negatively charged electrons and positively charged ions. Given the presence of the electromagnetic field, the electrons move to the positively charged sense wires, while the ions drift towards to the negatively charged sense wires. The subsequent collection and amplification of the signal pulse creates a detectable signal indicating the passing of the charged particle. These signals are collected by electronic read-out.

Before HERA II, the transverse momentum resolution for tracks with $p_T > 150$

MeV and passing through at least 3 SLs was given by $\sigma(p_T)/p_T = 0.0058 \cdot p_T \oplus 0.0065 \oplus 0.0014/p_T$, where p_T is in GeV and $\oplus$ means terms are added in quadrature. The first term is due to the hit position resolution while the second and third depend on the multiple scattering inside and before the volume of the chamber. In the data analysis, passing through at least 3 SLs is considered to be the minimal requirement for a good reconstruction of tracks in ZEUS. The CTD detector provides a position reference for the alignment of other components of the ZEUS detector, since it has the most accurate information on spatial coordinates during the HERA I period.

The situation of the resolution changed since the installation of the MVD in 2001. The influence of the new detector components on the tracking resolution is still under investigation. A not yet final approximation of resolution is $\sigma(p_T)/p_T = 0.0026 \cdot p_T \oplus 0.0104 \oplus 0.0019/p_T$ [25] for the combined CTD and MVD system.

3.2.2 The Uranium Calorimeter (CAL)

Calorimetry is used for energy and position measurements in particle physics. The energy of particles can be detected via the showers generated by interactions of the particle in the absorption medium, whereby all or part of the kinetic energy of the particle is deposited. With the help of a series of electronic apparatus, the deposited energy will be converted into the detectable signal, and thus the information like energy, position and angular orientation of the initiating particle is obtained. The ZEUS calorimeter [21, 26, 27] is a compensating calorimeter built up from depleted uranium[3] and scintillator plates. In practice, it is divided into three components:

- The forward calorimeter (FCAL) covering polar angles from $\theta = 2.2°$ to $39.9°$;
- The barrel calorimeter (BCAL) extending from $\theta = 36.7°$ to $129.1°$;
- The rear calorimeter (RCAL) covering from $\theta = 128.1°$ to $176.5°$.

Figure 3.7 shows the three sub-components of the calorimeter and their polar angle coverages. Longitudinally each calorimeter components is subdivided into two sections. The inner part is called the Electromagnetic Calorimeter (EMC), which leads to the Forward EMC (FEMC), the Barrel EMC (BEMC) and the Rear EMC (REMC) in each corresponding component of the CAL. The thickness of an EMC

[3] U^{238}(98.1%)+Nb(1.7%)+U^{235}(.2%)

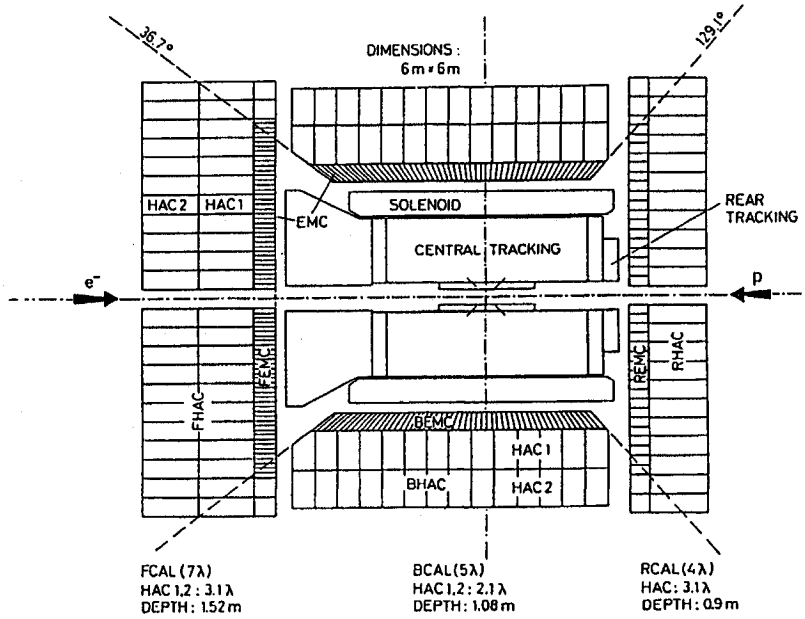

Figure 3.7: Three different components of the calorimeter and their polar angle coverages.

section is about 25 X_0 ($\sim 1\lambda$), where X_0 is the radiation length and λ is the interaction length. The outer section, named the Hadronic Calorimeter (HAC), has a depth varying from $\sim 3\lambda$ to $\sim 7\lambda$. The HAC is made up of three subparts as well, namely the FHAC, BHAC and RHAC.

FCAL and RCAL - The FCAL and RCAL have a similar structure, each of them is divided into 23 modules. A FCAL module is displayed in Figure 3.8. All these modules are segmented into towers, which are further segmented longitudinally into electromagnetic and hadronic cells. In each tower, the depleted uranium (DU) and scintillator plates are placed alternatively. The scintillator light of each cell is read out by the wavelength shifters on both sides of the module and is transported to two photomultiplier tubes (PMT) located at the back of the tower. The light signal is read out by the PMT's in a way of converting the light signal into an electrical signal.

BCAL - The BCAL is a cylindric calorimeter where the IP is located on its axis. The cylinder extends from an inner radius 123.2 cm to an outer radius 229.6 cm. It includes 32 wedge-shape modules in total, each one spanning 11.25° in azimuth. All module are tilted by 2.5° in the azimuthal plane so that all the non-projective

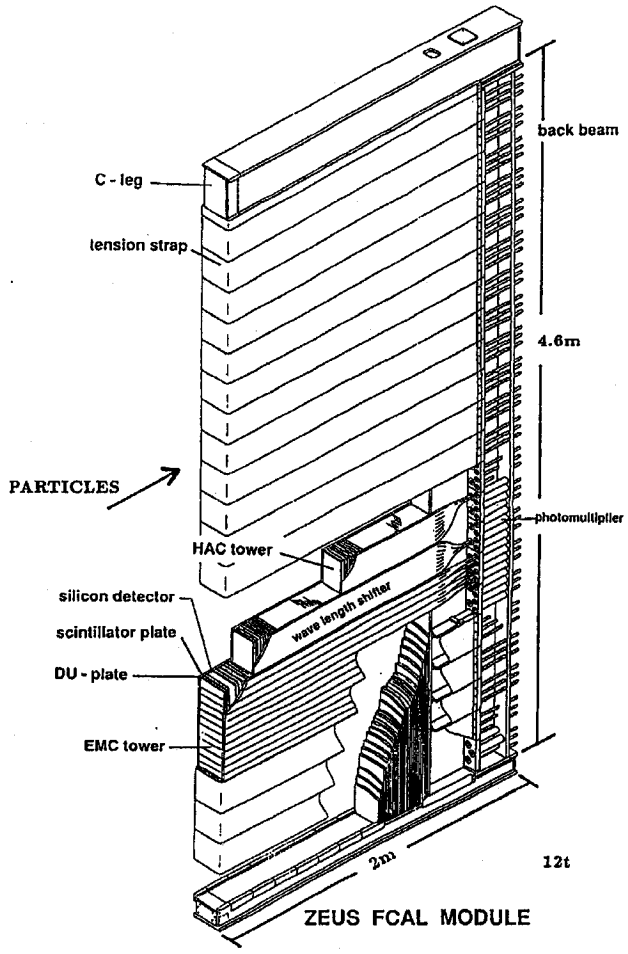

Figure 3.8: Schematic view of a FCAL module in ZEUS.

particles will be detected without escaping through the gap between modules.

The main features of the ZEUS calorimeter are:

- **Hermeticity** - a maximal solid angle coverage of the IP, 99.8% in the forward hemisphere and 99.5% in the backward hemisphere;

- **Good energy resolution** - a very efficient detector to measure energy for electrons and hadrons. The thickness and nature of the absorber and of the active material has been chosen in a way to obtain the equal energy response to electromagnetic and hadronic showers within $1 \sim 2\%$ uncertainties ($e/h = 1.00 \pm 0.02$). We get $\sigma(E)/E = 18\%/\sqrt{E}$ for electromagnetic showers and $\sigma(E)/E = 35\%/\sqrt{E}$ for hadronic showers, where E is given in GeV;

- **Fast readout** - The CAL must be able to handle the 10.4 MHz of the bunch

crossing rate with a very short dead-time, see Section 3.3;

- **Excellent time resolution** - a guarantee of high level of rejection of background due to cosmic ray and beam gas interactions. The time resolution of the ZEUS CAL is better than 1 ns if the deposited energy is above 4.5 GeV.

Various means are available in ZEUS, for example using cosmic rays, depleted uranium activity, laser and charge injection, to calibrate the calorimeter. The full electronic calibration of the voltage of the PMT's, of the Analog to Digital Converters (ADC) and of the electronic readout heavily depends upon the stable and independent natural radioactivity of uranium. Additionally, the readout electronics can be constantly calibrated with other calibration methods like charge injection and LED pulses.

3.2.3 Small Angle Rear Tracking Detector (SRTD)

The ZEUS SRTD [29] is designed to improve the measurement of the scattered electron and other charged particles in a small rear angular coverage ($162° - 176°$) with respective to the incident electron beam direction. It is positioned at z = -1.48 m from the nominal IP.

In the active part of the SRTD, the 1-cm wide scintillator strips are arranged in two overlapping layers, one containing horizontal, the other vertical strips. It covers the region of about 68 $\times$ 68 cm^2 in $x - y$ plane, except the 20 $\times$ 20 cm^2 cutout in the center of the beam pipe. The scattered electron position can be measured with a resolution of 3 mm in this plane, equivalent to an angular resolution of 0.12 degree.

3.2.4 Luminosity Measurement (LUMI)

The luminosity measurement is quite critical for cross section determination so that a precise measurement of luminosity is necessary and essential in experimental particle physics. In ZEUS, the luminosity monitoring is the detection in coincidence of an electron and of the photon emitted from the electron at a very small angle in the Bethe Heitler [30] bremsstrahlung process $ep \rightarrow e'\gamma p$ [31, 32]. The luminosity is determined by $\mathcal{L} = N/\sigma$, where N and σ are the number of events and the cross section of this process, respectively. The σ is well calculated and known to a precision of 0.5%.

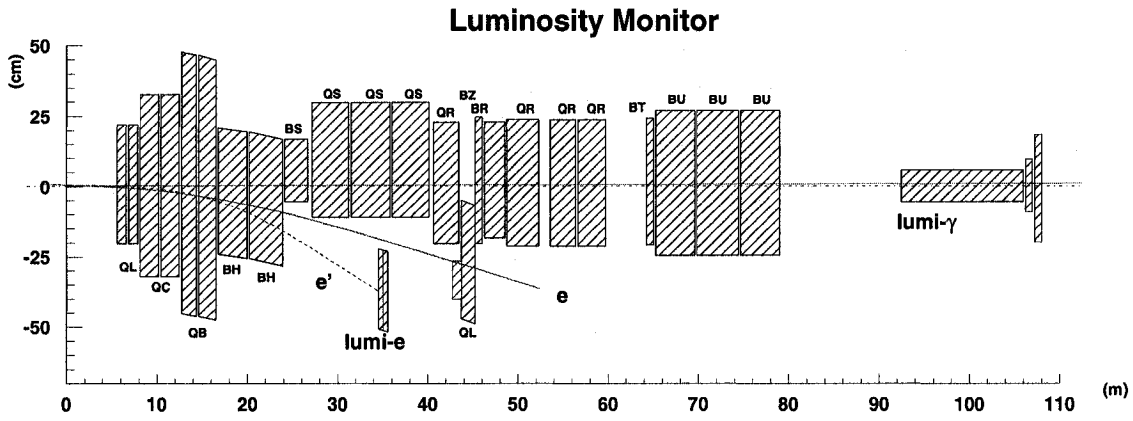

Figure 3.9: Luminosity monitoring system at ZEUS. Shown are the electron calorimeter (lumi-e), the photon calorimeter (lumi-γ) and the electron tagger at z= -44 m.

The ZEUS luminosity monitoring system includes two separate and independent small calorimeters detecting the outgoing electron and photon respectively, as shown in Figure 3.9. The electron detector is located at z = -35 m, downstream of the lepton beam and is labeled lumi-e. The other one is the photon calorimeter at z = -107 m away from the IP and is labeled lumi-γ. A small electron calorimeter, located at z = -44 m, is also shown in Figure 3.9. It is used as a photoproduction tagger.

The bremsstrahlung photon travels at a very small angle with respect to the beam direction and leaves the beam pipe after about 80 m flight from the IP, where the proton beam pipe bends towards to the center of HERA. After another few meters flight, the photon is detected in the photon calorimeter at z = -107 m away from the IP. The electron is deflected out of the beam pipe by a magnet and subsequently detected by the electron calorimeter at z = -35 m. The achieved precision on the luminosity measurement is 1.5-2.2%.

3.3 Trigger and Data Acquisition System

The majority of events in ZEUS which can cause a signal originate from backgrounds rather than the ep collisions of interest. Sources of these background events can be due to the synchrotron radiation by the electron beam, beam gas, beam pipe interactions or cosmic ray initiated events. The dominant one is the beam gas process. Since the amount of information is far beyond the physical limitation of the record

and storage, the ZEUS trigger system takes the responsibility of effectively selecting interesting physics events and ensuring a practical record rate.

The beam bunch crossing every 96 ns at HERA leads to about 10 MHz crossing rate per second. Although each crossing does not ensure a collision to happen, typically a huge background due to beam-gas interaction will be produced at a rate of 10 to 100 KHz. It turns out that the *ep* collision events generally account for only a small fraction of the total events. Concerning such high production rate from background, it is impossible and unnecessary to record each event. Therefore, a three-level ZEUS trigger system was designed. It reduces the event rate one level after the other from ~100 KHz at the beginning to a few Hz in the end.

3.3.1 First Level Trigger (FLT)

The FLT system has to strongly suppress background and to reduce the signal output below 1KHz for the Second Level Trigger system. Each component of the ZEUS detector is equipped with FLT electronics. Each FLT provides a fast trigger information based on such properties as energy sum, thresholds or timing information and passes its decision to the Global First Level Trigger (GFLT) system.

For every bunch crossing, all data are stored in a 5 μs pipeline. Each FLT makes its decision between 1.0 to 2.5 μs after the crossing occurred and another $\sim$ 1.9 μs (about 29 bunch crossings) is needed for the GFLT to take information from each FLT and distribute its decision back to each component. Therefore the GFLT is issued exactly 46 crossings, or 4.4 μs, after the crossing that produced it. The events that satisfy the GFLT logics will pass to the SLT while the rest is discarded.

The main backgrounds are due to beam gas and cosmic interactions at this stage and all of them can be reduced with the energy sum thresholds from the CAL and the CTD z-by-timing information.

3.3.2 Second Level Trigger (SLT)

The SLT is a parallel transputer network which aims to reduce the event rate by a factor of 10. Each detector component has its own SLT processor like in FLT. All the individual SLT informations are sent to the Global Second Level Trigger (GSLT) after the processing. The event quantities are recalculated to a higher degree of

precision at this stage. The beam gas background is rejected on the basis of the CAL timing information. Some other information like the E_T and $E - p_Z$ are well determined. The satisfactory events are sent to the event builder.

3.3.3 Event Builder (EVB)

After accepting the GSLT decision, the EVB collects information about the event from all components of the detector and organizes the information in a standard data format which is ready for next level trigger analyzing and data storage as well.

3.3.4 Third Level Trigger (TLT)

At the TLT level, a fully reconstruction of events is performed on the basis of the information available from the EVB. And the output rate is ~10 Hz compared to the input rate of about 100 Hz. In addition, the particular classes of *ep* interactions of interest are identified at this stage for future investigation.

If an event is accepted by TLT, the event will be written to disk for further offline reconstruction and data analysis.

3.4 Expectations and Challenges for HERA II

The HERA I operation ended up with a successful conclusion of completing luminosity delivery of 190 pb^{-1} in 2000. In order to obtain more luminosity for the second running phase, HERA has undergone an important upgrade in the 2000/2001 shutdown period. Meanwhile several major improvements have been made to the ZEUS detector. New components such as the MVD, the STT (Straw Tube Tracker) and a new luminosity monitor were installed while some other components like the FPC (Forward Plug Calorimeter) and the BPC (Beam Pipe Calorimeter) were removed.

Many challenges also come up due to the upgrades. Considerable efforts have been made to understand vacuum conditions, proton background and the dead material effects in the new system in ZEUS. The conditions steadily improved during the 2004 running period. The first results for HERA II data were presented to the ICHEP2004 conference in Beijing and much more exciting results are expected be coming up for HERA II data in the coming years.

Chapter 4

Event Reconstruction and Selection

The purpose of this thesis is to measure the inclusive neutral strangeness production in the processes

$$\gamma^*(\gamma)p \rightarrow \Lambda X, \tag{4.1}$$
$$\gamma^*(\gamma)p \rightarrow K^0_S X \tag{4.2}$$

for DIS (mainly γ^*p interactions) and photoproduction (γp interactions) events. The corresponding event reconstruction and selection for different phase spaces are given in this chapter.

The reconstruction of the event variables is introduced in the first part of this chapter. Then both online and offline cuts used to select events are described. Since several measurements in this thesis have been further investigated in certain specific sub-samples, additional explanations on the division of the event sample are addressed in the end.

4.1 Event Reconstruction

The method used to reconstruct the event variables varies depending on the event feature and the detector response to the event. For instance, the initial electron will be scattered with a large angle w.r.t. beam pipe direction for a typical DIS event

and subsequently it can be detected by the main components of the ZEUS detector. In this case, the event variables are better extracted with the precise knowledge of the scattered electron or/and the total hadronic final system. In contrast to DIS, photoproduction is characterized by the scattered electron undetectably escaping the main detectors, and thus lacks the information about the scattered electron for event reconstruction. Instead, the determination of event variables in photoproduction heavily relies on the measurement of the total hadronic final system.

4.1.1 Electron Finder

Before going forward to the specific reconstruction methods, the knowledge of how to identify and measure electrons in ZEUS should be clear first, since it is crucial for event identification and reconstruction, especially for DIS events. The standard approach available in ZEUS is a specialized electron finder named as Sinistra [33, 34] from which a high efficiency and purity of the electron reconstruction can be achieved. Sinistra is a neural-network based electron finder. The logic of this algorithm is to train itself first with MC studies to get knowledge of shower properties of electrons and hadrons in the CAL in term of a set of parameters. With the help of these parameters, in turn, a shower appearing in the CAL in the real data can be identified. The output variables in this algorithm can be interpreted as the electron finding probability, electron energy, event variables like x, Q^2 and y, etc.

4.1.2 Jet Reconstruction

One of the important physics phenomena at HERA is jet production. Because of the QCD color confinement, the colored partons, quarks or gluons, are however not observable directly in the experimental environment. The original information of the colored partons has already been smeared by the high order QCD effects and hadronization processes. Nevertheless the small amount of transverse energy created in the hadronization process is assumed to not affect the important properties of the underlying partonic process. Provided the momentum of the primary parton is sufficiently high, the hadrons resulting from it form a collimated flow of particles observed in the detector, called jet. Hence the jet topology is expected to be related to the partonic dynamics of the hard interaction. This is the basic idea behind jets.

Although no direct jet measurement has been done in this thesis, the cuts associated with jets in photoproduction process make a short description of jet reconstruction necessary.

The algorithm used to define jets in this thesis is a standard ZEUS jet reconstruction package, called the longitudinal invariant k_T algorithm [39, 40]. In the ZEUS coordinator reference system, an unidentified energy object i in the CAL can be parameterized by an azimuthal angle ϕ_i, a pseudorapidity[1] η_i, and a transverse energy $E_{T,i}$. The algorithm starts with a list of such objects and an empty list of jets. It proceeds recursively as follows

1. Two variables are defined first for later use. These are

$$d_i = E_{T,i}^2 \tag{4.3}$$
$$d_{ij} = min(E_{T,i}^2, E_{T,j}^2)[(\eta_i - \eta_j)^2 + (\phi_i - \phi_j)^2]/R^2 \tag{4.4}$$

   where d_i is the distance of object i to the beam and d_{ij} is the relative distance between two objects. R is the radius parameter of the jet algorithm and assumed to be one here.

2. In step 1, the smallest distance value out of d_i and d_{ij} is found and the value is assigned to a new variable, d_{min}.

3. In step 2, if d_{ij} was found to be the smallest, the objects i and j are then merged as a new object, for example k. The variables ϕ_k, η_k and $E_{T,k}$ are calculated to characterize the new object k according to

$$E_{T,k} = E_{T,i} + E_{T,j} \tag{4.5}$$
$$\phi_k = [\phi_i E_{T,i} + \phi_j E_{T,j}]/E_{T,k} \tag{4.6}$$
$$\eta_k = [\eta_i E_{T,i} + \eta_j E_{T,j}]/E_{T,k}\ . \tag{4.7}$$

   When going back to step 1, the distances of the new object k, for example d_k and d_{kl}, will be calculated as what object i did there. The l represents another object in the remaining objects in the list.

[1] the definition of pseudorapidity is $\eta = -ln[tan(\theta/2)]$, where θ is the polar angle of the particle in the ZEUS coordinator reference system.

4. In step 3, if d_{min} is d_i, the object i will then be removed from the list of objects and be added as one jet in jet list.

5. One loop is finished and a new one will start by going back to step 1. Such cycles will continue until the smallest value among d_i and d_{ij} is above a threshold d_{cut}. The d_{cut} represents an energy scale at which $\Lambda^2 \ll d_{cut} \ll s$ is satisfied, where Λ is the QCD scale (at a level of 200 MeV) and $\sqrt{s}$ is the center-of-mass energy ($\sim$ 300 GeV at HERA). In this analysis d_{cut} is set to 1 GeV^2.

Once the loop over all the objects is finished, a list of jets is formed wherein the jet information about the transverse energy, azimuthal angle and pseudorapidity are stored. Since it is not necessary in this thesis to use all the jets in an event, only the two which have the highest E_T^{jet} are considered.

4.1.3 DIS Event Reconstruction

There are several methods available in ZEUS to reconstruct the DIS event variables. No attempt is made to introduce all those methods except those which are generally used and related to the measurements in this thesis. Three methods, namely Electron method (e), Jacquet-Blondel method (JB) [36] and Double Angle method (DA) [37, 38], are reviewed:

- Electron method (e)
  This method depends exclusively on the measurement of the scattered electron. The event variables are defined as

$$Q^2_{\text{e}} = 2E_{\text{e}}E'_{\text{e}}(1 + cos\theta_{\text{e}}) , \tag{4.8}$$

$$y_{\text{e}} = 1 - \frac{E'_{\text{e}}}{2E_{\text{e}}}(1 - cos\theta_{\text{e}}) , \tag{4.9}$$

$$x_{\text{e}} = \frac{Q^2_{\text{e}}}{sy_{\text{e}}} . \tag{4.10}$$

  The variable E_{e} (E'_{e}) represents the energy of the initial (final) electron and θ_{e} is the polar angle of the scattered electron. The electron method has a very good resolution at large y where the scattered electron can be well detected by the CTD and CAL. However this method has a poor x resolution at smaller y and needs large radiative corrections. The subscript 'e' identifies the electron reconstruction method.

- Jacquet-Blondel method (JB)

  This method relies entirely on the measurement of the hadronic final system, hence it is also named the hadron method. The event variables reconstructed from this method are described in the following:

$$\delta_{\mathrm{had}} = E_{\mathrm{had}} - p_{\mathrm{Z,\,had}} \tag{4.11}$$

$$y_{\mathrm{JB}} = \frac{\delta_{\mathrm{had}}}{2E_{\mathrm{e}}} \tag{4.12}$$

$$Q^2_{\mathrm{JB}} = \frac{p^2_{\mathrm{T,\,had}}}{1 - y_{\mathrm{JB}}} \tag{4.13}$$

$$x_{\mathrm{JB}} = \frac{Q^2}{s y_{\mathrm{JB}}} \tag{4.14}$$

  Here $p_{\mathrm{Z,\,had}}$ is the longitudinal momentum of the hadronic final states and δ_{had} is the sum over energy and longitudinal momenta of all CAL cells. This method is sensitive to the calorimeter noise at relative smaller y and the energy loss in the rear beam pipe direction at larger y. Also a good understanding of energy scale and energy losses in inactive material is needed. The JB method is not very sensitive to the radiative corrections.

- Double Angle method (DA)

  This method takes information from both the scattered electron and hadronic final system for event variable reconstruction. The definition of the event variables is given below.

$$cos\,\gamma = \frac{p^2_{\mathrm{T,\,had}} - \delta^2_{\mathrm{had}}}{p^2_{\mathrm{T,\,had}} + \delta^2_{\mathrm{had}}} \tag{4.15}$$

$$Q^2_{\mathrm{DA}} = 4E^2_{\mathrm{e}} \frac{sin\,\gamma(1 + cos\,\theta_{\mathrm{e}})}{sin\,\gamma + sin\,\theta_{\mathrm{e}} - sin(\theta_{\mathrm{e}} + \gamma)} \tag{4.16}$$

$$x_{\mathrm{DA}} = \frac{E_{\mathrm{e}}}{E_{\mathrm{p}}} \frac{sin\,\gamma + sin\,\theta_{\mathrm{e}} + sin(\theta_{\mathrm{e}} + \gamma)}{sin\,\gamma + sin\,\theta_{\mathrm{e}} - sin(\theta_{\mathrm{e}} + \gamma)} \tag{4.17}$$

  Here γ is the polar angle of the scattered electron in the simple picture of electron-massless quark reaction $eq \rightarrow eq$. This method relies less on the energy scale than the JB method does, but small radiative corrections are necessary. The resolution is poor for smaller values of y.

A mixture of these three methods was used for reconstruction of the DIS event variables in this thesis, depending on which one is appropriate in the specific kinematic regions considered.

4.1.4 Photoproduction Event Reconstruction

The photoproduction process is characterized by the quasi-real exchange photon and a very small four-momentum-transfer, $Q^2 \simeq 0$ GeV^2. The scattered electron will escape the main detector without being detected in this process. So the event reconstruction methods relying on the scattered electron finding will not be suitable any more in photoproduction process. However, the JB method introduced in Section 4.1.3 totally relies on the hadronic final states, so the event variables can be determined this way. In this thesis, photoproduction variables are then calculated with the JB method.

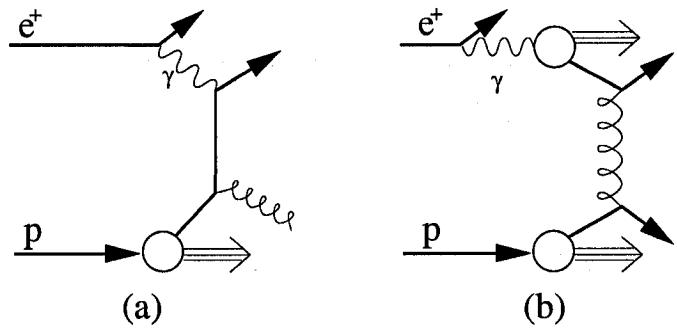

Figure 4.1: Examples of leading order diagrams in photoproduction process, (*a*) for direct process and (*b*) for resolved process.

The leading order photoproduction can be separated into two subprocesses according to the manner in which the photons interact with the partons in the proton. The photon may interact directly with a parton in the proton as what Figure 4.1(a) shows, which is tagged as direct process, or the photon can be resolved as a source of partons and one or more than one parton take part in the interaction with the proton, as shown in Figure 4.1(b), which case is called resolved process.

The fraction of the photon energy involved in the hard scattering process can not be determined directly at the partonic level due to the confinement effects. Therefore no direct way exists to separate the direct and resolved processes. Based on the correlation between the scattered parton and the jets mentioned above, the possible

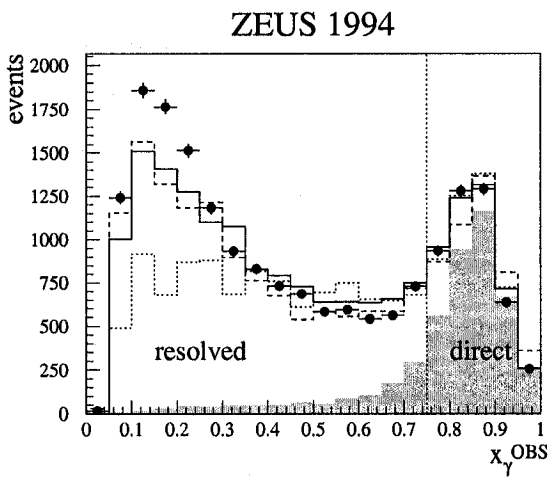

Figure 4.2: The x_γ^{OBS} distribution reconstructed in the dijet analysis in ZEUS [45]. The data (points) are compared to the predictions from a few Monte Carlo models, HERWIG (dotted line) without multiple interaction mechanism (MI) [54], HERWIG with MI (solid line) and PYTHIA with MI (dashed line).

approaches to make such a division are discussed in [41, 42, 43, 44] in an experimental point of view. The separation is then suggested to be made according to the following variable,

$$x_\gamma^{\mathrm{OBS}} = \frac{\sum_{\mathrm{jet}} E_T^{\mathrm{jet}} e^{-\eta^{\mathrm{jet}}}}{2yE_{\mathrm{e}}} \tag{4.18}$$

where $\sum$ runs over the first two highest E_T^{jet} jets and $yE_{\mathrm{e}} = E_\gamma$ represents the energy of the photon participating in the interaction. The variables E_T^{jet} and η^{jet} are the transverse energy and pseudorapidity of the jet respectively. Thus x_γ^{OBS} is used to represent the fraction of the photon energy carried by the two highest E_T^{jet} jets. Practically, x_γ^{OBS} will not be exactly one for the direct process due to the higher orders and hadronization effects. In ZEUS, the convention is to define the events with $x_\gamma^{\mathrm{OBS}} > 0.75$ as the direct-dominated process and the rest as the resolved-dominated one [45]. An example of the x_γ^{OBS} distribution which was determined in a dijet measurement in ZEUS [45] is shown in Figure 4.2.

4.2 Event Selection

The data used in this thesis were collected by the ZEUS detector during the data-taking period from 1996 to 2000. The total integrated luminosity is 121 pb^{-1}, of which 82 pb^{-1} corresponds to a center-of-mass energy of $\sqrt{s} \simeq 318\,\text{GeV}$ and 39 pb^{-1} to a lower $\sqrt{s} \simeq 300\,\text{GeV}$.

The chain of full event selection consists of two main steps: online filtering and offline selection. The triggers applied online are used to select specific interesting events while dramatically reducing the background event rate. In addition, specific interesting events can be selected offline with more advanced and stricter cuts.

4.2.1 Online Preselection

A three-level trigger strategy has been adopted in ZEUS to pick the interesting physics events. The trigger system used in this analysis is actually a logical combination of many binary decisions out of three-level triggers. In the following, a description of the selection criteria used at each stage of the trigger system is given.

The trigger configurations were different for the three different kinematic regions discussed in this thesis. All of them are discussed separately below.

The DIS Trigger Configuration

The filters applied in the FLT and SLT aim to select physics events while strongly reducing the backgrounds for a general purpose, so the criteria used are rather loose. In the following, the detailed information of these filters for DIS event selection is described first.

- FLT: There are many global vetoes to reject the obvious non-ep events, for instance, to reject the events with a wrong timing from the C5[2] counters or the identified beam gas events with the SRTD timing information. In addition, at least one of the further requirements listed below must be fulfilled [46, 47]:

  – the total electromagnetic energy in the CAL exceeds 15 GeV;

[2]The C5 counter is a small detector located 1.2 m (3.15 m before the 2001 upgrade) from the nominal IP in the electron flight direction. It is made of two layers of scintillator sandwiched between three lead sheets. It detects particles outside of the beam pipe produced mainly by beam-gas interactions.

  - the total transverse energy deposited in the CAL is larger than 18 GeV or 11.5 GeV if a track in the CTD is found;
  - an isolated electromagnetic energy deposit in the RCAL. This condition requires either that the deposit be greater than 2 GeV or that a signal in the SRTD and a track in the CTD are needed, or that the total energy deposit in the CAL exceeds 18 GeV when a track is present in the CTD;
  - an isolated electromagnetic deposit larger than 4.8 GeV in the BCAL and a track in the CTD;
  - an isolated electromagnetic deposit larger than 3.4 GeV in the RCAL and a track in the CTD.

- SLT: At this stage, the background events from photoproduction are removed by requiring a few GeV's energy deposited in the electromagnetic calorimeter (2.5 GeV in the RCAL or BCAL, or 10 GeV in the FCAL) or $E - p_Z + 2 * E_\gamma^{\mathrm{LUMI}} > 29\,\mathrm{GeV}$. Here E_γ^{LUMI} is the energy deposition in the photon calorimeter in the luminosity monitoring system.

- TLT: Two different TLT slots, DIS01 and DIS03 [46], are used to select the low Q^2 and high Q^2 DIS events, respectively. At this stage, these two triggers are subject to a few common cuts like $E - p_Z + 2 * E_\gamma^{\mathrm{LUMI}} > 30$ GeV and $E - p_Z < 100$ GeV. Beside these common requirements, further dedicated configurations of DIS01 an DIS03 are given in the following.
  - DIS01: it has a prescale on the accepted events of 1, $1/10^{th}$ or $1/100^{th}$, varying during different running periods. In addition, it also requires that the scattered electron with the energy above 4 GeV should be outside of a box region of 24×12 cm^2 in the RCAL.
  - DIS03: the scattered electron with energy above 4 GeV should be at least 26 cm (36 cm) away from the beam pipe in the $x - y$ plane of the RCAL for the running period 1996-1997 (1999-2000).

The Photoproduction Trigger Configuration

The trigger logic to select photoproduction events is described in the following.

- FLT: The requirements at this stage are quite similar to ones described in DIS events section, but there is no requirement on the scattered electron finding in the CTD or SRTD any more.

- SLT: According to the definition of the 'High E_T' trigger [50], a total $E - p_Z$ above 10 GeV in the CAL is required and the E_T in all the CAL cells, excluding the inner ring of the FCAL, should be above 8 GeV.

- TLT: A dedicated HPP14 dijet trigger [50] is used in this thesis. During the running period from 1996 to 1997, the HPP14 is defined as a dijet trigger: each jet has a E_T^{jet} above 4 GeV and the pseudorapidity is limited to $|\eta| < 2.5$. An extra cut on the dijet invariant mass, which should be greater than 16 GeV, is required since 1998. Before 1998, there was not any invariant mass cuts on the dijet system. After June 1999, all the cuts were kept unchanged except a stricter E_T^{jet} cut whereby a minimum value of 4.5 GeV was required.

4.2.2 Deep Inelastic Scattering

A DIS event is characterized by the scattered electron being detected in the CAL, balanced by jets in p_{T}. The scattered electron is identified with a neural network, based on the deposited energy in the CAL as what was discussed in Section 4.1.1. Specifically, the following requirements have been applied offline to select DIS events:

- $5 < Q^2_{\text{DA}} < 25\,\text{GeV}^2$: The events selected in this Q^2 range are tagged as the low Q^2 DIS events while events in $Q^2_{\text{DA}} > 25\,\text{GeV}^2$ range are called the high Q^2 DIS events. The Q^2 separation allows the dependence of many measurements on the hard scattering process to be investigated. In addition, events in the two Q^2 ranges differ from each other on prescale values as discussed in the previous section, giving another natural reason for the splitting of the data. The lower limit value of 5 GeV^2 is chosen so that a good description of the data by MC samples can be obtained;

- a scattered electron was found with energy above 10 GeV. This cut ensures a good understanding of the electron finding process and a good finding efficiency. The presence of the scattered electron in the main detector also suppresses the photoproduction background;

- $|z_{\text{vtx}}| < 50$ cm to reduce background from non-*ep* collisions, most of which are the beam-gas background events or cosmic interactions. Here z_{vtx} is the z coordinator determined from the track and vertex reconstructions with the CTD. In the case of no tracking reconstructed primary vertex, the average z vertex position was assigned;

- $y_{\text{JB}} > 0.02$ to improve the accuracy of the DA reconstruction. In order to obtain a good reconstruction using the DA method at the smaller y region, a requirement on the total hadronic system was imposed by applying this cut. Therefore the event variables reconstructed from the DA method, using information from both the scattered electron and hadronic system, can be improved with a better knowledge of the hadronic system of the event;

- $y_{\text{e}} < 0.95$ to remove events where fake electrons are found in the CAL. According to the definition $y_{\text{e}} = 1 - \frac{E'_{\text{e}}}{2E_{\text{e}}}(1 - cos\theta_{\text{e}})$, the upper limit of y_{e} can be obtained to be about ~0.95 when E'_{e} is the minimum energy of 10 GeV and θ_{e} is the maximum polar angle of the CTD, between ~0.3 and 2.6 (in rad). Therefore a y_{e} larger than 0.95 is not resulting from the real scattered electron;

- $38 < \delta < 65\,\text{GeV}$, where $\delta = \sum_i (E_i - p_{Z,i})$. The sum runs over the energy and longitudinal momentum of all CAL cells. Note that δ defined here differs from δ_{had} in Formula 4.11 of the JB method. δ_{had} excludes the contribution from the scattered electron while δ here includes it. This cut removes events with large initial-state radiative corrections and further reduces the background from photoproduction;

- the impact position of the scattered electron is required to be outside a box of dimension 26×14 cm^2 on the RCAL around the beam pipe. This cut is usually called the "box cut". It ensures that the impact position of the scattered electron is at least 2.5 cm away from the edge of the RCAL so that a total containment of the electromagnetic shower in the RCAL is guaranteed;

- to further reduce the photoproduction background, an isolated electron was selected only if the energy from all CAL cells, which are not associated with the scattered electron but within an $\eta - \phi$ cone of radius 0.8 centered on the electron, is not above 5 GeV [48];

- an electron track is required if the electron was found in the main detector region or outside this region but with $\delta > 44\,\text{GeV}$. The main detector covering polar angle is $0.3 < \theta < 2.6$ in rad ($17.2° < \theta < 150°$ in degree). This cut can further suppress the non-ep interaction and photoproduction events.

The trigger for the low Q^2 DIS event selection was often prescaled. After prescale, the 1996-2000 data corresponds to an effective luminosity of 16.6 pb^{-1}.

The same selection criteria were used to select the high Q^2 DIS events, except for the cuts on Q^2 and the position of the scattered electron, which were instead as follows:

- $Q^2_{\text{DA}} > 25\,\text{GeV}^2$;

- an event was accepted only if the impact position of the scattered electron on the RCAL satisfied $\sqrt{x^2 + y^2} > 36$ cm.

It should be noted that there is no jet requirement in the selection of the DIS events.

4.2.3 Breit Frame in DIS

Some work in this thesis has also been performed in the Breit frame, so a short description of the Breit frame is necessary. The Breit frame is defined as a reference system where the exchanged photon and the proton are collinear, and the virtual photon does not have energy or transverse momentum. In this frame, the photon only has a z-component momentum with a value of Q. Therefore its four-momentum can be expressed by $P_\gamma = (E, \vec{p_\gamma}) = (0, 0, 0, Q)$. A scheme of this frame is given in Figure 4.3.

In the QPM, the incoming quark absorbing the virtual photon does not change its energy and transverse momentum, but just reverses its longitudinal momentum with the same magnitude. The quark feels like if bounced back off a brick wall with the exact same momentum but opposite sign. So the Breit frame is also called the brick wall system. The quark brings a four-momentum of $P_q = (E_q, 0, 0, x_p P)$ before the absorption of the photon and $(E_q, 0, 0, -x_p P)$ after the absorption. Here $x_p P$ is the fraction of the proton momentum carried by the quark. The conservation of momentum of the system leads to the scaled momentum variable $x_p = -Q/2P$.

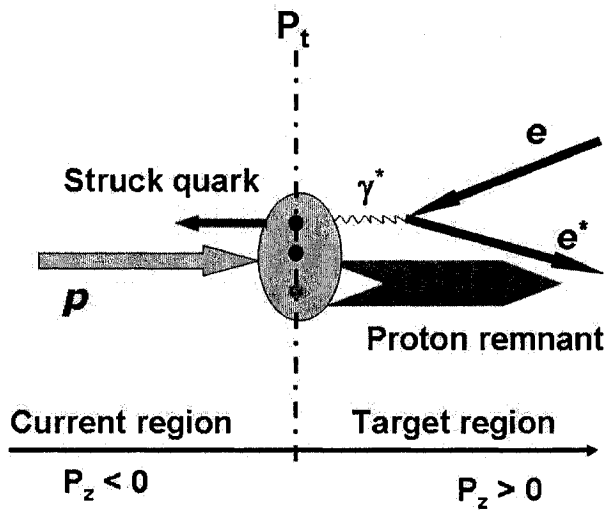

Figure 4.3: An illustration of the Breit frame at HERA. The current region, $z < 0$, contains the outgoing quark, while the target region refers to the region $z > 0$ containing the scattered electron and proton remnant. The initial proton, proton remnant, struck parton and the exchanged boson have only z-component momentum in the Breit frame.

Experimentally the DIS events are boosted and then rotated so that the virtual photon is along the negative z axis - this is to maximize the separation of the struck parton from the outgoing electron and the proton remnant. The region of $z < 0$ in this frame, containing the outgoing quark, corresponds to the current region (CR) while the target region (TR) refers to the region $z > 0$ containing the scattered electron and proton remnant.

The advantage of using the Breit frame is in that it can clearly separate the different contributions from the struck quark and the proton remnant. In the QPM, the outgoing struck quark in the current region would be analogous to one hemisphere of an e^+e^- annihilation event. Thus measurements in the Breit frame in ep collisions provide an appropriate reference frame to compare with the e^+e^- measurements.

4.2.4 Photoproduction Process

Photoproduction events were selected by requiring that no scattered electron candidate was identified. Furthermore, the following offline selection criteria were also

imposed:

- $|z_{\text{vtx}}| < 50$ cm, to reduce background from non-*ep* collisions due to the beam gas or cosmic ray;
- $y_{\text{JB}} > 0.2$, to further reduce background from non-*ep* collisions;
- $y_{\text{e}} > 0.85$. This cut is used to reduce the risk to reject photoproduction events which are wrongly considered as DIS events. This can be the case for some final pion, electron or photon present in the photoproduction events which can be misidentified as the scattered electron. The 'inelasticity' y_{e} reconstructed in this case is usually large. Therefore this kind of events are included by applying this cut;
- $y_{\text{JB}} < 0.85$, to reduce background from the neutral current DIS events where the electron is not identified;
- the charged current DIS events are removed by rejecting events where $P_T^{\text{miss}}/\sqrt{E_T} > 2.0\sqrt{\text{GeV}}$. Here P_T^{miss} is the missing transverse momentum carried away by the undetectable neutrino;
- an event is accepted if it contains at least two jets, reconstructed by the k_T cluster algorithm discussed in Section 4.1.2. The two jets must fulfill the criteria like $E_T^{\text{jet}} > 5\,\text{GeV}$ and $|\eta^{\text{jet}}| < 2.4$. These cuts are the minimum requirements to ensure a good jet finding efficiency while trying to select jets with a large range of transverse energy for the investigation of the fireball events.

4.2.5 Fireball Events in Photoproduction

In order to investigate further measurements such as the strange baryon to meson production ratio, the whole photoproduction sample was separated into two sub-samples bearing different topological event features, the fireball-enriched sample and fireball-depleted sample [49].

The fireball-enriched events are these events characterized by a highly isotropic transverse jet energy distribution. The term fireball is assigned to represent a specific physical picture with a scenario for the isotropic multiple particle production. These kind of events were selected by requiring the highest transverse energy of jet in an

event, $E_T^{\text{jet}(1)}$, to carry at most 30% of the total event transverse energy, E_T, while the other events are called fireball-depleted events. In figure 4.4(a), the distribution of the $E_T^{\text{jet}(1)}$ as a function of total event E_T is depicted. A visible valley in the gradient of the distribution gives a hint where the two different types of events merge together. The line, $E_T^{\text{jet}(1)}/E_T = 0.3$, across the distribution is the cut applied to divide the fireball-enriched and fireball-depleted samples. The region above the cut line includes the fireball-enriched events characterizing by a multiple low-E_T^{jet} jets production while in the region below the line the fireball-depleted events are contained. The fireball-depleted events are expected to have a clear jet structure.

Figure 4.5 shows an example of fireball-enriched events in ZEUS. In this event, the event transverse energy is about 65.7 GeV while the $E_T^{\text{jet}(1)}$ is less than 6.0 GeV and the highly isotropic multiple particle production can be seen. The other different topological event is the fireball-depleted event, as shown in Figure 4.6. In this event, two clear jets are produced and $E_T^{\text{jet}(1)}/E_T$ is about 0.5.

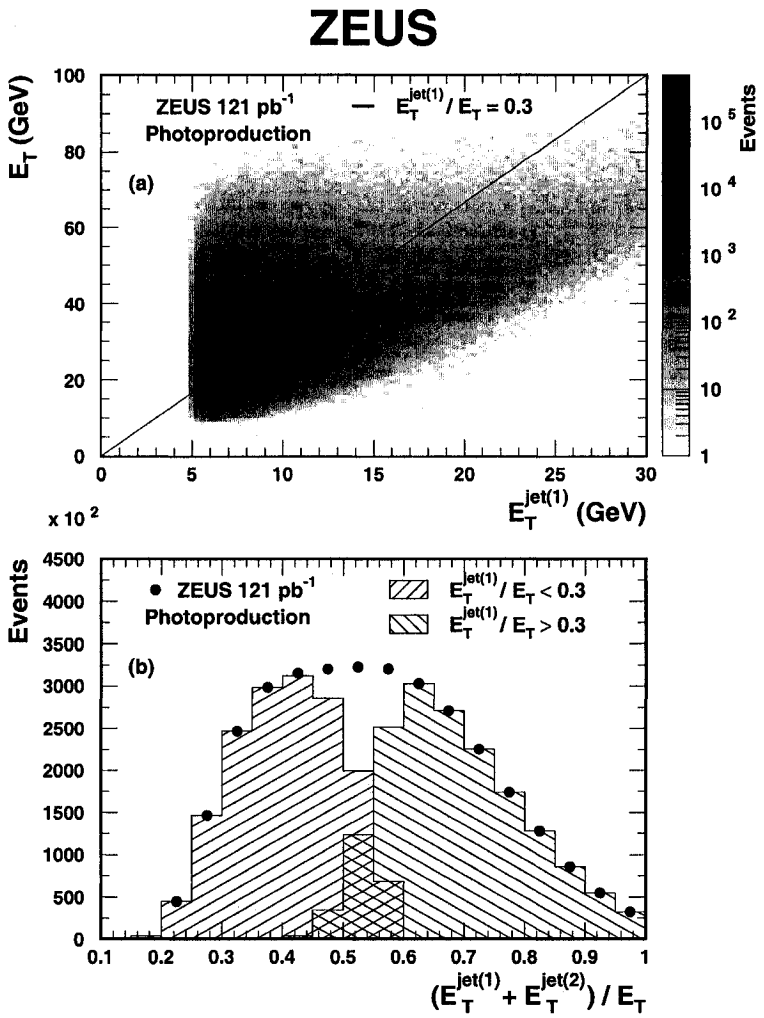

Figure 4.4: Figure (a) shows the distribution of $E_T^{\mathrm{jet}(1)}$ as a function of total transverse energy of the event, E_T, and (b) shows the distribution of the fraction of E_T carried by the two highest transverse energy jets for the fireball-enriched and fireball-depleted subsamples. The line displayed in (a) is the cut used to split the whole photoproduction samples. Here the events were selected without any strange hadron requirement.

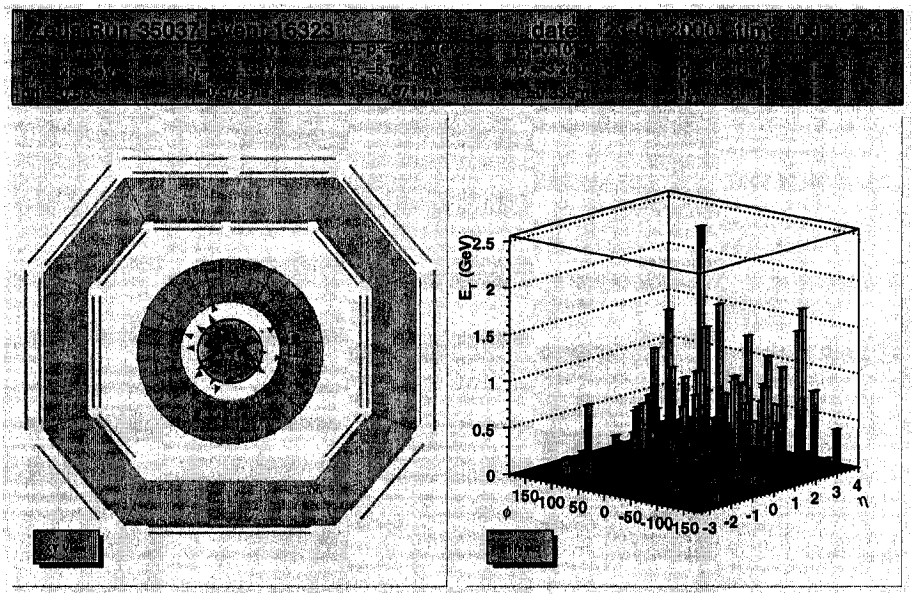

Figure 4.5: An example of fireball-enriched events in ZEUS. The left plot is the event view in the $x-y$ cross section plane. The right one is the CAL transverse energy distribution in the $\phi-\eta$ plane. No jet with special higher transverse energy is found. The isotropic multiple low E_T^{jet} jet production characterizes this kind of events.

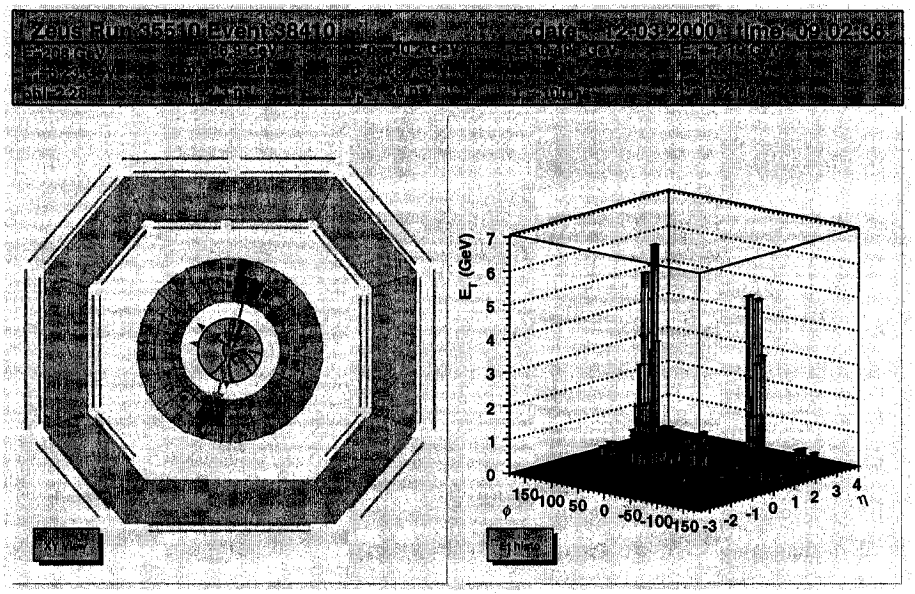

Figure 4.6: A fireball-depleted event with a clear dijet production observed in ZEUS. The left plot is the cross section view of the event in the $x-y$ plane. The right one is the CAL transverse energy distribution in the $\phi-\eta$ plane.

Chapter 5

Strange Particle Reconstruction

Strange particles can be produced copiously in ep collisions at HERA due to their relatively light masses and the high statistics luminosity accumulated. The total integrated luminosity used for the measurements is about 121 pb^{-1} and was collected during the HERA I running period of time from 1996 to 2000. A large number of neutral strange particles, K^0_S, Λ and $\bar{\Lambda}$, was thus gathered and analyzed in this thesis.

The procedures for how to identify these strange particles, how to reconstruct them and how to select them are discussed in this chapter.

5.1 Strange Hadrons of Interest

Three neutral strange particles, K^0_S, Λ and $\bar{\Lambda}$, were considered in the measurement. There are two main reasons why these particles were chosen rather than other strange particles. The first one lies in the consideration of the production statistics available. The particle K^0_S is one of the lightest strange mesons and Λ is the lightest strange baryon. Due to their relatively light masses, huge production quantities are more readily obtained. The other consideration stems from the quality of particle reconstruction. These three particles have 'golden' decay modes. Here 'golden' refers to the simple two-body decay mode with a large branching ratio. And more important, it also means that all the decay products are electrically charged so that the identification and measurement are easily performed using the CTD.

In Table 5.1, a few basic aspects of the strange hadron properties which are related to the measurements made in this thesis are listed. More details of the

	Contents	Mass (MeV)	$I(J^P)$	$c\tau$ (cm)	Decay Mode (BR %)
K^0_S	$d\bar{s}/\bar{d}s$	497.672 ± 0.031	$\frac{1}{2}(0^-)$	2.6786	$\pi^+\pi^-$ (68.6 ± 0.3)
$\Lambda(\bar{\Lambda})$	$uds(\bar{u}d\bar{s})$	1115.683 ± 0.006	$0(\frac{1}{2}^+)$	7.89	$p\pi$ (63.9 ± 0.5)

Table 5.1: Properties of the interested neutral strange particles. Term BR in the table means the branching ratio of the particular decay channel.

property of these strange particles are available from the Particle Data Group (PDG) [51].

In this thesis the decay channel $K^0_S \rightarrow \pi^+\pi^-$ was used for K^0_S reconstruction. It is a weak decay in that the strangeness conservation is violated during the process. Similarly, the decay model $\Lambda \rightarrow p\pi$, used for Λ reconstruction, is also a weak decay for the same reason. The relative larger time scale of the weak reaction, $\sim 10^{-10}$ seconds compared to $\sim 10^{-23}$ seconds in the strong interaction, allows a longer traveling distance before the decay takes place. The direct impact of the longer lifetime results in a measurable displacement of the decay point from the production place, namely a clear secondary vertex displaced from the primary vertex in terms of detector language. An example of a Λ decay is shown in Figure 5.1. The relationship of the decay length and decay time is given $\tau = l/c\beta\gamma$, where l is the decay length, τ is the decay time and $c\beta$ is the velocity of strange particle in the laboratory frame.

The strange hadrons were reconstructed and selected in the same way in all the three kinematic regions considered in this thesis.

5.2 Particle Reconstruction and Selection

As discussed above, the events containing these three neutral strange particles are characterized with a displaced secondary vertex (V0) and two oppositely charged tracks originating from it. Therefore all secondary vertices at which two oppositely charged tracks are fitted to meet are deemed to be V0 candidates. The two tracks fitted to this vertex were then investigated first, from which the mass (M) of the decaying particle was reconstructed.

Each secondary track was required to pass through at least the fifth CTD superlayer. In addition, The transverse momentum corresponding to each charged track

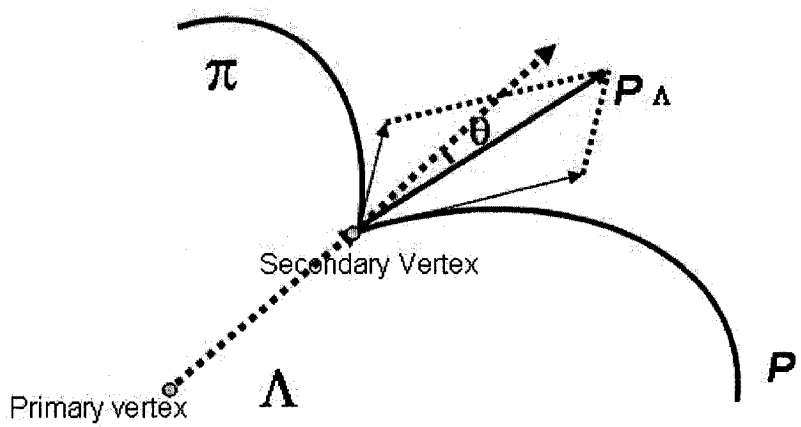

Figure 5.1: An example of Λ decay. The Λ produced at the primary vertex travels some distance before it decays. At the point labeled as secondary vertex, $\Lambda \rightarrow p\pi$ begins and the two decay products move apart in the electromagnetic field in CTD leaving two detectable tracks. The dotted line from primary vertex to secondary vertex shows the undetectable trajectory of the neutral Λ. The angle θ is used as a collinearity cut to remove backgrounds.

was required to be greater than 150 MeV and the absolute pseudorapidity in the laboratory frame to be less than 1.5. These constraints ensured good track resolution and acceptance.

5.2.1 Secondary Scattering Contamination

Before moving forward to the discussions of strange hadron reconstruction, some emphasis is put here to explain a significant type of background events, the Secondary Scattering Contaminations (SSC). This kind of contamination can be created in the secondary scattering of produced particles from *ep* with the wall of the beam pipe (inner radius 8.5 cm and outer radius 8.8 cm) and the inner surface of the CTD (inner radius 16.2 cm). As a consequence, this kind of fake[1] candidates would originate in

[1]Hereafter, a reconstructed particle is defined as a 'real' candidate if it is identified as the truly strange particle of interest from the *ep* collisions while a reconstructed particle is defined as 'fake' candidate if it is identified as not the particle of interest or a particle from non-*ep* collisions.

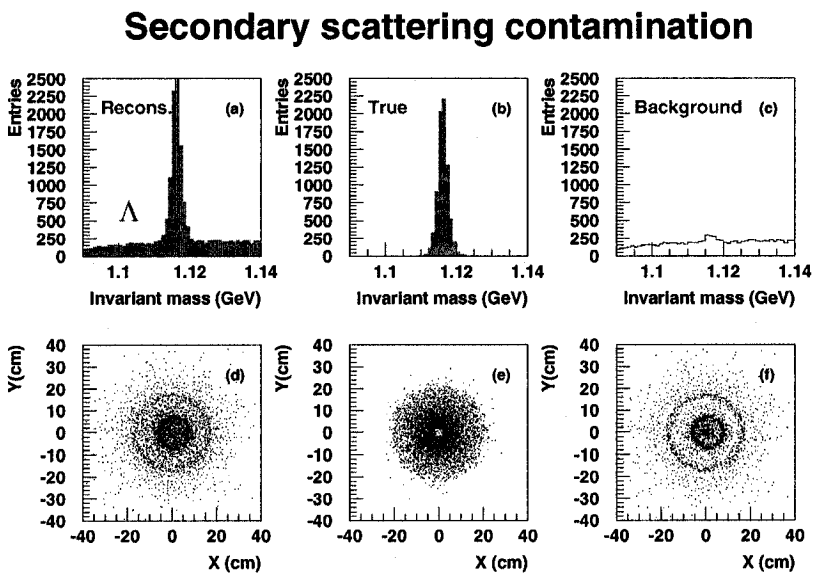

Figure 5.2: Study on the secondary scattering contamination events in MC. Figures (a) and (d) are the distributions of the reconstructed Λ invariant mass and the corresponding secondary vertex position in x-y plane respectively, (b) and (e) are the similar distributions for true Λ's which are matched to ones in hadron level while (c) and (f) for SSC.

the exact place where the beam pipe and the CTD inner cover are located, leading to an obvious signature of contaminations.

A dedicated investigation on SSC has been done using MC in the high Q^2 kinematic region. Figures 5.2(a) and (d) are the reconstructed Λ invariant mass distribution and 2-dimensional distribution of the position of the secondary vertex in the x-y plane, respectively. A clear bulk of Λ events populates the two rings shown in Figure 5.2(d). The real Λ's can be identified by matching the reconstructed candidate to the particle at the hadron level. The type of a particle at the hadron level can be identified in MC from the particle code identifying it. Therefore the distribution features of real Λ's and the fake ones can be distinguished. The invariant mass distribution of real Λ's is given in Figure 5.2(b) and their x-y distribution of V0 is given in Figure 5.2(e), while leaving Figures 5.2(c) and (f) for fake Λ's. According to the comparison of these distributions, the conclusion is reached that the SSC has non-negligible contributions to the reconstruction and it has a clear distribution signature.

In order to remove these events, a cut on the angle between the reconstructed

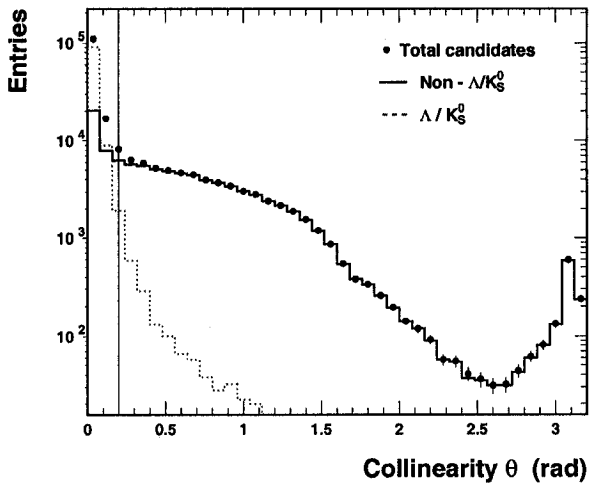

Figure 5.3: An investigation of the collinearity cut with MC studies. The vertical line represents the cut used, $\theta = 0.2$ rad.

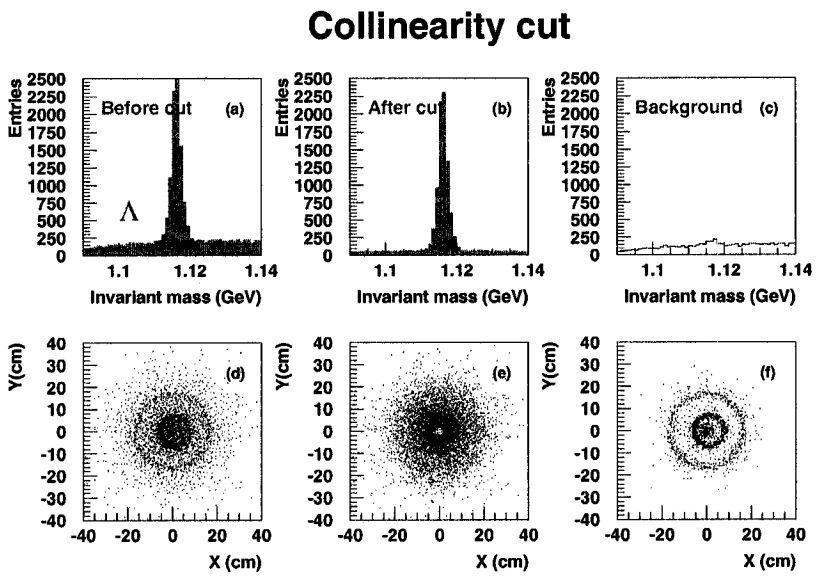

Figure 5.4: The study of the effect of the collinearity cut in the same MC sample as in Figure 5.2. Figures (a) and (d) are the distributions of the reconstructed Λ invariant mass and the corresponding secondary vertex position in x-y plane, respectively, before applying the collinearity cut. The figures (b) and (e) are the equivalent distributions but after the collinearity cut and (c) and (f) for the removed SSC candidates.

candidate momentum and the vector joining the primary vertex to the secondary vertex was applied, which is shown as θ in Figure 5.1. The MC study shows that the backgrounds, mainly due to the SSC, populate the range with larger θ values, as seen in Figure 5.3. In this thesis, this angle was restricted to be less than 0.2 rad.

With the help of the collinearity cut, the reconstructed signal is improved by rejecting these SSC contaminations. Figures 5.4(d), (e) and (f) show the x-y distribution of secondary vertices without the cut, with the cut and the rejected candidates respectively. The rejected events are highly SSC-like as Figure 5.4(f) shows. The invariant mass distribution of these events is rather similar to the background in Figure 5.4(a) and no special enhanced peak is present around the Λ mass position. A rough estimation found that the collinearity cut can remove on average 68.3% of the background while it rejects 1.3% of the signal. It is to be noted that these values may vary if different cuts have been used to select events and particles.

5.2.2 Λ Reconstruction

Partially because of the heavier mass of the proton over the pion mass, it is found from MC studies that the proton from Λ decay has a larger momentum than the other daughter pion with an extremely high probability, close to 100%, in the laboratory system, provided the Λ momentum is greater than 0.3 GeV. This phenomenon can be described with Figures 5.5(a) and (b), which shows the momentum distribution of Λ decay products and the momentum difference between them, respectively. The momentum difference distribution in Figure 5.5(b) clearly indicates an always larger proton momentum than pion's in the selected kinematic regions in this thesis. In order to procure a further understanding, a comparison has also been made by checking the momentum difference between the two K^0_S decay products, the charged pions. Figure 5.6 contains similar distributions to Figure 5.5. However it is clearly seen from Figure 5.6 that no significant momentum difference exist between two charged pions, resulting the distribution in Figure 5.6(b) centering around zero.

No particle identification was applied because of the insufficient description of dE/dx (the ionization energy loss per unit of length) by Monte Carlo. An attempt to investigate the differences between cases with and without particle identification was made and the effect was actually estimated to be rather small if dE/dx was used.

For each V0 candidate, we therefore assign the proton mass to the track with

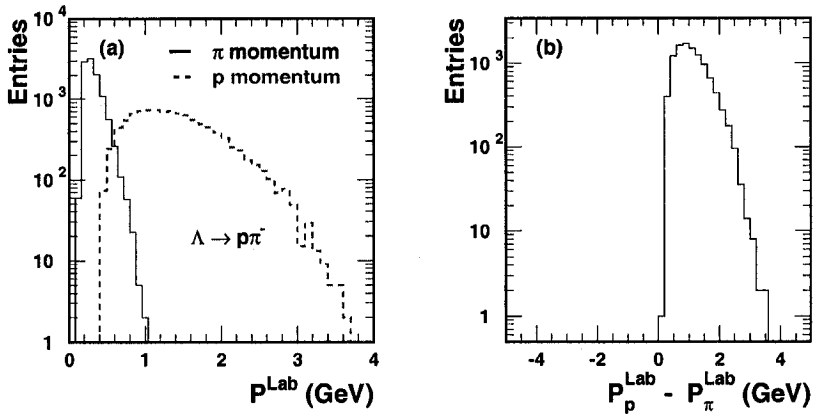

Figure 5.5: The momentum difference between the two Λ decay daughters in $\Lambda \rightarrow p\pi$. The distributions were measured with MC events in the high Q^2 DIS region in the laboratory frame and the Λ's were constrained with $0.6 < p_T < 2.5$ GeV and $|\eta| < 1.2$. Figure (a) shows the momentum distributions of Λ decay products while (b) is the momentum difference distribution between the two decay products.

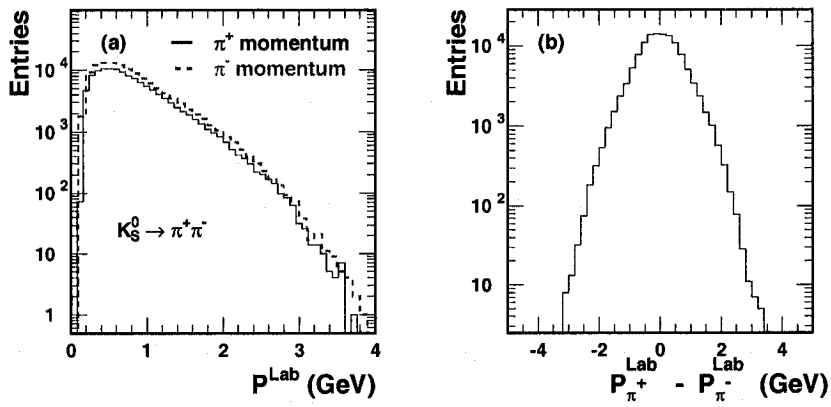

Figure 5.6: The momentum difference between the decay daughters pions in $K_S^0 \rightarrow \pi^+\pi^-$. The distributions were measured with MC events in the high Q^2 DIS region in the laboratory frame and K_S^0 was constrained with $0.6 < p_T < 2.5$ GeV and $|\eta| < 1.2$. Figure (a) shows the momentum distributions of the K_S^0 decay products while (b) is the momentum difference distribution between those two pions.

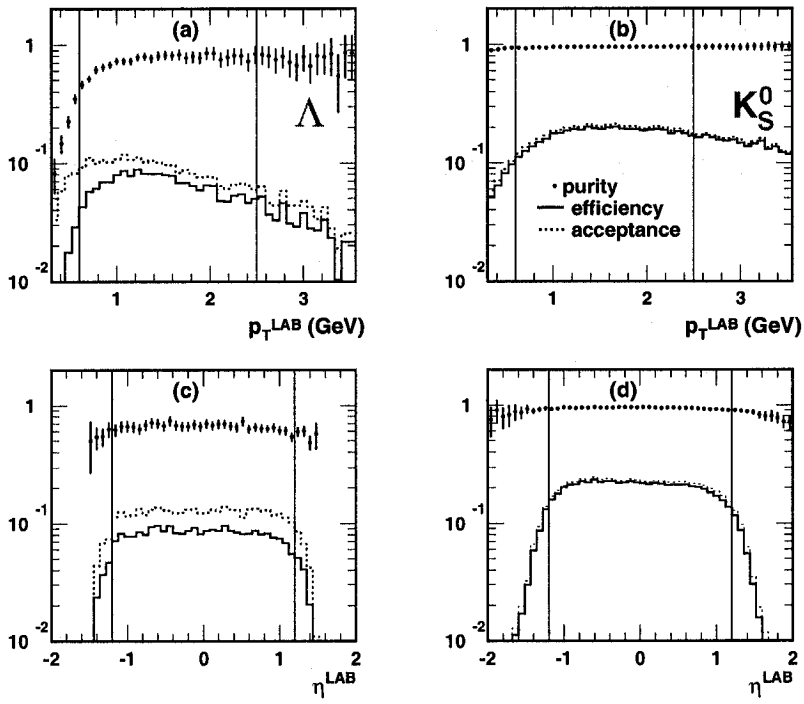

Figure 5.7: Consideration on the transverse momentum and pseudorapidity cuts based on the reconstruction efficiency and acceptance.

larger momentum and the pion mass to the other track to reconstruct Λ's. The Λ invariant mass, M($p\pi$), is derived from the reconstructed four-momentum of the V0 candidate then. Some additional requirements are listed below:

- $0.6 < p_T^{\Lambda} < 2.5$ GeV and $\mid \eta^{\Lambda} \mid < 1.2$, where p_T^{Λ} and η^{Λ} are the transverse momentum and the pseudorapidity of the reconstructed candidate in the laboratory frame, respectively. These selection criteria were determined by studying the reconstruction efficiency and acceptance (see Section 5.4 for more details about the description of these variables) in different p_{T} and η regions. A good reconstruction was found for the $0.6 < p_{\mathrm{T}} < 2.5$ GeV and $\mid \eta \mid < 1.2$ region, seen in Figures 5.7(a) and (c);

- M(e^+e^-) > 50 MeV to eliminate the background due to the electron pair production from the photon. Electron pair production from photon conversion is a type of background to the strange particle reconstruction. The invariant mass reconstructed from e^+e^- normally results in a value of a few of hundreds MeV if it is not from the photon conversion;

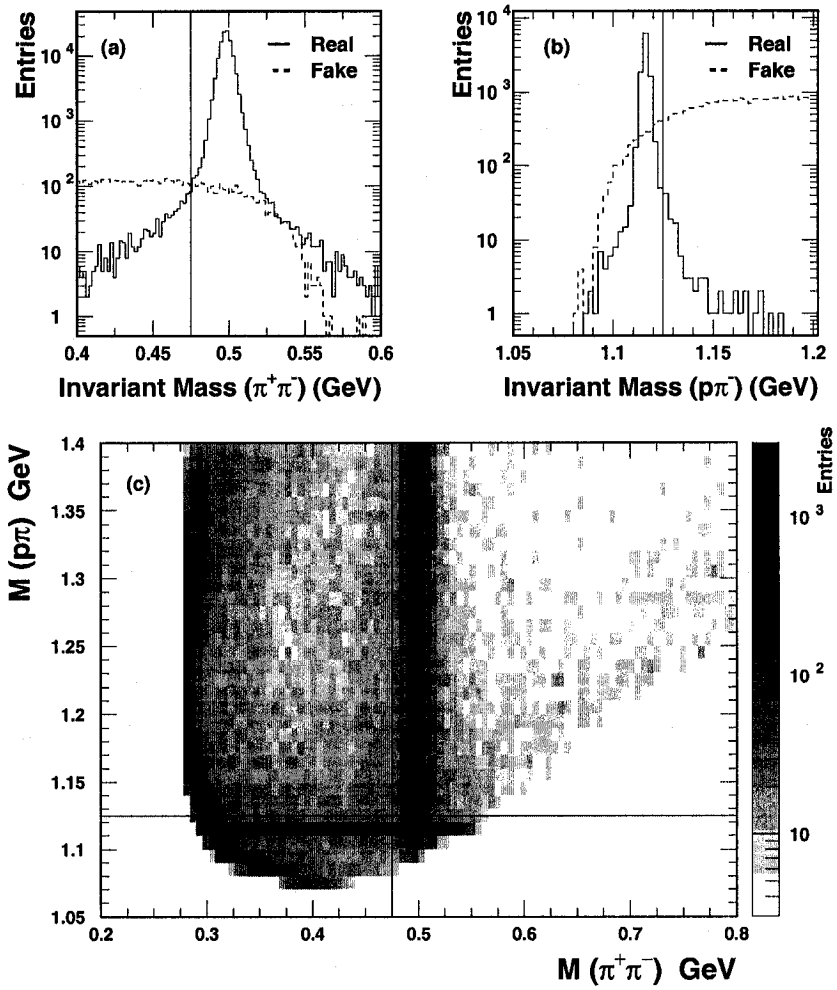

Figure 5.8: The invariant mass distribution of candidates assuming a $p\pi$ and $\pi^+\pi^-$ mass hypothesis for a V0 candidate. The distributions (a) and (b) were studied with MC while (c) is for the data. In (a), the histogram represents the $\pi^+\pi^-$ mass reconstruction for real K^0_S's and the dashed line is mistaking two Λ decay products $p\pi^-$ to reconstruct M($\pi^+\pi^-$). In (b) the histogram represents the $p\pi^-$ mass reconstruction from real Λ's and the dashed line is mistaking two K^0_S decay products $\pi^+\pi^-$ to reconstruct the Λ mass. The cut values are given by the vertical lines. The suggested cuts are applied to the data, shown in (c), which is the 2-dimensional distribution of $M(\pi^+\pi^-)$ and $M(p\pi)$.

- $M(\pi^+\pi^-) > 0.475$ GeV is applied to remove K^0_S contamination from the Λ signal. This cut is easily understood with Figures 5.8 (a) and (c). The real K^0_S decaying $\pi^+\pi^-$ will peak at ~0.498 GeV while a fake one populates a lower mass position. However here for Λ's, a real K^0_S is not wanted so that an optimal cut at 0.475 GeV is chosen to remove most of the contamination from K^0_S. The vertical line in Figure 5.8(c) represents this cut in the 2-dimensional invariant mass distribution of $M(\pi^+\pi^-)$ and $M(p\pi)$.

As an example, the Λ and $\bar{\Lambda}$ invariant mass distributions reconstructed for the high Q^2 DIS events are shown in Figure 5.9. The mean position of the reconstructed Λ and $\bar{\Lambda}$ is 1116.20 $\pm$ 0.01 MeV (statistical only) with a standard deviation of 2.2 MeV, consistent with the invariant mass 1115.7 MeV given in PDG [51]. Here the standard deviation is simply the average standard deviation value from the two gaussian functions. The uncorrected number of Λ ($\bar{\Lambda}$) is 5389 (5342). The Λ and $\bar{\Lambda}$ decay length distributions are shown in Figure 5.10. The line in the figure is the exponential fit on the *ct* distribution to determine the average lifetime of the hadrons. The average Λ decay length is derived to be 7.74 ± 0.09 cm which is consistent with the mean decay length 7.89 cm given in Table 5.1.

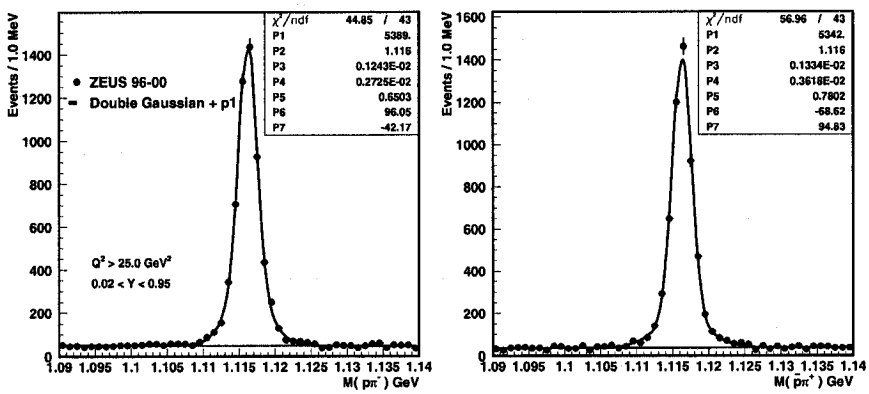

Figure 5.9: The Λ and $\bar{\Lambda}$ invariant mass distributions for the high Q^2 DIS events. The line represents the fit of a double Gaussian for the signal combined to a linear function for the background.

It should be noted that no direct *ct* cut was applied on Λ selection. However some other cuts like the CTD superlayer cut on the track could have an indirect impact on the flight distance of Λ.

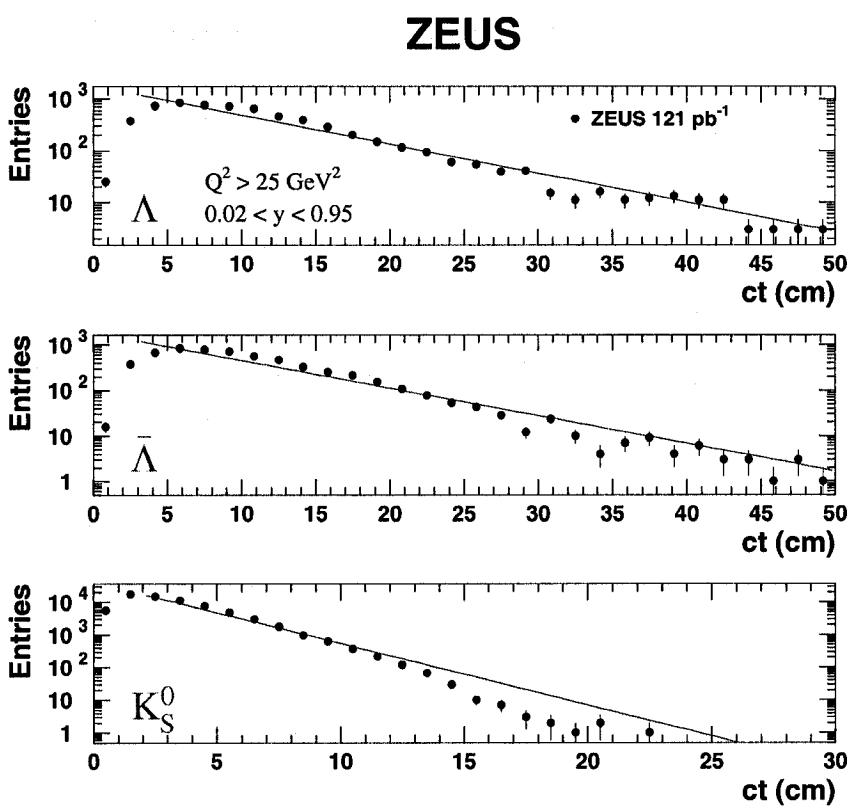

Figure 5.10: Λ, $\bar{\Lambda}$ and K^0_S decay length distributions. The line in the figure represents the exponential fit from which the lifetime of the strange hadron can be derived.

5.2.3 K^0_S Reconstruction and Selection

Only K^0_S decaying into $\pi^+\pi^-$ (branching ratio 68.6 $\pm$ 0.27%) were reconstructed. Both tracks from the same V0 were assigned the mass of the charged pion. Additional requirements are listed below:

- $0.6 < p_T^{K^0_S} < 2.5$ GeV and $\mid \eta^{K^0_S} \mid < 1.2$, where $p_T^{K^0_S}$ and $\eta^{K^0_S}$ are the transverse momentum and the pseudorapidity of the reconstructed candidate in the laboratory frame. For the same reason as explained in Λ reconstruction, the $p_T^{K^0_S}$ and $\eta^{K^0_S}$ cuts were suggested and determined according to the studies shown in Figures 5.7(b) and (d);

- M(e^+e^-) > 50 MeV to eliminate the electron pair production from photons;

- M($p\pi$) > 1.125 GeV is applied to eliminate Λ contamination from the K^0_S signal. Here the mass of the proton is assigned to the track with larger momentum

and the mass of the pion to the other track. A plot to illustrate this cut is available in Figure 5.8.

The K^0_S invariant mass reconstructed in the high Q^2 DIS region is shown in Figure 5.11. The mean position of the reconstructed K^0_S is 497.90 $\pm$ 0.01 MeV (statistical only) with a standard deviation of 6.1 MeV, consistent with the invariant mass 497.7 MeV given in PDG [51]. The uncorrected number of K^0_S is 73140. The K^0_S decay length distribution is also shown in Figure 5.10(c) and the average K^0_S lifetime $c\tau$ is determined by the fit to be 2.30 $\pm$ 0.01 cm, somehow smaller than the mean value of 2.68 cm given in Table 5.1. This could be due to the detector or to effects of the cuts. But since there is no direct ct cut applied on K^0_S selection and a very good agreement on the decay length distribution was obtained between MC and the data (see Figure 6.6), no significant impact on the final results is expected from this K^0_S ct distribution.

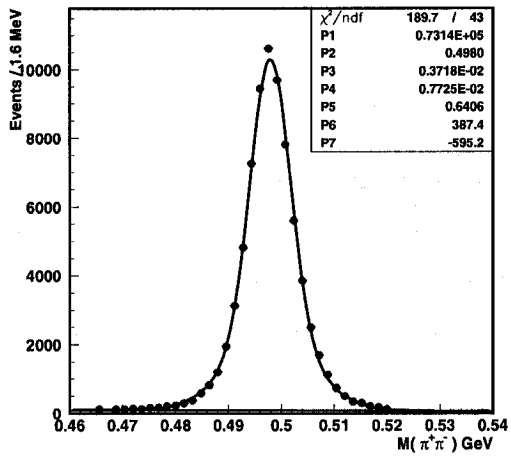

Figure 5.11: The K^0_S invariant mass distribution for the high Q^2 DIS events. The line represents the fit of a double Gaussian for the signal combined to a linear function for the background.

5.3 Signal Extraction

With the invariant mass distributions described above, the number of the total reconstructed particles is ready to be extracted. This number is achieved by counting the total entries located within a mass window around the nominal position of the

hadron mass. The mass window was chosen to be $\sim 3\sigma$ away from the mass position on each side of the mass distribution. The $\sim 3\sigma$ was used so that the mass resolution and the migration effect are considered. The mass window used in the measurement is 1.11 to 1.122 GeV for the Λ signal counting and 0.48 to 0.52 GeV in the K^0_S case.

However, there are inevitably some background candidates remaining in the distribution. In order to reduce the background without further identification measures, a linear background fit on the invariant mass distribution, across the full-range, was made. The full-range fit ensures a good background estimation. By integrating the linear function over the mass window range, the number of background candidates can thus be obtained. Therefore the number of the particle candidates within the mass window range can be determined by subtracting these background from the total entries in the same mass window.

5.4 Efficiency, Purity and Acceptance

The correction of the reconstructed particle at the hadron level was done by taking consideration of the detector acceptance ($\mathcal{C}$). The acceptance is evaluated with MC studies and defined as the relative ratio of the reconstructed candidates in the detector level to the total generated particles at the hadron level. For simplicity, hereafter, we use N^{had}_{mc} to stand for the Number of the generated particles in the hadron level, N^{det}_{real} for the Number of real particles of interest in the detector level and N^{det}_{cand} for the Number of reconstructed candidates in the detector level. Therefore we have $\mathcal{C} = N^{det}_{cand}/N^{had}_{mc}$. For differential measurements, the acceptance was determined bin by bin of the considered kinematic variables.

To ensure a good particle reconstruction and a plausible correction to the hadron level, two other associated variables are defined, the reconstruction efficiency ($\mathcal{E}$) and reconstruction purity ($\mathcal{P}$). These two variable are also calculated from the MC studies. The efficiency represents the fraction of the generated particles at the hadron level appearing in the reconstructed signal at the detector level. The larger $\mathcal{E}$ we have, the more real particles we can reconstruct in the detector level. The $\mathcal{P}$ tells how pure the reconstructed signal is. It is defined as the fraction of the real particles among the total reconstructed particle candidates. Their definitions and the relation with $\mathcal{C}$ are described by the following:

$$\mathcal{E} = \frac{N_{real}^{det}}{N_{mc}^{had}} \tag{5.1}$$

$$\mathcal{P} = \frac{N_{real}^{det}}{N_{cand}^{det}} \tag{5.2}$$

$$\mathcal{C} = \frac{\mathcal{E}}{\mathcal{P}} \tag{5.3}$$

The following few figures display the efficiencies, purities and acceptances of the reconstructed $\Lambda(\bar{\Lambda})$ and K_S^0 for the three different kinematic regions.

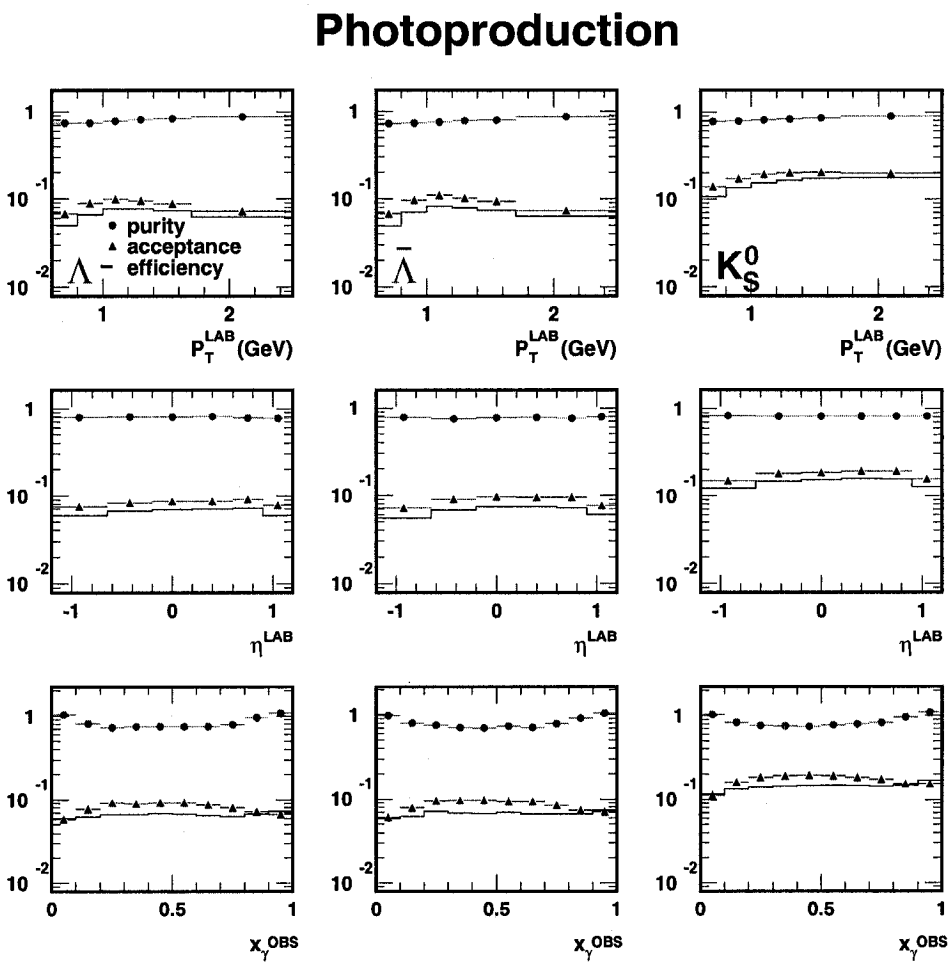

Figure 5.12: The Λ, $\bar{\Lambda}$ and K^0_S reconstruction efficiencies, purities and acceptances for photoproduction events as a function of the kinematic variables p_{T}, η and x_γ^{OBS}. These values were estimated with MC studies. The average $\mathcal{E}$, $\mathcal{P}$ and $\mathcal{C}$ were measured to be 6$\sim$7%, 8$\sim$9% and $\sim$80% for $\Lambda(\bar{\Lambda})$ reconstruction while $\sim$14%, $\sim$18% and $\sim$80% for K^0_S reconstruction.

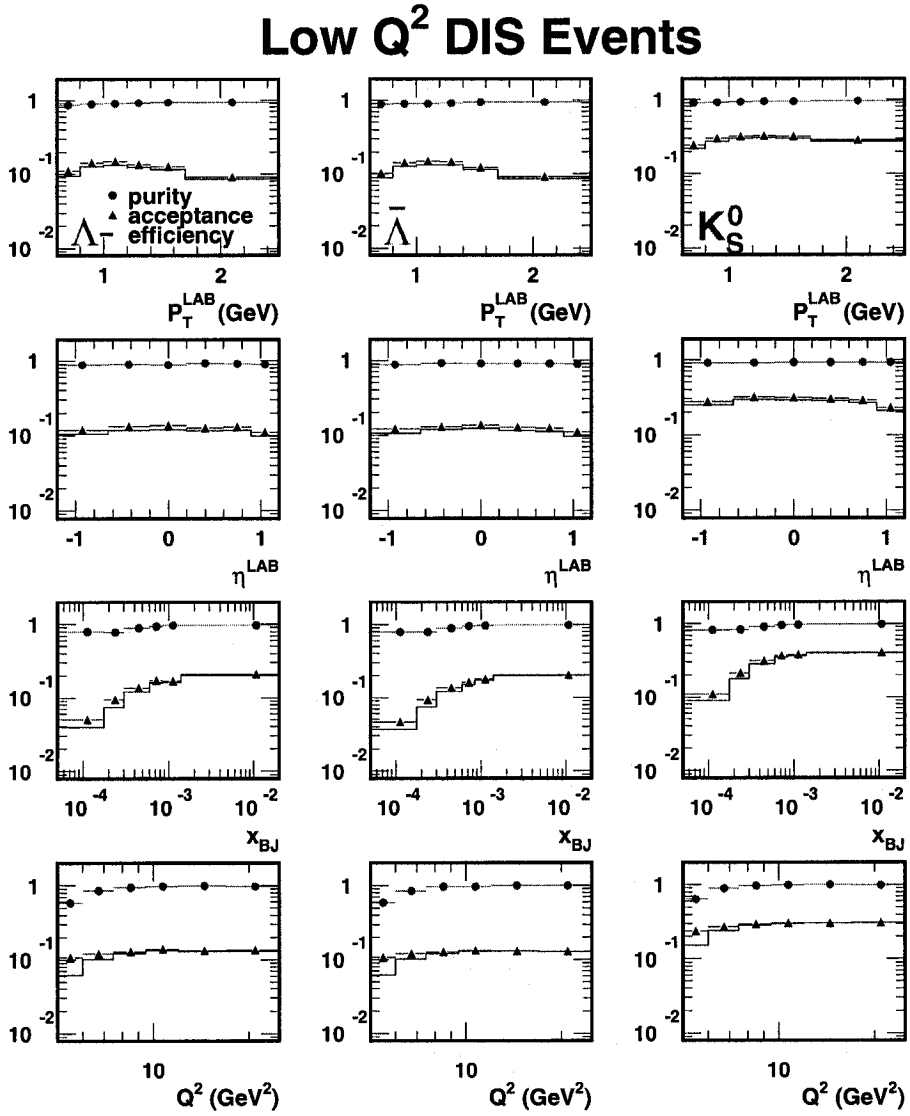

Figure 5.13: The Λ, $\bar{\Lambda}$ and K^0_S reconstruction efficiencies, purities and acceptances for low Q^2 DIS events as a function of the kinematic variables p_T, η, x_{Bj} and Q^2. These values were estimated with MC studies. The average $\mathcal{E}$, $\mathcal{P}$ and $\mathcal{C}$ were measured to be ~10%, ~11% and ~90% for $\Lambda(\bar{\Lambda})$ reconstruction while ~25%, ~28% and ~90% for K^0_S reconstruction.

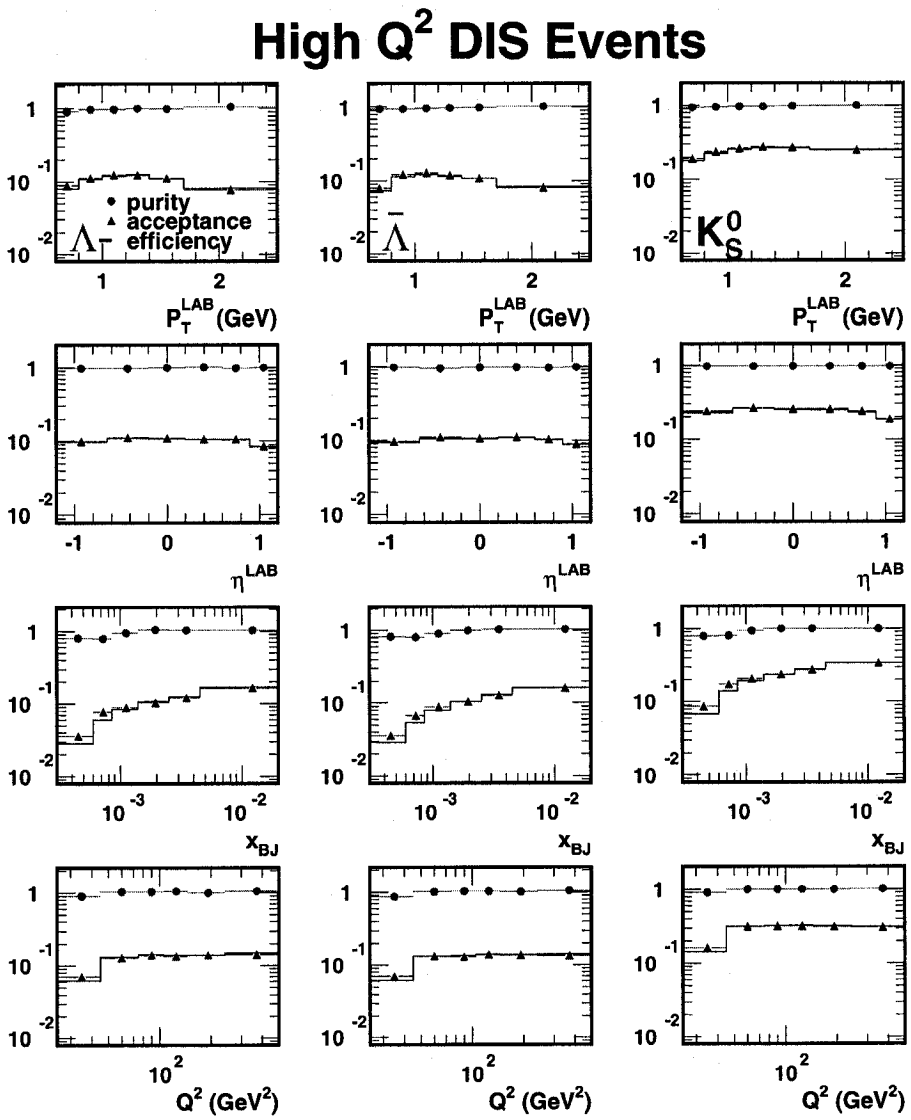

Figure 5.14: K^0_S, Λ and $\bar{\Lambda}$ reconstruction efficiency, purity and acceptance for $Q^2 >$ 25 GeV^2 events as a function of the kinematic variables p_{T}, η, x_{Bj} and Q^2. These values were estimated with MC studies. The average $\mathcal{E}$, $\mathcal{P}$ and $\mathcal{C}$ were measured to be ~10%, ~10% and ~97% for $\Lambda(\bar{\Lambda})$ reconstruction while ~25%, ~25% and ~99% for K^0_S reconstruction.

Chapter 6

Monte Carlo Simulation

Monte Carlo (MC) simulation is an essential tool in modern high energy physics. It plays a crucial role in the data analyses such as the detector effect corrections, systematic uncertainty evaluations and so on. Basically, a full simulation consists of two dedicated steps, namely, physics simulation and the actual detector simulation. Specific to HERA, the first step is to simulate the *ep* scattering process at parton level, QCD radiation and the fragmentation processes. The current MC programs available like LEPTO [71], HERWIG [52, 53] and PYTHIA [54] can serve the physics simulation needs. Concerning the actual detector simulation, a GEANT [68] based program was used, in which our best understanding of the detector components and trigger systems is incorporated. In this chapter, a basic description of the MC simulations is given, along with comparisons between the data and MC simulations used for the thesis.

6.1 Physics Simulation

Physics simulation, or event simulation, is assumed to be capable of simulating aspects as detailed and as close as possible to the real interactions. An event evolution can be factorized into many separate processes and each of them can be described by either theoretical or phenomenological models. The models used either rely on the best understanding of the experimental results or on the assumptions with which the MC can successfully describe certain physics results. A typical DIS event evolution in *ep* collisions can be simulated with three individual parts in a time order. It

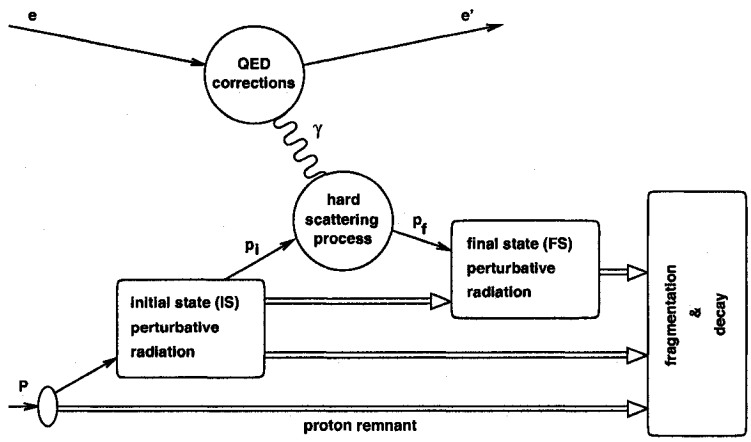

Figure 6.1: Different processes present in an *ep* event simulation in PYTHIA [54].

starts with a hard interaction process corrected with QED effects, then followed by QCD radiation and ends up with the fragmentation and decay processes. The initial parton radiation is grouped with the final state radiation into the second part, the QCD radiation, even if it happens before the hard scattering process. It is because the initial state radiation has quite similar features to the final state radiation but just with a backward time evolution. An illustration of these processes is shown in Figure 6.1.

6.1.1 Hard Scattering Process

The hard scattering process is the essential and core part of an interaction and determines the main features of the event. Normally a '$2 \rightarrow 2$' process is generated, for instance, '$ql \rightarrow ql$' for a DIS process or '$\gamma g \rightarrow q\bar{q}$' for a boson-gluon fusion process in photoproduction for *ep* collisions. Since one of the colliding beams at HERA contains protons, an inherently composite particle, the knowledge of the parton distribution in the proton is rather important to determine the cross section of the hard partonic process at this stage. Given a known parton distribution, this hard process is perturbatively calculable, as what is described in Section 2.3. However, the parton distribution can only be obtained from experimental measurements. A precise and thorough measurement of the parton distribution function (PDF) of the proton has been made at HERA, as shown in Figure 2.4. The PDFs are universal in the sense that once they are measured in one reaction, the results can be used for

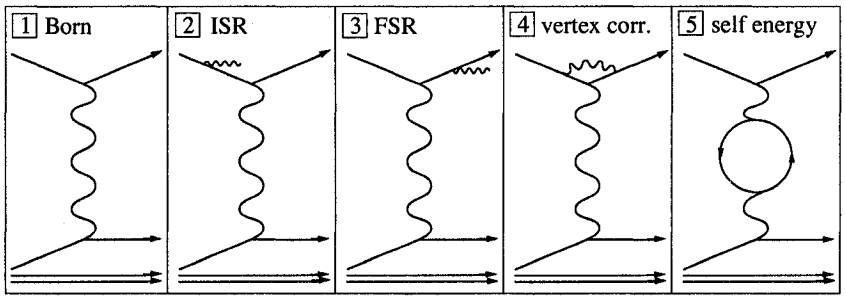

Figure 6.2: Feynman diagrams for QED radiation at HERA. 1 is the Born diagram without any radiation, while 2 and 3 show the initial state radiation and final state radiation. Higher order α QED effects are shown in 4 and 5.

calculations for the other processes.

QED radiation could have a non-negligible effects on certain cross section measurements. For example, the effects on K^0_S and Λ measurements in this thesis were estimated to be a few percent for DIS events based on MC studies. Figure 6.2 lists four different cases of QED radiation together with the Born process. Two of them, the initial state radiation (ISR) and the final state radiation (FSR), shown in Figures 6.2 2 and 3 respectively, can give rise to a change in the event topology. Figures 6.2 4 and 5 represent the higher order α QED effects. In this thesis the QED effects are taken into account during the event simulation, see Section 6.3 for more information.

6.1.2 Perturbative QCD Radiation

Analogous to QED radiation, the processes which contain the colored charged objects may give rise to QCD radiation before or after the hard scattering process. The QCD radiation will subsequently result in an iterative series of branching processes like $g \rightarrow q\bar{q}$, $g \rightarrow gg$ and $q \rightarrow qg$. These processes may lead to a non-negligible change of the overall topology of the event, especially significant with the increasing collision energy. For instance, the final event topology can change from simple '$2 \rightarrow 2$' to '$2 \rightarrow 3/4/..$' process.

Two complementary approaches exist to model the perturbative QCD radiation effects. One is the matrix element (ME) method which can precisely calculate the Feynman diagrams order by order. This method can therefore be applied to inclusive

jet measurements, but it becomes less than sufficient to describe the multiple soft gluon radiation with the increasing colliding energy. Moreover, the ME method is found to be too complicated to deal with the higher order calculations, in particular for loop graphs. Therefore the higher order calculations and loop graphs are usually not included. The other alternative approach is the parton shower (PS) method. It does not take the exact kinematics, full interference and helicity structure into account as does the ME method, but an approximation of them. The radiation in the PS is simulated by an arbitrary number of branching processes. The jet structure due to the soft radiation therefore can therefore be better described. The PS method is in practice matched to the first order matrix elements to describe the hard gluon emission region. The ME, PS or sometimes a combination of both methods (hence MEPS) can be used, depending on which application is most appropriate. In this thesis the Monte Carlo used to describe the QCD radiation is the MEPS method for the general purpose of including both the leading order and higher order radiation.

Another type of parton shower model used in this thesis is the color dipole model (CDM) [55, 56, 57, 58]. The parton emission in this model is considered to be from a color dipole between partons instead of from independent partons. Therefore, it is believed to have a more natural description of the parton radiation and shower development. In the case of a DIS event at HERA, the QCD radiation is assumed to start from the dipole between the struck quark and the proton remnant. One notes that no distinction is made between the initial state QCD radiation and the final state QCD radiation in the CDM.

The implementation procedure to describe QCD radiation can be understood this way: considering a final state shower first, a parton branching process is expressed as $a \rightarrow bc$. This process is time-like, $m^2 = E^2 - p^2 > 0$, and is characterized by a decreasing Q^2. The way parton a converts into b and c is determined by the splitting function $P_{a\rightarrow bc}$. The splitting function controls the fraction of energy carried by the daughters b and c and the probability of presence of such process. Subsequently b and c may continue to decay until Q^2 is not larger than a cut-off value Q_0^2. Typically Q_0 is set to be 1 GeV. This approach is known as the forward evolution in MC. In contrast, the initial parton shower is a space-like process, $m^2 = E^2 - p^2 < 0$, where the virtuality Q^2 is increasing with the shower evolution. A maximum scale Q_{max} is introduced whereby the parton shower stops when Q^2 reaches Q_{max}^2. Thereafter the

Variable	Description	Definition	Value (D)
PARJ(1)	suppression of diquark pair production	$\frac{\mathcal{P}(qq)}{\mathcal{P}(q)}$	0.10
PARJ(2)	strange suppression factor	$\frac{\mathcal{P}(s)}{\mathcal{P}(u)}$	0.30
PARJ(3)	strange diquark production suppression	$\frac{\mathcal{P}(us)/\mathcal{P}(ud)}{\mathcal{P}(s)/\mathcal{P}(d)}$	0.40
PARJ(4)	suppression of spin-1 diquarks	$1/3\frac{\mathcal{P}(ud_1)}{\mathcal{P}(ud_0)}$	0.05
PARJ(5)	popcorn baryon production ($BM\bar{B}$) factor	-	0.50
PARJ(6)	suppression of $s\bar{s}$ sharing by B and $\bar{B}$ in $BM\bar{B}$	-	0.50
PARJ(7)	suppression of having a strange M in $BM\bar{B}$	-	0.50

Table 6.1: A list of parameters related to strange hadron production implemented in the string model via the JETSET program [84]. The value (D) stands for the default value which is set in the model.

hard parton interaction is going to happen. The choice of Q_{max} could dramatically affect the jet measurement. In practice, the technique adopted to describe the initial parton showers is called the backward evolution, whereby a given parton will be traced back with time to its mother parton. The way in which parton evolves there is similar to one used the forward evolution.

6.1.3 Fragmentation, Hadronization and Decay

The perturbative QCD makes predictions for the *partonic* final states while experimentally the *hadronic* final states are observed in detector. To make a connection between the predictions and observations, the non-perturbative hadronization process has to be taken into account. Generally the terms hadronization and fragmentation can be used alternatively. They both refer to the non-perturbative process whereby the colored partons combine to form final hadrons observed at the detector level. Strictly speaking, however, a slight difference exists between them [59]: fragmentation includes extra factorization processes while hadronization does not. In this thesis both terms are used equivalently, just describing the non-perturbative process of hadron formation. Hadronization process is a long distance process in which only a small momentum transfer is involved. Therefore this process is not calculable by perturbative QCD. The current understanding on this process merely relies upon phenomenological models. Two main models available to simulate this process are

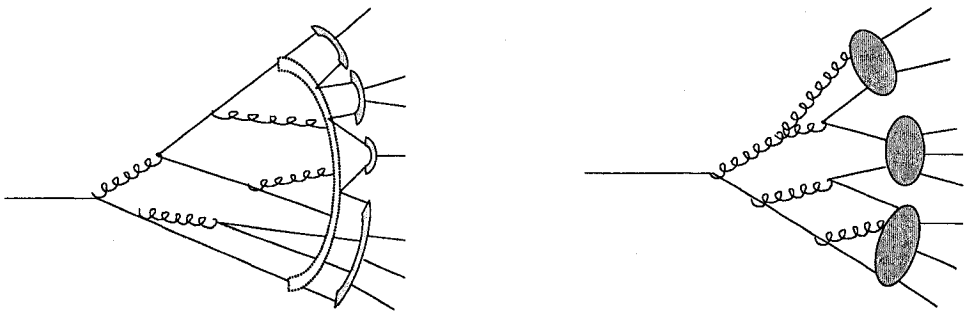

Figure 6.3: An illustration of hadronization models: the string model (left) and the cluster model (right).

the string model [60, 61, 62] and the cluster model [63, 64].

The string fragmentation model describes hadron formation from colored objects such as quarks and gluons. A picture illustrating the string model is shown in Figure 6.3 (left). A dynamic string is formed between two colored partons at the start and a tension force, stretching between two partons, appears along the string. This force varies with the change of distance between the two initial partons. The string breaks into piece strings as it extends apart to a certain level, creating some breaking-points at the same time. At these points a new $q\bar{q}$ or $Q\bar{Q}$ pair is created and each new parton belongs to the different piece strings. Here $q\bar{q}$ denotes a quark pair and $Q\bar{Q}$ a di-quark pair. In this way the string model takes into account the baryon (antibaryon) production along with the general meson production. The breakup of the string will continue until its energy is comparable to the energy of the final hadron at some point.

The string model can describe well the gross event features of the e^+e^- annihilation data, however its prediction on the specific baryon production is not good enough so far. In addition, many arbitrary parameters exist to control the hadron production, for instance at least seven parameters have to be assigned to govern the strange baryon production, shown in Table 6.1.

Another widely used fragmentation model is the cluster model. According to the idea of the 'preconfinement' [65, 66] feature of the parton shower, color connected partons tend to be developing closely in phase space. The combination of these partons at a later stage is assumed to form colorless clusters. The clusters will be subsequently undergoing isotropic decay to produce resonances or hadrons. The

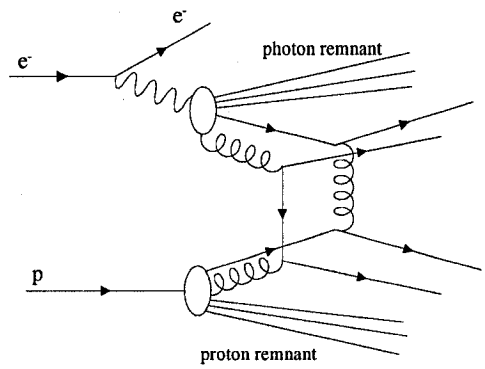

Figure 6.4: An example of the MI interaction in resolved photoproduction process. The photon remnant and proton remnant are shown.

final states are chosen to be produced according to appropriate quantum number requirements of clusters. A picture of the cluster model principle is given in Figure 6.3 (right). Compared to the string model, the cluster model has less parameters to be tuned to describe the hadron production. In this thesis, the cluster model was not used.

The decay of unstable particles or resonances follows once the hadronization process comes to an end. It is treated by making use of a table of particle information to decide the model and the probability of a particle decay. This table stores all the associated information about particles, for example, the particle properties, decay modes, branching ratios and so on.

6.1.4 Beam Remnant and Multiple Interaction

In a typical *ep* collision, only a fraction of the initial proton energy will be involved in the interaction while the proton remnant carries the rest away. The color connection between the proton remnant, if it has color, and the hard interaction will also result in a fragmentation process contributing to the final hadronic system. In MC simulations, the effect of the proton remnant is also taken into account.

Another similar case arises from the real photon in photoproduction process. A real photon in the resolved photoproduction process is assumed to have an inner structure and can thus be resolved by the parton from the proton. The partons in the photon which do not participate in the hard interaction will give rise to a photon

remnant. Due to the presence of the color correlation between photon remnant and the struck quark, extra soft production will emerge up together with the hard production. To a good approximation, a single interaction between exchanged boson and one parton from the proton will be the norm for a DIS event. However it might be possible to have multiple interactions (MI) between partons out of the photon and partons from the proton in the resolved photoproduction process. In order to simulate this physics phenomenon, a MI mechanism is considered in PYTHIA MC. An example of MI process is depicted in Figure 6.4.

6.2 Detector Simulation

A full simulation includes not only the physics event simulation, but also the detector response to these events. So here comes the second part of the MC simulation following the event simulation: the detector simulation. The purpose of detector simulation is to simulate the detector response as close as possible to the real situation in order to understand detector effects resulting from the resolution, acceptance, and presence of dead materials. In turn we apply these understandings in the experimental data to compensate for the detector response so that the detector independent results can be obtained. The package for the ZEUS detector simulation is MOZART (MOnte Carlo for Zeus Analysis, Reconstruction and Trigger) [67] which makes use of the framework of the CERN GEANT [68] program. The output of the detector simulation has the same format as the data output which makes possible the same analyzing procedures for both MC and the data.

6.3 MC Simulation for the Thesis

Many dedicated MC events are generated to suit different analysis needs. Since both DIS and photoproduction processes were considered in this thesis, two sets of MC files have been generated accordingly for the two processes.

The MC program has been tuned to generate *ep* collisions with different proton energies and different collision beams of electron or positron. For this thesis, based on MC studies, these differences have little impact on the final results. But still, to match the measurements, the combination of different MC samples was made

according to the relative ratio in the data so that the potential difference between the data and MC due to different event samples can be reduced.

The MC samples used for DIS were generated with QED radiative corrections by using the HERACLES 4.6.1 program [69, 70, 72] interfaced with the LEPTO 6.5.1 MC program [71] in the frame of the DJANGOH program [72]. The parton density parameterizations were taken from CTEQ [73, 74]. Two different treatments of the QCD cascade were taken, one is the CDM implemented in the ARIADNE MC program [75] while the other is the MEPS included in the LEPTO program. The program takes the LUND string model to simulate the fragmentation of partons.

Just as what was mentioned previously, several parameters, as coded in the JETSET program, exist in the string model controlling the strangeness production. They are shown in Table 6.1. There is no attempt to investigate how all of these values influence the strange particle production. So all parameters are set to the default values during the simulation, except the relative strange suppression factor, $\lambda_s = P(s)/P(u)$.

The λ_s is the key parameter which governs the relative strangeness production with respect to light u and d quarks in the string model. An optimum value of 0.3 was determined from LEP experiments [76, 77, 78, 79] and this value is also the default value in the current string model code. In addition to 0.3, a smaller $\lambda_s = 0.22$ value was used in the MC simulation as well and the corresponding results were compared to the data. The value of 0.22 is suggested by the previous ZEUS publication [80].

The photoproduction events were corrected with the PYTHIA MC program, which includes the leading order matrix element calculations to describe the hard parton scattering process and the initial and final parton showers to simulate the higher order processes. The LUND string model is adopted for the parton fragmentation, the same as in the DIS case. The proton and photon PDFs were taken from GRV [81] and SaS2D [82], respectively. To improve the description quality of the data, the MI mechanism has been implemented in the simulations.

The photoproduction MC's generated this way include only the leading order matrix element calculations for the hard scattering process. The lack of the higher order diagrams leads to an inadequate description of the real situation by MC. In order to get a better agreement between MC and the data, the direct and resolved processes were generated separately and the relative contributions between them are

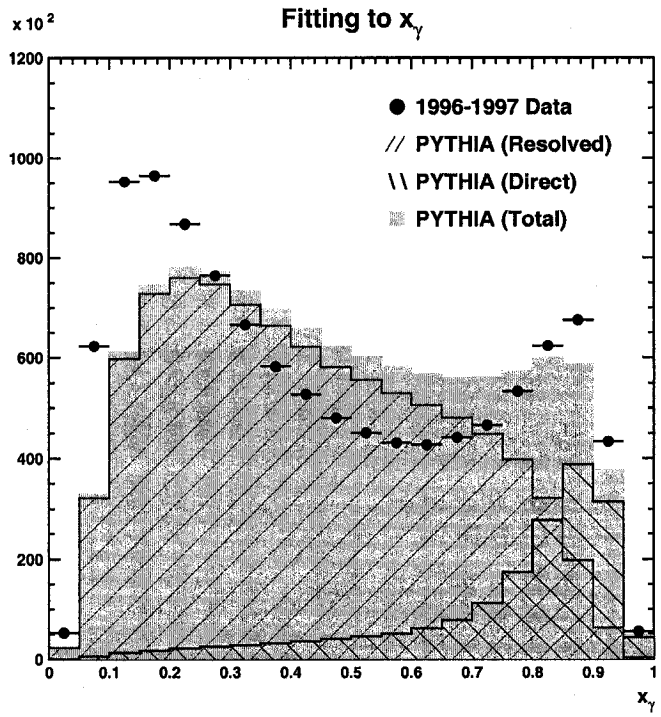

Figure 6.5: Rescaling of the direct and resolved processes for photoproduction events via the best fit of the x_γ^{OBS} distribution of the data by MC [83].

rescaled. The scaling factor is determined from the best fit to the x_γ^{OBS} distribution in the data by a combination of the direct and resolved samples in MC, see Figure 6.5. The optimally relative ratio was found to be 0.84:1 between the selected direct and resolved processes [83] for this thesis.

6.3.1 MC Files

The MC event samples which were generated with both interaction and detector simulations are listed in this section. These files are used to determine the detector response to the data, offer theoretical predictions and estimate systematic uncertainties. Table 6.2 shows two individual MC files which were generated with different Q^2 ranges in DIS. The sample with $Q^2 > 2$ GeV^2 was used for the low Q^2 DIS study while the other MC which has $Q^2 > 10$ GeV^2 for the high Q^2 DIS study. But in order to have larger MC statistics, the MC sample with $Q^2 > 2$ GeV^2 was also used for high Q^2 DIS study. A large amount of MC photoproduction events, $\sim$300 pb^{-1},

Q^2 cut	$Q^2 > 2\,\mathrm{GeV}^2$	$Q^2 > 10\,\mathrm{GeV}^2$
Author	-	Arno Benen
Program	DJANGOH + LEPTO	DJANGOH 1.1 + LEPTO 6.5.1
QED effect	HERACLES 4.6.1	HERACLES 4.6.1
QCD Cascade	ARIADNE 4.10	ARIADNE 4.08
PDF	CTEQ 5L	CTEQ 4D
No. of events	23 M	14 M
Lumi	55.04 pb^{-1}	109.05 pb^{-1}
Beam (GeV)	e^+(27.5) + p(920)	e(27.5) + p(920)

Table 6.2: Two MC samples used for the NC DIS studies. Some information like the author and program version for the low Q^2 MC sample is not available.

have been generated by Andrew Cottrell [83] in which different cuts and different proton energies were considered separately. All these photoproduction samples are listed in Table 6.3.

Further studies have been done by adjusting the strangeness suppression factor λ_s and the proton beam energy for different running periods. The MC events generated this way are not used for the detector response corrections but only for theoretical predictions at the hadron level. Therefore only physics event generation has been done. An independent MC generator interface package, AMADEUS, is available for this purpose at HERA. The AMADEUS provides an easy way to access all ZEUS MC generators and to get information at the hadron level with no need of a full ZEUS detector simulation.

6.3.2 Control Plots

An ideal MC simulation should be identical to the real situation of physics events and detector response. However, it is hard to get such perfect simulations on what really happens. There are always either known or unknown aspects which are not sufficiently simulated, such as the detector response, the trigger system or the hadronization processes, etc. Therefore it is necessary to check the simulation situation in the selected samples. This is done by comparing behaviors of the generated MC with that of the real data at detector level. The kinematic variables related to the se-

Set	Process	Filter	E_T^{jet} cut	#	Lumi	Beams(GeV)
1.	resolved	Dijet	2 GeV	6 M	6.58 pb^{-1}	e(27.5)/p(820)
2.	resolved	Dijet	3 GeV	5 M	11.75 pb^{-1}	e(27.5)/p(820)
3.	resolved	Direct K_S^0/Λ	3 GeV	5 M	29.27 pb^{-1}	e(27.5)/p(820)
4.	resolved	Other K_S^0/Λ	3 GeV	5 M	27.95 pb^{-1}	e(27.5)/p(820)
5.	direct	Dijet	2 GeV	4 M	20.15 pb^{-1}	e(27.5)/p(820)
6.	direct	Dijet	3 GeV	2 M	20.15 pb^{-1}	e(27.5)/p(820)
7.	resolved	Direct K_S^0/Λ	3 GeV	8.9 M	47.77 pb^{-1}	e(27.5)/p(920)
8.	resolved	Other K_S^0/Λ	3 GeV	8 M	40.82 pb^{-1}	e(27.5)/p(920)
9.	resolved	All K_S^0/Λ	3 GeV	30 M	103.68 pb^{-1}	e(27.5)/p(920)
10.	direct	Dijet	3 GeV	14 M	147.19 pb^{-1}	e(27.5)/p(920)
11.	resolved	Dijet	3 GeV	6 M	12.68 pb^{-1}	e(27.5)/p(920)

Table 6.3: A list of MC samples for photoproduction study purpose. The direct and resolved MC samples are given individually with different E_T^{jet} cut values, filters, and proton beam energies. The mark '#' in the table represents the 'Number of events'. Filter 'direct K_S^0/Λ' means a event was selected with at least one K_S^0 or Λ. Filter 'other K_S^0/Λ' requires to contain particles or resonances which can decay into K_S^0 or Λ but exclude events which pass 'direct K_S^0/Λ' filter. Filter 'All K_S^0/Λ' is the sum of above two cases.

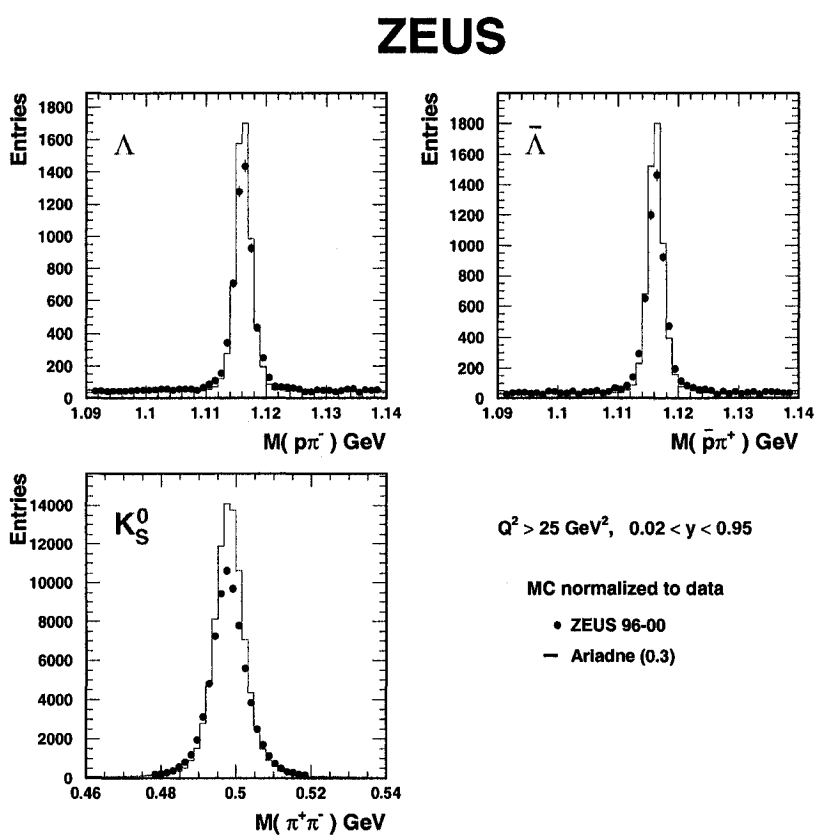

Figure 6.6: Comparison of the invariant mass distribution of Λ, $\bar{\Lambda}$ and K^0_S between MC and data for the high Q^2 DIS events. The MC is normalized to the data.

lected events and their particles were compared between the data and MC. The reconstruction of these variables has already been explained in Chapters 4 and 5.

One of the most important checks is on the invariant mass reconstruction of the strange hadrons between MC and the data. Examples are shown in Figure 6.6 for the high Q^2 DIS events, where a reasonable agreement on the mass position was found. In this figure, the event number in MC is normalized to that in the data.

Another important check is to see how well the secondary vertex is simulated in MC. This is done by measuring the 3-dimensional decay length of strange hadrons both in MC and in the data. As an example, the decay length distributions in MC and the data for the high Q^2 DIS events is given in Figure 6.7, where a well modeled decay length in MC was confirmed by the good agreement to the distribution.

In the following few plots, detailed comparisons of the event and particle kinematic variables are presented in the three regions of phase space of interest. These

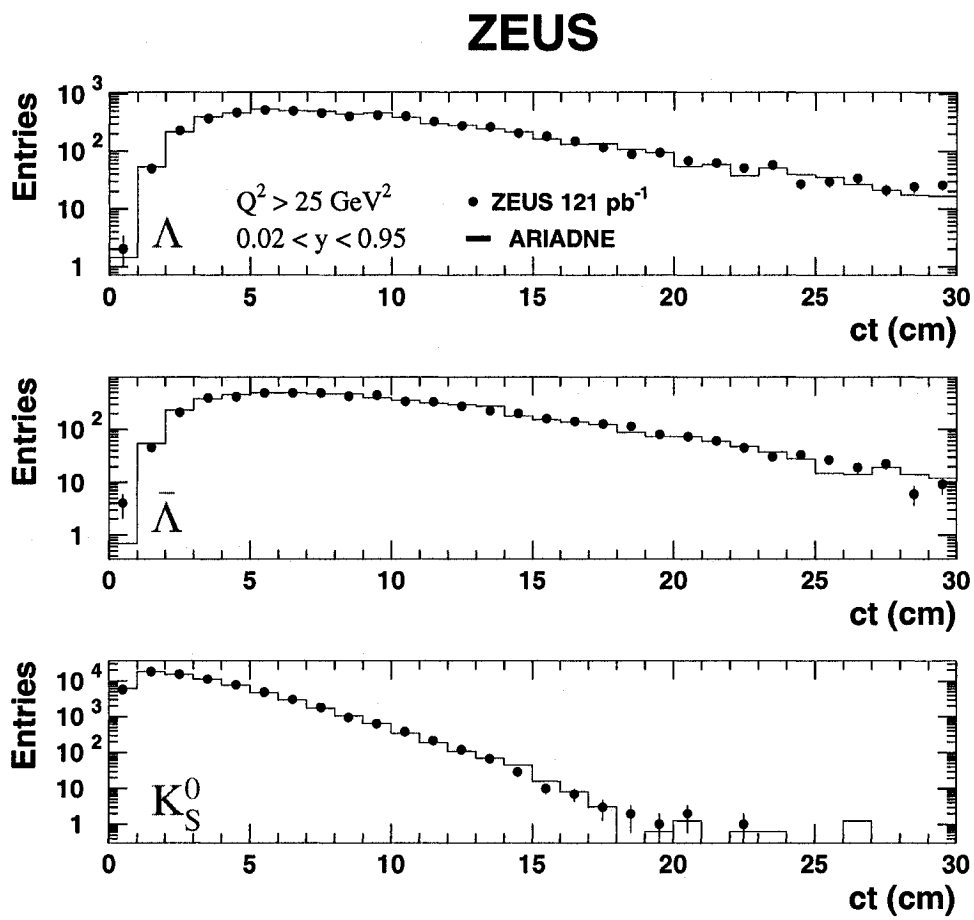

Figure 6.7: The distributions of ct of Λ, $\bar{\Lambda}$ and K^0_S at the detector level for high Q^2 DIS events, where t is the reconstructed lifetime. The data are presented by dots and the MC by histograms. The ARIADNE histogram is normalized to the event number of the data.

variables are the essential ones used to select events or particles, and therefore the quality of the comparison between the data and MC is crucial to justify how well the MC simulates the data. The MC is normalized to the data and then compared to them.

Figures 6.8 and 6.9 present the comparisons of different variables between the PYTHIA MC and the data for photoproduction events. As a reminder, the direct and resolved photoproduction processes were generated separately and combined according the fit on the $x_\gamma^{\rm OBS}$ distribution of the data. Also, in order to improve the description of the data in the resolved process, the multiple interaction mechanism has been implemented in PYTHIA. With all these efforts, the MC description of the

data has indeed been improved. But some regions of phase space were still found to be insufficiently described, for example in the $y_{\rm JB}$ and $x_\gamma^{\rm OBS}$ distributions. The relative differences between MC and the data are approximately estimated to go up to 60% in the very low $x_\gamma^{\rm OBS}$ region, 25% in the medium $x_\gamma^{\rm OBS}$ region and 15% in the large $p_{\rm T}$ region for both Λ and K_S^0 cases. Their average discrepancies are however 2.8% for K_S^0 and 3.6% for Λ. These disagreements will result in additional systematic uncertainties to these average levels. But such impact is expected to be mainly on the cross section measurement since the uncertainties due to the poor description by MC are expected to be canceled out at the first order for the other measurements such as the asymmetry, ratio and correlation studies (as in the Appendix). A good agreement was found in the other distributions.

The control plots for the low and high Q^2 DIS events are given in Figures 6.10 - 6.13. In all cases, a good agreement exists between the data and MC. The corrections on the data based on these MC's should therefore be reasonable and reliable.

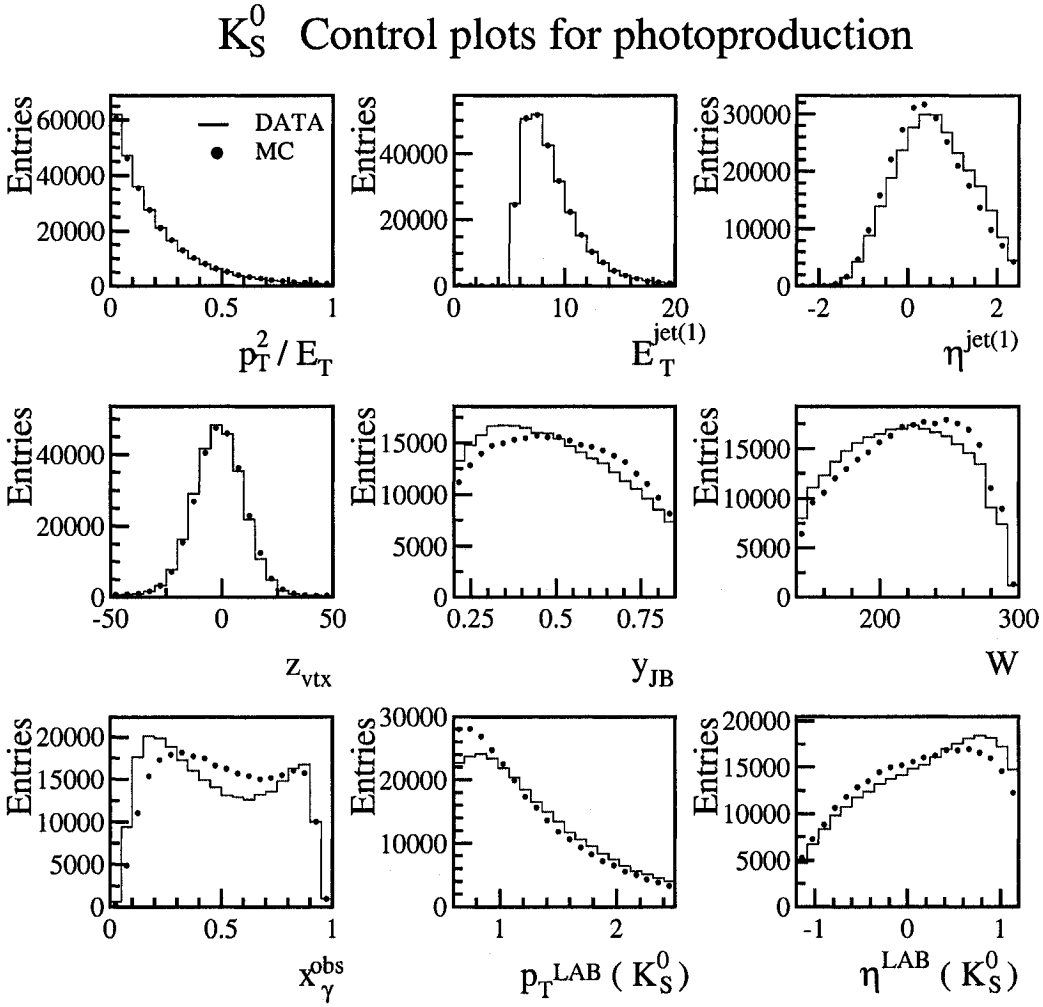

Figure 6.8: Control plots for photoproduction event and K_S^0 selections. Only these events are accepted in which at least one K_S^0 candidate is found. The MC is normalized to the data and represented by the lines.

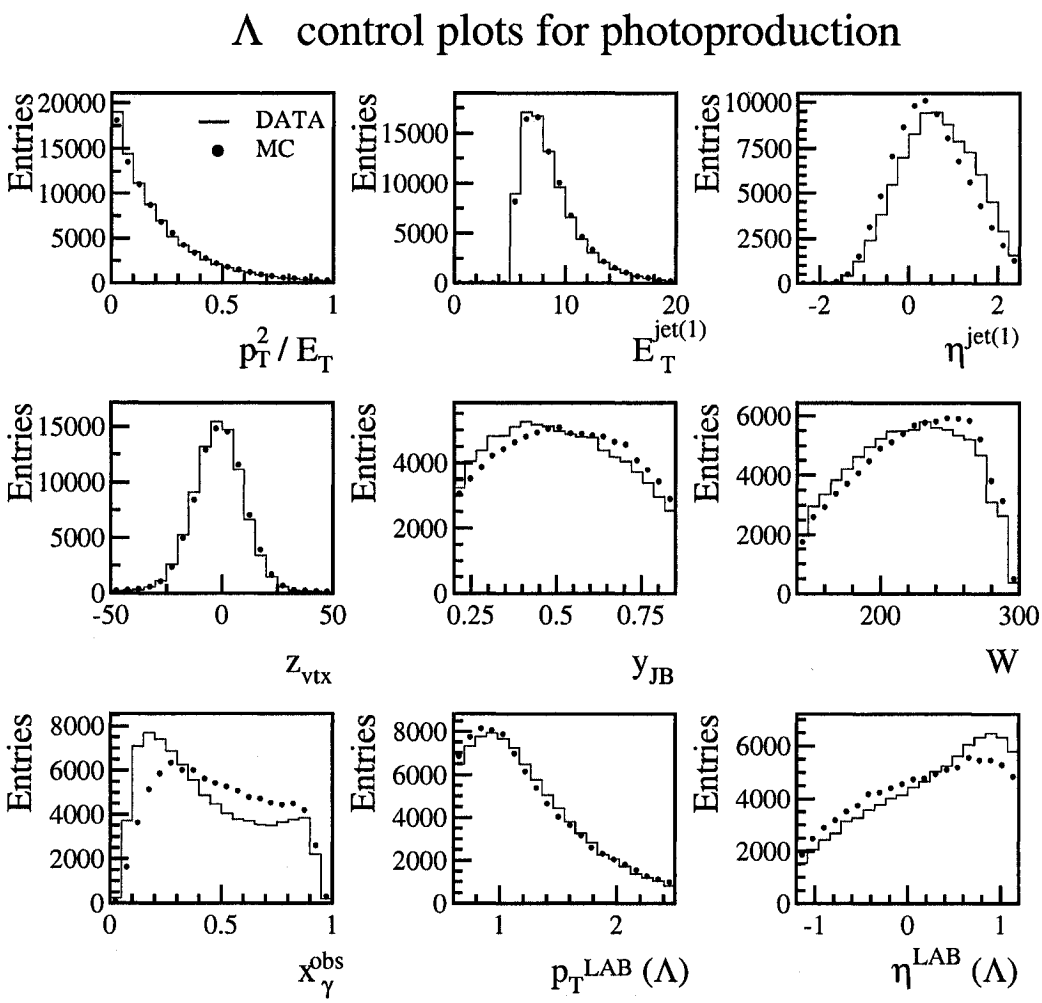

Figure 6.9: Control plots for photoproduction event and Λ selections. Only these events are accepted in which at least one Λ candidate is found. The MC is normalized to the data and represented by the lines.

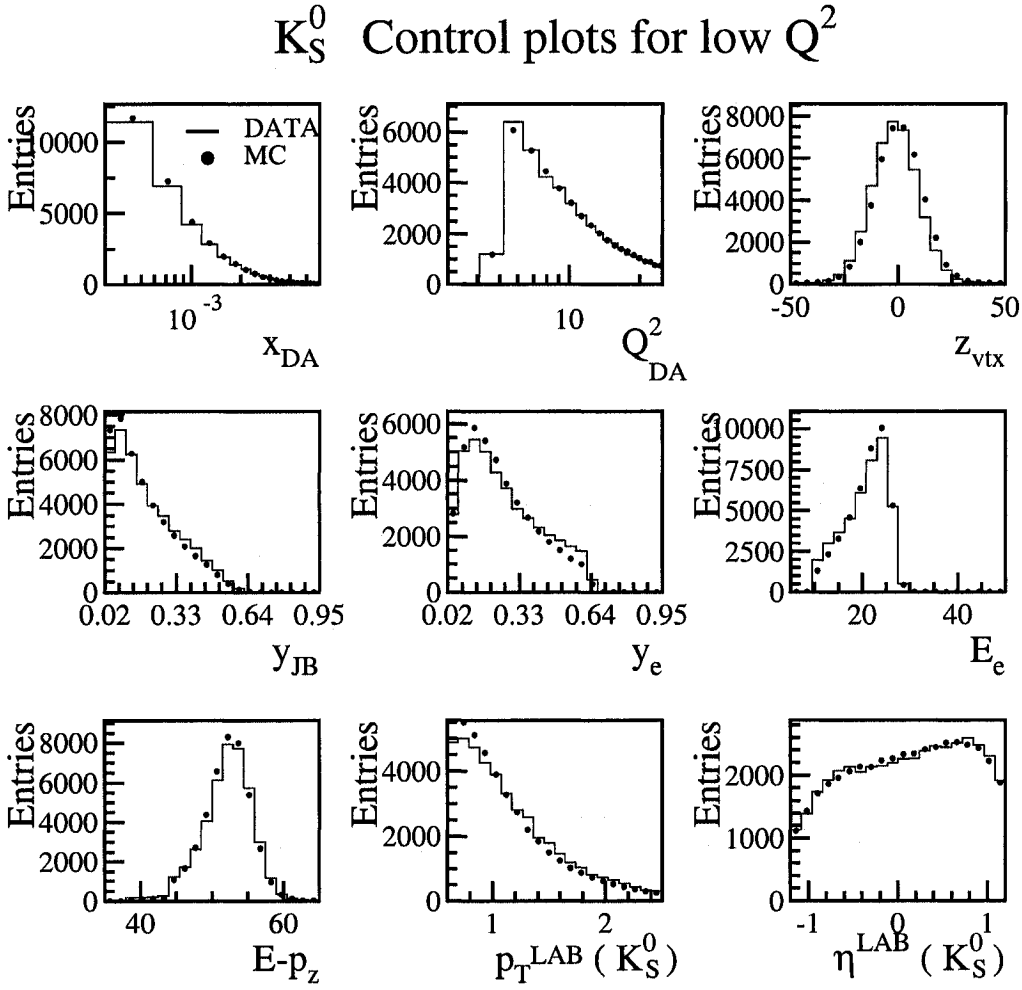

Figure 6.10: Control plots for $5 < Q^2 < 25\,\mathrm{GeV}^2$ event and K_S^0 selections. Only these events are accepted in which at least one K_S^0 candidate is found. The MC is normalized to the data and represented by the lines.

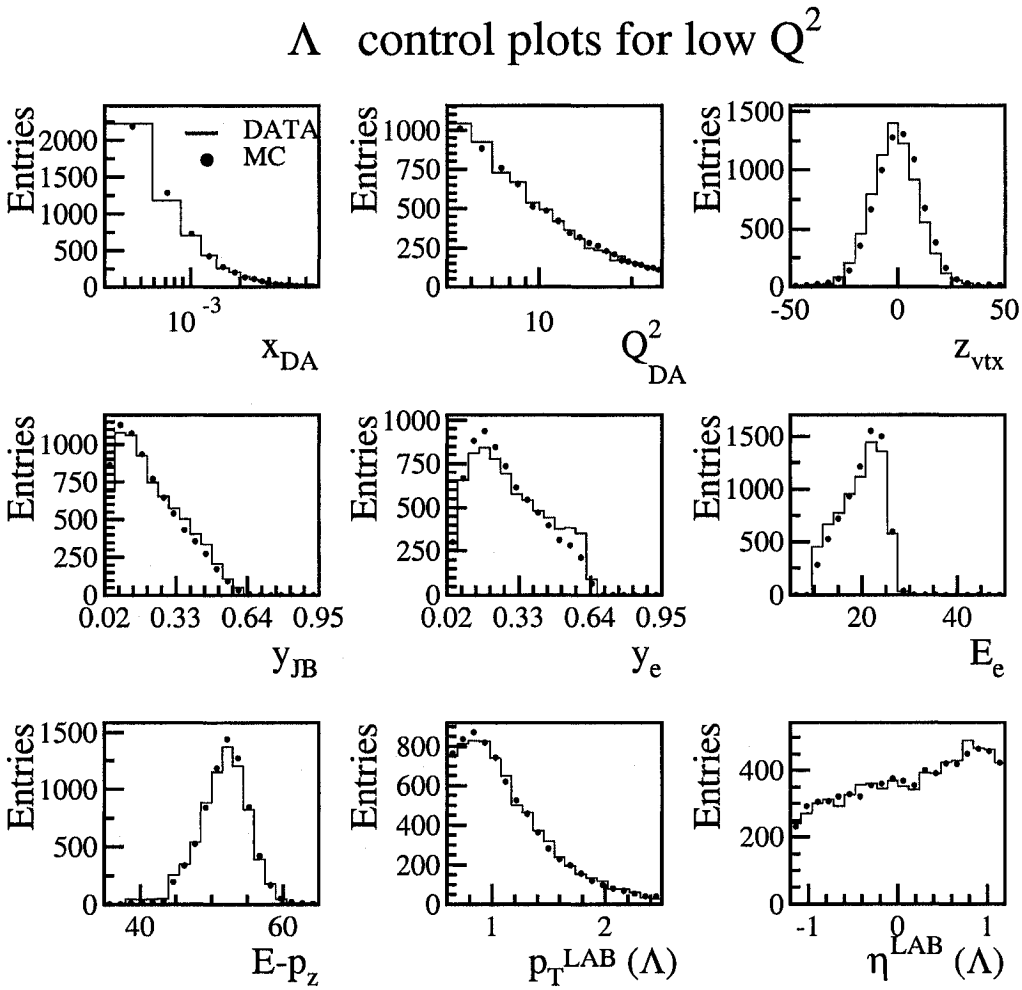

Figure 6.11: Control plots for $5 < Q^2 < 25\,\mathrm{GeV}^2$ event and Λ selections. Only these events are accepted in which at least one Λ candidate is found. The MC is normalized to the data and represented by the lines.

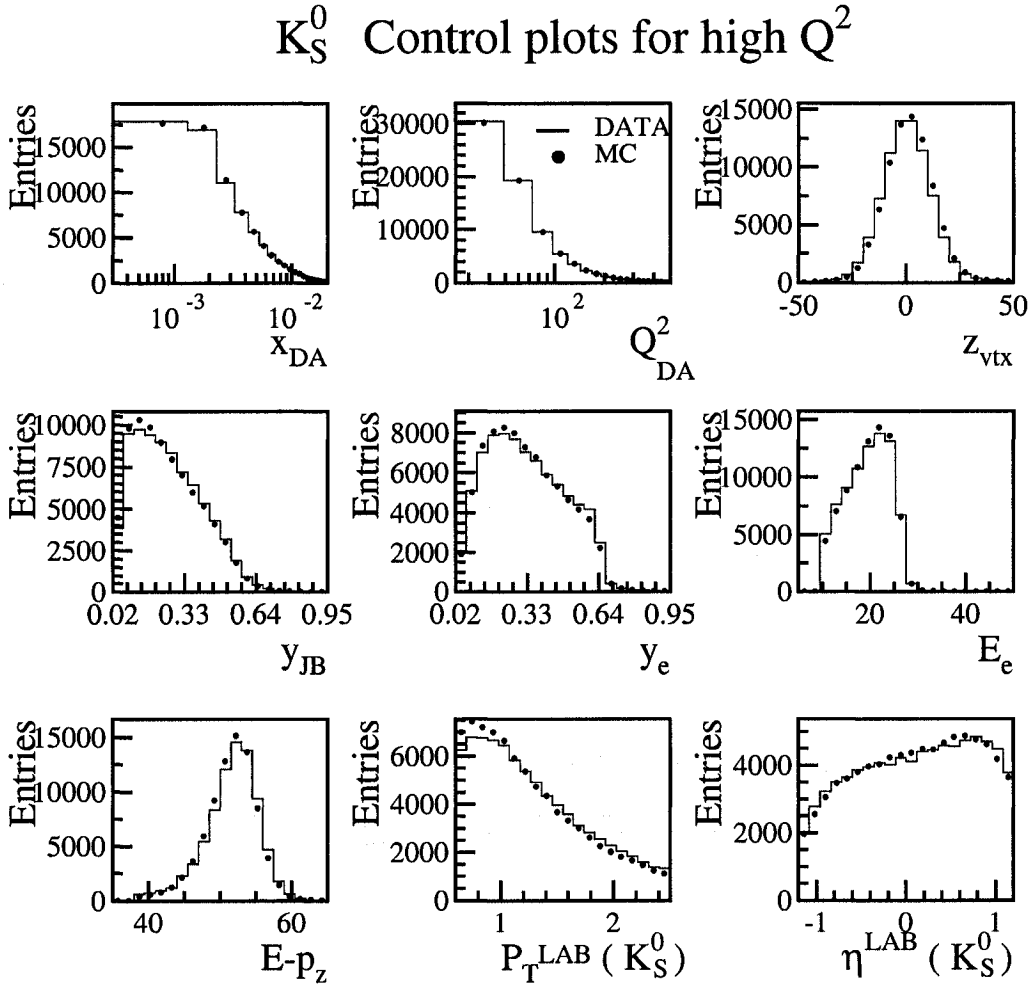

Figure 6.12: Control plots for $Q^2 > 25\,\mathrm{GeV}^2$ event and K_S^0 selections. Only these events are accepted in which at least one K_S^0 candidate is found. The MC is normalized to the data and represented by the lines.

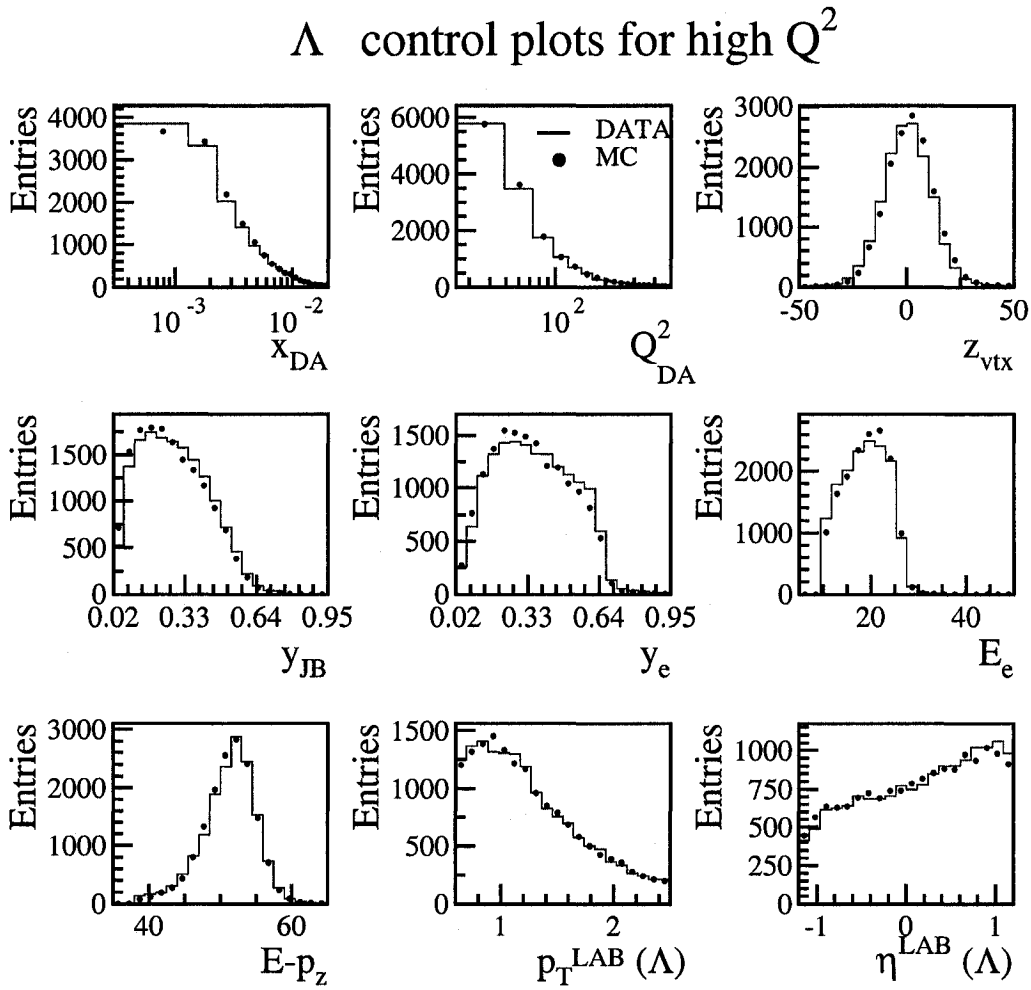

Figure 6.13: Control plots for $Q^2 > 25\,\mathrm{GeV}^2$ event and Λ selections. Only these events are accepted in which at least one Λ candidate is found. The MC is normalized to the data and represented by the lines.

Chapter 7

Results I: Cross Sections and Ratios

Based on the selection criteria described in Chapters 4 and 5, quantitative determinations of $\Lambda(\bar{\Lambda})$ and K^0_S production at HERA have been made with a total integrated luminosity of 121 pb^{-1}. The results obtained from these measurements include:

- cross sections: total and differential cross sections;
- relative production ratios: Λ to $\bar{\Lambda}$ production asymmetries and $\Lambda + \bar{\Lambda}$ to K^0_S production ratios;
- correlation studies: Bose-Einstein correlations and rapidity correlations;
- Λ and $\bar{\Lambda}$ polarizations.

Each result is followed up by discussions and comparisons with MC predictions or/and results from other experiments.

For a better organization, the results listed above are sorted and shown in two chapters. In this chapter, the results on cross sections and ratios are given while the following Chapter 8 covers the remaining results on correlation and polarization studies.

The cross section and ratio measurements, to be shown in this chapter, have been carried out in three different kinematic regimes available at HERA. These regimes, together with the selection criteria, are listed in the following.

- photoproduction: $Q^2 < 1$ GeV^2 and the presence of at least two hadronic jets;

- low Q^2 DIS: $5 < Q^2 < 25$ GeV^2 and $0.02 < y < 0.95$;
- high Q^2 DIS: $Q^2 > 25$ GeV^2 and $0.02 < y < 0.95$.

The transverse momenta and pseudorapidities of the reconstructed strange hadrons were constrained by $0.6 < p_T < 2.5$ GeV and $|\eta| < 1.2$, respectively.

A natural extension of the measurements into the Breit frame for high Q^2 DIS events was also performed, see Section 4.2.3 for more information about the definition of the Breit frame. In addition, the photoproduction events have been split into two sub-samples, the fireball-enriched and fireball-depleted events, for the relative production ratio studies, see Section 4.2.5 for more information about the division.

The MC PYTHIA was used to simulate the photoproduction events, as described in Section 6.3. As for DIS events, two sets of ARIADNE MC data were generated with different strangeness suppression factor (λ_s) values, 0.3 and 0.22, in order to study the λ_s influence on the measurements. The former value 0.3 was found to be the preferred value in e^+e^- experiments [85, 86, 14] and 0.22 was suggested by the previous ZEUS measurement [80]. The λ_s value in LEPTO was set to be 0.3. For clarity of MC models with different λ_s values, the λ_s value is also given as a MC model is mentioned, for example ARIADNE(0.3) means the MC model used is ARIADNE with a strangeness suppression factor 0.3. The similar situation is applicable for other MC models.

7.1 Total Cross Section

The cross section measurement in high energy physics represents the likelihood of the occurrence of a reaction process and is expressed in units of area, the barn (one barn equals to 10^{-24} cm^2). In this thesis, the measured total cross sections thus provide a quantitative view of the probability of the neutral strange particle production in the considered kinematic regimes of ep collisions at HERA. The total cross section (σ) is given by

$$\sigma = \frac{N}{A \cdot \mathcal{L} \cdot B}, \tag{7.1}$$

where N is the number of the reconstructed strange particles at the detector level, A is the acceptance, $\mathcal{L}$ is the integrated luminosity and B is the branching ratio. The

(a) Laboratory Frame

		$\sigma(\Lambda+\bar{\Lambda})$ (pb)	$\sigma(K^0_S)$ (pb)
Photoproduction	ZEUS 96-00	$9611 \pm 55^{+121}_{-497}$	$16719 \pm 45^{+103}_{-407}$
	PYTHIA(0.3)	-	-
Low Q^2 DIS	ZEUS 96-00	$4316 \pm 66^{+118}_{-72}$	$11803 \pm 67^{+98}_{-190}$
	ARIADNE(0.3)	4297 ± 18	11769 ± 30
	ARIADNE(0.22)	3469 ± 16	9988 ± 28
	LEPTO(0.3)	3883 ± 17	12054 ± 30
High Q^2 DIS	ZEUS 96-00	$1281 \pm 17^{+57}_{-36}$	$3515 \pm 17^{+43}_{-107}$
	ARIADNE(0.3)	1277 ± 5	3851 ± 8
	ARIADNE(0.22)	1019 ± 4	3286 ± 8
	LEPTO(0.3)	1486 ± 5	4493 ± 9
(b) Breit Frame (High Q^2 DIS)			
Current region	ZEUS 96-00	$244 \pm 8^{+7}_{-7}$	$1179 \pm 11^{+17}_{-7}$
	ARIADNE(0.3)	274 ± 2	1332 ± 5
	ARIADNE(0.22)	223 ± 2	1157 ± 5
	LEPTO(0.3)	277 ± 2	1387 ± 5
Target region	ZEUS 96-00	$1047 \pm 17^{+56}_{-35}$	$2325 \pm 17^{+40}_{-106}$
	ARIADNE(0.3)	996 ± 4	2514 ± 6
	ARIADNE(0.22)	795 ± 4	2125 ± 6
	LEPTO(0.3)	1215 ± 5	3108 ± 7

Table 7.1: Total cross sections of $\Lambda + \bar{\Lambda}$ and K^0_S production in three kinematic regions: photoproduction, low and high Q^2 DIS regimes in the laboratory frame (a). Further results in the Breit frame are presented in (b) but only for high Q^2 DIS events. Theoretical predictions from ARIADNE and LEPTO MC models (with strange suppression factor λ_s, 0.3) are provided. An additional prediction from ARIADNE MC sample generated with λ_s 0.22 is shown as well. Both statistical and systematic uncertainties are shown for the data.

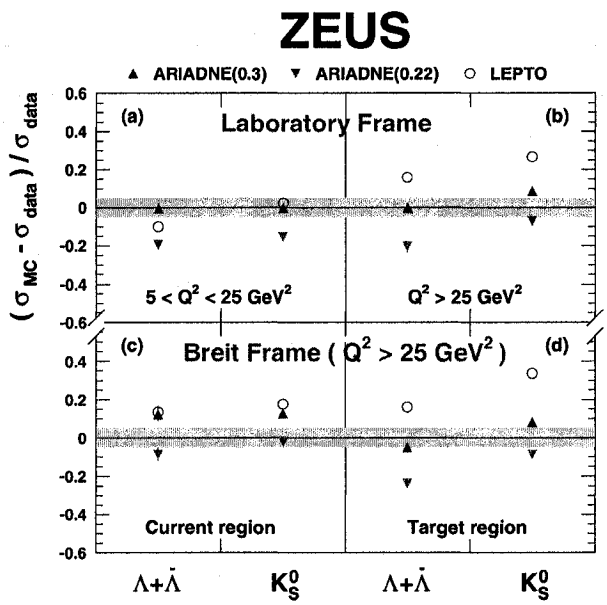

Figure 7.1: The MC predictions on the total cross sections with respect to the data. Figures (a) and (b) represent the MC predictions in the low and high Q^2 DIS regions respectively in the laboratory reference system. Figures (c) and (d) are for the current and the target regions in the Breit frame for the high Q^2 DIS events only. The statistical uncertainties are smaller than the size of the symbols. The shaded bands highlighting $\pm 5\%$ away from the nominal value of the data are provided for a scale purpose.

acceptance A was evaluated with Monte Carlo studies. The branching ratios were taken as $68.6 \pm 0.27\%$ and $63.9 \pm 0.5\%$ for $K^0_S \to \pi^+\pi^-$ and $\Lambda \to p\pi$ decay channels [51], respectively.

The measured total $\Lambda + \bar{\Lambda}$ and K^0_S cross sections are given in Table 7.1. As a comparison to the data, theoretical predictions from the Monte Carlo models are also presented. No absolute quantitative predictions are available for photoproduction events since the PYTHIA MC is rescaled according to the best fitting of the $x_\gamma^{\rm OBS}$ distribution of the data, as described in Section 6.3. According to the numerical values in Table 7.1, two issues are to be discussed with emphasis. The first one is the relative strange hadron yields in the current and target regions of the Breit frame, seen in Table 7.1(b). It is clear that the strange production in the target region contributes the major part of the whole production for high Q^2 DIS events, approximately 82% and 66% for $\Lambda + \bar{\Lambda}$ and K^0_S respectively.

The second point is about the MC description of the data. Figure 7.1, corresponding to the values in Table 7.1, is made to allow the comparison between the data and the MC predictions to be easily comprehended. Figures 7.1(a) and (b) show the relative difference of three MC predictions for the low and high Q^2 DIS events, respectively. The shaded band just serves as a scale and indicates a region of 5% away from the nominal value of the data. In both Q^2 regions, the ARIADNE(0.3) MC predicts $\Lambda + \bar{\Lambda}$ production well while the ARIADNE(0.22) MC underestimates the production. As to K^0_S production, the ARIADNE(0.3) MC seems to be sufficient to describe the data in the low Q^2 region. However, a λ_s value between 0.3 and 0.22 is preferred to reproduce the high Q^2 DIS events. The LEPTO MC fails for most of the cases, indicating that the MEPS approach used to describe the QCD radiation is not appropriate in our case. The results shown in Figures 7.1(a) and (b) suggest that the optimal λ_s value to fit the data varies depending on the type of particle and the kinematic region considered.

Similar comparisons have been done in the Breit frame for the high Q^2 DIS events, as shown in Figures 7.1(c) and (d). Although ARIADNE(0.3) has a good prediction for the $\Lambda + \bar{\Lambda}$ production in the laboratory system, the description in the current and target regions turns out to be poor. A λ_s value smaller than 0.3 is suggested for the current region while a larger one may be appropriate in the target region. This could be an indication that tuning only one parameter in MC is not enough to match the data even for specific single particle production in different kinematic regions. Furthermore, the current region is considered to be comparable to one half hemisphere in e^+e^- experiments. In this region, our data prefer a MC with a λ_s value smaller than the optimal value 0.3 found at LEP experiments, for both $\Lambda + \bar{\Lambda}$ and K^0_S cases.

The other way to obtain a basic and direct view of the strange particle production is to calculate its production rate per event (f). A rough evaluation of the rate f has been made for the strange hadron production in the data and the results are given in Table 7.2. Similar measurements have been done in ZEUS [10] in the kinematic region of $10 < Q^2 < 640$ GeV^2, $0.0003 < x < 0.01$ and $y > 0.04$ based on an integrated luminosity of 0.55 pb^{-1}. The Λ and K^0_S transverse momenta and pseudorapidities were constrained by $p_T > 0.5$ GeV and $|\eta| < 1.3$, respectively. From these results, the $\Lambda + \bar{\Lambda}$ and K^0 ($K^0_S + K^0_L$) production per event were $0.038 \pm 0.006(stat.) \pm 0.002$

	$f(\Lambda)$	$f(\bar{\Lambda})$	$f(K^0_S)$
Photoproduction	0.077 ± 0.001	0.078 ± 0.001	0.270 ± 0.001
Low Q^2 DIS	0.020 ± 0.003	0.019 ± 0.003	0.106 ± 0.005
High Q^2 DIS	0.017 ± 0.002	0.017 ± 0.002	0.093 ± 0.004

Table 7.2: The observed Λ, $\bar{\Lambda}$ and K^0_S production rates per event in three kinematic regions: photoproduction, low Q^2 DIS and high Q^2 DIS regimes in the laboratory frame. Only statistical uncertainties are shown.

(syst.) and $0.289 \pm 0.015(stat.) \pm 0.014(syst.)$, respectively. Since the rate f is subject to the considered kinematic regions, it would be hard to make a precise comparison in quantity to our results since the measurements are done in different kinematic regions. But to a good approximation, these results are consistent with the result obtained in DIS shown in Table 7.2.

In a short summary of this section, the total $\Lambda + \bar{\Lambda}$ and K^0_S cross sections have been measured and compared with MC predictions. The comparisons suggest that tuning only one parameter λ_s is not enough to fit the data in detail. The production rate has also been measured and it agrees reasonably well with the early ZEUS measurement.

7.2 Differential Cross Section

The total cross section can offer an overall view of the strange hadron production while the differential cross section provides more detailed information on both the production and the comparison between the data and Monte Carlo predictions. The differential cross section is defined as

$$\frac{d\sigma}{dY} = \frac{dN}{A \cdot \mathcal{L} \cdot B \cdot \Delta Y}, \tag{7.2}$$

where dN is the number of the strange hadrons in a bin of size ΔY, A is the acceptance evaluated with MC studies, $\mathcal{L}$ is the integrated luminosity and B is the branching ratio. In this thesis, the variable Y could be the kinematic variable p_T, η, Q^2 or x for DIS events, or p_T, η or x_γ^{OBS} for photoproduction events.

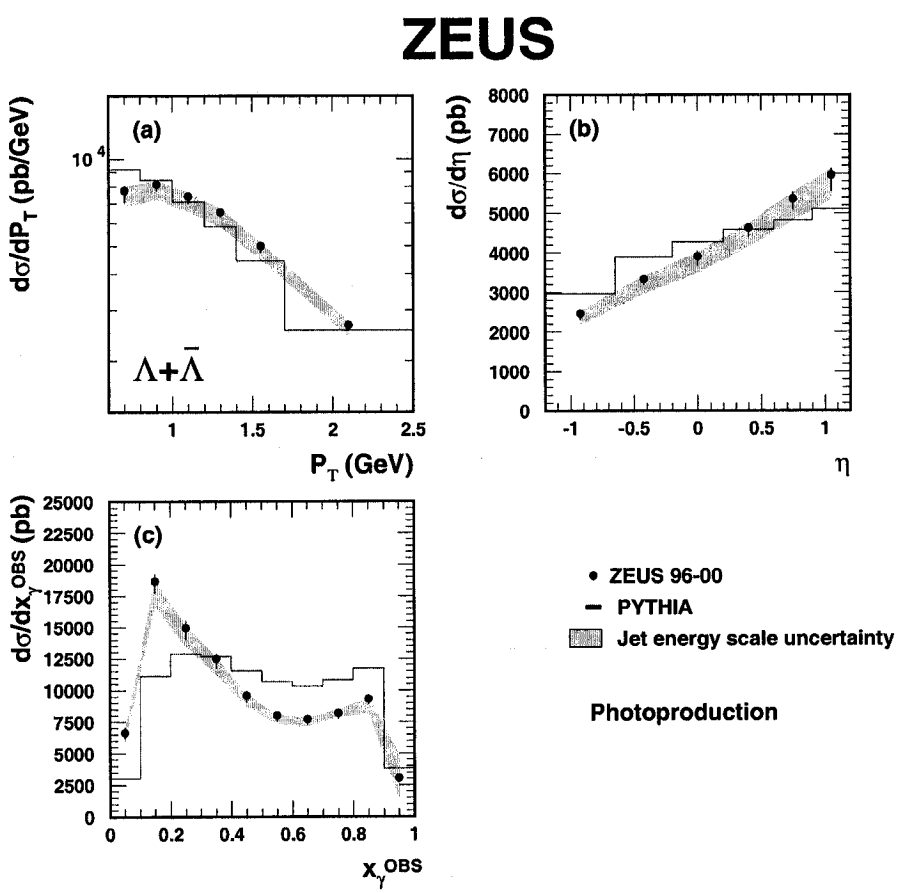

Figure 7.2: Differential $\Lambda + \bar{\Lambda}$ cross sections as a function of p_T, η and x_γ^{OBS} in the laboratory frame for photoproduction events. Statistical errors (inner error bars) and the systematic uncertainties (outer error bars) added in quadrature are shown. The solid histogram shows the prediction from PYTHIA with a strangeness suppression factor of 0.3.

7.2.1 Photoproduction Events

In Figures 7.2 and 7.3, differential $\Lambda + \bar{\Lambda}$ and K_S^0 cross sections as a function of p_T, η and x_γ^{OBS} are shown for photoproduction events in the laboratory frame. The MC used to describe the data is PYTHIA in which the λ_s was set to be 0.3. Since the PYTHIA MC can not correctly predict the absolute cross section of the inclusive photoproduction, its differential predictions shown here were normalized to the total cross section of the data and then were used to compare with the data.

The jet energy scale resulting uncertainties were highlighted by the shaded band. Generally PYTHIA can predict the distribution shapes as a function of p_T and η rea-

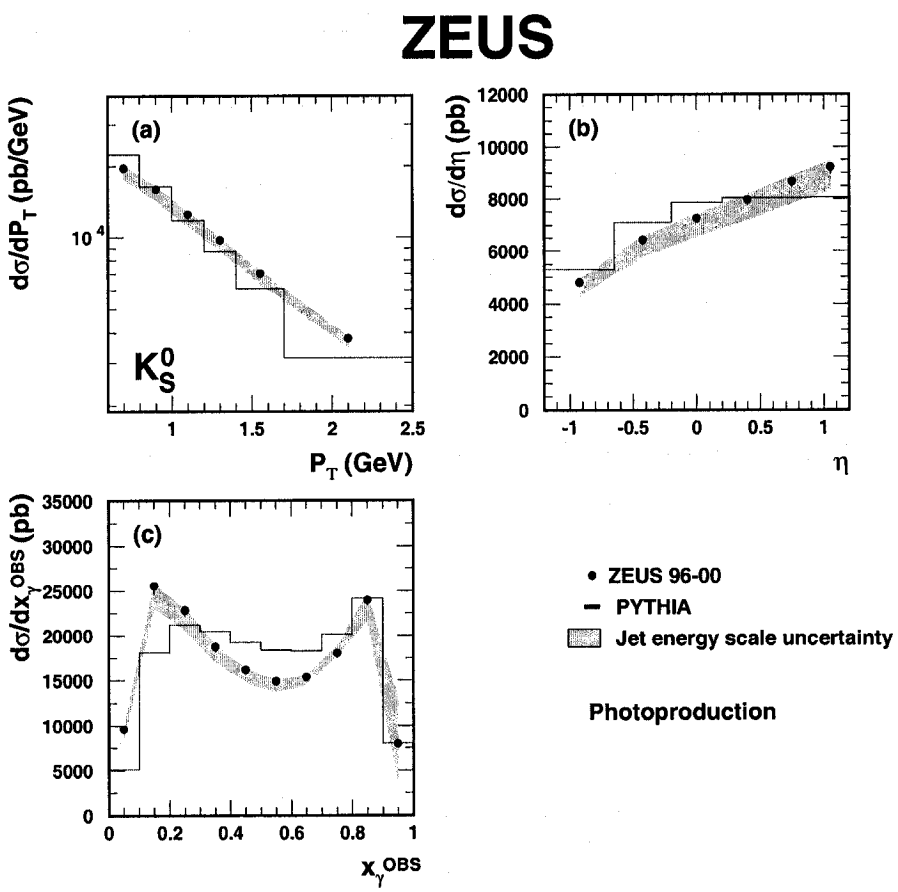

Figure 7.3: Differential K^0_S cross sections as a function of p_T, η and x_γ^{OBS} in the laboratory frame for photoproduction events. Statistical errors (inner error bars) and the systematic uncertainties (outer error bars) added in quadrature are shown. The solid histogram shows the prediction from PYTHIA with a strangeness suppression factor of 0.3.

sonably well, as shown in Figures 7.2(a) and (b) and Figures 7.3(a) and (b). However, clear discrepancies both in quantity and shape can be seen between the data and MC. The dropping tendency of the hadron production with the increasing transverse momentum reflects two phenomena. The first one is the production probability of 'harder' Λ's and K^0_S's becoming smaller and the other one is the decreasing number of the events which contain higher p_T hadrons. The rising strange hadron production becoming larger as function of η reflects the asymmetry of the initial beam energies and the proton remnant related effects.

The largest differences between the data and the MC prediction are found in

Figures 7.2(c) and 7.3(c): the differential $\Lambda + \bar{\Lambda}$ and K^0_S production cross sections as a function of $x_\gamma^{\rm OBS}$. Two peaks at $x_\gamma^{\rm OBS}$ around 0.15 and 0.85 in the data are considered to be associated with different physics processes. As was discussed in Chapter 4, in the smaller $x_\gamma^{\rm OBS}$ region (less than 0.75) which corresponds to the resolved process, only a small fraction of the photon energy takes part in the interaction with the proton, while in the region with $x_\gamma^{\rm OBS} > 0.75$, the direct process, the photon behaves point-like and gets involved in the interaction completely. Therefore the two peaks in the data characterize these two different processes. The multiple interaction mechanism was introduced in the PYTHIA MC to give a better description of the data in the resolved process. But further improvements are obviously needed when comparing the results from the data and from PYTHIA, shown in Figures 7.2(c) and 7.3(c). PYTHIA predicts a relative flat distribution and thus fails to reproduce the distribution structures, in particular for the $\Lambda + \bar{\Lambda}$ production. The contributions to this discrepancy due to the poor description of the data by the MC, shown in Figures 6.8 and 6.9, are estimated and included in the systematic section of Appendix A.

7.2.2 Low Q^2 DIS Events

The $\Lambda + \bar{\Lambda}$ hadrons and K^0_S meson differential cross sections have been measured as a function of two kinematic variables of the strange particle, $P_{\rm T}^{\rm LAB}$ and $\eta^{\rm LAB}$, and two event variables, $x_{\rm Bj}$ and Q^2 for low Q^2 events. Three Monte Carlo event samples were generated for comparison.

The measurement results of the differential $\Lambda + \bar{\Lambda}$ and K^0_S cross sections are reproduced in Figures 7.4 and 7.5. There is a general agreement on the cross sections when comparing the data with the ARIADNE(0.3) prediction, but not in detail. For instance, ARIADNE(0.3) overestimates the cross sections in the lower $P_{\rm T}^{\rm LAB}$ region while it underestimates them in the larger $P_{\rm T}^{\rm LAB}$ region in both $\Lambda + \bar{\Lambda}$ and K^0_S cases. Furthermore, none of three MC's can reproduce the excess of data in the lower $x_{\rm Bj}$ region, where the contributions from the sea quarks and gluons in the proton are expected to be dominant. The LEPTO MC with a strangeness suppression factor 0.3 fails to describe both the $\Lambda + \bar{\Lambda}$ and K^0_S productions.

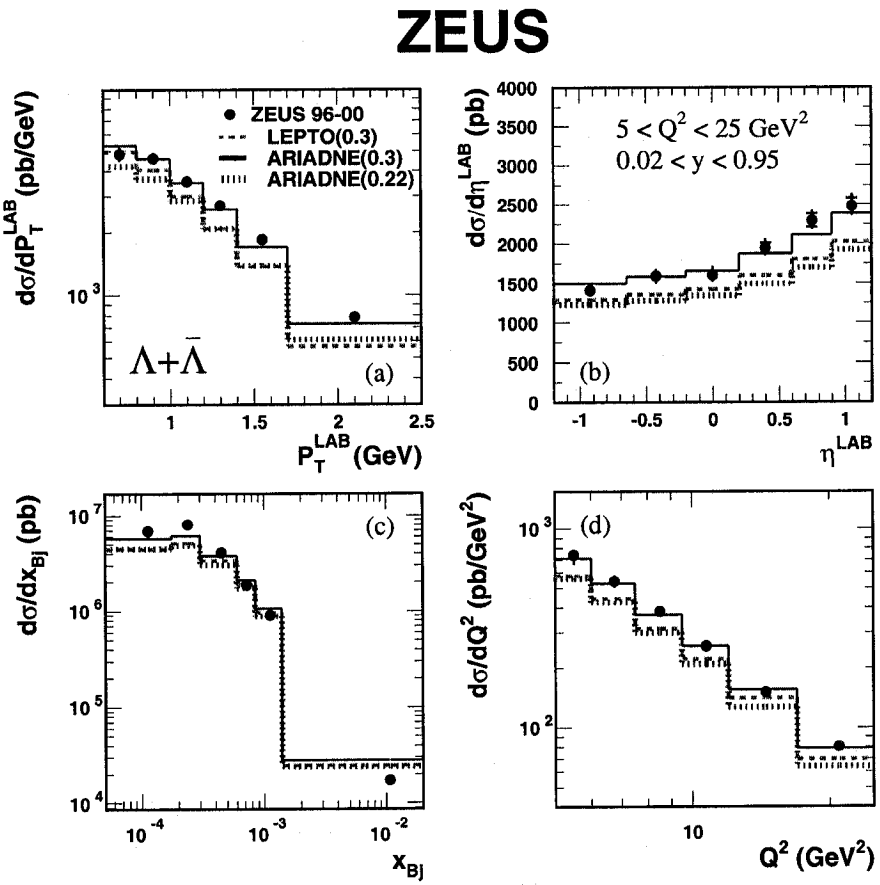

Figure 7.4: Differential $\Lambda + \bar{\Lambda}$ cross sections as a function of $P_{\mathrm{T}}^{\mathrm{LAB}}$, η^{LAB}, x_{Bj} and Q^2 in the laboratory system for the low Q^2 DIS events. Statistical errors (inner error bars) and the systematic uncertainties (outer error bars) added in quadrature are shown, unless smaller than the point size.

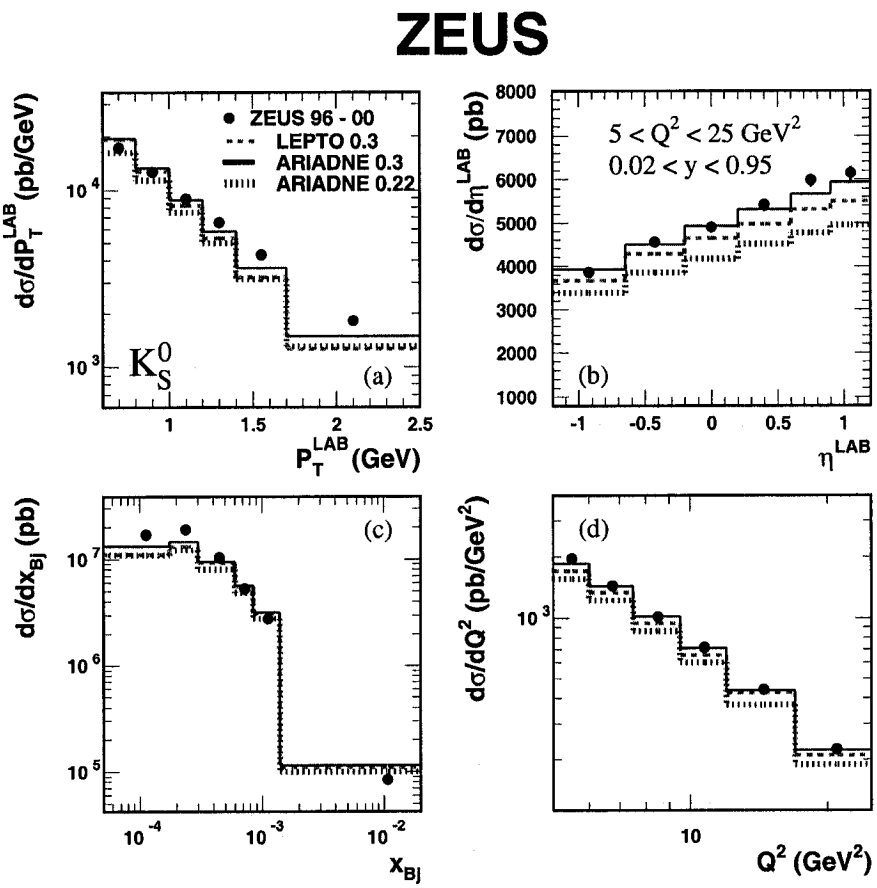

Figure 7.5: Differential K^0_S cross sections as a function of $P_{\mathrm{T}}^{\mathrm{LAB}}$, η^{LAB}, x_{Bj} and Q^2 in the laboratory frame for low Q^2 DIS events. Statistical errors (inner error bars) and the systematic uncertainties (outer error bars) added in quadrature are shown, unless smaller than the point size.

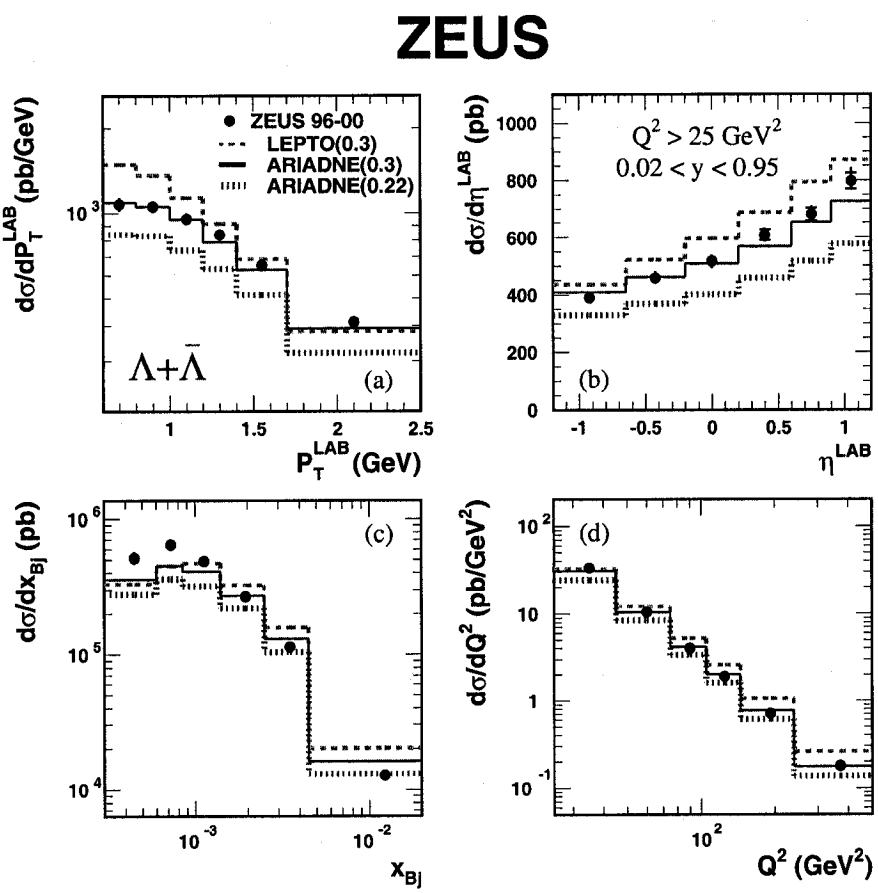

Figure 7.6: Differential $\Lambda + \bar{\Lambda}$ cross sections as a function of $P_{\mathrm{T}}^{\mathrm{LAB}}$, η^{LAB}, x_{Bj} and Q^2 in laboratory system for high Q^2 DIS events. Statistical errors (inner error bars) and the systematic uncertainties (outer error bars) added in quadrature are shown, unless smaller than the point size.

7.2.3 High Q^2 DIS Events

The differential $\Lambda + \bar{\Lambda}$ and K_S^0 cross sections are investigated as a function of $P_{\mathrm{T}}^{\mathrm{LAB}}$ and η^{LAB} of the hadrons and two event variables x_{Bj} and Q^2 for high Q^2 DIS events. Three MC predictions are presented as well.

The differential $\Lambda + \bar{\Lambda}$ and K_S^0 cross sections are shown in Figures 7.6 and 7.7, respectively. For the $\Lambda + \bar{\Lambda}$ production shown in Figure 7.6, a reasonable agreement on the cross sections was found between the data and the ARIADNE(0.3) prediction. The ARIADNE MC with a λ_s value of 0.22 always under-evaluates the data, except in the higher x_{Bj} region. However, concerning the K_S^0 production, shown in Figure 7.7, the data sit in the region between ARIADNE(0.3) and ARIADNE(0.22) predictions,

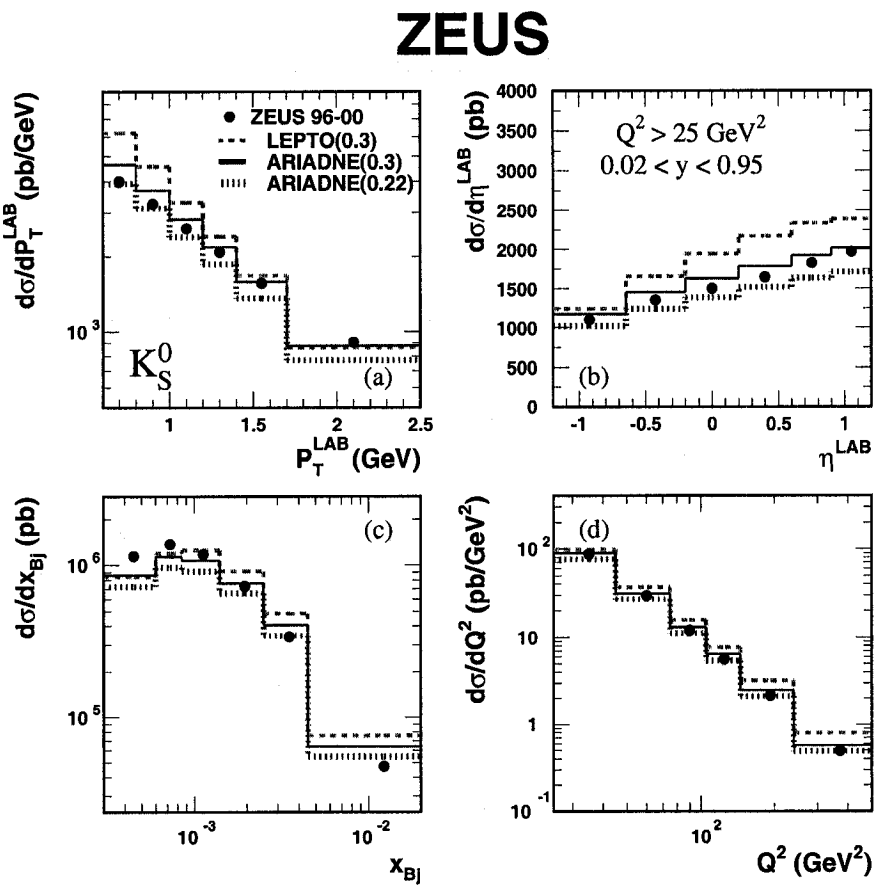

Figure 7.7: Differential K^0_S cross sections as a function of P_T^{LAB}, η^{LAB}, x_{Bj} and Q^2 in the laboratory frame for high Q^2 DIS events. Statistical errors (inner error bars) and the systematic uncertainties (outer error bars) added in quadrature are smaller than the point size.

suggesting an ARIADNE MC with a strangeness suppression factor between 0.3 and 0.22 can match the data well. None of the MC's can reproduce the data in the lower x_{Bj} region. Similar to the low Q^2 events, the LEPTO MC with a strangeness suppression factor 0.3 fails. But here it overestimates the $\Lambda + \bar{\Lambda}$ and K^0_S production instead.

The differential $\Lambda + \bar{\Lambda}$ and K^0_S cross sections were also studied in the Breit frame. The results are shown in Figures 7.8, 7.9, 7.10 and 7.11.

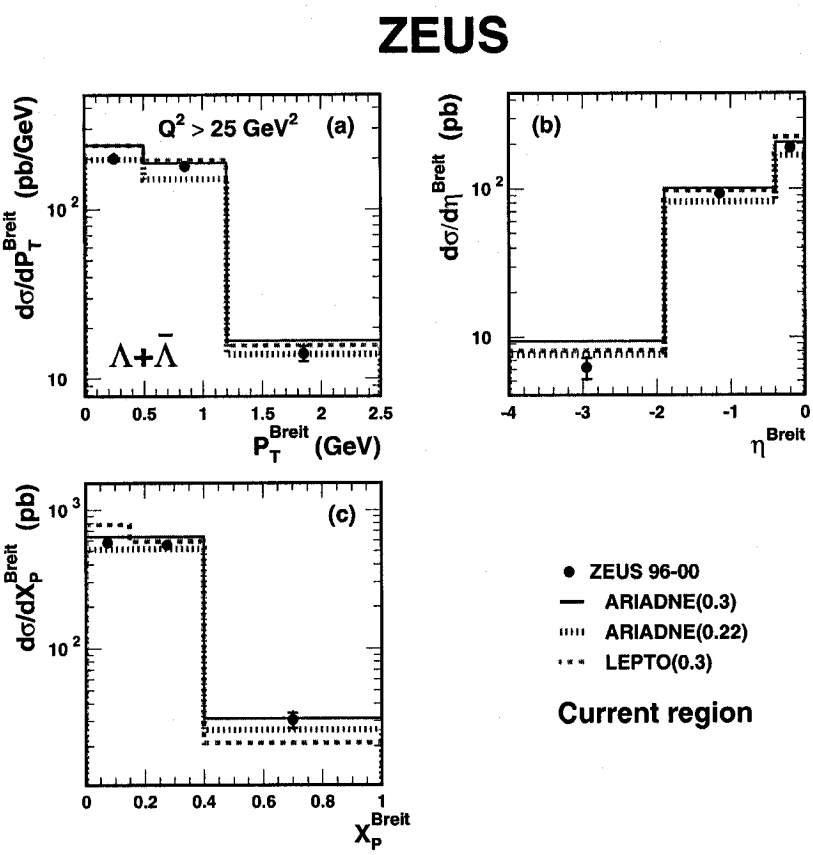

Figure 7.8: Differential $\Lambda + \bar{\Lambda}$ cross sections as a function of $P_{\mathrm{T}}^{\mathrm{Breit}}$, η^{Breit} and $x_{\mathrm{P}}^{\mathrm{Breit}}$ in the current region of the Breit frame. Statistical errors (inner error bars) and the systematic uncertainties (outer error bars) added in quadrature are shown, unless smaller than the point size.

Figure 7.8 shows the differential $\Lambda + \bar{\Lambda}$ cross sections as a function of $P_{\mathrm{T}}^{\mathrm{Breit}}$, η^{Breit} and $x_{\mathrm{P}}^{\mathrm{Breit}}$ in the current region of the Breit frame. Different from the situation in the laboratory system, the comparison of the results between the data and the ARIADNE MC's indicates a λ_s value smaller than 0.3 could fit the data well in general. No big difference exists between different MC predictions. It is worthwhile to point out that the difference between LEPTO and ARIADNE(0.3) was found to be small in the current region (see also Table 7.1 and Figure 7.1), indicating the large difference between them for the whole sample should come from the target region.

Figure 7.9 shows the differential $\Lambda + \bar{\Lambda}$ cross sections as a function of $P_{\mathrm{T}}^{\mathrm{Breit}}$, η^{Breit} and $x_{\mathrm{P}}^{\mathrm{Breit}}$ in the target region of the Breit frame. The predictions from ARIADNE(0.3) are acceptable in general and relatively better than the others. The clear

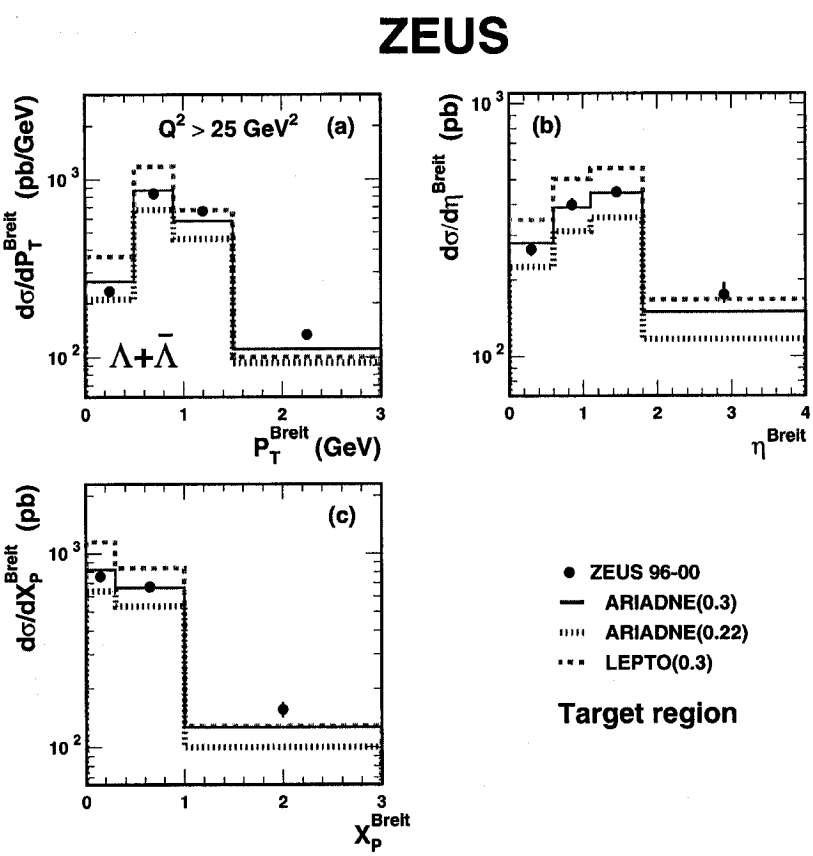

Figure 7.9: Differential $\Lambda + \bar{\Lambda}$ cross sections as a function of $P_{\mathrm{T}}^{\mathrm{Breit}}$, η^{Breit} and $x_{\mathrm{P}}^{\mathrm{Breit}}$ in the target region of the Breit frame. Statistical errors (inner error bars) and the systematic uncertainties (outer error bars) added in quadrature are shown, unless smaller than the point size.

difference between the two MC's LEPTO and ARIADNE(0.3), which is responsible for the difference for the whole sample, can be observed here. The deep dip in the lower $P_{\mathrm{T}}^{\mathrm{Breit}}$ region was found to be the side effect of the kinematic cuts applied in the laboratory frame. A similar drop happens in the forward η^{Breit} region which is considered to correspond to the lower $P_{\mathrm{T}}^{\mathrm{Breit}}$ region to some extent.

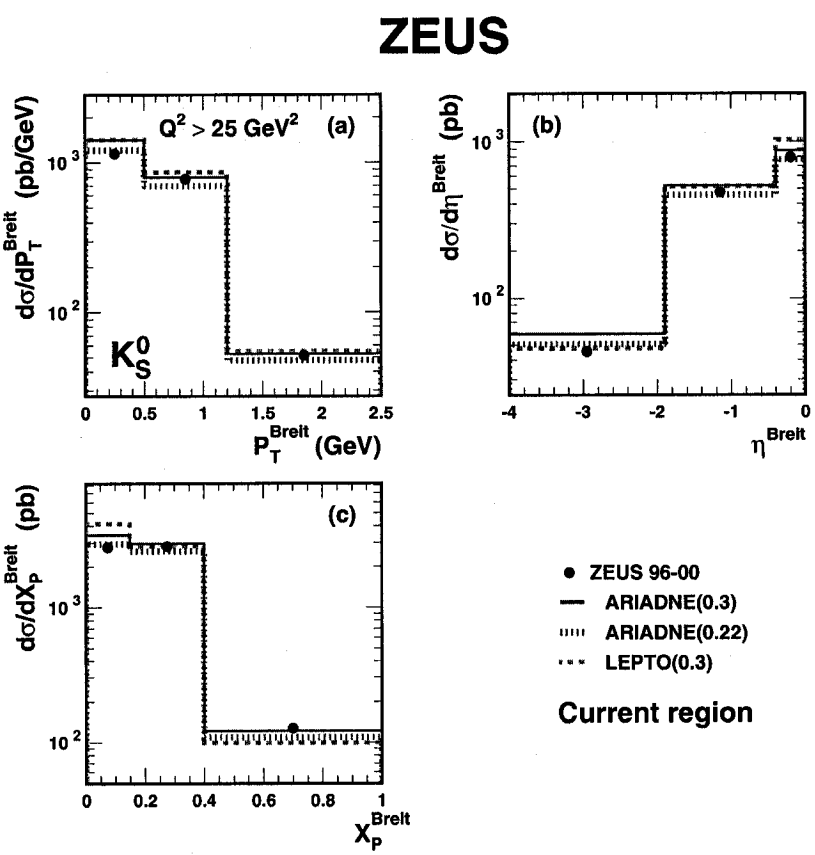

Figure 7.10: Differential K^0_S cross sections as a function of $P_{\mathrm{T}}^{\mathrm{Breit}}$, η^{Breit} and $x_{\mathrm{P}}^{\mathrm{Breit}}$ in the current region of the Breit frame. Statistical errors (inner error bars) and the systematic uncertainties (outer error bars) added in quadrature are smaller than the point size.

Figure 7.10 shows the results on differential K^0_S cross sections as a function of $P_{\mathrm{T}}^{\mathrm{Breit}}$, η^{Breit} and $x_{\mathrm{P}}^{\mathrm{Breit}}$ in the current region of the Breit frame. A good agreement was observed between the data and ARIADNE(0.22). And the predictions from the other two MC's are in general acceptable.

The similar distributions for events in the target region are shown in Figure 7.11. Both ARIADNE(0.3) and ARIADNE(0.22) can reproduce the data reasonably well while the LEPTO MC overestimates the production. Similarly to the $\Lambda + \bar{\Lambda}$ production in the target region, the sharp drop in the lower $P_{\mathrm{T}}^{\mathrm{Breit}}$ and higher η^{Breit} regions was caused by the cuts applied to select hadrons in the laboratory frame.

A short summary of this section: the differential $\Lambda + \bar{\Lambda}$ and K^0_S production cross sections have been determined for the three kinematic regions. The MC PYTHIA

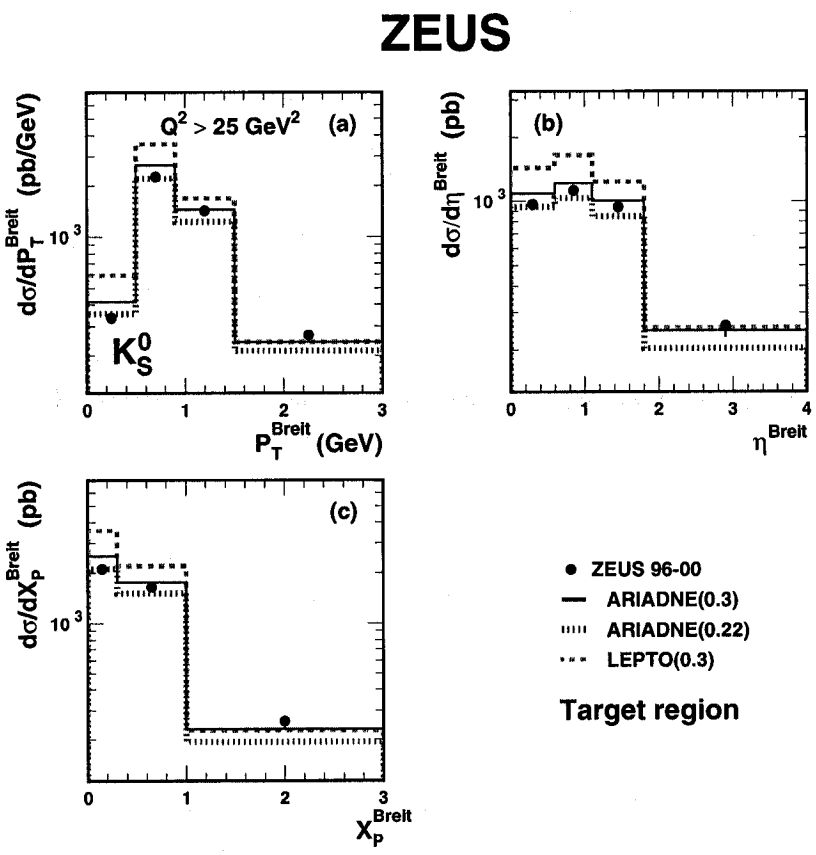

Figure 7.11: Differential K^0_S cross sections as a function of $P_{\mathrm{T}}^{\mathrm{Breit}}$, η^{Breit} and $x_{\mathrm{P}}^{\mathrm{Breit}}$ in the target region of the Breit frame. Statistical errors (inner error bars) and the systematic uncertainties (outer error bars) added in quadrature are shown, unless smaller than the point size.

cannot reproduce the x_γ^{OBS} distribution well in photoproduction. As to DIS events, a single tuning of λ_s is found to be insufficient to fit the data. Two combined figures, 7.12(a) and (b), are created to show the $\Lambda + \bar{\Lambda}$ and K^0_S differential cross sections as a function of Q^2 for DIS events with $\mathrm{Q}^2 > 5$ GeV^2. Each lower plot is the relative difference between the MC predictions and the data, defined as $(\sigma_{MC} - \sigma_{data})/\sigma_{data}$. From this ratio, one can clearly see how the MC's describe the data and how λ_s depends on Q^2.

Due to the different dominant fragmentation process in the current and target regions of the Breit frame, it was found that more strange hadrons are produced in the target region (see Table 7.1).

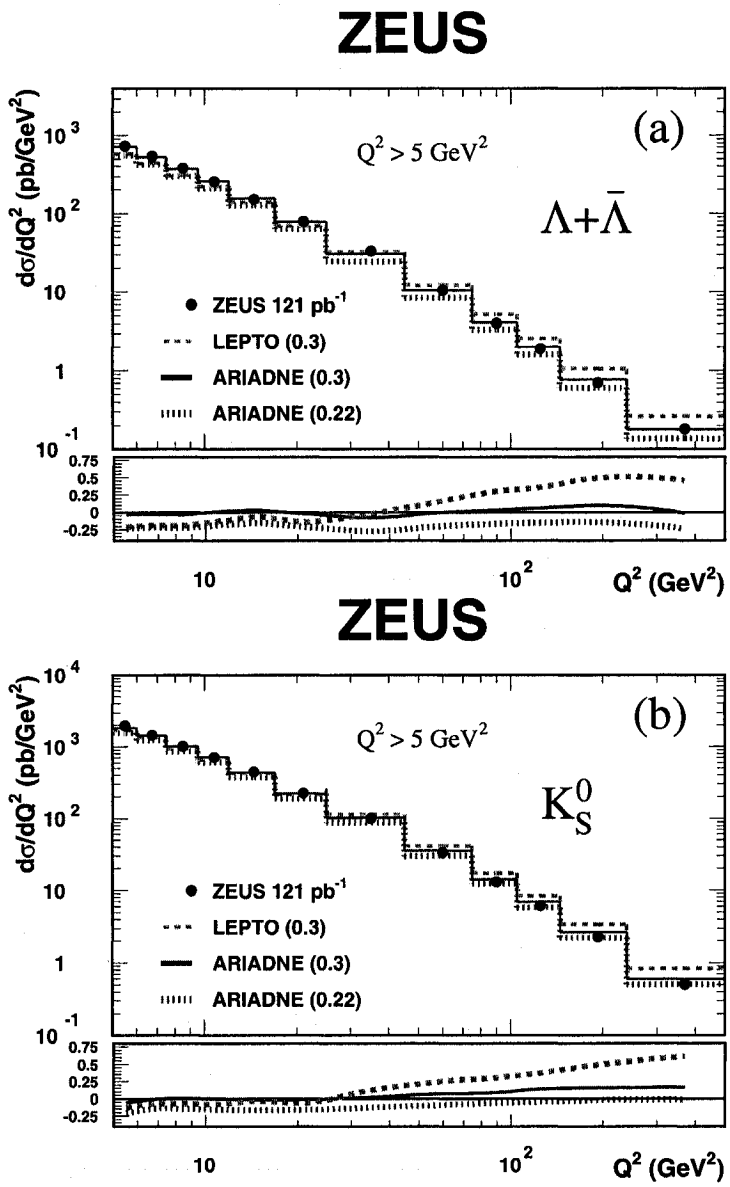

Figure 7.12: Differential $\Lambda + \bar{\Lambda}$ (a) and K^0_S (b) cross sections as a function of Q^2 for events with $Q^2 > 5$ GeV^2. The lower plot shows the relative difference of MC predictions to the data. Statistical errors and the systematic uncertainties are smaller than the point size.

7.3 Λ to $\bar{\Lambda}$ Production Asymmetry

The presence of the proton, one of the initial state colliding particles at HERA, inevitably results in a net Baryon Number (BN) of +1 in the final hadronic states. One possible way to trace down the BN transfer from the initial proton to a final baryon is to measure the production asymmetry of a baryon to its anti-partner. In the fixed target experiments where one has a very good acceptance in the forward region, the influence of the source particle on the final hadron production is manifest [88, 89, 90, 91]. Different from that, the general interesting region here at HERA is the central part of the detector where a good understanding of the acceptance and efficiency can be obtained. Therefore the impact of the initial proton on the baryon to antibaryon production asymmetry could be small or negligible in this region at HERA since the BN is expected to escape the detector in a different region: very forward region over several units of pseudorapidity.

In this thesis, the Λ to $\bar{\Lambda}$ production asymmetry was measured so that the results could give a hint of how the presence of the initial proton affects the Λ production and how significant the effect might be. Here we assume the sea quarks in the proton will not result in any production difference for a baryon to its antipartner. The $\bar{\Lambda}$ production in this measurement acts as a reference for baryon Λ production because it does not have any valence quarks in common with the initial proton while Λ could take a diquark from the proton to inherit the baryon number and result in an asymmetry.

The Λ to $\bar{\Lambda}$ production asymmetry was determined by the formula

$$\mathcal{A} = \frac{N_\Lambda - N_{\bar{\Lambda}}}{N_\Lambda + N_{\bar{\Lambda}}}, \tag{7.3}$$

where N_Λ and $N_{\bar{\Lambda}}$ represent the number of Λ and $\bar{\Lambda}$ over the kinematic range of interest, respectively.

The average $\mathcal{A}$ has been measured in the three kinematic regions and the results are shown in Table 7.3(a). Further investigation in the Breit frame for high Q^2 DIS events is also shown in Table 7.3(b). All results lead to the same conclusion that no Λ to $\bar{\Lambda}$ asymmetry was observed in the central region of the ZEUS detector in the three considered regions of phase space. The MC models arrive to the same conclusion.

(a) Laboratory Frame

		$\mathcal{A}$ (%)
photoproduction	ZEUS 96-00	$-0.03 \pm 0.57^{+0.24}_{-0.35}$
	PYTHIA(0.3)	0.84 ± 0.12
Low Q^2 DIS	ZEUS 96-00	$1.85 \pm 1.51^{+0.42}_{-2.68}$
	ARIADNE(0.3)	0.11 ± 0.42
	ARIADNE(0.22)	-0.14 ± 0.47
	LEPTO(0.3)	-0.57 ± 0.44
High Q^2 DIS	ZEUS 96-00	$0.64 \pm 1.31^{+3.01}_{-2.19}$
	ARIADNE(0.3)	0.20 ± 0.37
	ARIADNE(0.22)	0.41 ± 0.42
	LEPTO(0.3)	-0.17 ± 0.35
(b) Breit Frame (High Q^2 DIS)		
Current region	ZEUS 96-00	$1.35 \pm 3.28^{+1.42}_{-1.42}$
	ARIADNE(0.3)	-0.13 ± 0.85
	ARIADNE(0.22)	0.12 ± 0.90
	LEPTO(0.3)	0.99 ± 0.80
Target region	ZEUS 96-00	$1.52 \pm 1.62^{+2.66}_{-1.66}$
	ARIADNE(0.3)	0.19 ± 0.45
	ARIADNE(0.22)	0.22 ± 0.47
	LEPTO(0.3)	-0.70 ± 0.38

Table 7.3: The average Λ to $\bar{\Lambda}$ production asymmetries. Theoretical predictions from different MC models are presented. Both statistical and systematic uncertainties are shown for the data.

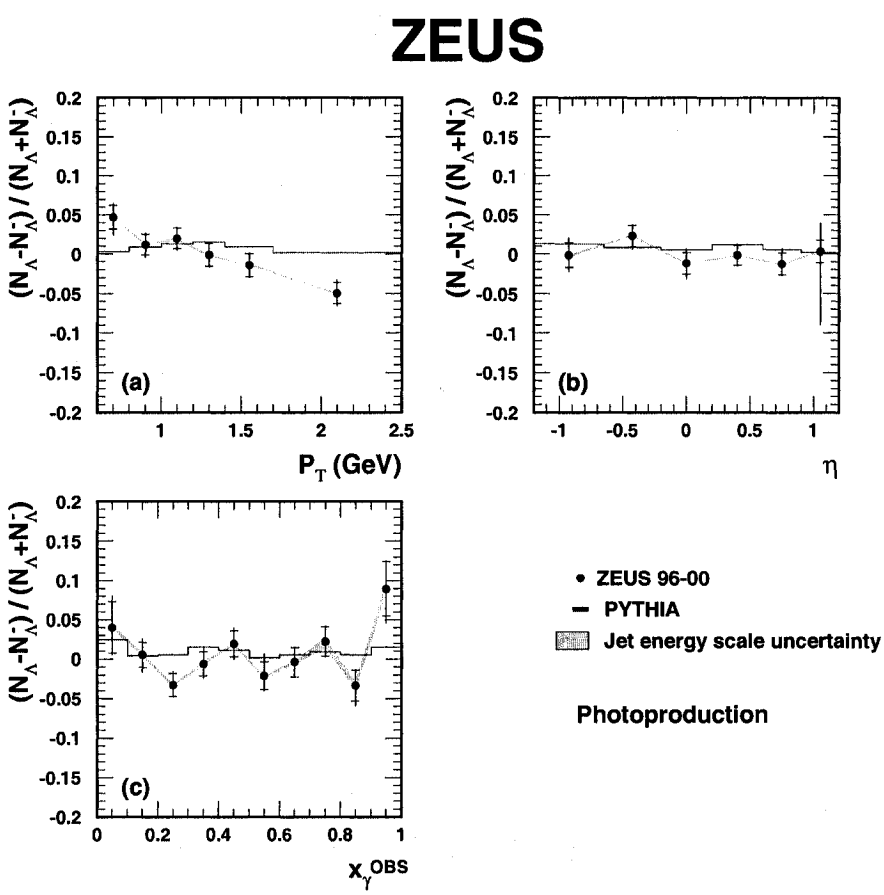

Figure 7.13: The asymmetry $\frac{N(\Lambda)-N(\bar{\Lambda})}{N(\Lambda)+N(\bar{\Lambda})}$ as a function of p_T, η and x_γ^{OBS} in the laboratory frame for photoproduction events. Statistical errors (inner error bars) and the systematic uncertainties (outer error bars) added in quadrature are shown.

7.3.1 Photoproduction Events

In addition to the overall asymmetry measurements discussed above, the differential Λ to $\bar{\Lambda}$ production asymmetry has also been measured in photoproduction as a function of p_T, η and x_γ^{OBS}. The results are shown in Figure 7.13. Consistently with the average results shown in Table 7.3(a), no significant asymmetries were found in all distributions of Figure 7.13. Some kinematic regions exist where a small asymmetry might be present, for example, in the lower or higher p_T regions. But limited by our measurement resolution, all results in these regions are considered to be consistent with zero.

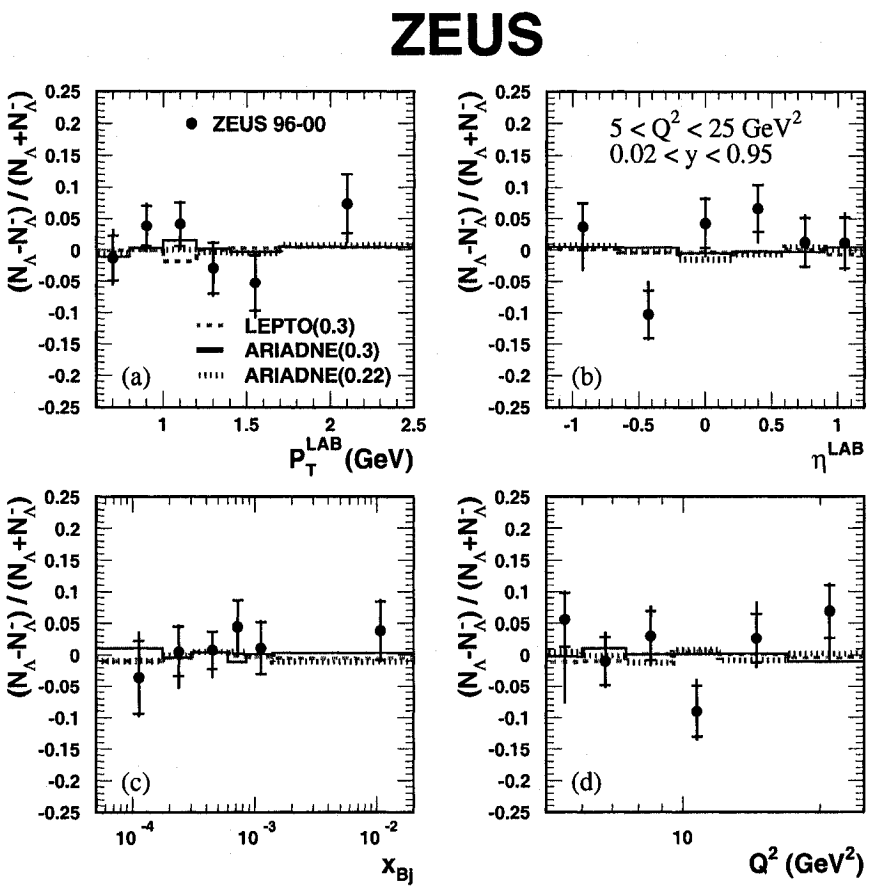

Figure 7.14: The asymmetry $\frac{N(\Lambda)-N(\bar{\Lambda})}{N(\Lambda)+N(\bar{\Lambda})}$ as a function of $P_{\mathrm{T}}^{\mathrm{LAB}}$, η^{LAB}, x_{Bj} and Q^2 in the laboratory frame for low Q^2 DIS events. Statistical errors (inner error bars) and the systematic uncertainties (outer error bars) added in quadrature are shown.

7.3.2 Low Q^2 DIS Events

The differential Λ to $\bar{\Lambda}$ production asymmetry as a function of $P_{\mathrm{T}}^{\mathrm{LAB}}$, η^{LAB}, x_{Bj} and Q^2 has been measured for the low Q^2 DIS events in the laboratory frame. No evidence was found for any significant asymmetry in all results presented in Figure 7.14. A zero asymmetry is predicted as well by the three MC models considered in this thesis.

7.3.3 High Q^2 DIS Events

The differential production asymmetry in the high Q^2 DIS region is shown in Figure 7.15. In the full considered $P_{\mathrm{T}}^{\mathrm{LAB}}$, η^{LAB}, x_{Bj} and Q^2 regions, no significant asymme-

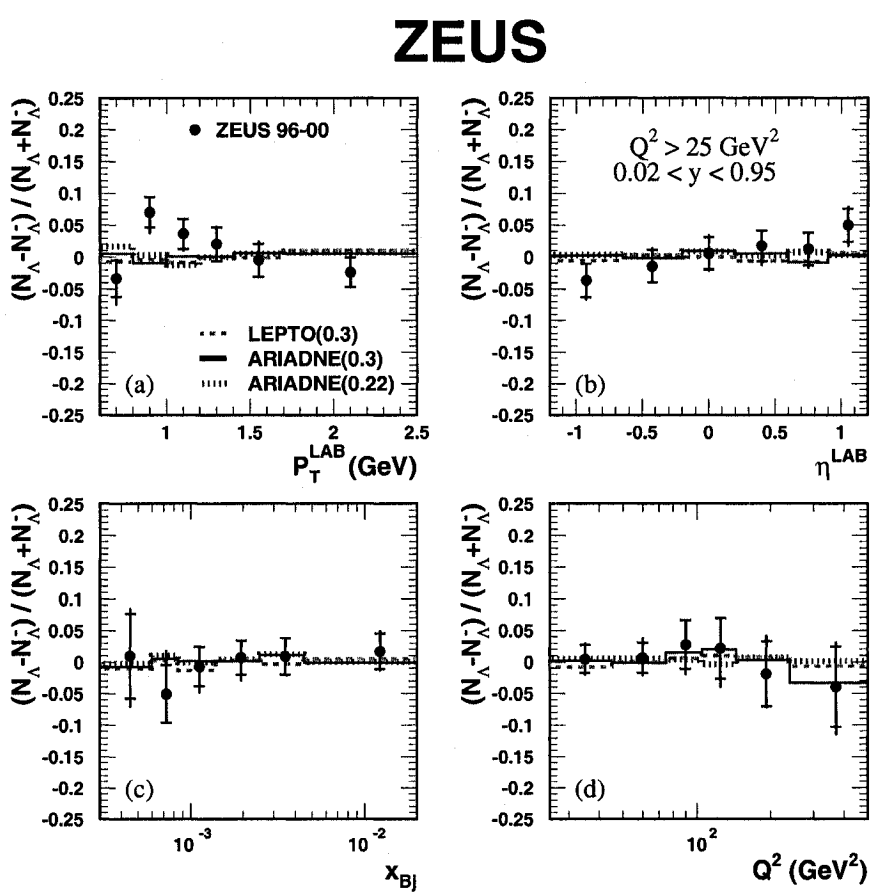

Figure 7.15: The asymmetry $\frac{N(\Lambda)-N(\bar{\Lambda})}{N(\Lambda)+N(\bar{\Lambda})}$ as a function of P_T^{LAB}, η^{LAB}, x_{Bj} and Q^2 in the laboratory frame for high Q^2 DIS events. Statistical errors (inner error bars) and the systematic uncertainties (outer error bars) added in quadrature are shown.

tries were seen. The same conclusions were drawn from the three MC predictions.

Even though no Λ to $\bar{\Lambda}$ production asymmetries were observed averagely and differentially in all cases, it might be interesting to notice some trends in the results, for instance, the increasing tendency of $\mathcal{A}$ as p_T decreases and as η increases, shown in Figures 7.15(a) and (b). As discussed at the beginning of this section, $\mathcal{A}$ is subject to the selected kinematic regions. Therefore a non-zero asymmetry could be observed if we extend the current acceptance coverage to, for example, larger η or lower P_T^{LAB} regions.

Furthermore, the $\mathcal{A}$ has also been measured in the two regions of the Breit frame, the current region and the target region, for the high Q^2 DIS. The corresponding results are shown in Figures 7.16 and 7.17. The separation of the high Q^2 events in

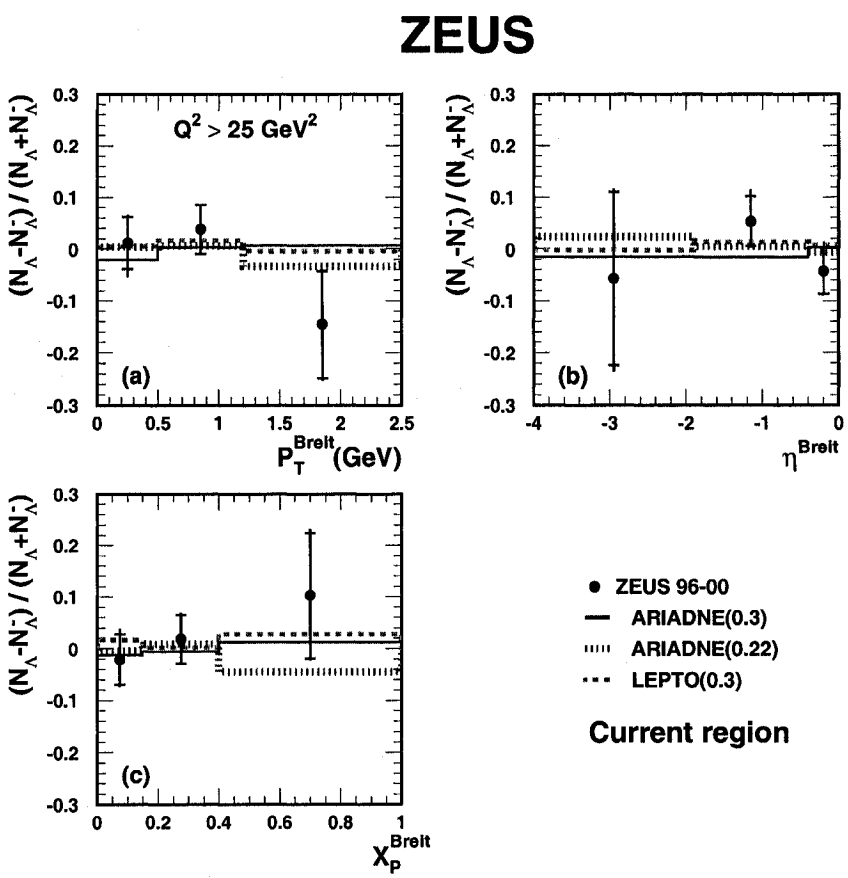

Figure 7.16: The measured asymmetry $\frac{N(\Lambda)-N(\bar{\Lambda})}{N(\Lambda)+N(\bar{\Lambda})}$ in the current region of the Breit frame as a function of P_T^{Breit}, η^{Breit} and x_P^{Breit} for high Q^2 DIS events. Statistical errors (inner error bars) and the systematic uncertainties (outer error bars) added in quadrature are shown.

the Breit frame does not result in any sizable non-zero asymmetries in both regions of the Breit frame. The MC predictions on $\mathcal{A}$ are consistent with zero and in an agreement with the data.

In all cases discussed above, the baryon to antibaryon asymmetry was consistent with zero asymmetry within the measurement uncertainties and well predicted by the MC's. This indicates, in our case, that the assumed proton influence on $\mathcal{A}$ is negligibly small. Consequently the baryons and antibaryons are suggested to be produced according to the same mechanism.

A so-called gluon junction mechanism [92] also exists. It configures the baryon as three valence quarks attached by three individual gluons at a 'gluon junction'.

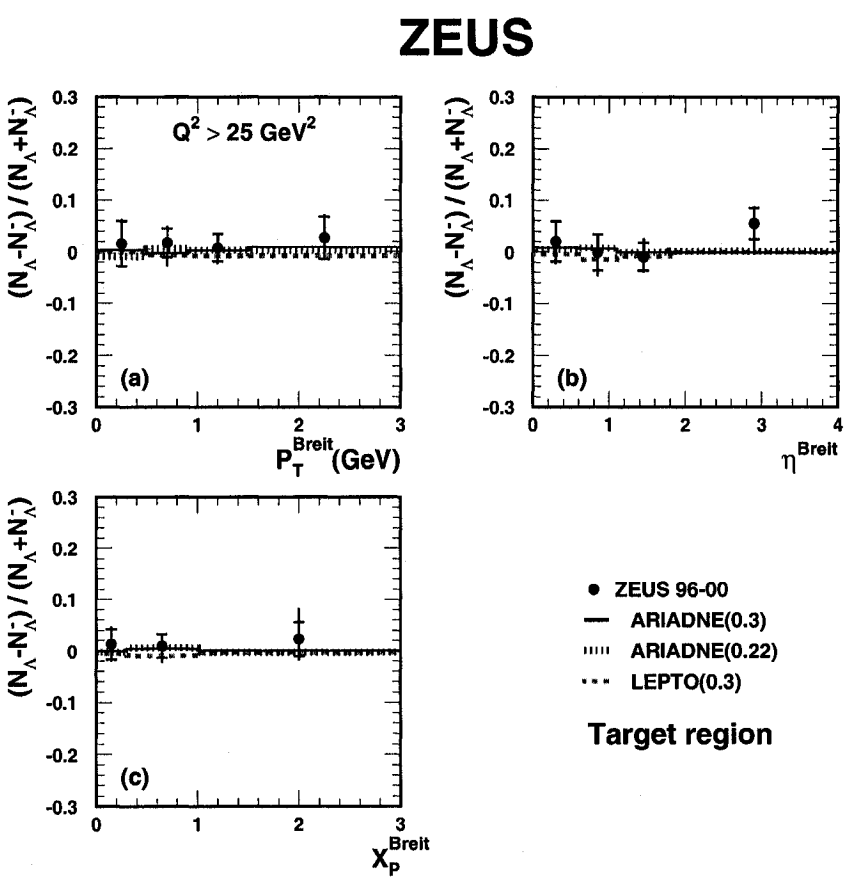

Figure 7.17: The measured asymmetry $\frac{N(\Lambda)-N(\bar{\Lambda})}{N(\Lambda)+N(\bar{\Lambda})}$ in the target region of the Breit frame as a function of P_T^{Breit}, η^{Breit} and x_P^{Breit} for high Q^2 DIS events. Statistical errors (inner error bars) and the systematic uncertainties (outer error bars) added in quadrature are shown.

In this model, the gluon junction carries the BN rather than the valence quarks. It can be used to explain the large degree of antibaryon to baryon production in the heavy nuclear system, for example in the results from RHIC where an asymmetry of around 70% was found in the central rapidity region [87]. A specific prediction [92] due to this mechanism was made for the HERA $\gamma^* p$ or γp events at a low x (a level of less than 10^{-3}). It predicted a non-zero asymmetry of +3.5%. Based on the data sample in this thesis, the average zero-asymmetries obtained in low x regions for the two DIS processes are not able to give a clear judgment on this model because our total uncertainties are also at a 3% level.

As our baryon-antibaryon asymmetry is consistent with no asymmetry, Λ and

$\bar{\Lambda}$ samples were often combined together for the baryon to meson production ratio results in the rest of this chapter.

7.4 Λ to K^0_S Production Ratio

The Λ to K^0_S production ratio ($\mathcal{R}$) was determined by the formula

$$\mathcal{R} = \frac{N_\Lambda + N_{\bar{\Lambda}}}{N_{K^0_S}}, \tag{7.4}$$

where N_Λ, $N_{\bar{\Lambda}}$ and $N_{K^0_S}$ represent the number of Λ, $\bar{\Lambda}$ and K^0_S respectively over the kinematic regions of interest in the hadron level.

The average $\mathcal{R}$ has been measured in the laboratory frame in the three kinematic regions and the results are shown in Table 7.4(a). The $\mathcal{R}$ values averaged 0.58 in photoproduction, approximately 30% more than the $\mathcal{R}$ values in the low and high Q^2 DIS regions where a similar value of 0.36 was observed in both cases. The PYTHIA MC does not account for such enhancement in the photoproduction process, predicting a $\mathcal{R}$ value of about 0.41. Concerning the low Q^2 DIS events, the prediction of $\mathcal{R}$ from ARIADNE(0.3) MC agrees well with the data while the other two MC's give a relatively smaller $\mathcal{R}$. In the case of the high Q^2 DIS events, however, none of the MC descriptions on $\mathcal{R}$ is satisfactory. Each of them gives rise to a smaller $\mathcal{R}$ value than the one from the data.

Further investigations on $\mathcal{R}$ have been carried out in the Breit frame and the results are shown in Table 7.4(b). Two general conclusions can be drawn according to the $\mathcal{R}$ values given in this table. First, the MC's predict the $\mathcal{R}$ ratio quite well for events in the current region but fail to describe the excess of $\mathcal{R}$ in the target region. Secondly, the Λ to K^0_S ratio in the target region is twice as large as that in the current region.

Apart from the average $\mathcal{A}$ measurements discussed above, the differential $\mathcal{R}$ measurements have also been performed in the three kinematic regions. The results will be presented in the following few sections.

(a) Laboratory Frame

		$\mathcal{R}(\%)$
photoproduction	ZEUS 96-00	$57.49 \pm 0.36^{+1.01}_{-2.80}$
	PYTHIA(0.3)	41.30 ± 0.60
Low Q^2 DIS	ZEUS 96-00	$36.57 \pm 0.60^{+1.43}_{-0.33}$
	ARIADNE(0.3)	36.49 ± 0.18
	ARIADNE(0.22)	34.73 ± 0.19
	LEPTO(0.3)	32.20 ± 0.16
High Q^2 DIS	ZEUS 96-00	$36.44 \pm 0.51^{+2.62}_{-2.63}$
	ARIADNE(0.3)	33.17 ± 0.14
	ARIADNE(0.22)	31.03 ± 0.15
	LEPTO(0.3)	33.08 ± 0.13
(b) Breit Frame (High Q^2 DIS)		
Current region	ZEUS 96-00	$20.67 \pm 0.71^{+0.66}_{-0.63}$
	ARIADNE(0.3)	20.58 ± 0.19
	ARIADNE(0.22)	19.30 ± 0.19
	LEPTO(0.3)	19.99 ± 0.18
Target region	ZEUS 96-00	$45.03 \pm 0.79^{+2.54}_{-2.55}$
	ARIADNE(0.3)	39.86 ± 0.20
	ARIADNE(0.22)	37.43 ± 0.21
	LEPTO(0.3)	39.11 ± 0.18

Table 7.4: The average Λ to K^0_S production ratio. Theoretical predictions from MC models are presented as well. Table (b) shows the results obtained in the current and target regions of the Breit frame. Both statistical and systematic uncertainties are shown for the data.

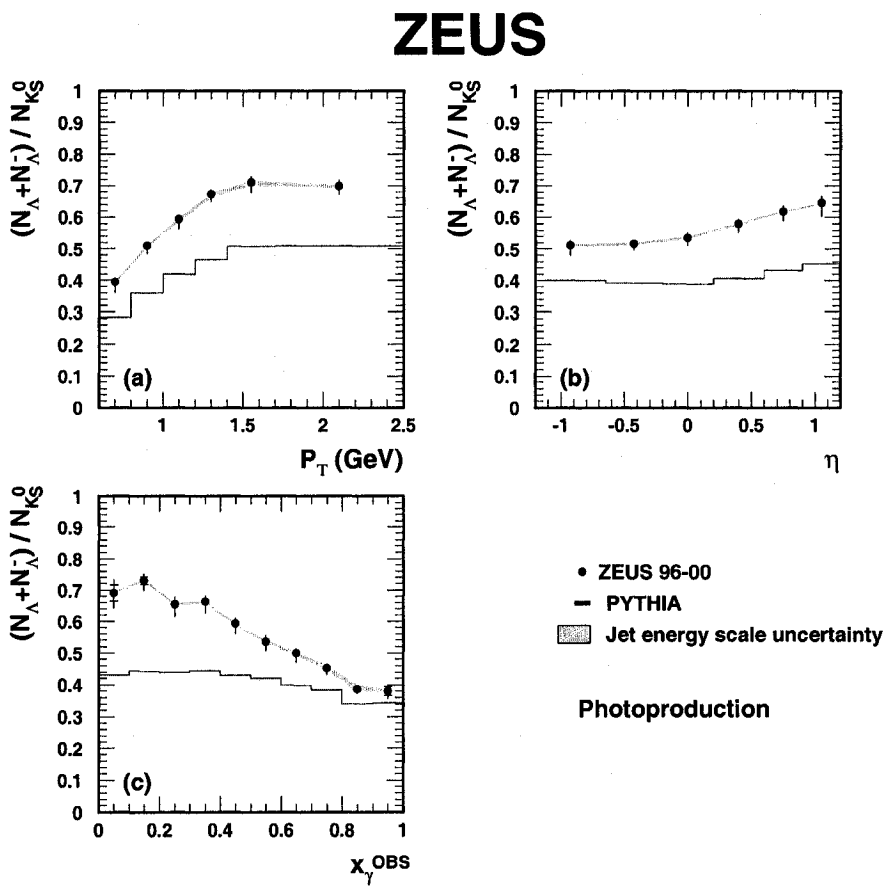

Figure 7.18: The ratio $\frac{N_\Lambda+N_{\bar\Lambda}}{N_{K^0_S}}$ as a function of p_T, η and x_γ^{OBS} for the photoproduction events. Statistical errors (inner error bars) and the systematic uncertainties (outer error bars) added in quadrature are shown. The solid histogram shows the prediction from PYTHIA with a strangeness suppression factor of 0.3.

7.4.1 Photoproduction Events

The Λ to K^0_S ratio has been measured as a function of p_T, η and x_γ^{OBS} for photoproduction events in the laboratory system. The result is given in Figure 7.18. A clear enhancement of the ratio $\mathcal{R}$ was found in the data over the PYTHIA prediction. Figures 7.18(a) and (b) show that the excess of the ratio $\mathcal{R}$ in the data covers the full kinematic regions of p_T and η. The main discrepancy between the data and the MC prediction takes place in the lower x_γ^{OBS} region, shown in Figure 7.18(c), which is dominated by the resolved photoproduction. In the lowest x_γ^{OBS} region, the PYTHIA MC predicts $\mathcal{R}$ to be around 0.45 while the measured $\mathcal{R}$ value from the data is up to 0.7.

In order to investigate this effect further, a division of the whole photoproduction sample was made. As what was discussed in Section 4.2.5, two topologically different sub-samples are defined, the fireball-enriched sample and fireball-depleted sample. The ratios of Λ to K^0_S for both sub-samples in photoproduction are shown in Figure 7.19. It is found that the large enhancement of $\mathcal{R}$ in the data over PYTHIA was observed mainly in the fireball-enriched region. The PYTHIA MC reproduces the $\mathcal{R}$ distribution reasonably well for the fireball-depleted events.

The RHIC experiment [93] has also reported a large enhancement of baryon to meson ratio in a moderate p_{T} region. The cause of this effect is still under debate. One possible interpretation is to consider a 3-dimensional evolution of the created partons. The overlap of the parton wave functions in highly dense phase space at RHIC is assumed to be much larger than the 1-dimension evolution of partons which is the case for e^+e^-, or ep DIS. The correlations between different parton originating jets could play an important role in the enhancement of the Λ to K^0_S ratio. Since the multiple interaction mechanism introduced into PYTHIA creates only 'independent' partons which fragment locally, the contribution from correlations between different partons is therefore not included. Thus a smaller $\mathcal{R}$ value could be expected in PYTHIA compared to the data.

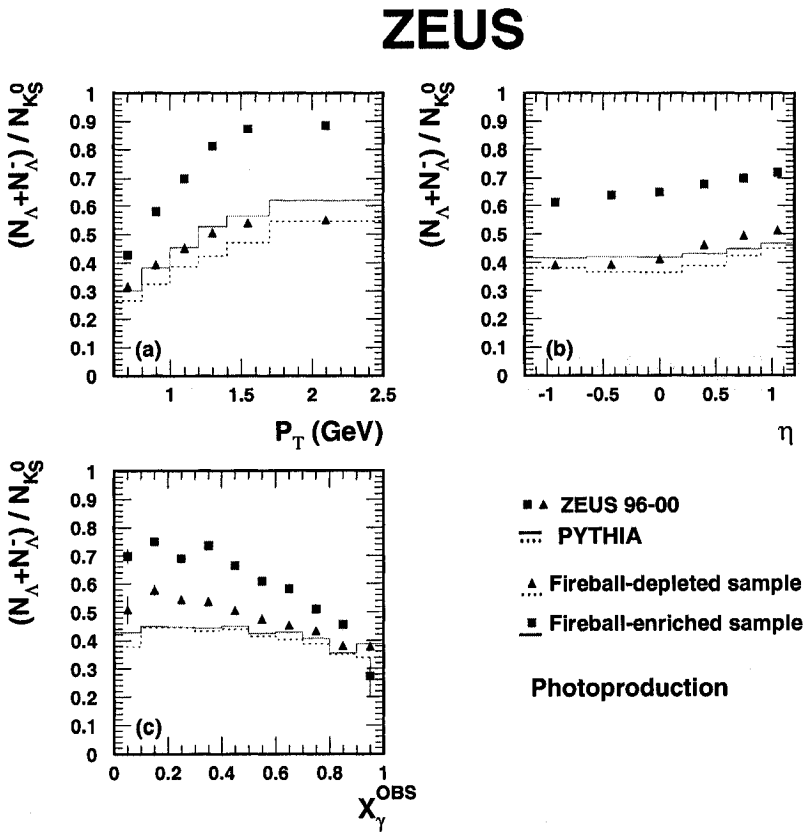

Figure 7.19: The ratio $\frac{N_\Lambda+N_{\bar{\Lambda}}}{N_{K^0_S}}$ as a function of p_T, η and x_γ^{OBS} in the fireball-enriched and fireball-depleted sub-samples in the photoproduction process. Statistical errors (inner error bars) and the systematic uncertainties (outer error bars) added in quadrature are shown. Two histograms show the prediction from PYTHIA with a strangeness suppression factor of 0.3.

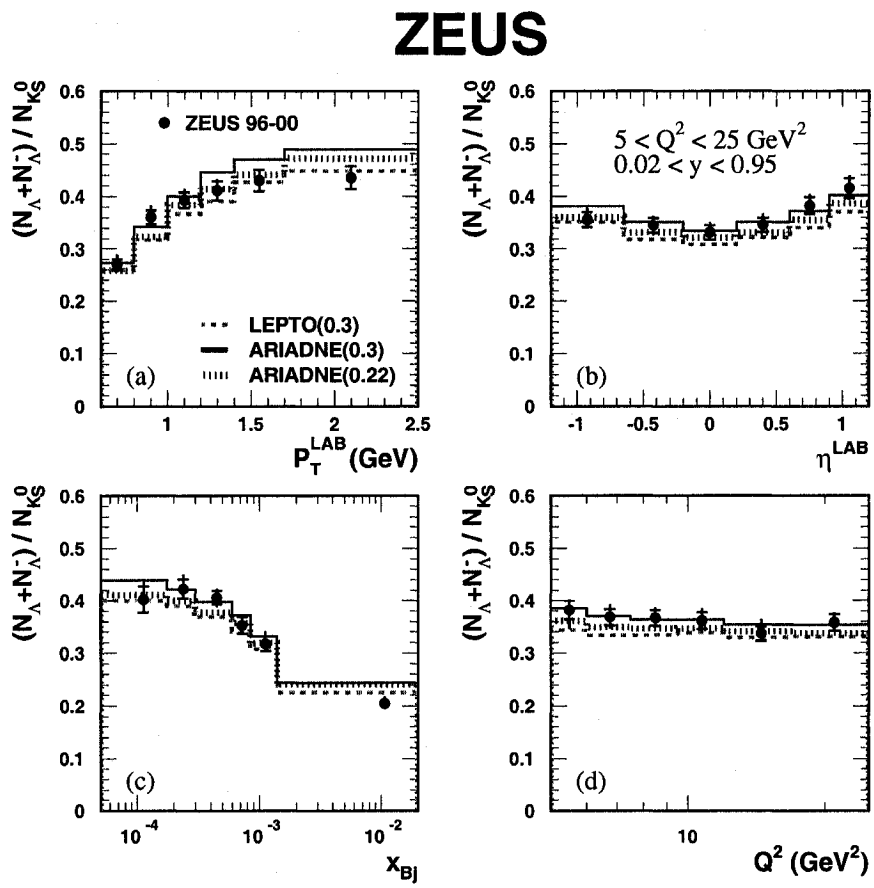

Figure 7.20: The ratio $\frac{N_\Lambda + N_{\bar{\Lambda}}}{N_{K^0_S}}$ as a function of $P_{\mathrm{T}}^{\mathrm{LAB}}$, η^{LAB}, x_{Bj} and Q^2 in the laboratory frame for low Q^2 DIS events. Statistical errors (inner error bars) and the systematic uncertainties (outer error bars) added in quadrature are shown. The MC predictions are shown as lines.

7.4.2 Low Q^2 DIS Events

Figure 7.20 shows the $\mathcal{R}$ distributions as a function of $P_{\mathrm{T}}^{\mathrm{LAB}}$, η^{LAB}, x_{Bj} and Q^2 in the laboratory frame for the low Q^2 DIS events. There is usually a fair agreement in $\mathcal{R}$ when comparing the data with ARIADNE(0.3) prediction. The other two MC models ARIADNE(0.22) and LEPTO(0.3) give a slightly poorer prediction of the ratio $\mathcal{R}$, but they all reproduce well the shape of the $\mathcal{R}$ distributions. Figure 7.20(d) shows an almost independent $\mathcal{R}$ distribution as a function of Q^2, all coming to a nearly constant value of 0.36 for the data.

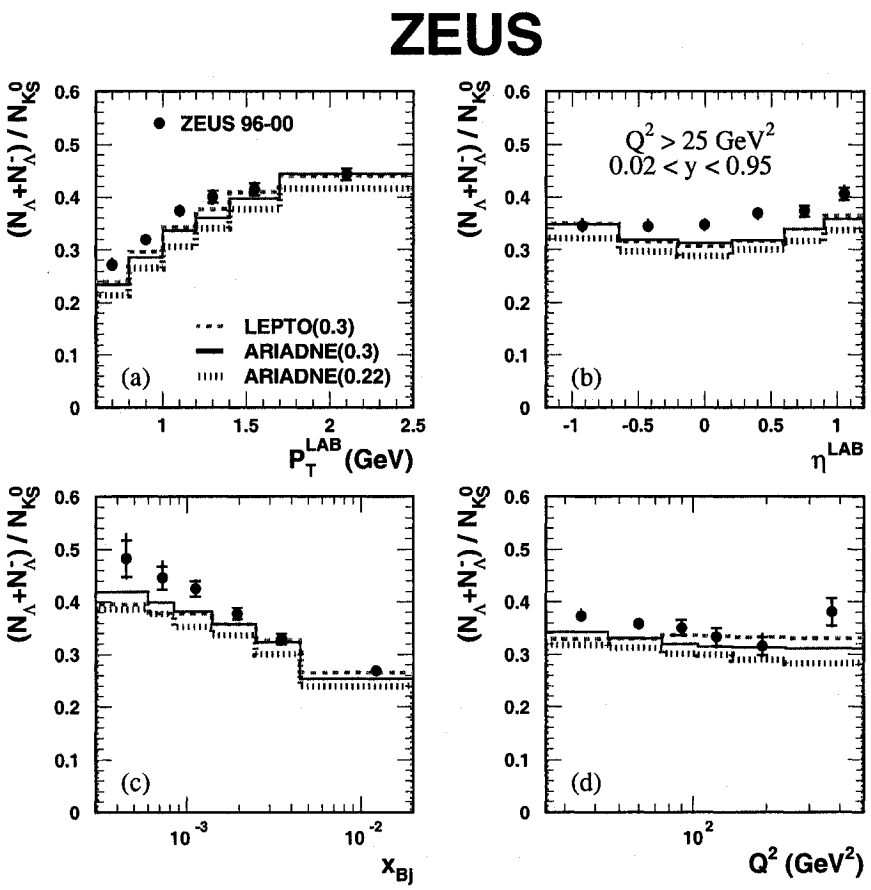

Figure 7.21: The ratio $\frac{N_\Lambda+N_{\bar\Lambda}}{N_{K^0_S}}$ as a function of P_T^{LAB}, η^{LAB}, x_{Bj} and Q^2 in the laboratory frame for high Q^2 DIS events. Statistical errors (inner error bars) and the systematic uncertainties (outer error bars) added in quadrature are shown. The MC predictions are shown as lines.

7.4.3 High Q^2 DIS Events

Figure 7.21 shows the $\mathcal{R}$ distribution as a function of P_T^{LAB}, η^{LAB}, x_{Bj} and Q^2 in the laboratory frame for the high Q^2 DIS events. It is reminded that ARIADNE(0.3) overestimates the K^0_S cross section in the lower p_T region, as shown in Figure 7.7(a), but reproduces fairly well the Λ production in the similar p_T region, as seen in Figure 7.6(a). As a result, the measured $\mathcal{R}$ was underestimated by the ARIADNE(0.3) MC in the same region, as shown in Figure 7.21(a). In Figure 7.21(b), the ratio $\mathcal{R}$ in data has a tendency to increase as η^{LAB} moves to a more forward region, whereas MC's are a bit more symmetric around $\eta^{LAB} = 0$. The $\mathcal{R}$ distribution as a function

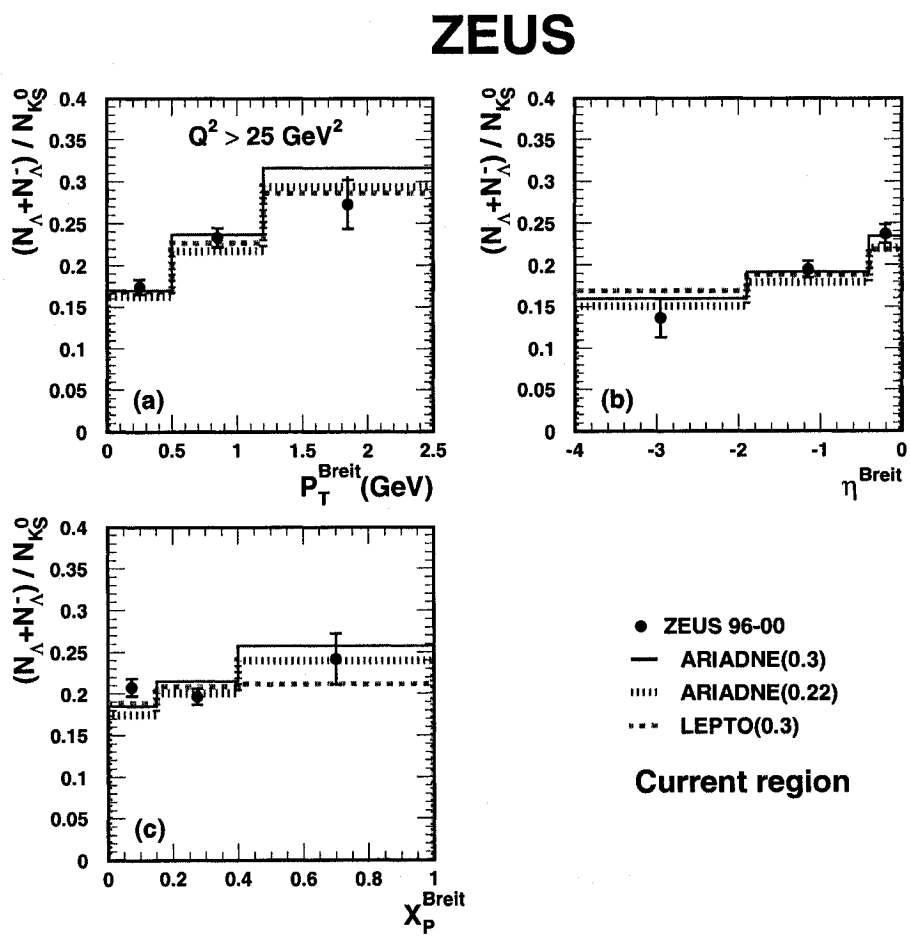

Figure 7.22: The ratio $\frac{N_\Lambda+N_{\bar{\Lambda}}}{N_{K^0_S}}$ in the current region of the Breit frame. Statistical errors (inner error bars) and the systematic uncertainties (outer error bars) added in quadrature are shown.

of x_{Bj} is shown in Figure 7.21(c), where a steep rise of the ratio $\mathcal{R}$ is observed as x_{Bj} decreases. At the smallest x_{Bj}, it is almost half as likely to get a baryon as a meson. ARIADNE(0.3) underestimates this ratio in the lower x_{Bj} region, although the same trend is present. The ratio $\mathcal{R}$ as a function of Q^2 is not perfectly described by all MC's.

Further studies have been also performed in the Breit frame for high Q^2 DIS events. The $\mathcal{R}$ distributions as a function of $P_{\mathrm{T}}^{\mathrm{Breit}}$, η^{Breit} and $x_{\mathrm{P}}^{\mathrm{Breit}}$ for events in the current region and target region are shown in Figures 7.22 and 7.23, respectively. In the case of the current region, shown in Figure 7.22, a reasonable agreement on $\mathcal{R}$ between MC predictions and data is found. Generally, no specific MC stands out

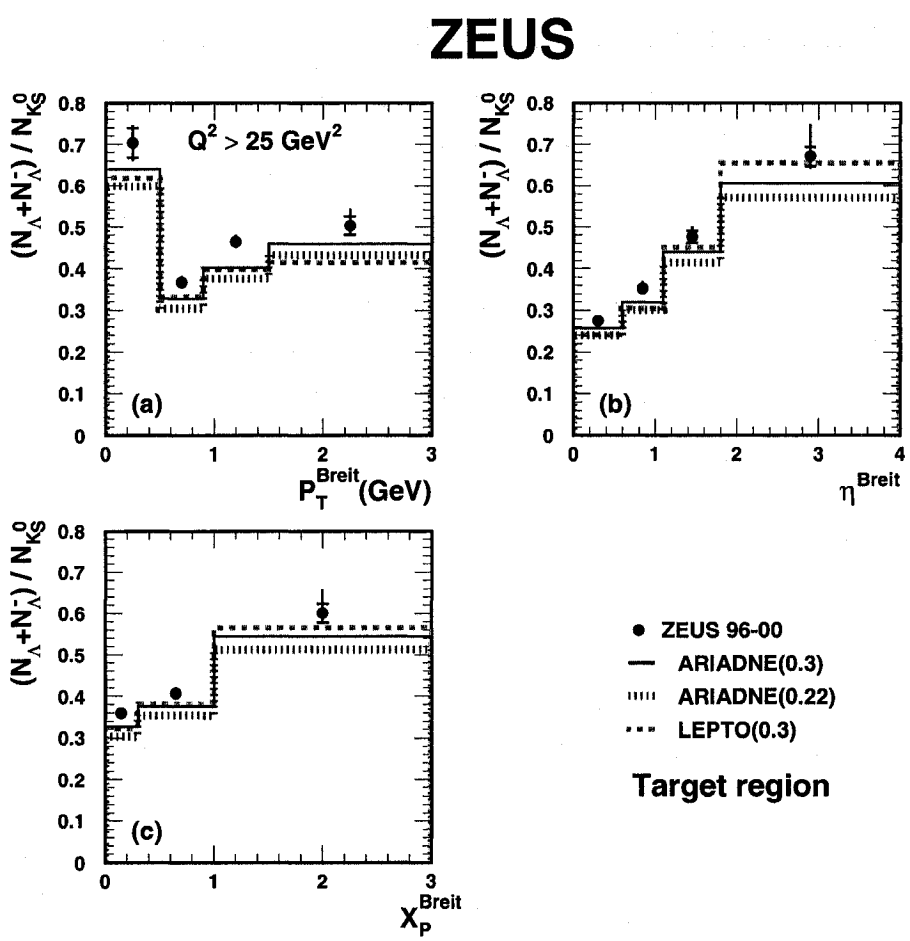

Figure 7.23: The ratio $\frac{N_\Lambda+N_{\bar\Lambda}}{N_{K^0_S}}$ in the target region of the Breit frame. Statistical errors (inner error bars) and the systematic uncertainties (outer error bars) added in quadrature are shown.

preferably by itself when comparing the predictions to the data. As to the target region, seen in Figure 7.23, an overall excess of $\mathcal{R}$ in the data over MC predictions was observed. None of the three MC's can reproduce this enhancement well.

In Figure 7.23(a), a steep rise of $\mathcal{R}$ value happens in the lowest P_T^{Breit} bin in both MC and the data. The reason for this rise is the cuts used in the laboratory frame. Studies on the effects of P_T^{LAB} and η^{LAB} cuts on the ratio $\mathcal{R}$ in the target region as presented in Figure 7.24. The P_T^{LAB} and η^{LAB} cuts effects are illustrated via MC studies. It was found that the $P_T^{LAB} > 0.6$ GeV cut, shown in Figure 7.24(b), gives rise to the significant $\mathcal{R}$ increase of the first P_T^{Breit} bin. Because of the asymmetric beam energies at HERA, the low p_T events in the laboratory frame

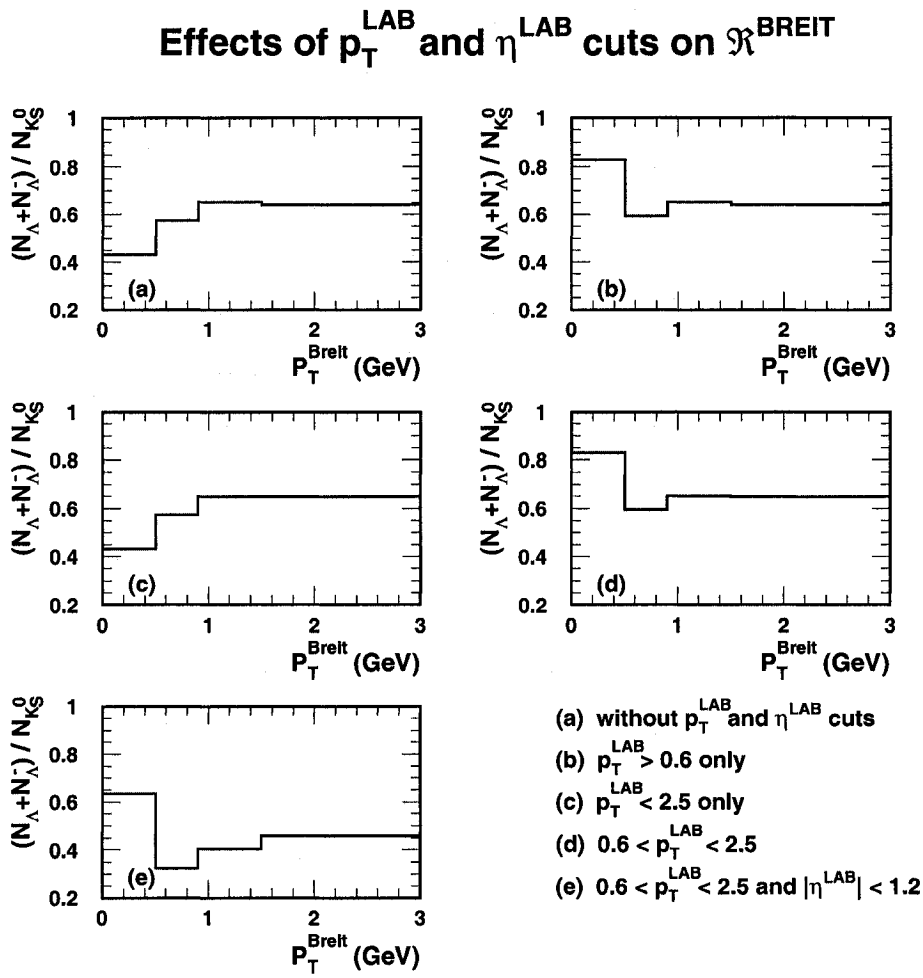

Figure 7.24: The effect of P_T^{LAB} and η^{LAB} cuts on the ratio $\frac{N_\Lambda+N_{\bar\Lambda}}{N_{K^0_S}}$ in the target region of the Breit frame. This is a MC based study.

should correspond to the low p_T events in the target region of the Breit frame. Therefore the p_T distribution in the target region, especially in low p_T region, should be especially sensitive to the p_T cut applied in the laboratory frame.

From Chapter 4, it is known that the Bjorken scaling variable, x_{Bj}, and the four-momentum-transfer squared of the exchange boson, Q^2, are correlated to each other. In order to investigate how $\mathcal{R}$ behaves for each independently, we divide x_{Bj} into four fixed bins while studying the $\mathcal{R}$ distribution as a function of Q^2. It is noted that the event sample here is the combined set of low and high Q^2 DIS events, hence corresponding to events with $Q^2 > 5\,GeV^2$.

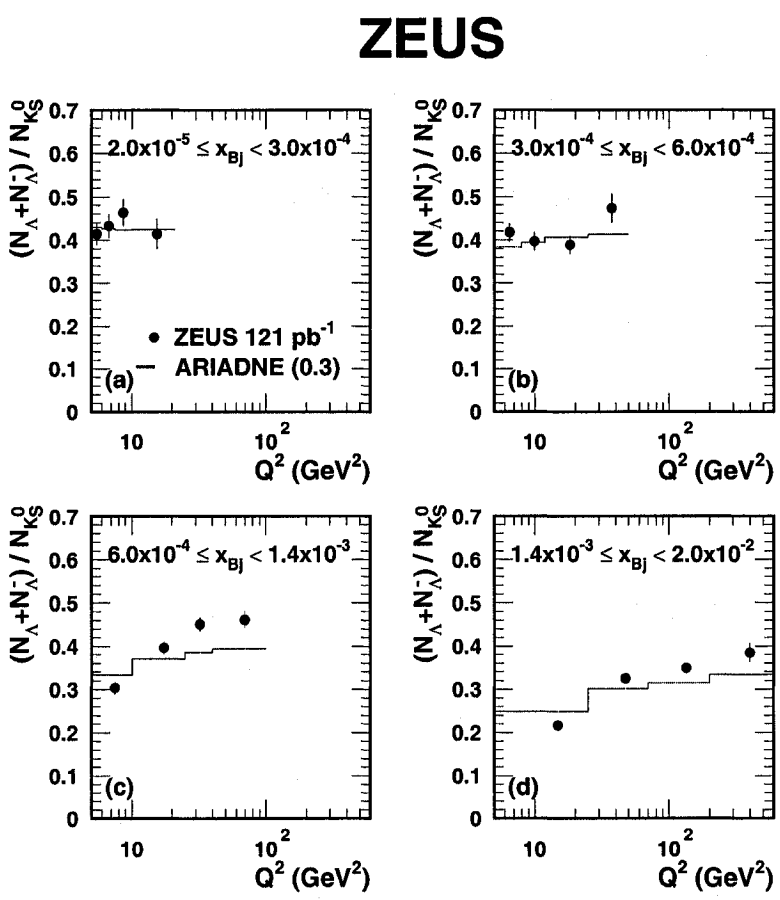

Figure 7.25: The ratio $\frac{N_\Lambda+N_{\bar\Lambda}}{N_{K^0_S}}$ as a function of Q^2 for four bins of x_{Bj}, in the range $0.6 < p_T^{LAB} < 2.5$ GeV and $|\eta^{LAB}| < 1.2$ for events with $Q^2 > 5$ GeV^2 and $0.02 < y < 0.95$. Statistical errors only are shown. The histograms all in four figures represent predictions from ARIADNE with a strangeness suppression factor of 0.3.

Figure 7.25 shows the ratio $\mathcal{R}$ as a function of Q^2 for four fixed bins of x_{Bj}. These four bins are $2.0 \times 10^{-5} \le x_{Bj} < 3.0 \times 10^{-4}$, $3.0 \times 10^{-4} \le x_{Bj} < 6.0 \times 10^{-4}$, $6.0 \times 10^{-4} \le x_{Bj} < 1.4 \times 10^{-3}$ and $1.4 \times 10^{-3} \le x_{Bj} < 2.0 \times 10^{-2}$. Figures 7.25(a) and (b) show the low x_{Bj} and low Q^2 DIS events, which display an almost constant $\mathcal{R}$ value above 0.4. ARIADNE(0.3) describes the data reasonably well there. In the case of Figures 7.25(c) and (d) which are corresponding to a higher x_{Bj} DIS region, the increasing tendency of $\mathcal{R}$ can be clearly seen with increasing Q^2. But the description of the data by MC becomes poorer.

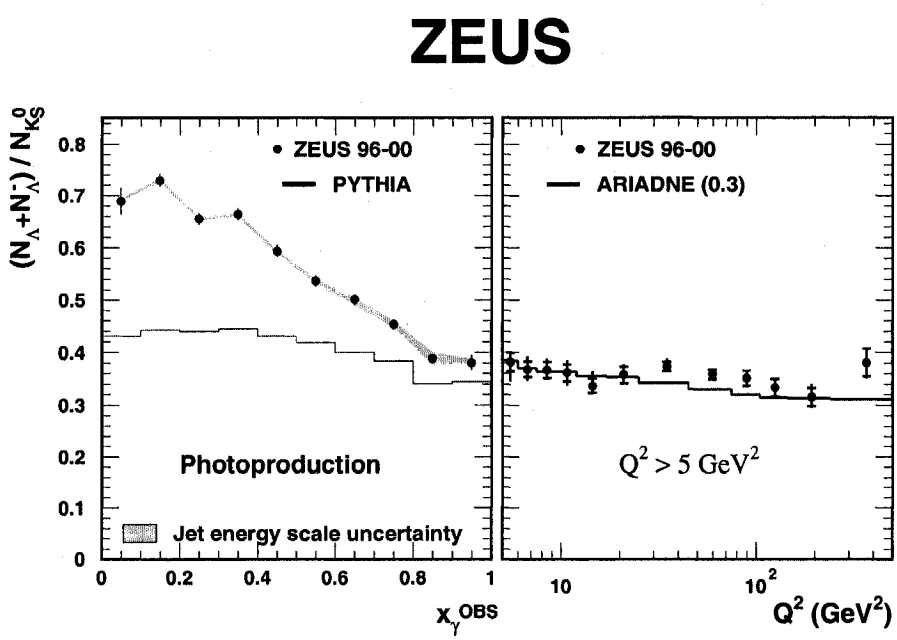

Figure 7.26: The ratio $\frac{N_\Lambda+N_{\bar{\Lambda}}}{N_{K^0_S}}$ as a function of x_γ^{OBS} for the photoproduction events (left) and as a function of Q^2 for events with $Q^2 > 5$ GeV^2 (right).

An overall view of how $\mathcal{R}$ develops with Q^2 can be obtained by combining Figures 7.20(d) and 7.21(d). Together with the ratio $\mathcal{R}$ in photoproduction, an extrapolation of $\mathcal{R}$ in the missing Q^2 interval of $1 < Q^2 < 5$ GeV^2 can be obtained, as seen below.

Figure 7.26 gives a hint of how the ratio $\mathcal{R}$ evolves in both the photoproduction and DIS processes. Since the photoproduction events were selected with $Q^2 < 1$ GeV^2 and the lowest Q^2 value for DIS events which this thesis can reach is 5 GeV^2. Therefore a gap of Q^2 region from 1 to 5 GeV^2 is left undetermined. The photon in the direct photoproduction ($x_\gamma^{\mathrm{OBS}} > 0.75$) process is considered to be point-like, similar to the one in the DIS case, but only at a smaller Q^2 value. Therefore it could be reasonable to consider the last point in Figure 7.26(left) corresponding to the end point $Q^2 = 1$ GeV^2 of the DIS events. Based on this assumption, a flat distribution of $\mathcal{R}$ as a function of Q^2 in the interval of 1 to 5 GeV^2 is expected, between 0.35 to 0.4.

Chapter 8

Results II: Correlations and Polarizations

In this chapter the second part of the results which include Bose-Einstein correlations, rapidity correlations and Λ polarizations are presented. Each result is followed up by discussions and comparisons with the MC predictions or the results from other experiments.

The Λ polarization measurements have been carried out in three different kinematic regimes available at HERA in the laboratory reference system, photoproduction, low Q^2 DIS and high Q^2 DIS regions. A natural extension of the polarization measurements into the Breit frame was also performed for the high Q^2 DIS events. The same cuts as those in the previous chapter were applied to select strange hadrons: the transverse momentum and pseudorapidity of the reconstructed strange hadrons were constrained by $0.6 < p_{\mathrm{T}} < 2.5$ GeV and $|\eta| < 1.2$.

Concerning the correlation measurements, larger statistics are preferred so that the corresponding analyses were done only for the photoproduction events. In addition, the selection criteria on strange hadrons are a little different from that for polarization studies. Alternatively, the p_{T} and η, for the correlation measurements, were loosely restricted to be $0.3 < p_T < 5.0$ GeV and $|\eta| < 1.5$ in order to obtain an event sample with larger statistics. Study showed that these looser cuts lead to 40% more $\Lambda\Lambda$ pair production events.

8.1 Bose-Einstein Correlation (BEC)

The Bose-Einstein (BE) effect describes the phenomenon of the enhanced production of identical bosons, having similar momenta, relative to the single particle production spectrum. This effect was observed for the first time by Goldhaber et. al. [94, 95] in $p\bar{p}$ annihilation. The underlying physics attributed to this enhancement is the Bose-Einstein statistics for a multi-boson system. When multiple bosons are emitted closely in phase space, their symmetric wavefunctions will result in a coincident spectrum. It is the interference of wavefunctions that gives rise to the enhancement observed in the production spectrum. In this way the statistical observation of the enhancement of particle pair production connects information of the pair production dynamics in phase space. Therefore the BEC measurement can be utilized as a tool to study the space-time structure of the particle emission source (emitter).

Preliminary results on $K^0_S K^0_S$ BEC measurement in DIS have been presented at several conferences (e.g. [96] and [97]) from ZEUS. By comparing the BEC results in different Q^2 kinematic regions, a check of the Q^2 dependence of the BEC is allowed. Furthermore, a hierarchy in the size of the emitter, 'r', was suggested from the results in LEP experiments [105], $r(m_\pi) > r(m_K) > r(m_p) > r(m_\Lambda)$. But in this hierarchy, the worst disagreement with the prediction is from the kaon BEC measurement. The kaon BEC result from this thesis, therefore, offers one more experimental data set to check the r dependence on the hadron mass.

In this thesis, the BEC between double K^0_S production was studied for the first time in photoproduction at HERA. Furthermore, the Fermi-Dirac correlation (FDC) for double $\Lambda(\bar{\Lambda})$ production, motivated by the Pauli exclusion principle, was studied as well. But due to limited statistics, no clear Fermi-Dirac effect was observed and therefore it is omitted from this thesis. In the theory [99], the correlation function is defined as follows,

$$R(p_1, p_2) = \frac{\rho(p_1, p_2)}{\rho(p_1)\rho(p_2)} = 1 + |f(p_1 - p_2)|^2 \tag{8.1}$$

where $\rho(p_1)$ and $\rho(p_2)$, the reference distributions in the absence of the BEC, are the single particle density distribution functions for particle 1 and 2 respectively, and $\rho(p_1, p_2)$ represents the particle pair density distribution function. The $f(p_1 - p_2)$ is the Fourier transform of the space-time density distribution of the emitter

in terms of the four-momentum difference of the particle pair, $p_1 - p_2$. In BEC studies, it is customary to make use of the Lorentz invariant variables to replace the four-momentum difference of the particle pair, $Q_{12}^2 = -(p_1 - p_2)^2 \equiv M^2 - 4\mu^2$. Here M is the invariant mass of the pair of two identical particles, each of which has a mass μ. Assuming that the emitter obeys a spherically symmetric Gaussian density distribution, the correlation function can then be parameterized by a standard Goldhaber-like function [100, 101],

$$R(Q_{12}) = \alpha(1 + \delta Q_{12})(1 + \lambda e^{-Q_{12}^2 r^2}), \tag{8.2}$$

where the quantity λ is the coherence strength factor which is zero for a coherent emitter and one for an incoherent source. The parameter r is the radius of the emission source. The factor α is the normalization constant and δ characterizes the possible long-range correlations.

Experimentally, the normalized distribution $\rho(Q_{12}) = 1/N \cdot dn/dQ_{12}$ is used to calculate the particle pair density distribution, where N is the number of total particle pairs and n is the number of particle pairs in a Q_{12} bin. The multiplication of single particle density $\rho(p_1)\rho(p_2)$ in Equation 8.1 is difficult to assess, however. Generally an alternative approach is taken instead of the direct calculation of it. In this thesis, a so-called mixed event (mix) technique is adopted: a normalized distribution $\rho_{mix}(Q_{12})$ for a particle pair is calculated in the way of $\rho(Q_{12})$, but the only difference is that the paired particles are from different events rather than in the same event. The $\rho_{mix}(Q_{12})$ calculated this way ensures the absence of BEC for the selected particle pair and is then used to replace $\rho(p_1)\rho(p_2)$ as the reference distribution. To reduce the non-BE effects and the long range correlations further, a MC sample was generated without BE effects and used as a further reference. Finally the BEC is determined by the so-called double ratio method

$$R(Q_{12}) = \frac{R^{data}(Q_{12})}{R^{MC}(Q_{12})} = \frac{\rho^{data}(Q_{12})}{\rho_{mix}^{data}(Q_{12})} \Big/ \frac{\rho^{MC,noBEC}(Q_{12})}{\rho_{mix}^{MC,noBEC}(Q_{12})} \tag{8.3}$$

The result on $K_S^0 K_S^0$ BEC is given in Figure 8.1, together with a Goldhaber function fit on the data distribution, according to Equation 8.2. The extracted parameters from the fit are

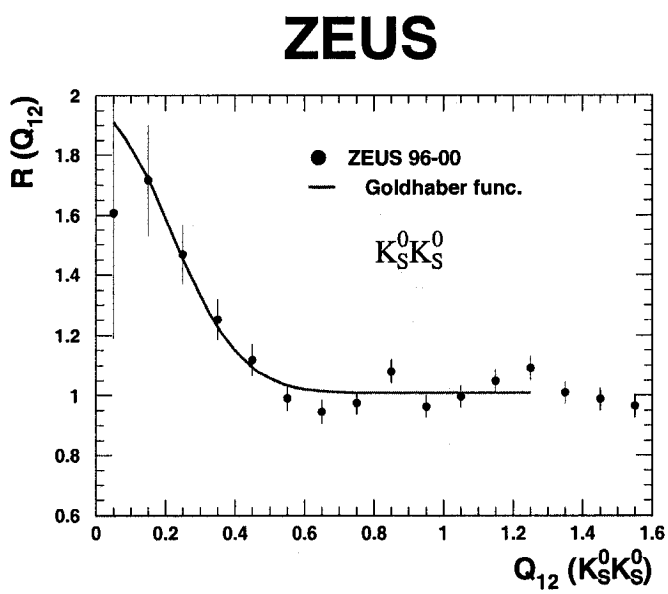

Figure 8.1: The measured BE correlation as a function of momentum difference of K_S^0 pairs, together with a Goldhaber function fit. The error bars show the statistical uncertainties.

$$r = 0.68 \pm 0.06\,(stat.)\ fm \tag{8.4}$$

$$\lambda = 0.92 \pm 0.19\,(stat.) \tag{8.5}$$

The above results extracted in photoproduction are in good agreement with the ZEUS preliminary results in DIS [96], but with an improvement on accuracy. In [96], the radius $r = 0.61 \pm 0.08(stat.)^{+0.07}_{-0.08}(syst.)\ fm$ and correlation strength $\lambda = 1.16 \pm 0.29(stat.)^{+0.28}_{-0.08}(syst.)$ were reported. The systematic uncertainties in this thesis are thus expected to have the same order of magnitude as for the previous measurement.

The consistency of the two results confirms that the BEC is insensitive to Q^2, one of the conclusions also made in the previous ZEUS publication on pion BEC study [98]. The independence of BEC on Q^2 agrees with the hypothesis in the LUND string model in which the region where BEC takes place is assumed to be determined exclusively in the fragmentation stage of the process.

Figure 8.2 shows the comparison between the result obtained in this thesis and the ones from similar studies in ZEUS [96, 98] and LEP experiments [102, 103, 104].

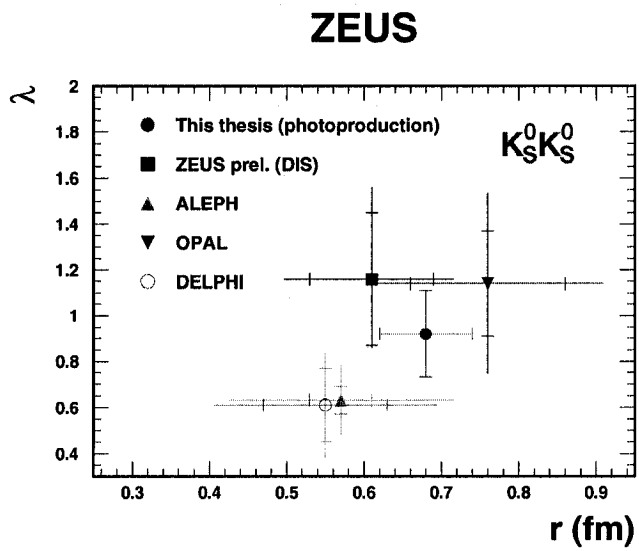

Figure 8.2: A comparison of the BEC results extracted from the $K^0_S K^0_S$ studies. Statistical errors (inner error bars) and the systematic uncertainties (outer error bars) added in quadrature are shown.

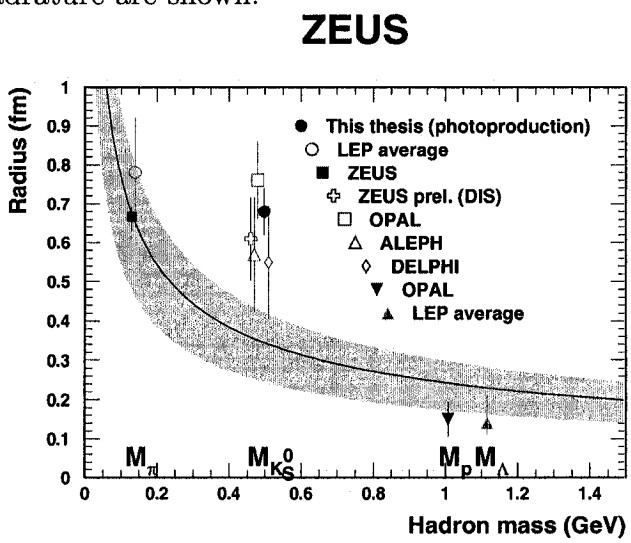

Figure 8.3: The emitter radius r as a function of hadron mass m. The result obtained in this thesis is shown together with the other results from ZEUS and LEP experiments. For clarity, the symbol positions of the hadrons were displaced slightly from the mass values. The solid line represents the expectation from the Heisenberg uncertainty relations with $\Delta t = 10^{-24}$ seconds, and the bands corresponds to the expected region between $\Delta t = 1.5 \times 10^{-24}$ (upper limit) and $\Delta t = 0.5 \times 10^{-24}$ (lower limit) seconds.

All r values are in a good agreement within errors. The discrepancy between the correlation strength λ's, however, can be seen, although most of them are consistent with each other within uncertainties. The reason for this discrepancy may be the different treatments of the influence from the resonance $f_0(980)$ decay. In the ALEPH and DELPHI measurements the effect from $f_0(980)$ resonance is excluded so that a smaller λ value was obtained compared to that from other experiments where the influence is in. But all the results in the latter case are in a good agreement.

The dependence of radius on hadron mass has been explored in this thesis. Together with results obtained from other experiments [103, 104, 102], the dependence is depicted in Figure 8.3. In this figure, the radius behavior as a function of mass is described by four sets of hadrons: pions, kaons, protons and lambdas. Some theoretical considerations have also been made to link the BEC and the Heisenberg uncertainty principle [105], from which a simple relation between radius and mass was predicted as $r(m) = A/\sqrt{m}$. Here $A \equiv c\sqrt{\hbar\Delta t} = 0.243\, fm\, GeV^{\frac{1}{2}}$ wherein c is the velocity of light and Δt takes the time scale of the strong interaction, 10^{-24} seconds. As a comparison with the data, a curve which corresponds to the prediction with $\Delta t = 10^{-24}$ seconds is given in Figure 8.3. The shaded band there refers to the prediction with a Δt region from 1.5×10^{-24} (upper limit) to 0.5×10^{-24} (lower limit) seconds.

In Figure 8.3 the results from kaon BEC measurements show a clear departure from the expected dependence behavior and the large uncertainties do not allow a strong conclusion to be drawn so far. Therefore more accurate BEC measurements, especially on kaons, are needed in order to check this dependence behavior.

8.2 Rapidity Correlation (RC)

In high energy physics, specific hadron production, especially the baryon production, is not well understood and therefore it relies much on phenomenological models like the string and cluster models, as discussed in Chapter 6. In the string model, the hadronization is described by several string break-ups whereby quark-antiquark ($q\bar{q}$) or diquark-antidiquark ($D\bar{D}$) pairs are created at the two ends of each string break-up. Combined with other neighboring quarks or antiquarks by color force, the hadrons are formed. In the case of the cluster model, hadrons are assumed to

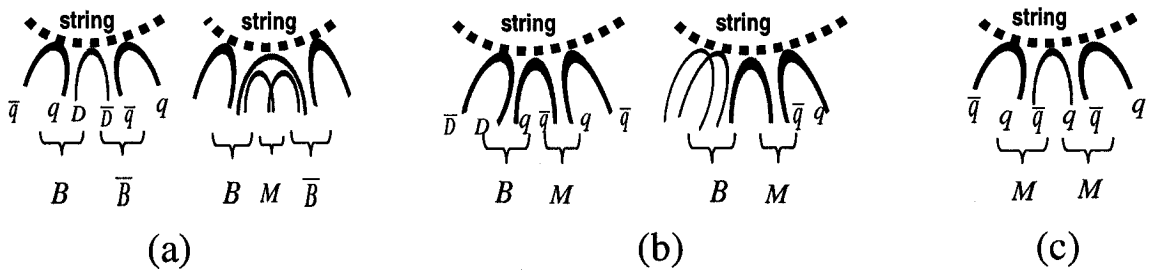

Figure 8.4: An illustration of the particle pair correlations proposed in the string model due to sharing of a common string break-up. The dotted line represents a string and the solid curves describe the development of a $q\bar{q}$ or $D\bar{D}$ pair created at some break-up points in a string. Here q, $\bar{q}$, D, $\bar{D}$, B, $\bar{B}$ and M denote a quark, antiquark, diquark, antidiquark, baryon, antibaryon and meson, respectively. Figure (a) shows the correlation between a baryon-antibaryon pair. The figures (b) and (c) show such correlation for baryon-meson and meson-meson pairs, respectively.

be created from the decay of colorless clusters. The following decays of clusters form hadrons. Concerning the description of hadron production, the string and the cluster models differ in many aspects, though some common features exist. One of these features is the local compensation of quantum numbers between the neighboring created hadrons. These quantum numbers could be electric charge, flavor and baryon number etc. As a consequence of this feature, the hadrons are expected to be produced close in rapidity if they share the same string break-up.

An illustration of the local quantum number conservation during the hadron production process in the string model is shown in Figure 8.4. The two pictures shown in Figure 8.4(a) are for the case of baryon-antibaryon pair production: in the left one, a baryon number compensation exists between the $B\bar{B}$ pair since they share the same string break-up from which a $D\bar{D}$ is produced. The way in which a baryon is produced from a combination of D and q is called direct production. The $B\bar{B}$ pair can also possibly be formed with a meson in between. The corresponding baryon production in this case is called popcorn mechanism [106, 107], as what the right figure represents. The $B\bar{B}$ pair produced according to the popcorn mechanism is less correlated than the pair from direct production, consequently leading to a larger rapidity difference between $B\bar{B}$ than that for direct production. In Figures 8.4(b) and (c), how two particles are possibly correlated is described for a baryon-meson pair and a meson-meson pair, respectively. Similarly, the pairs are correlated because

of the quark flavor compensation.

According to the above discussion above, a production enhancement in the small rapidity difference region is expected for the potentially correlated pairs like $\Lambda\bar{\Lambda}$, $K^0_S K^0_S$ and ΛK^0_S. Here the potentially correlated pairs are those which either the baryon number or at least one quark flavor compensates between two particles of the pair. But it is not the case for other pairs like $\Lambda\Lambda$ and $\bar{\Lambda}\bar{\Lambda}$. Experimentally, the effect due to the local quantum number compensation, if it exists, can be revealed by studying the rapidity correlation of particle pairs. And further detailed studies such as how far the correlation particles can separate and how strong the two particles correlate will lead to a better understanding of the hadron production in the hadronization process.

For the first time, the RC between strange particles was studied in the photoproduction process at HERA in this thesis. The definition of rapidity is

$$y = \frac{1}{2} ln \frac{E + p_Z}{E - p_Z} . \tag{8.6}$$

Here E is the energy of a particle in the laboratory frame and p_Z is the momentum component of the particle parallel to the event momentum direction of the total hadronic system. The rapidity correlation function is determined by taking the ratio of the normalized distribution density (NDD) of the potentially correlated particle pair to the NDD of the particle pair in the reference sample without RC.

$$C(|\Delta y|) = \frac{n(|\Delta y|)/N_{pair}}{[n(|\Delta y|)/N_{pair}]_{mix}} , \tag{8.7}$$

where Δy is the rapidity difference of the paired particles and n/N is the NDD of the pair. Here the numbers are from the detector level. The reference NDD is taken from the mixed (different) events in which the rapidity correlation for particle pairs is absent. To a good approximation, $C(|\Delta y|)$ is defined as a ratio so that the detector effects, uncertainties and efficiencies are canceled out at the first order.

Figure 8.5 shows the NDD for $\Lambda\Lambda + \bar{\Lambda}\bar{\Lambda}$ and $\Lambda\bar{\Lambda}$ pairs for both the data and reference sample (the uncorrelated sample in the data), together with the prediction from PYTHIA. For pairs with a non-zero baryon number ($\Lambda\Lambda + \bar{\Lambda}\bar{\Lambda}$), no difference was observed in the distributions between the data and PYTHIA and the uncorrelated

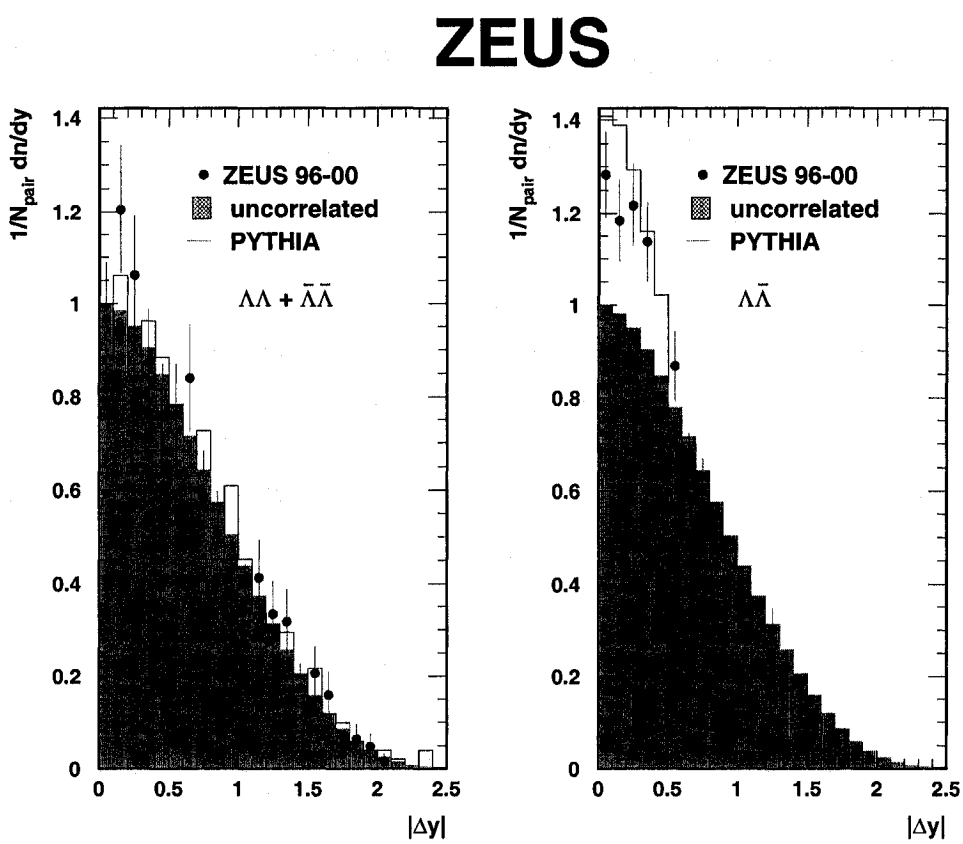

Figure 8.5: The normalized density distributions for $\Lambda\Lambda + \bar{\Lambda}\bar{\Lambda}$ and $\Lambda\bar{\Lambda}$ pairs. The uncorrelated density distribution is from the mixed event sample and the theoretical prediction is from PYTHIA. Only statistical errors are shown.

sample. In contrast, an obvious enhancement of the pair production in the small rapidity difference region is seen for $\Lambda\bar{\Lambda}$ pairs, shown in the right plot of Figure 8.5. The PYTHIA MC has predicted such an enhancement too. Comparing this two cases (left picture and right one), the difference could be easily understood. The local conservation of the baryon number or quark flavor results in the enhancement of $\Lambda\bar{\Lambda}$ pair production at the small rapidity difference region. As to the $\Lambda\Lambda$ and $\bar{\Lambda}\bar{\Lambda}$ production, however, no such quantum numbers compensates.

Figure 8.6 shows the NDD for the baryon-meson pair ΛK^0_S and the meson-meson pair $K^0_S K^0_S$ in the data and reference sample, together with the prediction from PYTHIA. Since the quark flavor could be compensated between Λ and K^0_S production, the PYTHIA predicts an enhancement of ΛK^0_S pair production with a smaller rapidity difference compared to the uncorrelated pairs, as what is shown in Figure 8.6(left).

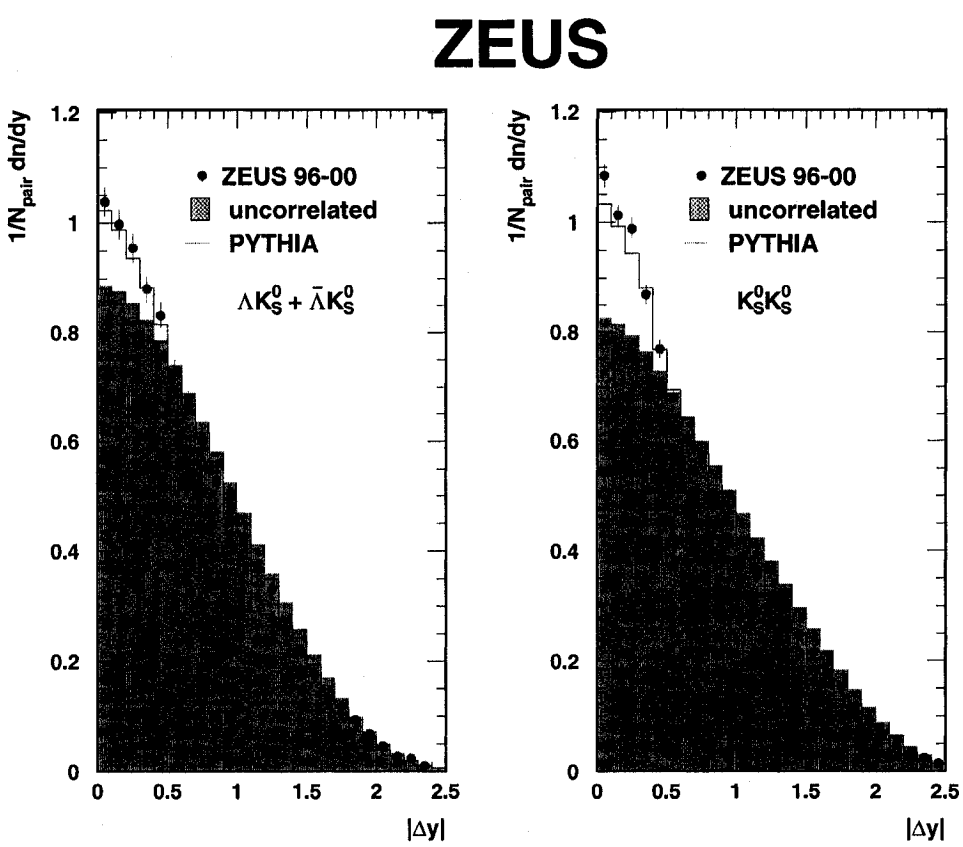

Figure 8.6: The normalized density distributions for ΛK_S^0 and $K_S^0 K_S^0$ pairs. The uncorrelated density distribution is from the mixed event sample and the theoretical prediction is from PYTHIA. Only statistical errors are shown.

In the data, a similar excess over the uncorrelated distribution at the small rapidity difference region is also found, supporting the local conservation of the quantum numbers. In the case of double K_S^0 production in Figure 8.6(right), the same effect occurs. An enhancement production appears in the data and MC in the low $|\Delta y|$ region compared to the distribution of the uncorrelated sample. However it should be noted that the resonances which decay into $K_S^0 K_S^0$ pair might give contributions to this effect too. No attempt was made to evaluate the individual contributions from each side in this thesis.

Taking the ratio of the NDD from the data to the one from the uncorrelated sample, the rapidity correlation as a function of the rapidity difference is obtained and shown in Figure 8.7. Except for the $\Lambda\Lambda + \bar{\Lambda}\bar{\Lambda}$ distribution in Figure 8.7(a), all other three sets of pairs display a feature of a rising $C(|\Delta y|)$ with decreasing

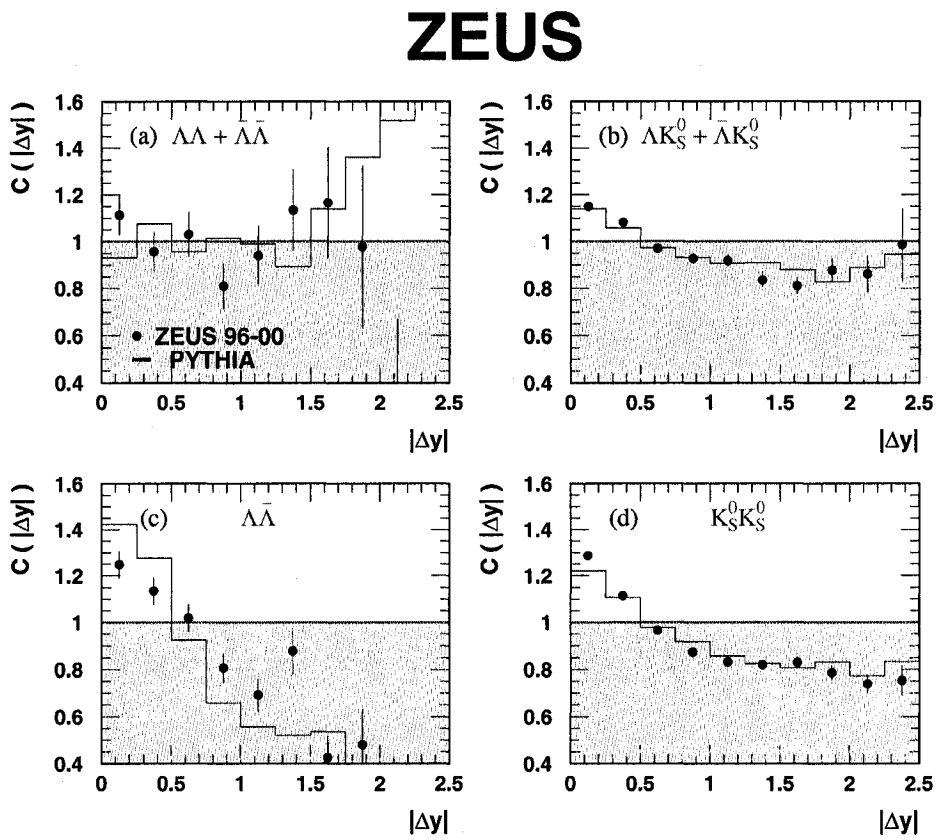

Figure 8.7: Rapidity correlations as a function of the rapidity difference for four sets of particle pairs. The MC prediction from PYTHIA is shown. Only statistic errors are given.

$|\Delta y|$. At somewhere around $|\Delta y| = 0.6 \sim 0.7$, $C(|\Delta y|)$ goes up to a value larger than 1, indicating the start region of the visible correlation effect. In analogy to BEC (Section 8.1), further parameterization of the RC can be assessed with a linear function fit in the lower $|\Delta y|$ region. There might be some other functions which can be used to extract these parameters, but here just for simplification, a first order polynomial function is applied. Also, because the rapidity correlation happens mainly in the lower $|\Delta y|$ region, the fit is only performed in the region $|\Delta y| < 1.0$, therefore the effects due to some possible long-range correlations could be reduced.

An example of the parameter extraction is given in Figure 8.8. The left plot shows the RC of ΛK^0_S pairs and the linear fit to the data. The plot in the right hand shows how the parameters which characterize the RC are extracted. The intercepts of the fit in the x and y coordinate axes are defined as the correlation range, r, and

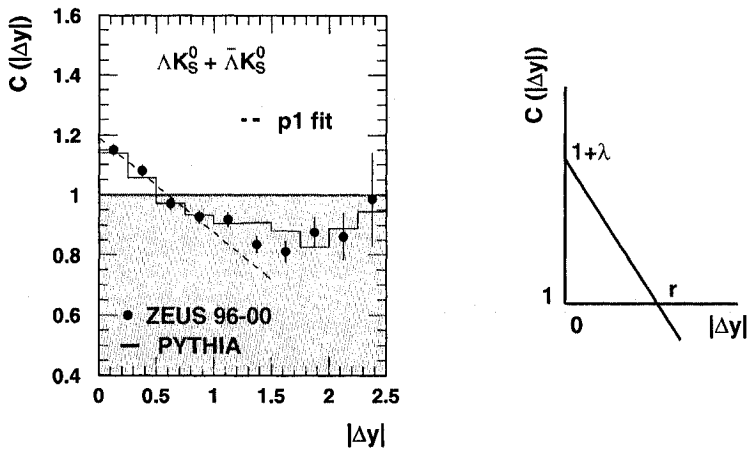

Figure 8.8: An example of the parameter extraction for rapidity correlations. The first order polynomial function was applied to fit the data in the small Δy region $\Delta y < 1.0$. The right plot shows how the x-intercept and y-intercept of the fit correspond to the parameters r and λ respectively.

the correlation strength, λ. The parameter r tells how far the correlated particles can separate from each other in rapidity and the λ is interpreted as the strength of the rapidity correlation existing within the particle pairs. It is noted that the same procedure was applied to the RC from the MC PYTHIA, therefore the values of r and λ from Monte Carlo were also offered for comparison with the data.

The extracted r and λ results for $\Lambda\bar{\Lambda}$, ΛK^0_S and $K^0_S K^0_S$ pairs are shown in Figure 8.9. The predicted values from the PYTHIA MC are also shown. Concerning the extracted r, it is obviously seen that radii, for all pairs in data and PYTHIA, are consistent with each other within the uncertainties. The clear correlation in rapidity takes place in the lower rapidity difference range somewhere below 0.6 and PYTHIA has a good prediction on that. However, λ values differ from each other for different pairs, and the MC predictions on λ are poor. Large λ differences between the data and PYTHIA happen for $\Lambda\Lambda$ and $K^0_S K^0_S$ pairs. Two possible reasons account for the discrepancy. The first one is the inadequate description of single Λ and K^0_S production by the PYTHIA MC in photoproduction, as discussed in Section 7.2, and even more pronounced for the Λ and $\bar{\Lambda}$ production. The second one is the influence of uncounted possible resonances in PYTHIA.

A check on the stability of the results was performed by varying many kinematic cuts used for this analysis. No significant changes on the result was found.

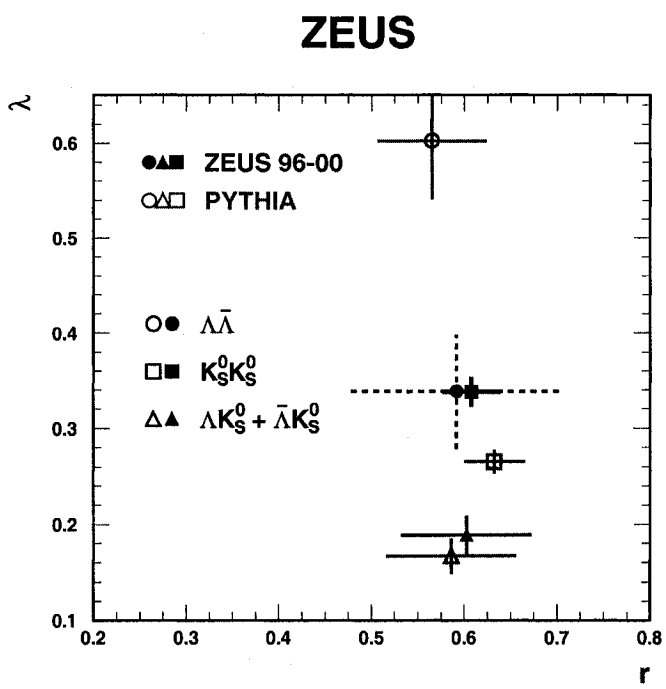

Figure 8.9: The extracted values of the correlation range and strength for three sets of potentially correlated particle pairs. The MC predictions from PYTHIA are shown. Only statistic errors are given.

Further RC studies could be carried on by adding more MC predictions from different models, for example the cluster model. And even more, the popcorn mechanism implemented in the string model could also be checked. By adjusting the parameters relevant to the popcorn mechanism, the optimal values to describe the data could be found and therefore a better understanding on the fragmentation process could be obtained.

8.3 Polarization

The Λ polarization has been investigated previously both experimentally [111] and theoretically [115, 112, 113, 114] since the striking discovery of Λ polarization in inclusive production processes in the 1970s [116, 117]. The interest of the study on Λ polarization is that it offers an easy and effective way to study spin physics. First, the parity violating Λ decay into $p\pi^-$ automatically reveals the Λ polarization through the angular distribution of its decay products. Secondly, in the framework

of the simple quark model, the *ud* diquark in Λ is in a spin and isospin singlet state, leaving the s quark to carry the total spin of Λ hyperon. Therefore the presence of Λ polarization indicates a polarized s-quark in Λ.

The $\Lambda(\bar{\Lambda})$ polarization is derived from the slope of the angular distribution of the positively charged decay product of the $\Lambda(\bar{\Lambda})$ hyperon. If we take the Λ polarization as an example, then the polarization is defined as

$$\frac{dN}{d\Omega} \propto \frac{1}{4\pi}(1 + \alpha P \cos\theta) \tag{8.8}$$

in the Λ rest frame, where $\alpha = 0.642 \pm 0.013$ [51] is the decay asymmetry parameter and P is either the longitudinal ($P_{\parallel}$) or transverse polarization ($P_{\perp}$). If θ is the angle between the decay proton momentum and the Λ momentum, then the measured P is the longitudinal polarization. On the other hand, if θ is the angle between proton momentum and $\vec{n} = \vec{p}_{\text{beam}} \times \vec{p}_{\Lambda}$, where $\vec{p}_{\text{beam}}$ and $\vec{p}_{\Lambda}$ are the momenta of the electron beam and Λ respectively, then the measured P is the transverse polarization. The Λ polarization measurement reported in this thesis was performed in ep collisions, therefore the spin structure of the proton and the quark to hadron fragmentation process in ep collisions are closely related to the measured results.

Similarly, a measurement of K^0_S polarization was performed as well, even though no K^0_S polarization is known or predicted. We provide its results just as a cross check of the analysis procedure and a systematic uncertainty reference for the Λ polarization. The decay product π^+ from K^0_S was considered for the angular distribution.

It is worthwhile to mention that an opposite sign of the polarization could be possible for the same measurement when results are derived from the angular distribution of a different decay product. Since the sign of the polarization is also a key argument of some theoretical predictions, care must be taken in the sign discussions.

The angular distributions of the Λ, $\bar{\Lambda}$ and K^0_S decay particles in the high Q^2 DIS are presented in Figures 8.10 and 8.11 for transverse and longitudinal polarizations respectively. The value of the polarization is determined from a first order polynomial fit of the data. Since the outcomes are similar in the other polarization measurements for photoproduction and in the low Q^2 DIS regions, the other figures need not be presented here.

Averaged over the full kinematic range, the measured results are listed in Table 8.1 for Λ, $\bar{\Lambda}$ and K^0_S in the three kinematic regions: photoproduction, low Q^2 DIS

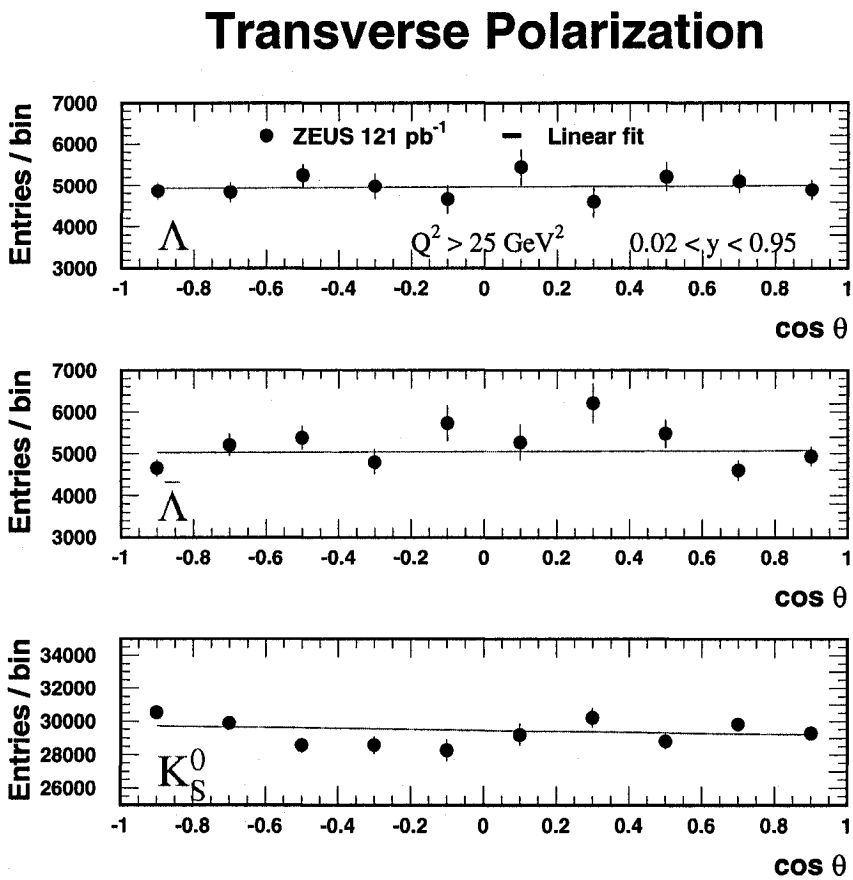

Figure 8.10: Transverse polarization measurement in the high Q^2 DIS region. The figures show the angular distributions of the positively charged decay particle from Λ, $\bar{\Lambda}$ or K^0_S. Statistical errors are shown. The first order polynomial fit (solid line) from which the polarization is obtained is also shown.

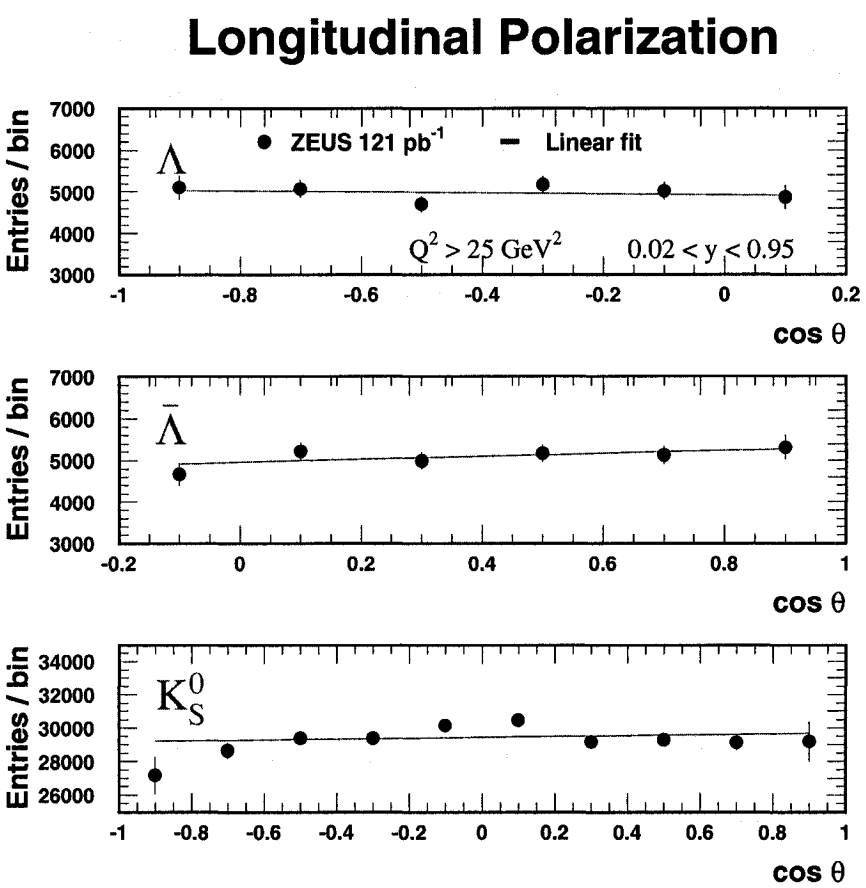

Figure 8.11: Longitudinal polarization measurement in the high Q^2 DIS region. The figures show the angular distributions of the positively charged decay particle from Λ, $\bar{\Lambda}$ or K^0_S. Statistical errors are shown. The first order polynomial fit (solid line) from which the polarization is obtained is also shown.

and high Q^2 DIS processes. The measured Λ and $\bar{\Lambda}$ polarizations, both transverse and longitudinal, are consistent with zero within the resolution of the analyses. The reference polarization of K^0_S was indeed measured to be zero, verifying the procedures of the measurement. Further investigations in the current and target regions of the Breit frame for high Q^2 DIS events, shown in Table 8.2, do not give any significant polarizations either.

All in all, the measured Λ polarizations are consistent with zero and therefore no preferential planes were suggested to exist for Λ production.

To date, the mechanism of the Λ polarization is still not clear. Several theoretical considerations exist attempting to explain the underlying physics. For example,

	photoproduction (%)	$5 < Q^2 < 25$ GeV^2 (%)	$Q^2 > 25$ GeV^2 (%)
$P_\perp^\Lambda$	$-2.0 \pm 2.0^{+6.0}_{-2.0}$	$+1.6 \pm 4.9^{+3.0}_{-4.8}$	$+1.4 \pm 4.3^{+2.7}_{-2.2}$
$P_\parallel^\Lambda$	$-2.7 \pm 4.2^{+9.7}_{-5.3}$	$-10.3 \pm 11.1^{+4.4}_{-13.4}$	$-4.1 \pm 9.3^{+0.1}_{-26.5}$
$P_\perp^{\bar\Lambda}$	$-6.1 \pm 1.9^{+5.6}_{-3.0}$	$-3.3 \pm 5.1^{+0.7}_{-2.3}$	$+0.9 \pm 4.1^{+2.0}_{-5.0}$
$P_\parallel^{\bar\Lambda}$	$+11.1 \pm 4.1^{+12.6}_{-11.7}$	$+32.2 \pm 12.2^{+8.5}_{-19.2}$	$+10.7 \pm 9.5^{+8.0}_{-10.2}$
$P_\perp^{K^0_S}$	$-1.2 \pm 0.7^{+1.5}_{-0.4}$	$-1.9 \pm 1.3^{+0.4}_{-0.8}$	$-1.5 \pm 1.1^{+0.3}_{-0.8}$
$P_\parallel^{K^0_S}$	$+3.7 \pm 1.0^{+1.3}_{-0.7}$	$-3.6 \pm 2.0^{+0.2}_{-0.9}$	$+1.3 \pm 1.6^{+1.3}_{-2.0}$

Table 8.1: The Λ, $\bar\Lambda$ and K^0_S polarizations measured in the three interested kinematic regimes in the Laboratory system. Both statistical and systematic uncertainties are shown for the data.

$Q^2 > 25$ GeV^2	Current region (%)	Target region (%)
$P_\perp^\Lambda$	$+11.8 \pm 11.1^{+5.2}_{-3.2}$	$+2.9 \pm 5.5^{+2.7}_{-3.3}$
$P_\parallel^\Lambda$	$-11.5 \pm 24.5^{+7.9}_{-20.5}$	$-8.8 \pm 11.7^{+19.0}_{-1.7}$
$P_\perp^{\bar\Lambda}$	$+9.3 \pm 10.9^{+5.6}_{-4.3}$	$-5.6 \pm 5.2^{+5.7}_{-3.1}$
$P_\parallel^{\bar\Lambda}$	$+34.3 \pm 26.0^{+27.9}_{-21.2}$	$+25.4 \pm 12.7^{+8.6}_{-13.6}$
$P_\perp^{K^0_S}$	$+0.3 \pm 2.3^{+0.2}_{-0.2}$	$-2.1 \pm 1.7^{+2.2}_{-1.2}$
$P_\parallel^{K^0_S}$	$-0.4 \pm 2.9^{+0.3}_{-0.2}$	$-1.5 \pm 2.2^{+0.5}_{-0.8}$

Table 8.2: The Λ, $\bar\Lambda$ and K^0_S polarizations measured in the Breit system for high Q^2 DIS events. Both statistical and systematic uncertainties are shown for the data.

theoretical models like the DeGrand-Miettinen model [118] assume that the Λ polarization is exclusively due to the spin of the s constituent quark while, on the other hand, others [119, 120] argue that the polarization also contains contributions from the other constituent quarks of Λ and might come from gluons as well. But none of them is decisive or satisfactory enough to interpret all of the data. More information about the theoretical models can be found in [115].

Since there is no intention of discussing all the possibilities from theoretical predictions in this thesis, only the possible s contributions to the Λ polarization is considered and used to understand the results. The s polarization could be related to the Thomas precession effect proposed in the DeGrand-Miettinen model [118] or from the gluon bremsstrahlung or heavy flavor decay in the fragmentation process

suggested in the quark parton model [119]. As discussed in Section 2.5, the dominant contribution to the strange hadron production in this study is the pure fragmentation process. This means that the $s(\bar{s})$ created during this process does not possess a sizable spin polarization. On the other hand, the prevalent contribution from the fragmentation process makes the study on the rest contributions difficult, provided that no separation is made. A Monte Carlo study based on the high Q^2 DIS events shows that the struck $s(\bar{s})$ quark induced $\Lambda(\bar{\Lambda})$ production accounts for at most 15% of the total Λ production on average. According to the DeGrand-Miettinen model, it is this 15% Λ attributed process in which the s-quark polarization and the consequent Λ polarization could happen. Here the argument is that even if it is possible that there is Λ polarization in this 15% Λ's, but it might become too small to be observed in the overall Λ production within the resolution of the study. Or there may be no polarization at all. Further studies are expected to provide a better understanding of the polarization mechanism, for example a study based on larger statistics or with a different set of cuts (extending to forward region or low p_{T} regions) can provide a more sensitive measurement.

The HERA II data provide a source of the spin in the polarized electron beam. The longitudinally polarized electron is expected to transfer its spin, more or less, to the struck quark via the mediator photon and consequently result in a polarization of final hadrons which inherit the spin. Therefore, similar Λ polarization studies can in principle observe the polarization. But the measured polarization might be small because the spin transferred from the initial electron will be diluted in most cases by the large multiplicity of the final hadrons.

Chapter 9

Conclusions and Outlook

The inclusive production of neutral strange particles, Λ, $\bar{\Lambda}$ and K^0_S, has been studied extensively in deep inelastic scattering and photoproduction processes with the ZEUS detector at HERA. The total integrated luminosity used for this thesis is 121 pb^{-1}, which was collected by the ZEUS detector at the HERA running period from 1996 to 2000. Three kinematic regimes are considered: high Q^2 DIS events selected with $Q^2 > 25$ GeV^2 and $0.02 < y < 0.95$; low Q^2 DIS events with $5 < Q^2 < 25$ GeV^2 and $0.02 < y < 0.95$ and photoproduction process ($Q^2 < 1$ GeV^2) where at least two jets are required. For all measurements except the correlation studies, the transverse momentum and pseudorapidity of the selected hadrons were constrained by $0.6 < p_T < 2.5$ GeV and $| \eta | < 1.2$ in the laboratory frame, respectively. In order to accumulate larger statistics, the p_T and η were restricted loosely to be $0.3 < p_T < 5.0$ GeV and $|\eta| < 1.5$ for correlation measurements.

Several individual results have been obtained in this thesis and the conclusion on each of them is given in the following few sections.

9.1 Cross Section Measurements

The total cross sections and the differential cross sections of the strange hadron production at HERA have been measured for both DIS and photoproduction events, and the results were compared with the available Monte Carlo models.

In general, the ARIADNE MC gives a reasonable description of the DIS data, but discrepancies can be clearly seen in the details. The λ_s (strangeness suppression

parameter) influence has been further checked by using two different λ_s values, 0.22 and 0.3, to be compared with the data. The comparisons between the data and Monte Carlos imply that the optimal λ_s depends on the type of strange hadrons and the selected kinematic regions. This conclusion agrees with the observation from [14]. Correspondingly, more than one parameters are suggested to be tuned together in order to reproduce the data better. The LEPTO MC fails to predict the data.

The extended cross section measurements in the Breit frame for high Q^2 DIS events show that the strange hadrons are mainly produced in the target region, where the proton remnant fragmentation is expected to be dominant. The production in the target region are estimated to be approximately 80% and 66% of the whole production for Λ and K^0_S, respectively.

The PYTHIA MC, generated with the multiple interaction mechanism [54], was used to describe the photoproduction data. The strange particle cross sections as a function of x_γ^{OBS} are not well described by the PYTHIA MC, especially in the low x_γ^{OBS} region. Even though the implementation of the multiple interaction mechanism improves the description of the photoproduction data in the low x_γ^{OBS} region [45], the shortcomings of PYTHIA can be still clearly seen.

9.2 Baryon to Antibaryon Asymmetry

The baryon to antibaryon production asymmetry has been studied by measuring Λ to $\bar{\Lambda}$ asymmetry, $\mathcal{A} = \frac{N_\Lambda - N_{\bar{\Lambda}}}{N_\Lambda + N_{\bar{\Lambda}}}$, in the three selected kinematic regions. In all cases, neither the average nor the differential $\mathcal{A}$ was different from zero asymmetry in the phase spaces of interest. All MC's available have a good prediction on the symmetric strange baryon to antibaryon production.

No asymmetry implies that the baryon number flow from the initial proton hardly affects the strange hadron production in the main detector region at HERA. In another word, it also means that the possible baryon number carrier (or carriers) is considered to pass through the detector without being detected. As a result, Λ and $\bar{\Lambda}$ are assumed to be produced according to the same mechanism.

One kind of possible baryon number carrier is related to the valence quarks in the framework of the Quark Parton Model [7, 8]. The resulting signature of this hypothesis can be an increasing $\mathcal{A}$ with increasing η because of the large asymmetric

momenta of the colliding beams at HERA. Such kind of tendency seems to appear in Figure 7.15(b), even though not significantly. However, later observation in the target region (Figure 7.17) does not confirm the possible larger $\mathcal{A}$ in the region where the proton remnant plays an important role. Therefore no baryon number transfer from the proton beam to strange hadrons via valence quarks was observed in the central detector region.

As previously mentioned in Section 2.6.2, the baryon number can also be described to be associated with the gluon junction instead of the valence quarks in the work of gluon junction mechanism [92]. This mechanism is able to predict the baryon to antibaryon asymmetry measured at RHIC [87]. A dedicated prediction [92] on the baryon to antibaryon production asymmetry at HERA was made according to this mechanism, from which a positive $\mathcal{A}$ of 3.5% was expected at low x. However, the $\mathcal{A}$ observations in this thesis, $+1.85 \pm 1.51^{+0.4}_{-2.7}\%$ in the low Q^2 DIS and $+0.64 \pm 1.31^{+3.01}_{-2.19}\%$ in the high Q^2 DIS, have a total uncertainty of the order of 3%, so these values can not be applied to judge the gluon junction mechanism with sufficient accuracy.

9.3 Baryon to Meson Ratio

The production ratio of strange baryons to mesons, $\mathcal{R} = \frac{N_\Lambda + N_{\bar{\Lambda}}}{N_{K^0_S}}$, has been investigated by studying the relative Λ and K^0_S production yields. The measured ratios were compared to theoretical predictions and to results from other experiments.

The $\mathcal{R}$ values measured in the high and low Q^2 DIS events are about 36% and the ARIADNE(0.3) MC gives a reasonable description on this value. The comparisons of the differential $\mathcal{R}$ between the data and MC's, across the variables investigated, confirm that more parameters rather than the mere λ_s are needed to be tuned in order to fit the data.

A nearly independent behavior of $\mathcal{R}$ as a function of Q^2 was observed across the whole Q^2 coverage region from 5 to 500 GeV^2. It might be hard to interpret the results in the light of the results from the strange production in e^+e^- annihilation where an increasing baryon to meson ratio was shown as the center-of-mass energy increases. The e^+e^- results can be explained in a way that the larger energy provides larger phase space available where relatively more Λ's are produced than K^0_S's. In

our case, the Q^2 itself does not represent the effective colliding energy and therefore the other correlated kinematic variable x should be considered. Further study of the $\mathcal{R}$ at fixed x values as a function of Q^2 was investigated and the result is given in Figure 7.25. The rising trend of $\mathcal{R}$ was found as Q^2 increases.

An extrapolation of the $\mathcal{R}$ value in the range from 1 to 5 GeV^2 which is not covered in this thesis was made. The $\mathcal{R}$ value was determined to be about 0.35 to 0.4 in this range.

Studies in the Breit frame bring deeper understanding of the strange hadron production. The $\mathcal{R}$ value in the current region of the Breit frame was evaluated to be about 0.2. This value is consistent with that from the e^+e^- annihilation data. At e^+e^- [121], for center of mass energy from 10 to 200 GeV, $\mathcal{R}$ varies from about 0.2 to 0.4. The $\mathcal{R}$ value measured in the target region was found to be twice as large as that in the current region. It is already known, from the Λ to $\bar{\Lambda}$ asymmetry study in the target region, that no extra influence from the proton beam on the baryon production was showing up. So the difference should be associated with something else related to the features of the two regions in the Breit frame. We will discuss this later together with $\mathcal{R}$ results from the photoproduction events.

A clear enhancement of $\mathcal{R}$ was found in photoproduction, especially in the resolved process. The introduced multiple interaction mechanism in PYTHIA can improve the strange hadron production in the resolved process to some extent. However, it can not adjust the relative yield of strange hadrons and mesons, as shown in Figure 7.18. Some theoretical models like recombination (or coalescence model) were developed to interpret the large relative baryon to meson production observed at RHIC experiments [93]. In the recombination model, the overlap of the wavefunctions of the multiple jets is considered to provide a larger phase space for the dense area where the baryon production is increased relative to the meson production. Based on this concept, the fragmentation in the target region in our DIS case can be thought to be more complex or dense than the single parton fragmentation in the current region and therefore a $\mathcal{R}$ of 0.45 is found, larger than the 0.20 in the current region. Here the proton remnant fragmentation region can contain more than one parton initiated evolutions which is however not the case for the current region.

As mentioned previously, the photoproduction at HERA behaves like hadronic collisions where multiple interactions are assumed to be present. Compared to the

DIS, multiple jets production can readily occur in photoproduction. The overlaps of the jets in close phase space allows a baryon production larger than for mesons. The increasing $\mathcal{R}$ with decreasing x_γ^{OBS} gives a hint that the larger the probability of multiple jets, the larger the baryon production enhancement will be. Such trend can be proven further with the two subsamples which have different jet scenario, fireball-enriched and fireball-depleted samples. The fireball-enrich sample corresponds to an highly isotropic jet distribution (or not clear jet structure, or like fireball) in the phase space while the fireball-depleted sample refers to the events which have a clear jet structure. It can easily be imagined that extent overlaps of the multi-jets in the fireball-enriched events should bring larger effect on $\mathcal{R}$ than that in the fireball-depleted sample. Therefore the larger $\mathcal{R}$ takes place in the fireball-enriched events.

The effect of the correlations or the overlaps of the multi-jets also give a hint where the shortcomings of the PYTHIA MC in describing $\mathcal{R}$ could be. It indicates that the deficit in PYTHIA could be the multiple interaction mechanism, provided we believe the string model, used in both ARIADNE and PYTHIA, from its description in DIS. Since multiple interactions are produced independently in PYTHIA, one may think that the absence of correlations between these interactions, subsequently between the jets developed from these interactions, is responsible for the failure in the $\mathcal{R}$ description.

9.4 Bose-Einstein Correlation (BEC)

The Bose-Einstein correlation of $K_S^0 K_S^0$ pairs has been investigated in the photoproduction sample at HERA. The extracted source radius r and the correlation strength λ were $0.68 \pm 0.06\ fm$ and 0.92 ± 0.19, respectively. These results are consistent with the ZEUS preliminary results in DIS but have a better accuracy. Also a good agreement with the LEP results was found.

The BEC dependence on Q^2 was investigated and the results do not show a sensitivity of BEC with respect to Q^2. This observation agrees with the string model hypothesis in which the BEC is assumed to be determined exclusively in the fragmentation process.

Furthermore, the r dependence on the hadron mass was checked with the radius

result obtained in this thesis. An overall mass dependent trend can be seen with the radius results from pion BEC, and proton and lambda Fermi-Dirac Correlation (FDC) studies. In Figure 8.3, it can be seen that the result for kaons is the one which is in poor agreement with the predictions. So more studies on the kaon BEC with better precision or higher statistics are needed.

9.5 Rapidity Correlation (RC)

The rapidity correlations have been measured for the first time at HERA to study the local quantum number conservation during the hadron formation process. The expected relative production enhancement in rapidity, predicted by the string model, was clearly observed for particle pairs for which either the quark flavor or baryon number compensation exists. The enhanced production supports the local quantum number conservation concept adopted in the string and cluster models.

In analogy to BEC studies, the RC effect was parameterized with two variables, r and λ. The variable r tells how far the pair particles can be separated from each other in rapidity and λ is interpreted as the strength of the rapidity correlation existing within the particle pairs. For all the potentially correlated particle pairs like $\Lambda\bar{\Lambda}$, ΛK^0_S and $K^0_S K^0_S$, the r was measured to be about the same, ~ 0.6, while λs differ from each other. Since the λ is somehow related to the situation of the quantum number conservation, for example the different type of quark flavor compensation or different number of flavors involved in the compensation, λ varies.

The PYTHIA MC predicts the r values well. But discrepancies exist on λ between the predictions and the data for $\Lambda\bar{\Lambda}$ and $K^0_S K^0_S$ pairs. A reasonable explanation on the discrepancy is the absence in the MC simulation of resonances which can decay into these pairs. But it does not exclude other reasons. Further studies to understand this difference are needed.

9.6 Λ Polarizations

Both the transverse and longitudinal Λ polarizations have been measured for the first time with HERA I data in the three event samples. The determination of the polarizations was performed by measuring the decay proton distributions in the

Λ production planes. In all cases, the measured Λ polarizations were consistent with zero within the uncertainties. The same conclusions can be drawn from further studies in the Breit frame for high Q^2 DIS events. The cross check on K^0_S polarizations verified the procedure of the measurement.

In the framework of the DeGrand and Miettinen [118], a sizable transverse polarization will be obtained if the strange quark gains acceleration or deceleration during the processes from its production to the formation of a Λ with two other quarks. The polarizations appearing this way will give an indication of any preferred planes for Λ production. The understanding of the results obtained in this thesis could be as following in the light of the DeGrand and Miettinen mechanism. The possible Λ production which could show polarization due to the acceleration or deceleration of the struck quark was estimated to be at most 15% of the whole Λ production according to Monte Carlo studies. Since no polarization was measured in this thesis, we may think that the polarization of this 15% Λ's, if non-zero, averages to a much smaller value once we determine the polarization for the whole sample, or there is no polarization at all. No preferential direction for Λ production in the selected kinematic regions was suggested by the measurement in the thesis.

Because the longitudinal Λ polarization is expected to be related to the beam polarizations, the zero longitudinal polarization measured in this thesis is plausible for HERA I data which were produced with unpolarized beams. But for HERA II data since 2000, the electron beam has been longitudinally polarized at a level of about 40%. Some fraction of the electron polarization thus will be expected to transferred to the final hadrons. As a consequence, the final Λ's will also inherit, more or less, longitudinal polarizations. However, it is worthwhile to note that Λ polarization obtained this way could be small, or even smaller than the uncertainties of the measurement since the total electron polarization will be shared and diluted by the whole or al least part of the final hadronic system.

9.7 Outlook

Some analyses mentioned above are not yet completed due to the limited time and restricted scope of this work, but it could be of interest to investigate further on the issues listed below:

- Does the BEC behave differently in the fireball subsamples and two regions in the Breit frame? This will check the BEC dependence on the fragmentation regions with different features and it will eventually lead to a better understanding of the hadron production;
- The FDC should be determined using a combined HERA I and HERA II data. Then the radius dependence on the hadron mass can be investigated with solely HERA results;
- Quantitative predictions on RC from the cluster model should be strongly supported. The parameterized RC provides a tool to discriminate different Monte Carlo models. Further study on the popcorn mechanism will allow us to understand more details of the hadron production;
- The polarizations must be measured again with the HERA II data. The longitudinal polarized electron beam is expected to result in the observation of the strange hadron polarization.

Appendix A

Determination of Systematic Uncertainties

The main sources which contribute to the systematic uncertainties were investigated by repeating the measurement procedure with numerous variations of the cuts or methods used. The amount of the variation was determined according to the resolution of the cut. Generally a value of three times the standard deviation is used. Then the total systematic error was calculated by combining in quadrature each individual contribution. The uncertainties due to the choice of MC could be evaluated by comparing the results to the actual MC from a different MC model, but no alternate models were available for this purpose and consequently one should keep in mind that no such kind of uncertainty is given in this work.

In the following sections all effects on differential cross sections and polarization from the variations of cuts and procedures are summarized. The systematic uncertainties on baryon to antibaryon production asymmetry and baryon to meson production ratio measurements are derived from the corresponding uncertainties of cross section measurements. Therefore we do not provide explicitly the uncertainties of the production asymmetry and ratio measurements.

The sources of systematic uncertainty will be given below in decreasing order of dominance.

A.1 Photoproduction Sample

- The transverse energy of the dijet was varied by ±0.2 GeV. The changes of Λ cross sections were generally about 1%. The effects on K^0_S cross section were less than 1% except in the lowest $x_\gamma^{\rm OBS}$ region where ~1% effect was observed.

- The variation of cut $y_{\rm JB}$ by ±0.0006 has a general ~1% effect on both Λ and K^0_S cross sections. The largest effect was found at the lowest $x_\gamma^{\rm OBS}$ region where the effect is up to 2%.

- The transverse energy of the tracks was changed by ±0.03 GeV and the overall contributions from this variation was found to be 2~4% for Λ, but a few percent for K^0_S productions. The largest uncertainty about 4~6% was observed in the lowest $p_{\rm T}$ and lowest $x_\gamma^{\rm OBS}$ regions for Λ cross sections.

- The Λ selection mass window was tightened to 1.107~1.125 GeV. An overall 4% effect has appeared. The mass window for K^0_S was also changed tighter to 0.47~0.53 GeV, but a general ~1% effect was found.

- The variation due to the energy scale uncertainties of the calorimeter was given separately as a shaded band on the cross section figures. It is determined with MC studies via varying $E_T^{\rm jet}$ by its uncertainty of ±1% for events with $E_T^{\rm jet} > 10$ GeV and ±3% for the rest events [122].

- The contributions from variations of the requirements on $y_{\rm e}$ (±0.5), $p_{\rm T}^2/E_{\rm T}$ (±0.2), $Z_{\rm vertex}$ (±5 cm), $\eta^{\rm trk}$ (±0.1), the collinearity cut (±0.05), the mass cuts to reject Λ from K^0_S selection and the mass cut to reject K^0_S from Λ selection were considered. The effects arising from these cuts were typically below 1%.

A 2% uncertainty due to the luminosity measurement was included for the cross section. The uncertainty related to the branching ratios was neglected.

The systematic uncertainties due to the poor agreement (Figures 6.7 and 6.8) between the data and MC are estimated. The relative differences between the data and MC are estimated to go up to 60% in the very low $x_\gamma^{\rm OBS}$ region, 25% in the medium $x_\gamma^{\rm OBS}$ region and 15% in the large $p_{\rm T}$ region for both Λ and K^0_S cases. Their average discrepancies are however 2.8% for K^0_S and 3.6% for Λ. These disagreements will result in additional systematic uncertainties to these average levels. But such

impact is expected to be mainly on the cross section measurement since these uncertainties due to the poor description by MC are expected to be canceled out at the first order for the other measurements such as the asymmetry, ratio and correlation studies. These uncertainties are NOT included in the final uncertainties shown in the previous result chapters.

As an example, the systematic uncertainties for K^0_S total cross section measurement are given in Table A.1. The uncertainty resulting from the variation of each cut is shown. The total uncertainty, calculated by adding all contributions in quadrature first and then calculating the square root value of this sum, was determined to be -2.5 $\times$ 10^{-2} and +6.0 $\times$ 10^{-3}. These two lower and upper values were used to calculate the uncertainties for the K^0_S total cross section measurement shown in Table 7.1.

The dependence of the cross sections on these variations are shown bin by bin in Figures A.1 and A.2. Figure A.3 shows the similar systematic uncertainties for polarization measurements.

Cut	Variation	$\frac{\sigma'-\sigma}{\sigma}$	
		+	−
$E_{\mathrm{T}}^{\mathrm{jet}}$	±0.2 GeV	-6.5 × 10^{-5}	1.6 × 10^{-3}
y_e	±0.5	-6.6 × 10^{-3}	non-significant
$p_{\mathrm{T}}^{\mathrm{miss}}$	$\pm\sqrt{0.2}$	5.6 × 10^{-6}	non-significant
y_{JB}	±0.0006	-1.6 × 10^{-2}	-2.9 × 10^{-3}
Z_{vertex}	±5 cm	-9.3 × 10^{-4}	6.8 × 10^{-4}
Collinearity angle	±0.05	2.2 × 10^{-3}	-5.4 × 10^{-3}
η^{trk}	±0.1	-3.6 × 10^{-4}	-1.0 × 10^{-3}
$p_{\mathrm{T}}^{\mathrm{trk}}$	±0.03 GeV	5.5 × 10^{-3}	-2.7 × 10^{-3}
K_S^0 mass window	0.47-0.53 GeV	-1.56 × 10^{-2}	
Mass cut to remove Λ	1.107-1.125 GeV	5.9 × 10^{-4}	

Table A.1: The systematic uncertainties for the K_S^0 total cross section measurement in photoproduction. The variable σ' represents the cross section measured after varying the cuts. When $\frac{\sigma'-\sigma}{\sigma}$ gives two values with the same sign after variation of one specific cut, the larger one is taken for the uncertainty attributed to this cut. According to these values, the total systematic uncertainties were determined to be +0.6% (upper limit) and -2.5% (lower limit) for the K_S^0 total cross section measurement, see Table 7.1.

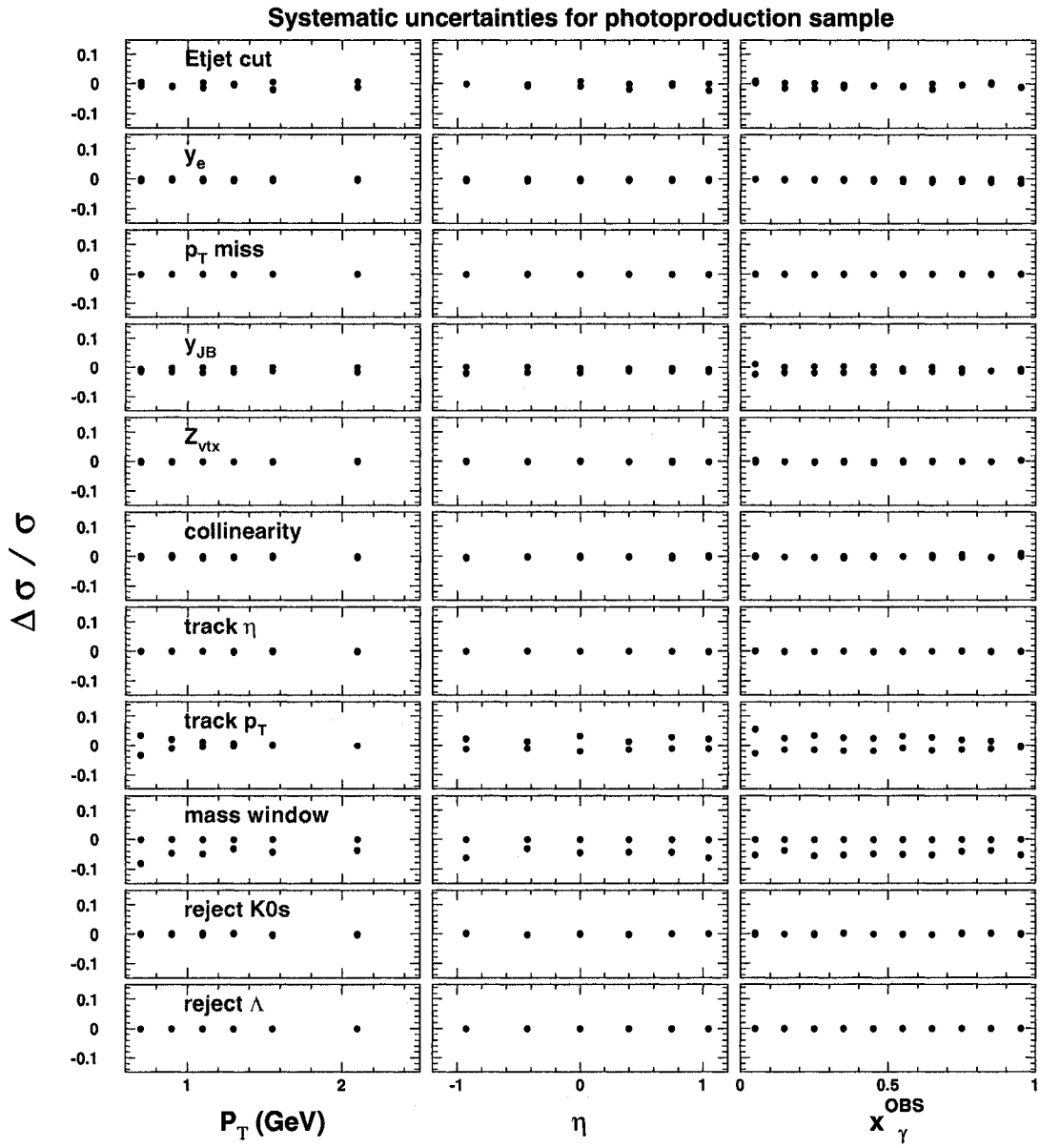

Figure A.1: The relative effect of various systematic variations for Λ cross section measurements in photoproduction processes.

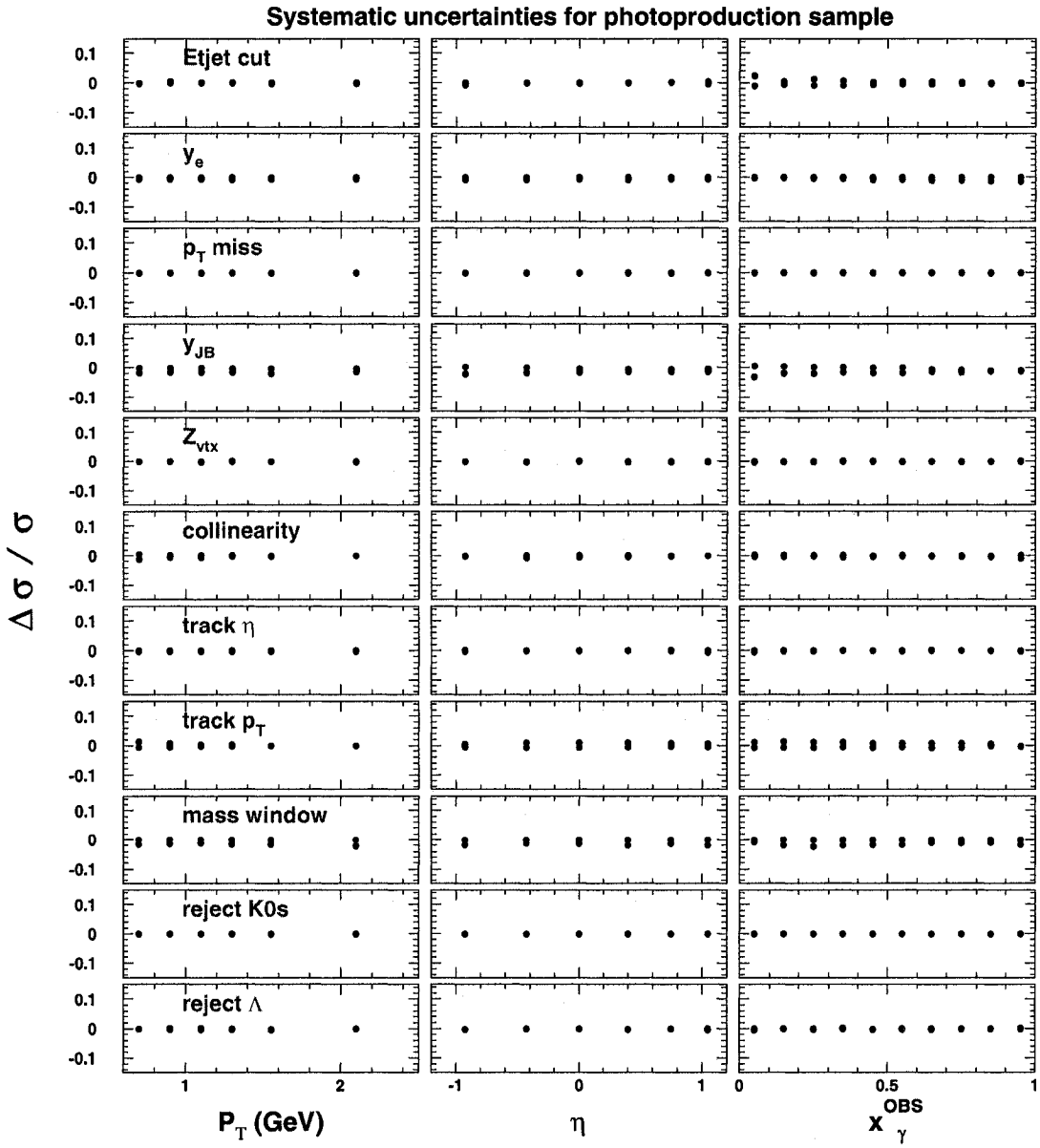

Figure A.2: The relative effect of various systematic variations for K_S^0 cross section measurements in photoproduction process.

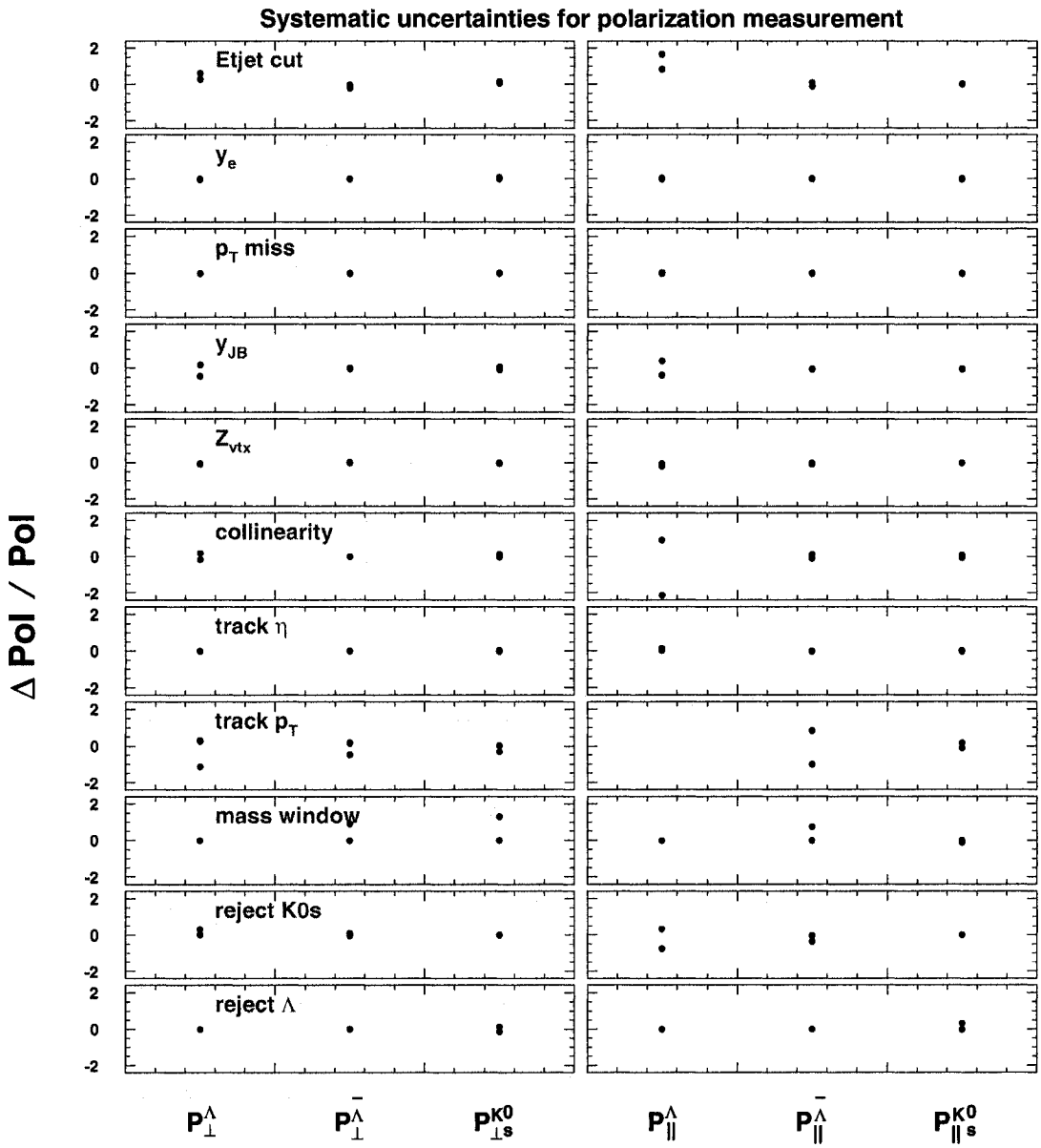

Figure A.3: The relative effect of various systematic variations for polarization measurements in photoproduction process.

A.2 DIS Samples

Since variations of the cuts used and the effects due to these variations were found to be similar for both the low Q^2 and high Q^2 samples, the systematic uncertainties for these two DIS samples are described together in this section for both Λ and K^0_S cross sections.

- The box cut for low Q^2 events and radius cut for high Q^2 events were changed by ± 1 cm. A few cross sections were affected by $\sim$1%, particularly in the lowest Q^2 region.
- The scattered electron energy was varied by $\pm$ 1 GeV. The changes of cross sections were generally 1$\sim$2%. The largest uncertainty (8%) was observed in the lowest x region.
- the value of Q^2 calculated from the electron method compared to the DA method. This changes the cross sections generally by 1$\sim$3%. The effect was up to 10% for Λ cross sections in the low x and low Q^2 region.
- The collinearity cut was varied by ± 0.05 and the typical effects on the cross sections were around 1%.
- The transverse energy of the tracks was changed by ± 0.03 GeV and the contributions from this variation were found to be 1$\sim$3% for Λ and less than 1% for K^0_S cross sections.
- The selection mass window for Λ was tightened to 1.107$\sim$1.125 GeV and the mass window for K^0_S was also changed tighter to 0.47$\sim$0.53 GeV. A general 1% effect was found for all cross sections except the 5$\sim$10% effect was shown in the high Q^2 DIS region for Λ cross sections .
- The contributions from variations of the requirements on $E - p_Z$ (± 2 GeV), $y_{\rm JB}$ (± 0.0006), $Z_{\rm vertex}$ (± 5 cm), $\eta^{\rm trk}$ (± 0.1), the mass cuts to reject Λ from K^0_S selection and the mass cut to reject K^0_S from Λ selection were considered. The effects arising from these cuts were typically below 1%.

A 2% uncertainty due to the luminosity measurement was included for the cross section. The uncertainty related to the branching ratio was neglected. The dependence of the cross sections on these variations are shown bin by bin in figures A.4 and A.5 for low Q^2 DIS events and Figures A.7 and A.8 for high Q^2 DIS events. Figures A.6

and A.9 show the similar systematic uncertainties for polarization measurements in the low and high Q^2 DIS, respectively.

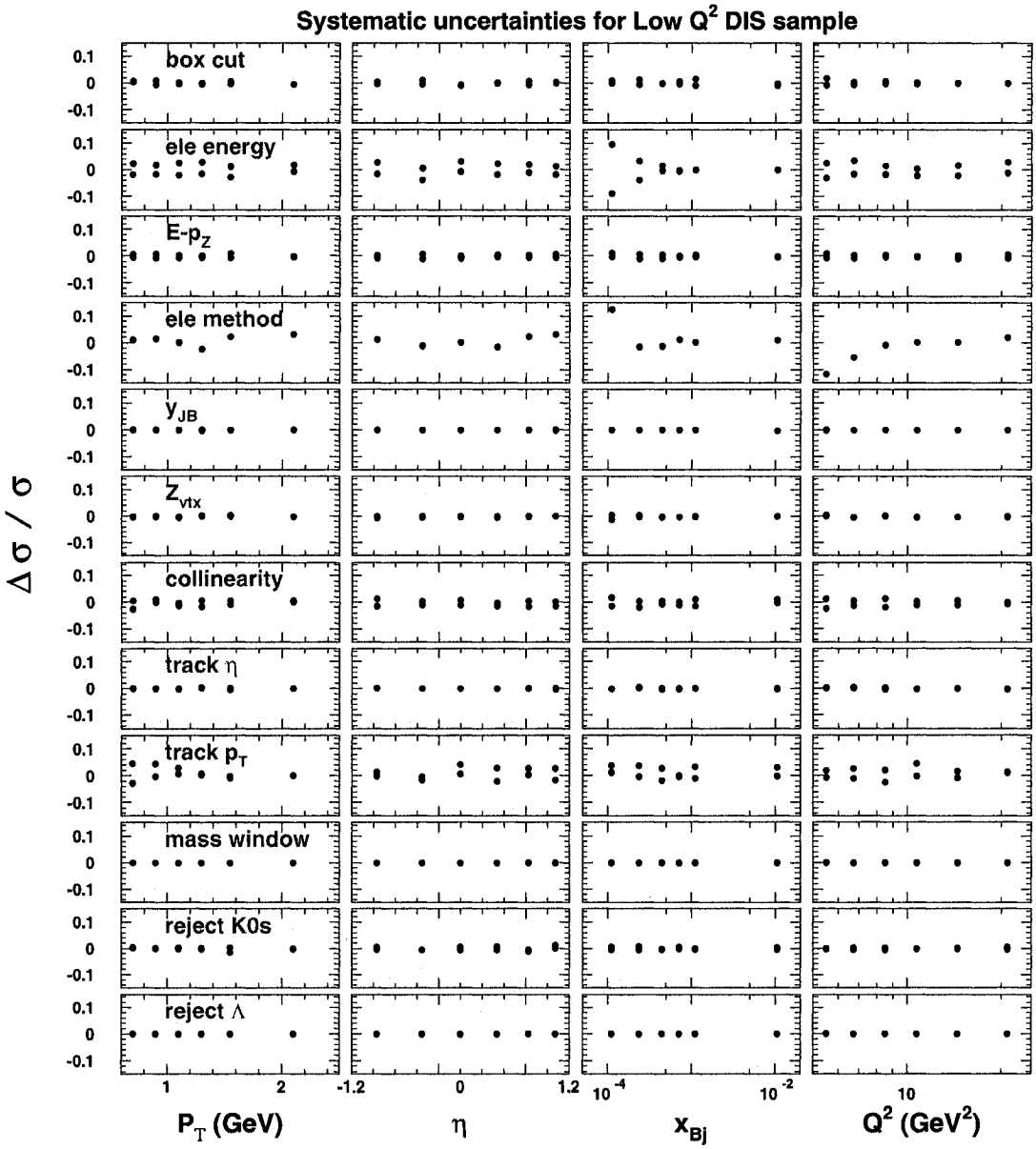

Figure A.4: The relative effect of various systematic variations for Λ cross section measurements in the low Q^2 DIS region.

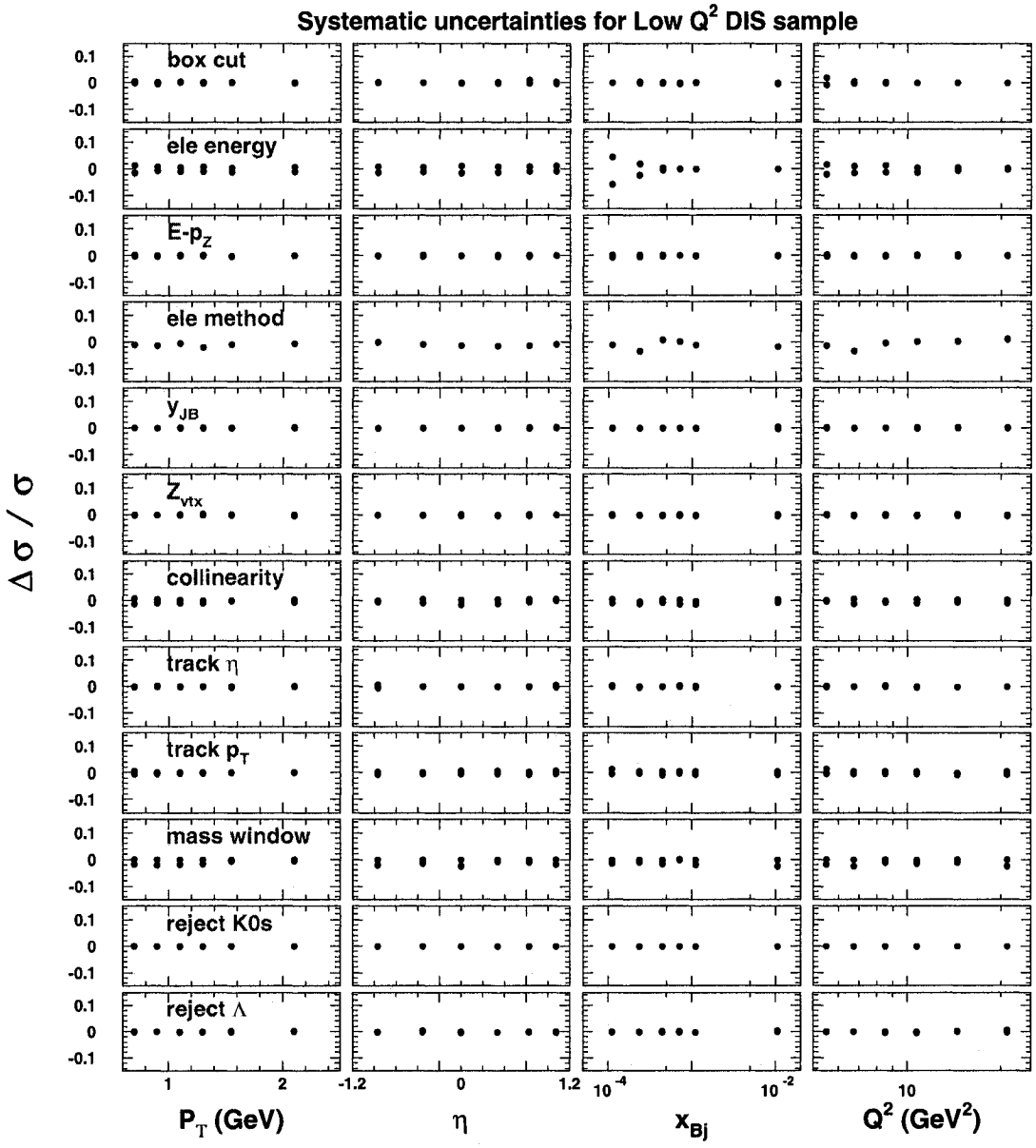

Figure A.5: The relative effect of various systematic variations for K^0_S cross section measurements in the low Q^2 DIS region.

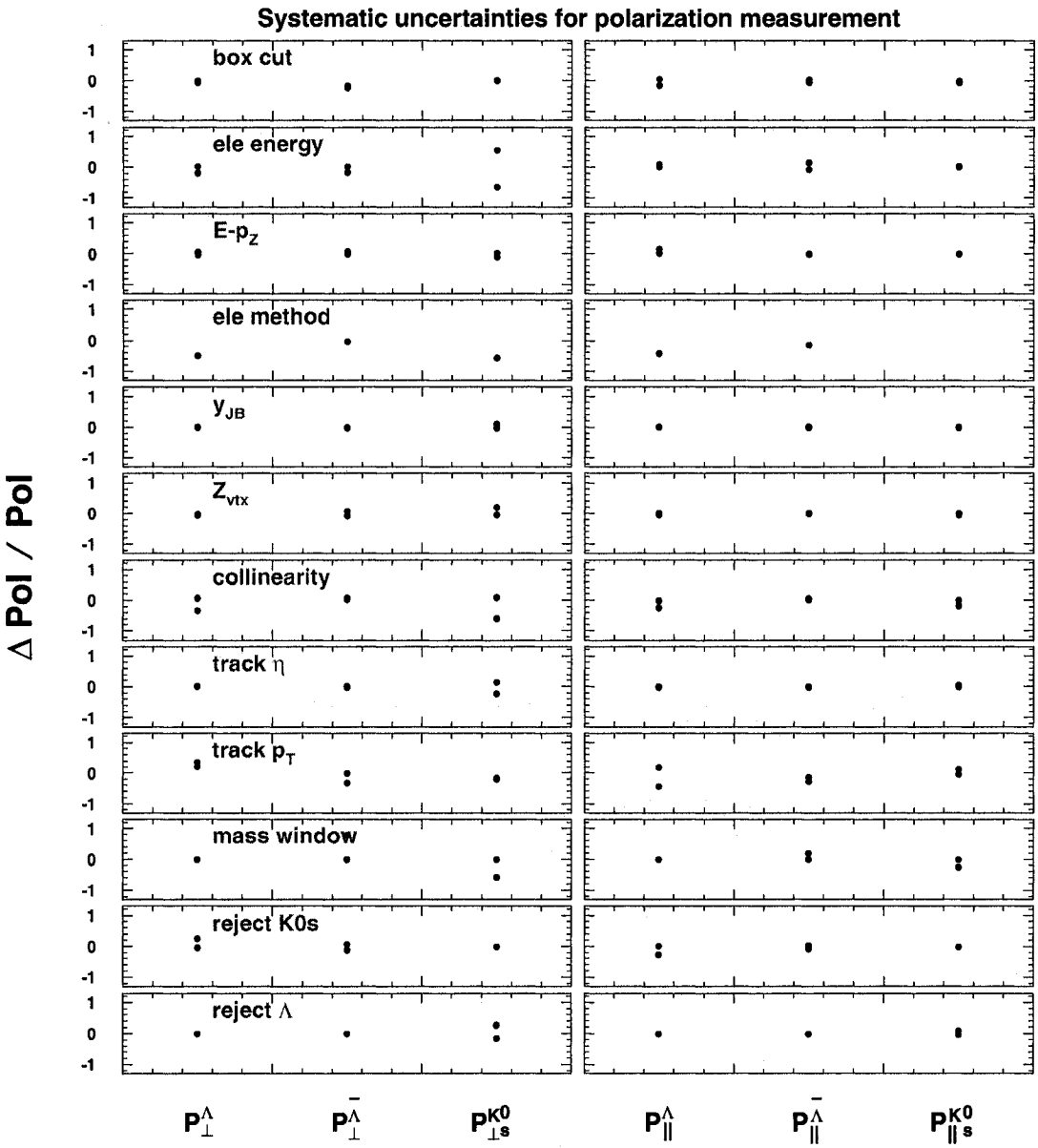

Figure A.6: The relative effect of various systematic variations for polarization measurements in low Q^2 DIS.

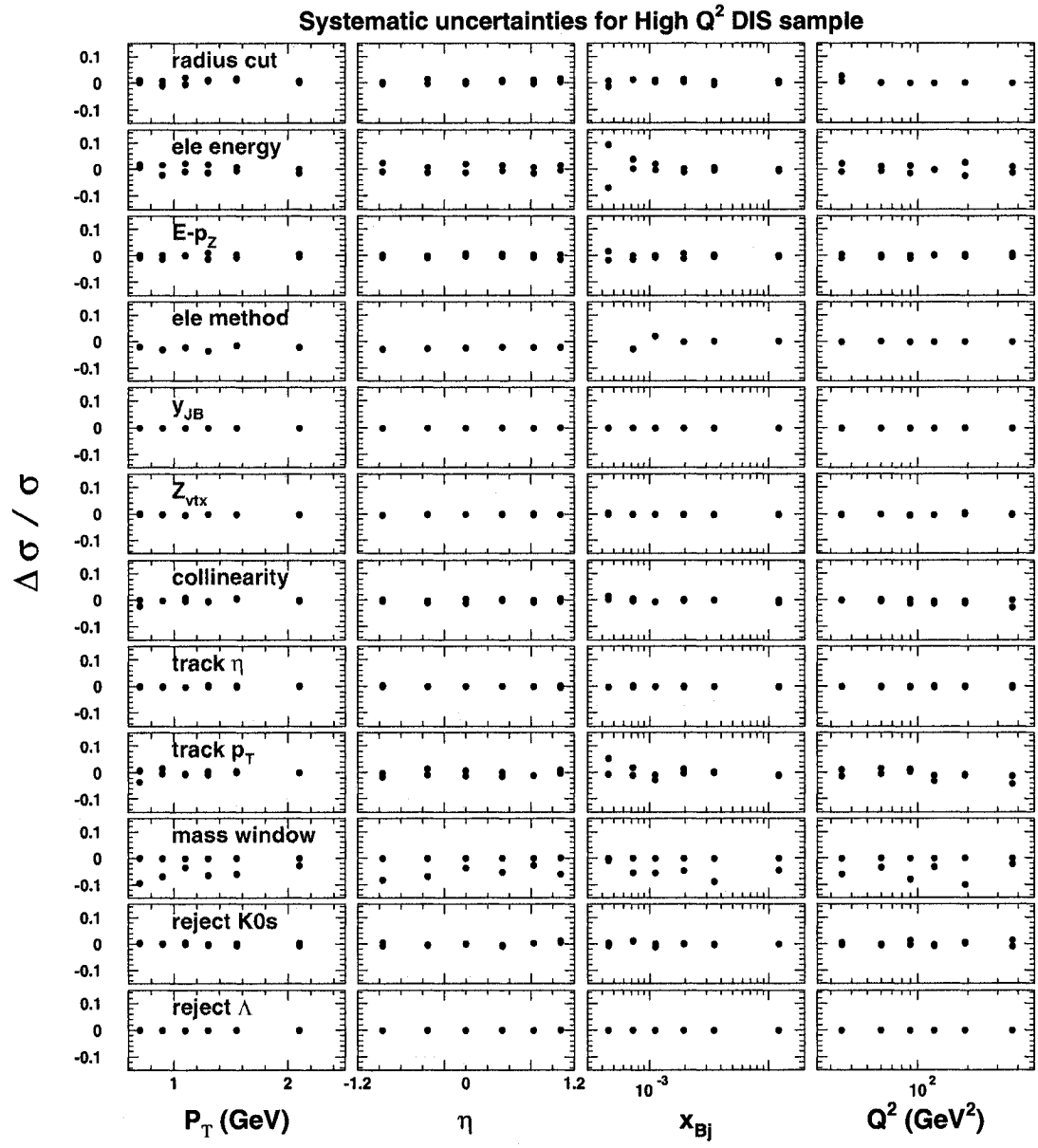

Figure A.7: The relative effect of various systematic variations for Λ cross section measurements in the high Q^2 DIS region.

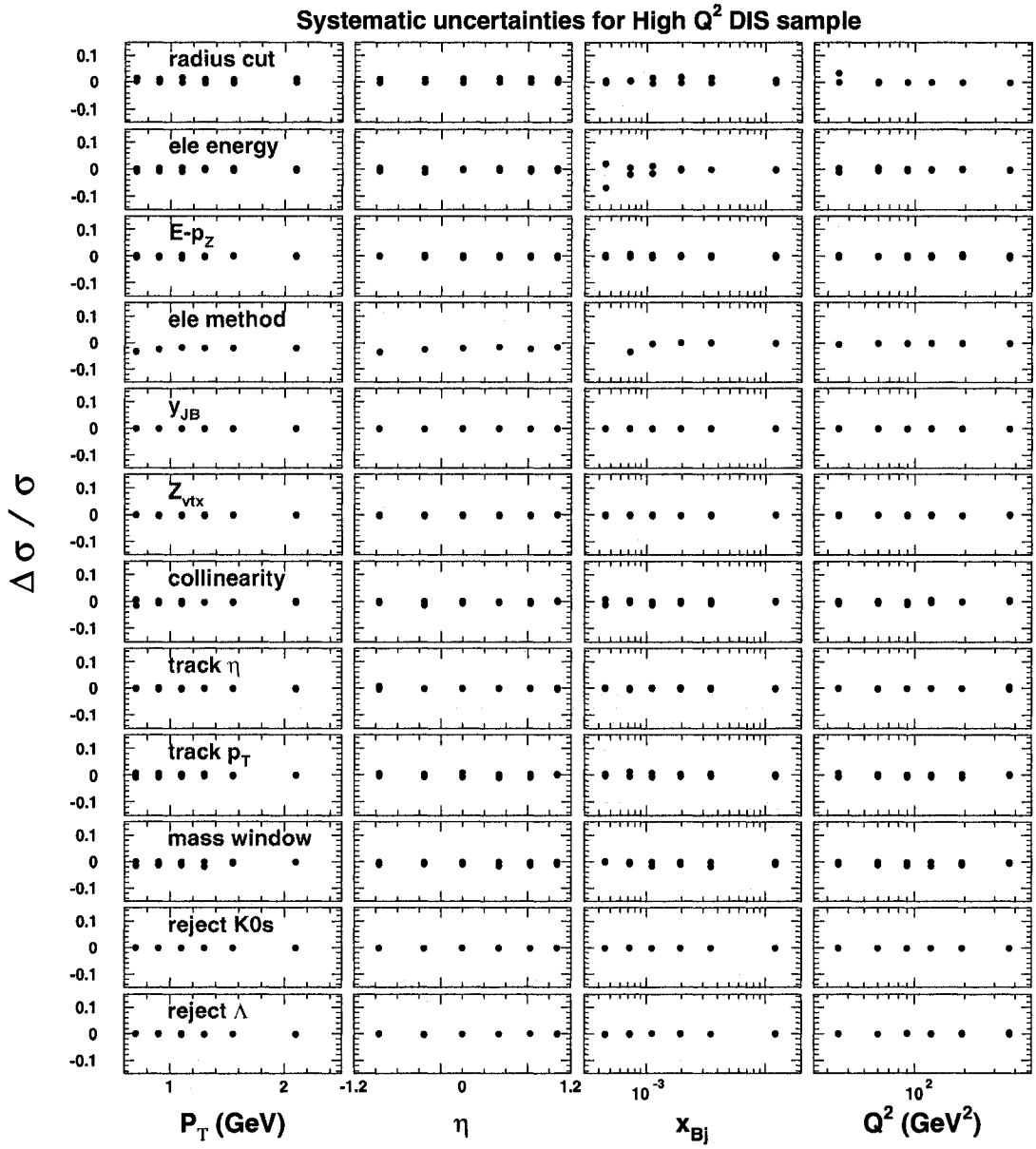

Figure A.8: The relative effect of various systematic variations for K^0_S cross section measurements in the high Q^2 DIS region.

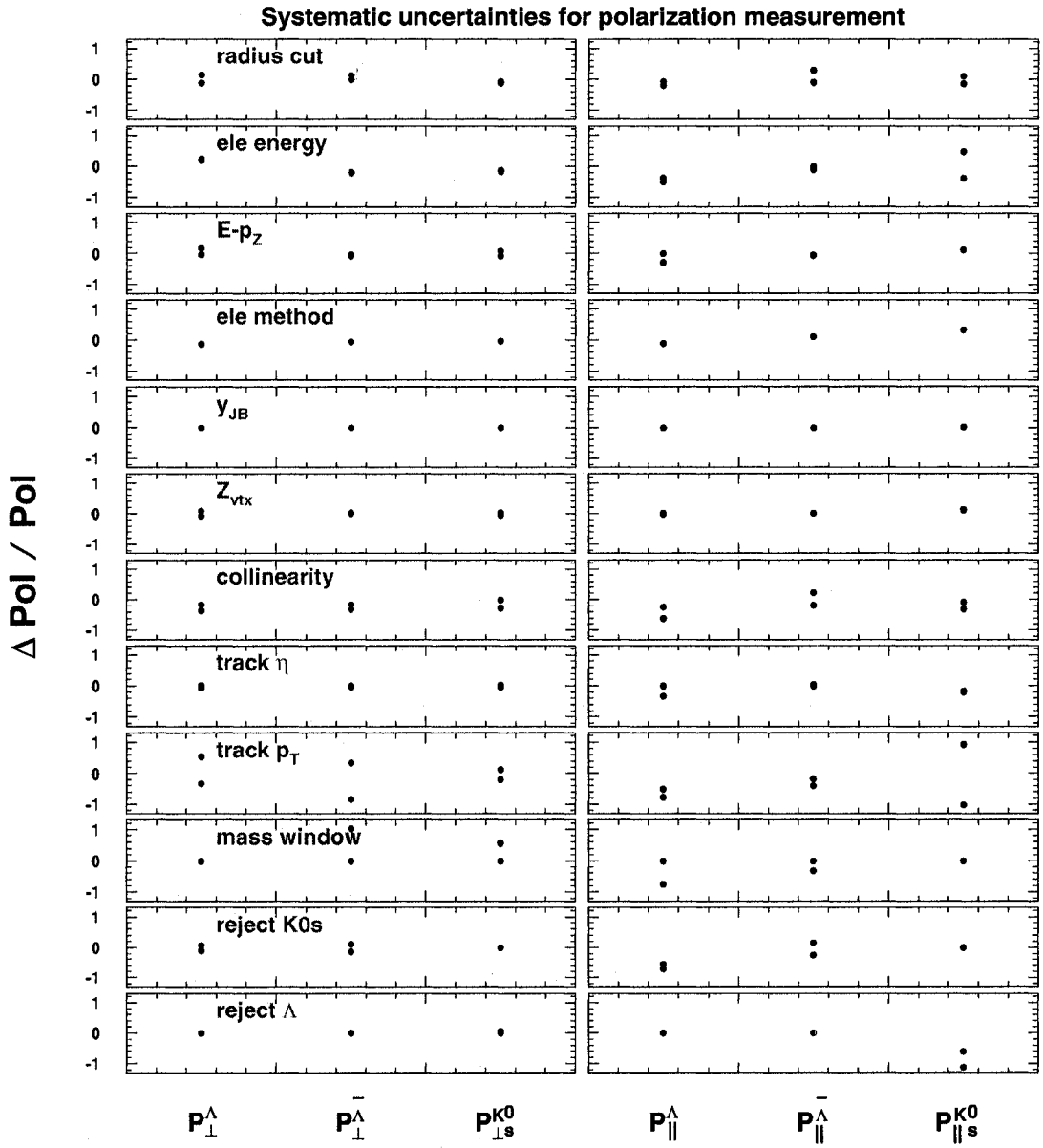

Figure A.9: The relative effect of various systematic variations for polarization measurements in high Q^2 DIS.

Glossary

ADC:	Analog to Digital Converter
BAC:	Backing Calorimeter
BCAL:	Barrel Calorimeter
BE:	Bose-Einstein
BEC:	Bose-Einstein Correlation
BMUON:	Barrel Muon chambers
BN:	Baryon Number
C5:	Collimator 5 Veto counter
CAL:	Calorimeter
CC:	Charged Current
CTD:	Central Tracking Detector
DA:	Double Angle method
DAQ:	Data Acquisition System
DESY:	Deutsches Elektronen Synchrotron
DIS:	Deep Inelastic Scattering
DST:	Data Summary Tape
EMC:	Electromagnetic section of the CAL
EVB:	Event Builder
FCAL:	Forward Calorimeter
FDC:	Fermi-Dirac Correlation
FDET:	The combination of FTD and TRD
FMUON:	Forward Muon chambers
FTD:	Forward Tracking Detector
FLT:	First Level Trigger
GFLT:	Global First Level Trigger

GSLT: Global Second Level Trigger
HAC: Hadronic section of the CAL
HERA: Hadron Elektron Ring Anlage
ILC: International Linear Collider
LHC: Large Hadron Collider
LO: Leading Order
LUMI: Luminosity monitoring system
MC: Monte Carlo
MOZART: Monte Carlo for ZEUS Analysis, Reconstruction and Trigger
NC: Neutral Current
NDD: Normalized Distribution Density
NLO: Next Leading Order
PDF: Parton Density Function
PMT: Photomultiplier Tuber
pQCD: perturbative Quantum ChromoDynamics
PYTHIA: Monte Carlo simulation implementing a string model for hadronization
QCD: Quantum ChromoDynamics
QED: Quantum ElectroDynamics
QPM: Quark Partion Model
RCAL: Rear Calorimeter
RHIC: The Relativistic Heavy Ion Collider
RMUON: Rear Muon system
RTD: Rear Tracking Detector
SM: Standard Model
SLAC: Standford Linear Accelerator Center
SLT: Second Level Trigger
SSC: Secondary Scattering Contaminations
SUSY: Supersymmetry
TLT: Third Level Trigger
ZGANA: The offline TLT simulation
UCAL: Uranium Calorimeter

Bibliography

[1] M. Gell-Mann, *A Schematic Model Of Baryons And Mesons*, Phys. Lett. **8**, 214 (1964)

[2] G. Zweig, Preprint CERN Rep. 8182/TH 401 (1964) (unpublished)

[3] H1 Collab., *The H1 detector at HERA*, DESY 93-103, (1993)

[4] TASSO Collab., R. Bradelik et al., *Evidence For Planar Events In e^+e^- Annihilation At High-Energies*, Phys. Lett. **B 86**, 243 (1979)

[5] H1 Collab., S. Aid et al., *A study of the fragmentation of quarks in ep collisions at HERA*, Nucl. Phys. **B 445**, 3 (1995)

[6] ZEUS Collab., M. Derrick et al., *Measurement of Multiplicity and Momentum Spectra in the Current Region of the Breit Frame at HERA* , Zeit. Phys. **C 67**, 93 (1995)

[7] F.E. Close, *The Quark Parton Model*, Rep. Prog. Phys. **42**, (1979)

[8] G.M. Arafat, *Recent electroweak measurements from the H1 and ZEUS experiments*, Preprint hep-ex/0406036 (2004)

[9] ZEUS Collab., M. Derrick et al., *Neutral Strange Particle Production in Deep Inelastic Scattering at HERA*, Zeit. Phys. **C 68**, 29 (1995)

[10] ZEUS Collab., J. Breitweg et al., *Charged Particles and Neutral Kaons in Photoproduced Jets at HERA*, Eur. Phys. J. **C 2**, 77 (1998)

[11] H1 Collab., S. Aid et al., *Strangeness production in deep-inelastic positron-proton scattering at HERA*, Nucl. Phys. **B 480**, 3 (1996)

[12] H1 Collab., C. Adloff et al., *Photoproduction of K0 and lambda at HERA and a Comparison with Deep Inelastic Scattering*, Zeit. Phys. **C 76**, 213 (1997)

[13] OPAL Collab., G. Abbiendi et al., *Leading Particle Production in Light Flavour Jets*, Eur. Phys. J. **C 16**, 407 (2000)

[14] SLD Collab., K. Abe et at., *Production of π^+, K^+, K^0, K^{*0}, ϕ, p and Λ^0 in hadronic Z^0 decays*, Phys. Rev. **D 59**, 052001 (1999)

[15] H1 Collab., T. Ahmed et al., *First measurement of the deep-inelastic structure of proton diffraction*, Phys. Lett. **B 348**, 681 (1995)

[16] ZEUS Collab., M. Derrick et al., *Measurement of the Diffractive Structure Function in Deep Inelastic Scattering at HERA*, Zeit. Phys. **C 68**, 569 (1995)

[17] STAR Collab., J. Adams et al., *Strange antiparticle-to-particle ratios at mid-rapidity in $\sqrt{s_{NN}} = 130$ GeV Au+Au collisions*, Phys. Lett. **B 567**, 167 (2003)

[18] PHENIX Collab., K. Adcox, *Measurement of Λ and $\bar{\Lambda}$ Particles in Au+Au Collisions at $\sqrt{s_{NN}} = 130$ GeV*, Phys. Rev. Lett. **89**, 092302 (2002)

[19] H.Z. Huang and J. Rafelski, *Hadronization and Quark Probes of Deconfinement at RHIC*, hep-ph/0501187

[20] ZEUS Collab., *A Micro Vertex Detector for ZEUS - Tech. Report*, unpublished, DESYPRC 97/01, 1997

[21] ZEUS Collab., *The ZEUS Detector - Status Report*, unpublished, DESY (1993)

[22] N. Harnew et al., *Vertex triggering using time difference measurements in the ZEUS central tracking detector*, Nucl. Inst. Meth. **A 279**, 290 (1989)

[23] B. Foster et at., *The performance of the ZEUS central tracking detector z-by-timing electronics in a transputer based data acquisition system*, Nucl. Phys. Proc. Suppl. **B 32**, 181 (1993)

[24] B. Foster et al., *The design and construction of the ZEUS central tracking detector*, Nucl. Inst. Meth. **A 338**, 254 (1994)

[25] O. Gutsche, *Measurement of Beauty Quark Cross Sections in Photoproduction with the ZEUS Experiment at the Electron-Proton Collider HERA*, DESY-THESIS-2005-010

[26] M. Derrick et al., *Design and construction of the ZEUS barrel calorimeter*, Nucl. Inst. Meth. **A 309**, 77 (1991)

[27] A. Andresen et al., *Construction and beam test of the ZEUS forward and rear calorimeter*, Nucl. Inst. Meth. **A 309**, 101 (1991)

[28] M. Barbi, *Calibration and Monitoring of the ZEUS uranium scintillator calorimeter at HERA*, Proceedings of the 30th International Conference on High Energy Physics, Pasadena, USA, 25-29 Mar (2002)

[29] A. Bamberger et al., *The small angle rear tracking detector of ZEUS*, Nucl. Instr. Meth. **A 401**, 63 (1997)

[30] H. Bethe and W. Heitler, *On the Stopping of Fast Particles and on the Creation of Positive Electrons*, Proc. Roy. Soc., **A 146**, 83 (1934)

[31] D. Kisielewska et al., *Fast Luminosity Monitoring at HERA*, DESY - HERA report 85-25.

[32] L. Suszycki, *Luminosity Monitoring, Photon Tagging and QED Tests*, Proc. of the HERA Workshop , Vol.2 , p.505 (1987).

[33] H. Abramowicz, A. Caldwell, R. Sinkus, *Neural network based electron identification in the ZEUS calorimeter*, Nucl. Inst. Meth. **A 365**, 508 (1995)

[34] R. Sinkus, T. Voss, *Particle identification with neural networks using a rotational invariant moment representation*, Nucl. Inst. Meth. **A 391**, 360 (1997)

[35] J. Ng and W. Verkerke, *An Overview of SRTD Analysis*, unpublished, ZEUS note 95-037

[36] F. Jacquet and A. Blondel, *Proceeding of the study for an ep facility for Europe*, U. Amaldi(ed.), p. 391, Hamburg, Germany(1979). Also in preprint DESY 79/48

[37] S. Bentvelsen, J. Engelen and P. kooijman, *Proc. Workshop on Physics at HERA*, W. Buchmüller and G. Ingelman (eds.), Vol. 1, p. 23. Hamburg, Germany, DESY (1992)

[38] K.C. Höger, *Proc. Workshop on Physics at HERA*, W. Buchmüller and G. Ingelman (eds.), Vol. 1, p. 43. Hamburg, Germany, DESY (1992)

[39] S. Catani, Dokshitzer, L. Yuri, B.R. Webber, *The K-perpendicular clustering algorithm for jets in deep inelastic scattering and hadron collisions*, Phys. Lett. **B 285**, 291 (1992)

[40] S. Catani, Dokshitzer, L. Yuri, B.R. Webber, *Longitudinal invariant K(t) clustering algorithms for hadron collisions*, Nucl. Phys. **B 406**, 187 (1993)

[41] ZEUS Collab., M. Derrick et al., *Observation of Direct Processes in Photoproduction at HERA*, Phys. Lett. **B 322**, 287 (1994)

[42] H1 Collab., T. Ahmed et al., *Hard scattering in γp interactions*, Phys. Lett. **B 297**, 205 (1992)

[43] ZEUS Collab., M. Derrick et al., *Observation of Hard Scattering in Photoproduction at HERA*. Phys. Lett. **B 297**, 404 (1992)

[44] ZEUS Collab., M. Derrick et al., *Dijet Cross Sections in Photoproduction at HERA*, Phys. Lett. **B 348**, 665 (1995)

[45] ZEUS Collab., J. Breitweg et al., *Measurement of jet shape in photoproduction at HERA* , Eur. Phys. J. **C 2**, 61 (1998)

[46] E. Gallo, *The TLT and DST filters for the DIS group in 1995*, ZEUS note, 96-001 (1996)

[47] W.H. Smith et at., *The ZEUS Calorimeter First Level Trigger*, Nucl. Instr. Meth. **A 355**, 322 (1995)

[48] ZEUS Collab., S. Chekanov et al., *Measurement of the neutral current cross section and F_2 structure function for deep inelastic e^+p scattering at HERA*, Eur. Phys. J. **C 21**, 443 (2001)

[49] ZEUS Collab., S. Chekanov et al., *Measurement of K^0_S, Λ and $\bar{\Lambda}$ production at HERA*, Preprint hep-ex/0612023.

[50] ZEUS Collab., J. Breitweg et al., *Dijet Cross Sections in Photoproduction at HERA*, Eur. Phys. J. **C 1**, 109 (1998)

[51] Particle Data Group, S. Eidelman et al., *Review Of Particle Physics*, Phys. Lett. **B 592**, 1 (2004)

[52] G. Marchesini, B.R. Webber, G. Abbiendi, I.G. Knowles, M.H. Seymour and L. Stanco, *HERWIG 5.1 - a Monte Carlo event generator for simulating hadron emission reactions with interfering gluons*, Comp. Phys. Comm. **67**, 465 (1992)

[53] G. Corcella, I.G. Knowles, G. Marchesini, S. Moretti, K. Odagiri, P. Richardson, M.H. Seymour and B.R. Webber, *HERWIG 6.5*, JHEP **0101** 010 (2001)[hep-ph/0011363]; hep-ph/0210213.

[54] T. Sjöstrand et al., *High-energy-physics event generation with 6.1*, Comp. Phys. Comm. **135**, 238 (2001)

[55] L. Lönnblad, *Ariadne version 4.12 program and manual*, Comp. Phys. Comm. 71, 15 (1992)

[56] G. Gustafson, *Dual description of a confined colour field*, Phys. Lett. **B 175**, 453 (1986)

[57] G. Gustafson, U. Pettersson, *Dipole formulation of QCD cascades*, Nucl. Phys. **B 306**, 746 (1988)

[58] B. Andersson et al., *Coherence effects in deep inelastic scattering*, Zeit. Phys. **C 43**, 625 (1989)

[59] B. R. Webber, *Fragmentation and hadronization*, hep-ph/9912292

[60] B. Andersson, G. Gustafson, G. Ingelman and T. Sjöstrand, *Parton fragmentation and string dynamics*, Phys. Rept. **97**, 31 (1983)

[61] T. Sjöstrand, *High-energy-physics event generation with PYTHIA 5.7 and JETSET 7.4*, Comp. Phys. Comm. **82**, 74 (1994)

[62] T. Sjöstrand, *PYTHIA 5.7 and JETSET 7.4 Physics and Manual*, hep-ph/9508391

[63] R.D. Field and S. Wolfram, *A QCD model for e^+e^- annihilation*, Nucl. Phys. **B 213**, 65 (1983)

[64] B.R. Webber, *A QCD model for jet fragmentation including soft gluon interference*, Nucl. Phys. **B 238**, 492 (1984)

[65] D. Amati and G. Veneziano, *Preconfinement as a property of perturbative QCD*, Phys. Lett. **B 83**, 87 (1979)

[66] G. Marchesini, L. Trentadue and G. Veneziano, *Space-time description of colour screening via jet calculus techniques*, Nucl. Phys. **B 181**, 335 (1981)

[67] *MOZART - Zeus Detector Simulation*, ZEUS internal document

[68] R. Brun et al., *GEANT3*, Technical Report CERN-DD/EE/84-1, CERN, 1987

[69] A. Kwiatkowski, H. Spiesberger and H.J. Möhring, *HERACLES: an event generator for ep interactions at HERA energies including radiative processes*, Comp. Phys. Comm. **69**, 155 (1992)

[70] K. Charchula, G.A. Schuler and H. Spiesberger, *Combined QED and QCD radiative effects in deep inelastic lepton-proton scattering: the Monte Carlo generator DJANGO6*, Comp. Phys. Comm. **81**, 381 (1994)

[71] G. Ingelman, A. Edin and J. Rathsma, *LEPTO 6.5 - A Monte Carlo generator for deep inelastic lepton-nucleon scattering*, Comp. Phys. Comm. **101**, 108 (1997)

[72] H. Spiesberger, *HERACLES and DJANGO: Event Generation for ep Interactions at HERA Including Radiative Processes*, 1998, available at http://www.desy.de/~hspiesb/heracles.html.

[73] H.L. Lai et al., *Improved parton distributions from global analysis of recent deep inelastic scattering and inclusive jet data*, Phys. Rev. **D 55**, 1280 (1997)

[74] CTEQ Collab., H.L. Lai et al., *Global QCD Analysis of Parton Structure of the Nucleon: CTEQ5 Parton Distributions*, Eur. Phys. J. **C 12**, 375 (2000)

[75] L. Lönnblad, *Ariadne version 4 – A program for simulation of QDC cascades implementing the colour dipole model*, Comp. Phys. Comm. **71**, 15 (1992)

[76] OPAL Collab., P.D. Acton et al., *Inclusive Neutral Vector Meson Production in Hadronic Z0 Decays*, Zeit. Phys. **C 56**, 521 (1992)

[77] OPAL Collab., R. Akers et al., *Inclusive Strange Vector and Tensor Meson Production in Hadronic Z Decays*, Zeit. Phys. **C 68**, 1 (1995)

[78] ALEPH Collab., D. Buskukic et al., *Inclusive production of neutral vector mesons in hadronic Z decays*, Zeit. Phys. **C 69**, 379 (1996)

[79] DELPHI Collab., P. Abreu et al., *Measurement of Inclusive $K^{*0}(892)$, $\phi(1020)$ and $K_2^{*0}(1430)$ Production in Hadronic Z Decays*, Zeit. Phys. **C 73**, 61 (1996)

[80] ZEUS Collab., S. Chekanov et al., *Observation of the strange sea in the proton via inclusive ϕ-meson production in neutral current deep inelastic scattering at HERA*, Phys. Lett. **B 553**, 141 (2003)

[81] G.A. Schuler and T. Sjöstrand, *Low- and high-mass components of the photon distribution functions*, Zeit. Phys. **C 68**, 607 (1995)

[82] ZEUS Collab., S. Chekanov et al., *Measurement of Charm Fragmentation Ratios and Fractions in Photoproduction at HERA*, Eur. Phys. J. **C 44**, 351 (2005)

[83] Andrew Cottrell, Ph.D thesis, University of Oxford (2005)

[84] T. Sjöstrand, P. Edén, C. Friberg, L. Lönnblad, G. Miu, S. Mrenna and E. Norrbin, *High-energy-physics event generation with Pythia 6.1*, Comp Phys Commun. **135**, 238 (2001)

[85] DELPHI Collab., P. Abreu et al., *Production Characteristics of K^0 and Light Meson Resonances in Hadronic Decays of the Z*, Zeit. Phys. **C 65**, 587 (1995)

[86] E665 Collab., M. Adams et al., *Production of neutral strange particles in muon-nucleon scattering at 490 GeV*, Zeit. Phys. **C 61**, 539 (1994)

[87] S.E. Vance, M. Gyulassy and X.N. Wang, *Baryon number transport via Gluonic Junctions*, nucl-th/9806008, (1998)

[88] E791 Collab., E. M.Aitala et al., *Asymmetries in the production of lambda zero, cascade minus, and omega minus hyperons in 500 GeV/c pi minus-Nucleon Interactions*, Phys. Lett. **B 496**, 9 (2000)

[89] E769 Collab., G. A.Alves et al., *Enhanced leading production of $D^{\pm}$ and D^{*} in 250 GeV $\pi^{\pm}$-nucleon interactions*, Phys. Rev. Lett. **72**, 812 (1994) and **72**, 1946 (1994)

[90] WA92 Collab., M. Adamovich et al., *Measurements of charmed-meson production in interactions between 350 GeV/c π^{-} particles and nuclei*, Nucl. Phys. **B 495**, 3 (1997)

[91] E791 Collab., E. M.Aitala et al., *Asymmetries between the production of D_s^- and D_s^+ mesons from 500 GeV/c π^{-} nucleon interaction as functions of x_F and p_t^2*, Phys. Lett. **B 411**, 230 (1997)

[92] B. Kopeliovich and B. Povh, *Baryon Asymmetry of the Proton Sea at Low x*, Zeit. Phys. **C 75**, 693 (1997)

[93] PHENIX Collab. S. Adler et al., *Identified charged particle spectra and yields in Au+Au collisions at $\sqrt{s_{NN}}$=200 GeV*, Phys. Rev. **C 69**, 034909 (2004)

[94] G. Goldhaber et al., *Pion-pion correlations in antiproton proton annihilation events*, Phys. Rev. Lett. **3**, 181 (1959)

[95] G. Goldhaber et al., *Influence of Bose-Einstein statistics on the antiproton proton annihilation process*, Phys. Rev. **120**, 300 (1960)

[96] C. Liu, *Particle production at HERA*, Proceeding of Science 2005:110 (2005) (hep-ex/0603025)

[97] A. Galas, *Neutral- and charged-kaon Bose-Einstein correlations in DIS*, AIP Conference Proceedings Volume 792, 718 (2005)

[98] ZEUS Collab., S. Chekanov et al., *Bose-Einstein correlations in one and two dimensions in deep inelastic scattering*, Phys. Lett. **B 583**, 231 (2004)

[99] G. Alexander, *Bose-Einstein and Fermi-Dirac interferometry in particle physics*, Rep. Prog. Phys. **66**, 481 (2003)

[100] G. Goldhaber et al., *Pion-Pion Correlations in Antiproton Annihilation Events*, Phys. Rev. Lett. **3**, 181 (1959)

[101] G. Goldhaber et al., *Influence of Bose-Einstein Statistics on the Antiproton-Proton Annihilation Process*, Phys. Rev **120**, 300 (1960)

[102] ALEPH Collab., S. Schael et al., *Two-particle correlations in pp, $\bar{p}\bar{p}$, and $K^0_S K^0_S$ pairs from hadronic z decays*, Phys. Lett. **B 611**, 66 (2005)

[103] OPAL Collab., R. Akers et al., *The production of neutral kaons in Z^0 decays and their Bose-Einstein Correlations*, Zeit. Phys. **C 67**, 389 (1995)

[104] DELPHI Collab., S. Abreu et al., *Kaon interference in the hadronic decays of the Z^0*, Phys. Lett. **B 379**, 330 (1996)

[105] G. Alexander, I. Cohen and E. Levin, *The dependence of the emission size on the hadron mass*, Phys. Lett. **B 452**, 159 (1999)

[106] A. Casher, H. Neuberger and S. Nussinov, *Chromoelectric Flux Tube Model Of Particle Production*, Phys. Rev **D 20**, 179 (1979)

[107] B. Anderson, G. Gustafson and T. Sjöstrand, *Baryon Production in Jet Fragmentation and γ-Decay*, Physica Scripta **32**, 574 (1985)

[108] OPAL Collab., P.D. Acton et al., *Evidence for Chain-Like Production of Strange Baryon Pairs in Jets*, Phys. Lett. **B 305**, 415 (1993)

[109] DELPHI Collab., P. Abreu et al., *Rapidity Correlations in Lambda Baryon and Proton Production in Hadronic Z Decays*, Phys. Lett. **B 416** 247 (1998)

[110] BRAHMS Collab., M. Adamczyk et al., *The BRAHMS Experiment at RHIC*, Nucl. Instr. and Meth. **A 499**, 437 (2003)

[111] K. Heller, *In Proceedings of the 12th International Symposium on High Energy Spin Physics*, p.23, Amsterdam, Netherlands, 1996. edited by C.W. DeJager, T.J. Ketel, P.J. Muders, J.E.J. Oberski and M. Oskam-Tamboezer (World Scientific, Singapore, 1997).

[112] T.A. DeGrand and H.I. Miettinen, *Models for polarization asymmetry in inclusive hadron production*, Phys. Rev. **D 24**, 2419 (1981)

[113] J. Soffer and N.A. Törnqvist, *Origin of the polarization for inclusive* Λ *production in pp collisions*, Phys. Rev. Lett. **68**, 907 (1992)

[114] Liang Zuo-tang and C. Boros, *Hyperon Polarization and Single Spin Left-Right Asymmetry in Inclusive Production Processes at High Energies*, Phys. Rev. Lett. **79**, 3608 (1997)

[115] A. D.Panagiotou, Λ^0 *Polarization in Hadron-Nucleon Hadron-Nucleus and Nucleus-Nucleus Interactions*, International Journal of Modern Physics A, Volume 5, Issue 07, pp. 1197-1266 (1990)

[116] A. Lesnik et al., *Observation of a Difference between Polarization and Analyzing Power in* Λ^0 *Production with 6-GeV/c Polarized Protons*, Phys. Rev. Lett. **35**, 770 (1975)

[117] G. Bunce et al., Λ^0 *Hyperon Polarization in Inclusive Production by 300-GeV Protons on Beryllium*, Phys. Rev. Lett. **36**, 1113 (1976)

[118] T. DeGrand and H.I Miettinen, *Quark dynamics of polarization in inclusive hadron production*, Phys. Rev. **D 23**, 1227 (1981) and **D 24**, 2419 (1981)

[119] A. Kotzinian, A. Bravar and D. von Harrach, Λ *and* $\bar{\Lambda}$ *polarization in Lepton induced processes*, Eur. Phys. J. **C 2**, 329 (1998)

[120] M. Burkardt and R.L. Jaffe, *Polarized* $q \to \Lambda$ *fragmentation functions from* $e^+e^- \to \Lambda + X$, Phys. Rev. Lett. **70**, 2537 (1993)

[121] Particle Data Group, S. Eidelman et al., *Review of particle physics*, Phys. Lett. **B 592**, 1 (2004)

[122] M. Wing, *Setting the jet energy scale for the ZEUS calorimeter*, hep-ex/0206036